Universidade de Aveiro Departamento de Física
2011

Carlos Alberto Fernandes Marques

Energética da atmosfera global no clima actual e num clima futuro

Global atmospheric energetics under present and future climate conditions

Universidade de Aveiro Departamento de Física
2011

Carlos Alberto Fernandes Marques

Energética da atmosfera global no clima actual e num clima futuro

Global atmospheric energetics under present and future climate conditions

Dissertação apresentada à Universidade de Aveiro para cumprimento dos requisitos necessários à obtenção do grau de Doutor em Física, realizada sob a orientação científica do Prof. Doutor Alfredo Rocha, Professor associado com agregação do Departamento de Física da Universidade de Aveiro, e do Prof. Doutor João Corte-Real, Professor catedrático da Universidade de Évora.

Este trabalho foi financiado desde 01-03-2006 a 01-03-2007, por uma bolsa de doutoramento da Universidade de Aveiro.

Este trabalho foi financiado desde 01-03-2007 a 01-03-2011, por uma bolsa de doutoramento da Fundação para a Ciência e a Tecnologia (SFRH/BD/29341/2006).

universidade de aveiro

QUADRO DE REFERÊNCIA ESTRATÉGICO NACIONAL PORTUGAL 2007.2013

UNIÃO EUROPEIA
Fundo Social Europeu

This work is dedicated to my wife Sofia and our son Miguel, and to my parents, my brother and my three sisters for their lovingness and moral support.

o júri

presidente

Prof. Doutor Carlos Alberto Diogo Soares Borrego
professor catedrático da Universidade de Aveiro

Prof. Doutor Carlos do Carmo de Portugal e Castro da Câmara
professor associado da Faculdade de Ciências da Universidade de Lisboa

Prof. Doutor João Carlos Andrade dos Santos
professor auxiliar da Universidade de Trás-os-Montes e Alto Douro

Prof. Doutor José Manuel Henriques Castanheira
professor auxiliar da Universidade de Aveiro

Prof. Doutor João Alexandre Medina Corte-Real
professor catedrático aposentado da Universidade de Évora (Co-orientador)

Prof. Doutor Alfredo Moreira Caseiro Rocha
professor associado com agregação da Universidade de Aveiro (Orientador)

agradecimentos/
acknowledgements

I want to express my deep gratitude to my advisors, Professor Alfredo Rocha and Professor João Corte-Real, for their encouragement, their guidance and support throughout the course of this work.
I am also particular grateful to Professor José Castanheira for his assistance, the fruitful discussions and invaluable suggestions.
I want to thank all the climate modelling Institutions mentioned in the text, for providing the atmospheric datasets used in this study.
I am also thankful to my friends and colleagues at the Physics Department of the University of Aveiro, for their cooperation and companionship.

palavras-chave

energética da atmosfera global, dados das reanálises, modelos climáticos, clima actual, clima futuro.

resumo

Apresenta-se uma avaliação da energética da atmosfera global, segundo a decomposição básica nas componentes média zonal e das perturbações, a decomposição no domínio do número de onda zonal, e a decomposição em modos normais tridimensionais. A formulação da energética em modos normais é estendida, de modo a permitir o cálculo explícito das taxas de conversão de energia potencial disponível em energia cinética, bem como das suas taxas de geração e dissipação, nos domínios do número de onda zonal e vertical. Além disso, é proposto um novo diagrama para o ciclo da energia na atmosfera, estendido de modo a descrever o fluxo da energia nas componentes média zonal e das perturbações, e nas componentes barotrópica e baroclínica.

A energética é calculada com base em três conjuntos de dados das reanálises e em dados simulados por cinco modelos climáticos recentes, os quais são considerados como representações das condições do clima presente. Segue-se uma análise comparativa dos resultados da energética obtidos com base nos dados observados (reanálises) e simulados. De modo a estimar possíveis alterações na energética da atmosfera num cenário de clima futuro relativamente às condições de clima actual, a análise é estendida usando as simulações efectuadas pelos mesmos cinco modelos climáticos para um cenário de clima futuro, tal como definido no Relatório Especial dos Cenários de Emissões do Painel Intergovernamental para as Alterações Climáticas.

keywords global atmospheric energetics, reanalysis datasets, climate models, present climate, future climate.

abstract An evaluation of the global atmospheric energetics is presented in the framework of the basic decomposition into the zonal mean and eddy components, the zonal wavenumber decomposition, and the three-dimensional normal mode decomposition. An extension to the normal mode energetics formulation is also presented in the study, which enables the explicit evaluation of the conversion rate between available potential energy and kinetic energy along with their generation and dissipation rates, in both the zonal wavenumber and vertical mode domains. In addition, it has been proposed an extended energy cycle diagram describing the flow of energy among the zonal mean and eddy components, and also among the barotropic and baroclinic components. The energetics is first assessed for three reanalysis datasets and five state-of-the-art climate models simulations representing the present climate conditions. It is performed a comparative analysis between the observationally based energetics and that based on the climate models' simulations. In order to appraise possible changes in the atmospheric energetics of a future climate scenario relative to that of the present climate conditions, the analysis is extended using the datasets simulated by the same five climate models for a future climate scenario experiment, as defined in the Special Report on Emissions Scenarios (SRES) of the Intergovernmental Panel on Climate Change (IPCC).

Contents

List of Figures

List of Tables

List of Acronyms

20C3M	20^{th} Century Climate in Coupled Models
AMIP	Atmospheric Model Intercomparison Project
AMSU	Advanced Microwave Sounding Unit
ATOVS	Advanced TOVS
CCCma	Canadian Centre for Climate Modelling and Analysis
CCM2	Community Climate Model, version 2
CCSM3	Community Climate System Model, version 3.0
CDO	Climate Data Operators
CGCM2	second generation Coupled Global Climate Model
CGCM3.1	Third generation Coupled Global Climate Model
CMIP3	Coupled Model Intercomparison Project, phase three
CNRM-CM3	Centre National de Recherches Météorologiques Coupled global climate Model, version 3
CRIEPI	Central Research Institute of Electric Power Industry
DOE	Department of Energy
ECMWF	European Centre for Medium-Range Weather Forecasts
ERA-15	ECMWF 15-year Re-Analysis

ERA-40	ECMWF 40-year Re-Analysis
ESG	Earth System Grid
FGGE	First GARP Global Experiment
GARP	Global Atmospheric Research Program
GCM	General Circulation Model
GFDL	Geophysical Fluid Dynamics Laboratory
GHG	greenhouse gas
GISS	Goddard Institute for Space Studies
GLA	Goddard Laboratory for Atmospheres
HadAM3	Hadley Centre Atmospheric Climate Model version 3
IGY	International Geophysical Year
IPCC-AR4	Intergovernmental Panel on Climate Change - Fourth Assessment Report
JMA	Japan Meteorological Agency
JRA-25	Japanese 25-year Reanalysis
MIROC3.2	Model for Interdisciplinary Research on Climate
MPIM	Max Planck Institute for Meteorology
NCAR	National Center for Atmospheric Research
NCEP	National Centers for Environmental Prediction
NCL	NCAR Command Language

NESDIS National Environmental Satellite, Data and Information Service

NH Northern Hemisphere

NMC National Meteorological Center

NOAA National Oceanic and Atmospheric Administration

NWS National Weather Service

PCMDI Program for Climate Model Diagnosis and Intercomparison

SH Southern Hemisphere

SOP-1 First Special Observation Period

SOP-2 Second Special Observation Period

SRES Special Report on Emissions Scenarios

SSM/I Special Sensor Microwave/Imager

TOVS Television Infrared Observation Satellite Operational Vertical Sounder

UTLS Upper Troposphere/Lower Stratosphere

List of Symbols

K	Kinetic energy	1
A	Available potential energy	1
K_Z	Zonal mean kinetic energy	1
A_Z	Zonal mean available potential energy	1
K_E	Eddy kinetic energy	1
A_E	Eddy available potential energy	1
C_Z	Rate of conversion of A_Z to K_Z	6
G_E	Rate of generation of A_E	6
G_Z	Rate of generation of A_Z due to the zonally averaged heating	6
G_E	Rate of generation of A_E	6
C_A	Rate of conversion/transfer of A_Z to A_E	7
C_E	Rate of conversion of A_E to K_E	7
D_E	Rate of dissipation of K_E	7
C_K	Rate of conversion/transfer of K_E to K_Z	7
D_Z	Rate of viscous dissipation of K_Z	7
C_Z	Rate of conversion of A_Z to K_Z	7
$\mathcal{P}$	Atmospheric potential energy	11
I	Atmospheric internal energy	11
c_p	Specific heat at constant pressure	11
c_v	Specific heat at constant volume	11
P	Total potential energy	11
T	Air temperature	11

Chapter 1

Introduction

The global energy cycle in the atmosphere, which may be named more compactly as atmospheric energetics, was introduced by Lorenz (1955). Lorenz used the concept of available potential energy, by generalising the analysis of Margules (1903) for the energy budget of an individual storm to the global domain. It has laid down the foundations for a concise thermodynamical description of the atmosphere. In the formulation of Lorenz (1955) (see also Lorenz, 1967), the global energy cycle is described by a set of balance equations for the kinetic, K, and available potential, A, energies, decomposed into their zonal means, K_Z and A_Z, and eddy contributions, K_E and A_E, respectively. It accounts for the amounts of available potential and kinetic energies and the ways by which they are generated, transformed and dissipated in the atmosphere.

Since its introduction by Lorenz (1955), the energetics of the atmospheric general circulation has been further investigated with orthogonal projections of the circulation field onto various basis functions. Saltzman (1957) presented the energetics in the zonal wavenumber domain, using a zonal harmonic expansion, which allows for the analysis of energy amounts and energy conversion/transfer rates in eddies of given wavenumber as well as the interaction between the eddies. Kao (1968) and Hayashi (1980) extended the approach of Saltzman (1957) to the wavenumber-frequency domain using a two-dimensional Fourier expansion. Other expansions were also pursued in the zonal and meridional directions using a spherical harmonic expansion (Eliasen and Machenhauer,

1965; Lambert, 1984), and in the vertical direction with empirical orthogonal functions (Holmström, 1963). Tanaka (1985) and Tanaka and Kung (1988) developed a three-dimensional (3-D) normal mode energetics scheme, using the 3-D normal mode functions as the expansion basis, which have been obtained as the eigensolutions of the linearised primitive equations over a sphere by Kasahara (1976) and Kasahara and Puri (1981). The 3-D normal mode energetics combines three one-dimensional spectral energetics in domains of zonal wavenumbers, a meridional mode index and a vertical mode index. The scheme can diagnose the 3-D spectral distribution of energy and energy conversions and also the energetics characteristics of Rossby waves and gravity waves, and the energy conversion between the barotropic and baroclinic modes (Tanaka and Kung, 1988).

With the recognition of the energy cycle there is the problem of explaining its intensity and accounting for the directions in which the various steps proceed, which may be more complicated than it might at first seem to be (Lorenz, 1967). For example, based on numerous observational studies, the eddy transport of heat is mainly toward colder latitudes, as classical turbulence theory would suggest, so that A_Z is converted into A_E. On the other hand, the eddy transport of angular momentum is on the average toward latitudes of higher angular velocity, so that K_E is converted into K_Z, which is the opposite of what would be predicted by classical turbulence theory (Lorenz, 1967). Therefore, it was only through observations that the direction of the energy cycle has been ascertained.

Following different analysis schemes, the atmospheric energetics has been assessed in many studies for observations/analysis. One of the first tentatives to select representative values for the yearly energy cycle in the Northern Hemisphere (NH) was provided by Oort (1964), based on a critical survey of statistics obtained by several investigators. Krueger et al. (1965) used atmospheric temperature and geopotential height data analysed at the National Weather Service (NWS) of National Oceanic and Atmospheric Administration (NOAA), for the area north of 20 ° N, to identify the annual cycle in some of the energetics terms. Their work was extended in the spectral domain by Wiin-Nielsen (1967). The work of Oort (1964) has been extended by Peixoto and Oort (1974)

and Oort and Peixoto (1974), giving a detailed description of the annual cycle of the energetics of the atmosphere. Their estimates were based in the collection of five years of daily upper air data from more than 600 radiosonde stations, encompassing the region north of 15° S. A review of several observational studies concerning the atmospheric energetics in the wavenumber domain was given by Saltzman (1970). He showed that the kinetic energy is generated at the synoptic scale wavenumbers ($\sim n = 5 - 10$), being transferred to both planetary waves and short waves. Nevertheless, the need for further work has been acknowledged by Saltzman (1970) due to the inadequacies of data coverage, since those studies where all based on data for NH with variable spatial extent, and also due to imbalances and omissions, as the maximum wavenumber used in the analysis. In fact, most of the earlier computations of the energy components of the atmosphere were based on data sets encompassing, at best, the region north of 15° S. An assessment of the cycle of the energetics in the Southern Hemisphere (SH) is given in Peixoto and Corte-Real (1982, 1983), obtained from direct values of the observations of temperature, wind and geopotential taken during the calendar year 1958 of the International Geophysical Year (IGY) in more than hundred SH stations.

The balance equations for the energetics of a system with at least an open boundary, as is the atmosphere of the NH or SH, needs extra terms in order to account for the flux of energy across that boundary. Due to the lack of data for the whole atmosphere, this approach had to be adopted in the earlier studies, although without a rigorous justification because the concept of available potential energy cannot be rigorously defined for a portion of the atmosphere, since it is a property of the entire atmosphere (Lorenz, 1955). The availability of the data sets from the First Global Atmospheric Research Program (GARP) Global Experiment (FGGE) has relieved the energetics studies from the difficulty of inadequate coverage of the reporting upper air stations. The four-dimensional (4-D) assimilation of an unprecedented volume of atmospheric data during the FGGE period provided adequate global grid coverage for an energetics evaluation at a global scale. A global energetics analysis for two separate sets of FGGE data, during the first and second special observation periods (SOP-1 and SOP-2) of FGGE, pro-

duced by the European Centre for Medium-Range Weather Forecasts (ECMWF) and the Geophysical Fluid Dynamics Laboratory (GFDL), was made by Kung and Tanaka (1983). Their analysis revealed a large discrepancy between the FGGE analysis and previous estimates for the levels of kinetic and available potential energies, which was attributed to the earlier restriction of data coverage. In addition, they found considerable differences between the energy transformations obtained with the ECMWF and GFDL data versions, that was traced to the specific 4-D data assimilation processes involved in each FGGE data production. It was noted that the GFDL analysis of the FGGE data is noisy, containing excessive small-scale structures, and is unbalanced for the mass and momentum fields. The over excitation of the small-scale disturbances resulted mainly from the continuous data insertion in the GFDL analysis scheme. On the other hand, the vertical velocity is too weak in the ECMWF, and the divergent wind is damped by a factor of two due to the adiabatic version of the nonlinear normal mode initialisation of the ECMWF (Kung and Tanaka, 1983).

Based on the knowledge gained after the FGGE, the original analyses data sets were later re-analysed by the ECMWF and the GFDL. Using the normal mode energetics scheme, Tanaka and Ji (1995) found that the GFDL re-analysis is now smoother, and the ECMWF re-analysis contains much divergent wind. However, they also found that the discrepancy in the gravity mode energy between the ECMWF and GFDL has been grown rather than been reduced by the re-analysis. Therefore, the models and techniques involved in data assimilation may influence the data sets produced and consequently their energetics, as pointed out by Kung and Tanaka (1983) and Lorenc and Swinbank (1984). Using the normal mode energetics scheme, Tanaka and Kimura (1996) concluded that the total energy levels of the gravity modes in more recent operational global analysis by the ECMWF, the National Meteorological Center (NMC) and the Japan Meteorological Agency (JMA) are converging to the value of ECMWF FGGE re-analysis data.

The atmospheric energetics became a usefull tool to analyse important characteristic processes of the general circulation of the observed atmosphere, and to assess the per-

formance of global atmospheric/climate models. For example, an energetics analysis of the Goddard Institute for Space Studies (GISS) model is given in Tenenbaum (1975), where indirect conclusions concerning unresolved subgrid-scale processes were possible from a wavenumber energetics analysis. Using a 3-D normal mode expansion, Tanaka et al. (1989) found that the gravity mode energy levels in the Goddard Laboratory for Atmospheres (GLA) General Circulation Model (GCM) were significantly reduced in the higher wavenumbers and higher order vertical modes, and that the prediction error of the model was reduced in the planetary waves of the barotropic mode and in the synoptic waves of the baroclinic modes, by the increase of horizontal resolution. Based on a comparative energetics analysis of the National Center for Atmospheric Research (NCAR) Community Climate Model, version 2 (CCM2) with different horizontal resolutions, Hasegawa et al. (1997) found that the large-scale zonal motions are diffusive against the short waves beyond wavenumber 30, which can be parameterized by various forms of the diffusion schemes. Hence, the results obtained in previous studies that K_Z is supplied by the eddies, in terms of zonal-wave interactions of kinetic energy, is only valid for wavenumbers up to about 30. Additionally, a minimum model resolution of T42 has been suggested by Hasegawa et al. (1997) in order to represent the general circulation properly.

In the last two decades, various reanalysis cooperating projects have been established to fulfil the needs of global atmospheric datasets for the climate research communities. The target of a reanalysis project is to produce a consistent and high-quality historical analysis dataset using a frozen state-of-the-art analysis/forecast model and a data assimilation system. Following the advent of high-quality datasets, the atmospheric energetics has been continuously assessed both for observations/analysis (e.g. Watarai and Tanaka, 2007; Li et al., 2007; Terasaki and Tanaka, 2007a; Marques et al., 2009, 2010a) and for global atmospheric/climate models (e.g. Ulbrich and Ponater, 1992; Boer and Lambert, 2008; Marques et al., 2010b). The comparison between the earlier and the more recent estimates, expose noticeable discrepancies in some of the energy components and conversion/transfer rates. These must be related to the inferiority of the

old datasets in density, continuity, and quality of observation and physical consistency and uniformity of data (Li et al., 2007). Some of the discrepancies between the various energetics estimates can also be attributed to specific characteristics of the analysis scheme used, as, for example, the different methods of separating the total kinetic and available potential energies, which have been reviewed in Oort (1964).

Despite the limitations of the old datasets, which have clearly improved in the modern reanalysis datasets, many features of the earlier studies still hold true. Even the data assimilated by reanalysis, such as radiosondes and satellite retrievals, contains spurious errors, drifts, and discontinuities. However, there has been a considerably better agreement, both qualitative and quantitative, between the various energetics estimates within the more recent studies, which should be associated to the higher quality of the present atmospheric datasets. The numerous earlier energetics studies were mostly in a qualitative agreement, the only exceptions being the directions for the conversion of A_Z into K_Z, term C_Z, and for the generation of eddy available potential energy, term G_E. Estimated values for these two terms have been yielding opposite signs among different investigators, depending also on the time periods and the extent of the spatial domain used in each estimate.

Based in the more recent estimates, including three observationally-based estimates by Marques et al. (2010a), the maintenance of the atmospheric general circulation, characterised by the Lorenz energy cycle within its decomposition into zonal mean and eddy components, may be illustrated as in Figure 1.1. The four boxes represent the reservoirs for each energy form and the arrows indicate the directions in which the energy flows. Climatologically, the global energy cycle may be described as follows (This follows closely the earlier description provided by Lorenz (1955), except for the directions in terms C_Z and G_E): The net heating of the atmosphere in the warmer low latitudes and the net cooling in the colder high latitudes generates (term G_Z) zonal mean available potential energy A_Z. Some A_E is also generated by heating processes, possibly by the release of latent heat in warm regions (term G_E). Due to baroclinic instabilities, almost all the energy generated in A_Z is converted (or transferred) into

eddy available potential energy A_E, through horizontal and vertical transport of sensible heat by the eddies across the temperature gradient (term C_A), and then $G_E + C_A$ is converted into eddy kinetic energy K_E, by rising of warmer air and sinking of colder air at the same latitude (term C_E). A large part of this energy is dissipated by friction (term D_E) and the remainder is converted (or transferred) into zonal mean kinetic energy K_Z, through horizontal and vertical transport of angular momentum by the eddies (term C_K), which are related to wave-mean flow interactions, being afterwards dissipated by friction (term D_Z). The direct conversion between A_Z and K_Z (term C_Z) is related to the zonal mean meridional overturnings. This involves processes like the Hadley cell, where mostly A_Z is converted into K_Z, but also the indirect Ferrel cells, where mostly K_Z is converted into A_Z. The net result of this conversion term tends to be close to zero, although the estimates mentioned above have yielded a small positive value for C_Z.

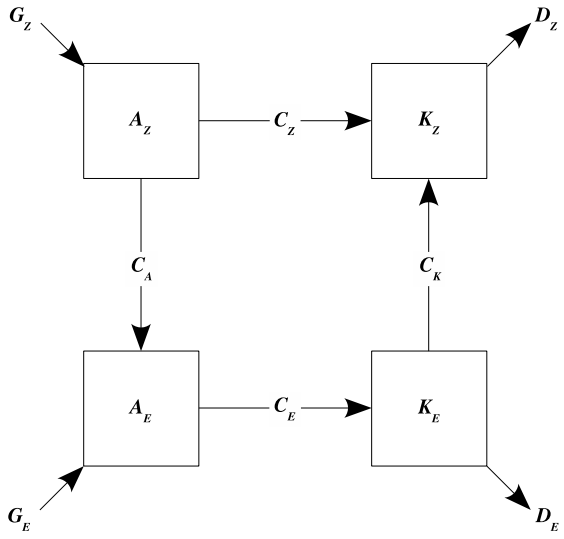

Figure 1.1: Lorenz energy cycle diagram.

Beyond an exclusive assessment of the flow of energy in the atmosphere, several studies have also been conducted using atmospheric energetics schemes on the analysis of specific atmospheric phenomena. For example, the effects of wave-wave and wave-mean flow interactions on the growth and maintenance of extratropical tropospheric transient waves in the presence of a mean thermal restoring force, were studied by Hayashi and Golder (1987). They have found that the wave-wave interactions play a more important role in the growth of ultralong waves than in their maintenance, implying that the energy transfer by nonlinear wave-wave interactions is sensitive to phase relations and is more efficient during the growing stage. Wavenumber and normal mode energetics were used by Kung et al. (1989) for the examination of winter blocking simulations in the NH with the GLA GCM. Enough kinetic energy was simulated at the synoptic-scale range, but the energy transfer from this source to wavenumber 1 was insufficient, due in part to the coarse model resolution. The characteristics of the energy slope for the barotropic component of the atmosphere have been examined in the framework of the 3-D normal mode energetics by Terasaki and Tanaka (2007b). Their results show that the spectral slope agrees quite well with the -4 power law for the barotropic component of the atmosphere, which is consistent from what is inferred from the Rossby wave saturation theory (Tanaka et al., 2004). Observational evidence of an increase of the baroclinic wave components in the Upper Troposphere/Lower Stratosphere (UTLS) circulation, during the second half of the 20^{th} century was given by Castanheira et al. (2009). The evidence is given by significant positive trends in the energy of baroclinic normal modes of the National Centers for Environmental Prediction (NCEP)/NCAR reanalysis, and significant positive trends in the UTLS eddy available potential energy of the NCEP/NCAR, ECMWF 40-year Re-Analysis (ERA-40), NCEP/Department of Energy (DOE) and Japanese 25-year Reanalysis (JRA-25) reanalyses.

In this study the atmospheric energetics is evaluated in the framework of the basic decomposition of zonal mean and eddy components of Lorenz (1955), the zonal wavenumber decomposition of Saltzman (1957), and the 3-D normal mode energetics scheme of Tanaka (1985). An extension to the normal mode energetics formulation

is presented in the study, which enables an explicit evaluation of the conversion rate between available potential energy and kinetic energy along with their generation and dissipation rates, in both the zonal wavenumber and vertical mode domains. In addition, it is proposed an extended energy cycle diagram describing the flow of energy among the zonal mean and eddy components, and also among the barotropic and baroclinic components. The energetics is first assessed for three reanalysis datasets and five state-of-the-art climate models simulations representing the present climate conditions. The analysis is then extended using the datasets simulated by the same five climate models for a future climate scenario, as defined in the Special Report on Emissions Scenarios (SRES) of the Intergovernmental Panel on Climate Change (IPCC).

The relevant theoretical background is accounted in Chapter 2, with further details given in Appendix A. The observationally-based and simulation-based datasets are described in Chapter 3, along with the adopted methodology. An energetics analysis, assessed from both the observationally-based and simulation-based datasets, that represent the present climate, is presented in Chapter 4. Chapter 5 discusses the energetics obtained from the climate models simulations for both the present climate and future climate scenario. The summary and conclusions of this study are finally addressed in Chapter 6.

Chapter 2

Theoretical Framework

2.1 The concept of available potential energy

The sequence of events through which a small portion of solar energy reaching the earth is converted into kinetic energy of the atmospheric motions, replacing thereby kinetic energy dissipated by friction, led Lorenz (1955) to the concept of *available potential energy*. It is essentially a measure of how much energy contained in the atmosphere in the form of heat and potential energy, is *available* for conversion into kinetic energy.

The only relevant sources for the kinetic energy of the whole atmosphere are atmospheric potential and internal energies, $\mathcal{P}$ and I respectively, which under hydrostatic equilibrium bear a constant ratio to each other, $\mathcal{P}/I = (c_p - c_v)/c_v$ (Lorenz, 1955). It is therefore convenient to combine these two forms of energy into only one form, which is usually called *total potential energy*, $P = \mathcal{P} + I$. Thus, since $I = c_v \mathrm{T}$, the total potential energy, P, integrated over the mass, $\mathcal{M}$, of the whole atmosphere is given by

$$P = \int_{\mathcal{M}} c_p \,\mathrm{T}\,\mathrm{d}m = \frac{1}{g}\int_0^{p_s}\int_S c_p \,\mathrm{T}\,\mathrm{d}s\,\mathrm{d}p, \tag{2.1}$$

where c_v is the specific heat at constant volume, c_p the specific heat at constant pressure and T the temperature. A complete description of the symbols used here, which are mostly customary, may be found in the **List of Symbols**. Substituting $\mathrm{T} = \Theta\, p^{\chi}\, p_0^{-\chi}$

into (2.1), yields

$$P = \frac{c_p}{g\, p_0^{\chi}} \int_0^{p_s} \int_S \Theta\, p^{\chi}\, \mathrm{d}s\, \mathrm{d}p, \tag{2.2}$$

where $p_0 = 1000$ hPa, $\chi = R/c_p$, Θ is the potential temperature and R the specific gas constant. Integrating equation (2.2) by parts yields

$$P = \frac{c_p}{g\, p_0^{\chi}\,(1+\chi)} \left(\int_S \left[\Theta\, p^{1+\chi}\right]_0^{p_s} \mathrm{d}s - \int_0^{p_s} \int_S p^{1+\chi}\, \mathrm{d}s\, \frac{\mathrm{d}\Theta}{\mathrm{d}p} \mathrm{d}p \right), \tag{2.3}$$

or, since $\Theta = \infty$ at $p = 0$ and denoting $\Theta = \Theta_s$ at $p = p_s$,

$$P = \frac{c_p}{g\, p_0^{\chi}\,(1+\chi)} \left(\int_S \left[\Theta\, p^{1+\chi}\right]_0^{p_s} \mathrm{d}s + \int_{\Theta_s}^{\infty} \int_S p^{1+\chi}\, \mathrm{d}s\, \mathrm{d}\Theta \right). \tag{2.4}$$

Since $\Theta\, p^{1+\chi} \to 0$ when $p \to 0$ (e.g. Dutton, 1995), equation (2.4) may be written as

$$P = \frac{c_p}{g\, p_0^{\chi}\,(1+\chi)} \left(\int_S \Theta_s\, {p_s}^{1+\chi}\, \mathrm{d}s + \int_{\Theta_s}^{\infty} \int_S p^{1+\chi}\, \mathrm{d}s\, \mathrm{d}\Theta \right), \tag{2.5}$$

Using an extended definition of $p(\Theta)$ below the earth's surface ($p > p_s$) regarded as horizontal, in which $p(\Theta) = p_s$ for all subsurface $\Theta \leq \Theta_s$, equation (2.5) is written as

$$P = \frac{c_p}{g\, p_0^{\chi}\,(1+\chi)} \left(\int_S \int_0^{\Theta_s} p^{1+\chi}\, \mathrm{d}\theta\, \mathrm{d}s + \int_{\Theta_s}^{\infty} \int_S p^{1+\chi}\, \mathrm{d}s\, \mathrm{d}\Theta \right), \tag{2.6}$$

Therefore, the expression for the total potential energy may be written as

$$P = \frac{c_p}{g\, p_0^{\chi}\,(1+\chi)} \int_0^{\infty} \int_S p^{1+\chi}\, \mathrm{d}s\, \mathrm{d}\Theta. \tag{2.7}$$

The minimum total potential energy which can result from an adiabatic rearrangement of mass occurs when $p = \widetilde{p}$ everywhere, and is obtained setting $p = \widetilde{p}$ in (2.7), where the wavy bar denotes an average over an isentropic surface. The portion of total potential energy that is available for conversion into kinetic energy is the difference between the total potential energy and the minimum total potential energy which could result from any adiabatic redistribution of mass. As such, this quantity was called by Lorenz (1955) as available potential energy, A, and is given by

$$A = \frac{c_p}{g\, p_0^{\chi}\,(1+\chi)} \int_0^{\infty} \int_S \left(p^{1+\chi} - \widetilde{p}^{\,1+\chi}\right) \mathrm{d}s\, \mathrm{d}\Theta. \tag{2.8}$$

Under hydrostatic equilibrium and neglecting topography, equation (2.8) is the exact formula for A. However, equation (2.8) is not very usefull for numerical computations since the atmospheric data are usually given at pressure levels rather than isentropic levels. Additionally, the features of the atmosphere which are associated with significant amounts of A may not be apparent (Lorenz, 1967). This led Lorenz (1955) to devise an approximate expression for A with pressure as the vertical coordinate. He obtained the approximation by observing first that since $p > 0$, $\chi > 0$ and $\widetilde{p}$ is an average of p, the integral of $p^{1+\chi} - \widetilde{p}^{1+\chi}$ is positive definite for each isentropic surface. Second, provided that the isentropic surfaces are not too greatly inclined to the horizontal, the variance of p on an isentropic surface may be approximated in terms of the variance of Θ on an isobaric surface. Thus, if $p = \widetilde{p} + p''$, where the double prime denotes the deviations from the average over an isentropic surface, and using the binomial theorem

$$(a+b)^n = \sum_{i=0}^{n} \frac{n!}{i!\ (n-i)!} a^{n-i}\, b^i, \tag{2.9}$$

applied to $p^{1+\chi} = (\widetilde{p} + p'')^{1+\chi}$, results in

$$\begin{aligned}
(\widetilde{p} + p'')^{1+\chi} &= \sum_{i=0}^{1+\chi} \frac{(1+\chi)!}{i!\ (1+\chi-i)!}\, \widetilde{p}^{\,1+\chi-i}\, (p'')^i \\
&= \frac{(1+\chi)!}{0!\ (1+\chi)!}\, \widetilde{p}^{\,1+\chi} + \frac{(1+\chi)!}{1!\ (\chi)!}\, \widetilde{p}^{\,\chi}\, p'' + \frac{(1+\chi)!}{2!\ (\chi-1)!}\, \widetilde{p}^{\,\chi-1}\, (p'')^2 + \cdots \\
&= \widetilde{p}^{\,1+\chi} + (1+\chi)\, \widetilde{p}^{\,\chi}\, p'' + \frac{(1+\chi)\chi(\chi-1)!}{2!\ (\chi-1)!}\, \widetilde{p}^{\,\chi-1}\, (p'')^2 + \cdots \\
&= \widetilde{p}^{\,1+\chi} \left[1 + (1+\chi)\frac{p''}{\widetilde{p}} + \frac{(1+\chi)\chi}{2!} \left(\frac{p''}{\widetilde{p}} \right)^2 + \cdots \right].
\end{aligned} \tag{2.10}$$

Hence,

$$\begin{aligned}
p^{1+\chi} - \widetilde{p}^{\,1+\chi} &= \widetilde{p}^{\,1+\chi} \left[1 + (1+\chi)\frac{p''}{\widetilde{p}} + \frac{(1+\chi)\chi}{2!} \left(\frac{p''}{\widetilde{p}} \right)^2 + \cdots + (-1) \right] \\
&= \widetilde{p}^{\,1+\chi} \left[(1+\chi)\frac{p''}{\widetilde{p}} + \frac{(1+\chi)\chi}{2!} \left(\frac{p''}{\widetilde{p}} \right)^2 + \cdots \right].
\end{aligned} \tag{2.11}$$

In (2.11), the term containing $p''/\widetilde{p}$ will vanish in the horizontal integration when introduced into (2.8). In addition, the expansion is well represented by its remaining leading term, as was shown by Lorenz (1955) in a rather extreme case. Therefore, equation

(2.8) may be approximated as

$$A = \frac{\chi\, c_p}{2\, g\, p_0^{\chi}} \int_0^{\infty} \int_S \widetilde{p}^{\,1+\chi} \left(\frac{p''}{\widetilde{p}}\right)^2 \mathrm{d}s\, \mathrm{d}\Theta. \tag{2.12}$$

If $\widetilde{\Theta}$ and $\widetilde{\mathrm{T}}$ are the averages of Θ and T over an isobaric surface, and Θ'' and T'' the deviations from this average, the function $\widetilde{\Theta}(p)$ is not completely determined by the function $\widetilde{p}(\Theta)$ but approximately $p = \widetilde{p}(\widetilde{\Theta}(p))$, provided that the isentropic surfaces are not too greatly inclined to the horizontal (Lorenz, 1955, 1967). That is, for example, let $p = 500$ hPa and $\widetilde{\Theta}(p = 500) = 300$ K, then approximately $p = \widetilde{p}(300) = 500$ hPa. Then, one may write

$$\begin{aligned} p'' &= p(\Theta) - \widetilde{p}(\Theta) \\ &= \widetilde{p}(\widetilde{\Theta}(p)) - \widetilde{p}(\Theta) \\ &= \widetilde{p}(\Theta - \Theta'') - \widetilde{p}(\Theta), \end{aligned} \tag{2.13}$$

or, by expanding (2.13) in Taylor series

$$p'' \simeq -\Theta'' \frac{\partial \widetilde{p}}{\partial \Theta}. \tag{2.14}$$

An equivalent relation to that of equation (2.14) is proved in Grotjahn (1993). Thus, (2.12) is written as

$$A = \frac{\chi\, c_p}{2\, g\, p_0^{\chi}} \int_0^{\infty} \int_S \frac{\widetilde{p}^{\,1+\chi}}{\widetilde{p}^{\,2}} \left(-\Theta'' \frac{\partial \widetilde{p}}{\partial \Theta}\right)^2 \mathrm{d}s\, \mathrm{d}\Theta. \tag{2.15}$$

The expression for available potential energy, A, with pressure as vertical coordinate may now be written by replacing the averages over isentropic surfaces by averages over isobaric surfaces, i.e. $\widetilde{p}$ is replaced by p, $\partial\widetilde{p}$ by ∂p and $\partial\Theta$ by $\partial\widetilde{\Theta}$. Therefore, using

$$\mathrm{d}\Theta = \frac{\partial \Theta}{\partial p} \mathrm{d}p, \tag{2.16}$$

equation (2.15) is written as

$$A = \frac{\chi\, c_p}{2\, g} \int_{p_s}^{0} \int_S \left(\frac{p}{p_0}\right)^{\chi} \frac{\Theta^2}{p} \left(\frac{\Theta''}{\Theta}\right)^2 \left(-\frac{\partial \widetilde{\Theta}}{\partial p}\right)^{-1} \mathrm{d}s\, (-\mathrm{d}p)\,. \tag{2.17}$$

Since $\Theta''\Theta^{-1} = \mathrm{T}''\mathrm{T}^{-1}$, then

$$\begin{aligned} A &= \frac{\chi\, c_p}{2\, g} \int_0^{p_s} \int_S \left(\frac{p}{p_0}\right)^{\chi} \frac{\mathrm{T}^2}{p} \left(\frac{p_0}{p}\right)^{2\chi} \left(\frac{\mathrm{T}''}{\mathrm{T}}\right)^2 \left(-\frac{\partial\widetilde{\Theta}}{\partial p}\right)^{-1} \mathrm{d}s\, \mathrm{d}p \\ &= \frac{c_p}{2\, g} \int_0^{p_s} \int_S \frac{R}{p\, c_p} \frac{\Theta}{\mathrm{T}} \left(-\frac{\partial\widetilde{\Theta}}{\partial p}\right)^{-1} \left(\mathrm{T}''\right)^2 \mathrm{d}s\, \mathrm{d}p \\ &= \frac{c_p}{2\, g} \int_0^{p_s} \int_S \gamma \left(\mathrm{T}''\right)^2 \mathrm{d}s\, \mathrm{d}p, \end{aligned} \tag{2.18}$$

where γ represents the stability parameter, and is given by

$$\gamma = -\frac{R}{p\, c_p} \frac{\Theta}{\mathrm{T}} \left(\frac{\partial\widetilde{\Theta}}{\partial p}\right)^{-1}. \tag{2.19}$$

2.2 Atmospheric energetics

2.2.1 Fundamental equations

Using the fact that, to a high degree of accuracy, the atmosphere is in a state of hydrostatic equilibrium, we may take the pressure, p, as the vertical coordinate. Thus, neglecting the Coriolis-force terms involving the vertical component of the wind, the equations of motion, the continuity equation, the thermodynamical energy equation and the equation of state may be expressed as follows in spherical coordinates (e.g.

Saltzman, 1957):

$$\frac{\partial u}{\partial t} + \vec{V} \cdot \nabla u + \omega \frac{\partial u}{\partial p} = v \left(f + \frac{u \tan\theta}{a} \right) - \frac{g}{a \cos\theta} \frac{\partial z}{\partial \lambda} - F_u, \tag{2.20}$$

$$\frac{\partial v}{\partial t} + \vec{V} \cdot \nabla v + \omega \frac{\partial v}{\partial p} = -u \left(f + \frac{u \tan\theta}{a} \right) - \frac{g}{a} \frac{\partial z}{\partial \theta} - F_v, \tag{2.21}$$

$$0 = -g \frac{\partial z}{\partial p} - \alpha, \tag{2.22}$$

$$\frac{\partial \omega}{\partial p} = -\nabla \cdot \vec{V} = -\left(\frac{1}{a \cos\theta} \frac{\partial u}{\partial \lambda} + \frac{1}{a} \frac{\partial v}{\partial \theta} - \frac{v \tan\theta}{a} \right), \tag{2.23}$$

$$q = c_p \frac{\mathrm{dT}}{\mathrm{d}t} - \omega\alpha, \tag{2.24}$$

$$\alpha = \frac{R\mathrm{T}}{p}, \tag{2.25}$$

where $f = 2\Omega \sin\theta$, $\nabla = \hat{\imath} \frac{1}{a \cos\theta} \frac{\partial}{\partial \lambda} + \hat{\jmath} \frac{1}{a} \frac{\partial}{\partial \theta}$ and $\vec{V} = u\hat{\imath} + v\hat{\jmath}$, which denote the Coriolis parameter, the Del operator in a pressure surface and the two-dimensional horizontal wind vector, respectively.

2.2.2 Zonal mean and eddy energetics

By decomposing the field of motion onto the mean zonal motion and associated eddies, the atmospheric kinetic energy, K, may be partitioned into *zonal mean kinetic energy*, K_Z, and *eddy kinetic energy*, K_E, which corresponds essentially to an analysis of variance of the wind field. A similar analysis of variance is possible for the temperature field, leading thereby to a partion of available potential energy into *zonal mean available potential energy*, A_Z, and *eddy available potential energy*, A_E. The maintenance of each type of energy, the ways by which they are generated, transformed and dissipated in the atmosphere, characterises the atmospheric energy cycle, which is described by a set of balance equations for each type of energy.

The set of balance equations for K_Z, K_E, A_Z and A_E, may be derived from equations (2.20) to (2.25) by applying suitable averaging processes (see Appendix A). They may be written as

$$\frac{\partial}{\partial t}K_Z = C_K + C_Z - D_Z, \tag{2.26}$$

$$\frac{\partial}{\partial t}K_E = -C_K + C_E - D_E, \tag{2.27}$$

$$\frac{\partial}{\partial t}A_Z = -C_Z - C_A + G_Z, \tag{2.28}$$

$$\frac{\partial}{\partial t}A_E = C_A - C_E + G_E, \tag{2.29}$$

where,

$$K_Z = \int_{\mathcal{M}} \frac{[u]^2 + [v]^2}{2}\,\mathrm{d}m, \tag{2.30}$$

$$K_E = \int_{\mathcal{M}} \frac{\left[(u^*)^2\right] + \left[(v^*)^2\right]}{2}\,\mathrm{d}m, \tag{2.31}$$

$$A_Z = \int_{\mathcal{M}} \gamma\,\frac{c_p}{2}\,\left([\mathrm{T}]''\right)^2\,\mathrm{d}m, \tag{2.32}$$

$$A_E = \int_{\mathcal{M}} \gamma\,\frac{c_p}{2}\,\left[(\mathrm{T}^*)^2\right]\,\mathrm{d}m, \tag{2.33}$$

$$\begin{aligned} C_K = \int_{\mathcal{M}} \Bigg(& [u^*v^*]\,\frac{\cos\theta}{a}\frac{\partial}{\partial\theta}\left(\frac{[u]}{\cos\theta}\right) + [v^*v^*]\,\frac{1}{a}\frac{\partial\,[v]}{\partial\theta} - [u^*u^*]\,[v]\,\frac{\tan\theta}{a} \\ & + [u^*\omega^*]\,\frac{\partial\,[u]}{\partial p} + [v^*\omega^*]\,\frac{\partial\,[v]}{\partial p}\Bigg)\,\mathrm{d}m, \end{aligned} \tag{2.34}$$

$$\begin{aligned} C_Z &= -\int_{\mathcal{M}} \frac{g}{a}\,[v]\,\frac{\partial\,[z]}{\partial\theta}\,\mathrm{d}m \\ &= -\int_{\mathcal{M}} \frac{R}{p}\,[\omega]''\,[\mathrm{T}]''\,\mathrm{d}m, \end{aligned} \tag{2.35}$$

$$D_Z = -\int_{\mathcal{M}} \left([u]\,[F_u] + [v]\,[F_v]\right)\,\mathrm{d}m, \tag{2.36}$$

$$C_E = -\int_{\mathcal{M}} \left(\frac{g}{a\cos\theta} \left[u^* \frac{\partial z^*}{\partial \lambda} \right] + \frac{g}{a} \left[v^* \frac{\partial z^*}{\partial \theta} \right] \right) \mathrm{d}m$$
$$= -\int_{\mathcal{M}} \frac{R}{p} \left[\omega^* \mathrm{T}^* \right] \, \mathrm{d}m, \tag{2.37}$$

$$D_E = -\int_{\mathcal{M}} \left([u^* F_u^*] + [v^* F_v^*] \right) \mathrm{d}m, \tag{2.38}$$

$$C_A = -\int_{\mathcal{M}} \gamma \, c_p \left([v^* \mathrm{T}^*] \, \frac{1}{a} \frac{\partial [\mathrm{T}]}{\partial \theta} + [\omega^* \mathrm{T}^*] \, \frac{\mathrm{T}}{\Theta} \frac{\partial [\Theta]''}{\partial p} \right) \mathrm{d}m, \tag{2.39}$$

$$G_Z = \int_{\mathcal{M}} \gamma \, [\mathrm{T}]'' \, [q]'' \, \mathrm{d}m, \tag{2.40}$$

$$G_E = \int_{\mathcal{M}} \gamma \, [\mathrm{T}^* q^*] \, \mathrm{d}m, \tag{2.41}$$

and the square brackets, [ ], denoting the zonal mean operator and the asterisk, $*$, the deviation from the zonal mean. The stability parameter γ is given by (2.19).

The left-hand sides of (2.26)-(2.29) contain the rates of change of each energy type. The energy conversion/transfer terms appear with opposite signs in these equations. Term C_K represents the transfer from eddy to zonal mean kinetic energy, terms C_Z and C_E the conversions of available potential energy to kinetic energy in the mean and eddy components of the flow, respectively, and C_A the transfer from zonal mean to eddy available potential energy. The dissipation of zonal and eddy kinetic energy, D_Z and D_E respectively, and the generation of zonal and eddy available potential energy, G_Z and G_E respectively, complete the balance of energy. The two alternative expressions for C_Z and C_E, in (2.35) and (2.37) respectively, are equivalent provided that global integrals are considered (Peixoto and Oort, 1992).

2.2.3 Energetics in the zonal wavenumber domain

As mentioned in the previous section, the global energy cycle derived by Lorenz (1955) is described by a set of balance equations for the kinetic and available potential energies, partitioned into their zonal mean and eddy contributions. Further decomposition of the

eddies has been proposed by Saltzman (1957), by applying a Fourier analysis along the latitude circles, which is considered bellow.

The basic equations (2.20) to (2.24) may be transformed from the space domain to the wavenumber domain, by multiplying them by $\frac{1}{2\pi}e^{-in\lambda}$, integrating around a latitude circle, and using relations (A.32) to (A.37) and (A.39), given in Appendix A (section A.2.1). By applying a similar procedure used to derive the balance equations (2.26), (2.27), (2.28) and (2.29) to the basic equations in the wavenumber domain, Saltzman (1957) obtained the balance equations in the wavenumber space corresponding to (2.26), (2.27), (2.28) and (2.29). These equations may be written as:

$$\frac{\partial}{\partial t}K(0) = \sum_{n=1}^{\infty} M(n) + C(0) - D(0), \tag{2.42}$$

$$\frac{\partial}{\partial t}K(n) = -M(n) + L(n) + C(n) - D(n), \tag{2.43}$$

$$\frac{\partial}{\partial t}A(0) = -\sum_{n=1}^{\infty} R(n) - C(0) + G(0), \tag{2.44}$$

$$\frac{\partial}{\partial t}A(n) = R(n) + S(n) - C(n) + G(n). \tag{2.45}$$

In Appendix A (section A.2), the derivation of equations (2.42) to (2.45) is presented, along with the detailed expressions for all its terms.

The set of equations derived by Lorenz (1955) may be obtained from those of Saltzman (1957) by summing Equations (2.43) and (2.45) over all wavenumbers, excluding wavenumber zero, and noting that $\sum_{n=1}^{\infty} S(n) = \sum_{n=1}^{\infty} L(n) = 0$. The correspondence between the terms in both formulations is as follows

$$A_Z = A(0) \qquad A_E = \sum_{n=1}^{\infty} A(n) \qquad K_Z = K(0) \qquad K_E = \sum_{n=1}^{\infty} K(n)$$

$$C_A = \sum_{n=1}^{\infty} R(n) \qquad C_E = \sum_{n=1}^{\infty} C(n) \qquad C_K = \sum_{n=1}^{\infty} M(n) \qquad C_Z = C(0)$$

$$G_Z = G(0) \qquad G_E = \sum_{n=1}^{\infty} G(n) \qquad D_Z = D(0) \qquad G_E = \sum_{n=1}^{\infty} G(n)$$

According to Saltzman (1957), the terms $L(n)$ and $S(n)$ in (2.43) and (2.45), respectively, which do not have counterpart in (2.27) and (2.29) since they sum to zero, are measures of energy transfer, due to nonlinear interactions, between a disturbance of a given wavenumber and disturbances of all other wavenumbers. Therefore, these terms are usually called as wave-wave interactions of kinetic and available potential energy, respectively. On this basis, terms $M(n)$ and $R(n)$ may be called as zonal-wave interactions of kinetic and available potential energy, respectively. The conversion rates of available potential energy of wavenumber n to eddy kinetic energy of wavenumber n and of zonal mean available potential energy to zonal mean kinetic energy are given by the terms $C(n)$ and $C(0)$, respectively. Terms $G(n)$ and $G(0)$, represent the generation rates of available potential energy of wavenumber n due to nonadiabatic heating and of zonal mean available potential energy due to the zonally averaged heating, respectively, while $D(n)$ and $D(0)$ give the viscous dissipation rates of the kinetic energy of eddies of wavenumber n and of zonal mean kinetic energy.

The transfer of available potential or kinetic energy, due to nonlinear interaction, between pairs of wavenumbers, i.e. between a disturbance of wavenumber n and a disturbance of wavenumber m ($n \neq m$), may be achieved by not performing the summations in (A.54) or (A.59). A similar approach has been adopted by DaCamara (1991) in the analysis of planetary wave activities, for the kinetic energy of an open system (Northern Hemisphere).

2.2.4 3-D Normal mode energetics

The equations of horizontal motion and thermodynamics with three dependent variables (u, v, ϕ) may be written in the (λ, θ, p, t) coordinate system as (e.g. Tanaka and Kung,

1988)

$$\frac{\partial u}{\partial t} - fv + \frac{1}{a\cos\theta}\frac{\partial \phi}{\partial \lambda} = -\vec{V}\cdot\nabla u - \omega\frac{\partial u}{\partial p} + \frac{\tan\theta}{a}uv + F_u, \tag{2.46}$$

$$\frac{\partial v}{\partial t} + fu + \frac{1}{a}\frac{\partial \phi}{\partial \theta} = -\vec{V}\cdot\nabla v - \omega\frac{\partial v}{\partial p} - \frac{\tan\theta}{a}u^2 + F_v, \tag{2.47}$$

$$-\frac{\partial}{\partial t}\left[\frac{\partial}{\partial p}\left(\frac{1}{S_0}\frac{\partial \phi}{\partial p}\right)\right] + \nabla\cdot\vec{V} = \frac{\partial}{\partial p}\left[\frac{R}{pS_0}\left(-\vec{V}\cdot\nabla T - \omega\frac{\partial T}{\partial p}\right)\right] + \frac{\partial}{\partial p}\left(\frac{q\,R}{p\,c_p\,S_0}\right), \tag{2.48}$$

where T is the departure of the temperature from the reference state temperature T_0, ϕ is the departure of geopotential from a reference state geopotential, ϕ_0, and S_0 is the static stability parameter of the reference state, which is defined as in Kasahara (1984) by

$$S_0 = \frac{R}{p}\left(\frac{RT_0}{pc_p} - \frac{\mathrm{d}T_0}{\mathrm{d}p}\right). \tag{2.49}$$

The remaining symbols are the same as in (2.20)-(2.25). Since a scaling of $T_0 \gg T$ has been introduced in (2.48), the associated term $\omega RT/pc_p$ has been neglected.

Vertical structure equation

The vertical structure equation is a Sturm-Liouville ordinary differential equation whose eigensolutions describe the vertical structure of the normal modes of the linearised primitive equations (Cohn and Dee, 1989). It is obtained by a separation of variables for the linearised versions of (2.46)-(2.48) about a reference state at rest in which the temperature is a function of pressure only. Thus, the *vertical structure equation* may be written as (e.g. Kasahara, 1984; Castanheira, 2000)

$$\frac{\partial}{\partial p}\left(\frac{1}{S_0}\frac{\partial G_k(p)}{\partial p}\right) + \frac{1}{g\,h_k}G_k(p) = 0, \tag{2.50}$$

where h_k are equivalent heights. The k^{th} vertical eigenvector, $G_k(p)$, satisfy the orthonormal condition

$$\frac{1}{p_s}\int_0^{p_s} G_k(p)G_j(p)\mathrm{d}p = \delta_{kj}, \tag{2.51}$$

where δ_{kj} denotes the Kronecker delta and is equal to unity if $k = j$ and zero otherwise.

Using (2.51), a set of vertical transforms may be defined as

$$f(p) = \sum_{k=0}^{\infty} f_k G_k(p), \tag{2.52}$$

$$f_k = \frac{1}{p_s}\int_0^{p_s} f(p)G_k(p)\mathrm{d}p, \tag{2.53}$$

where $f(p)$ is an arbitrary function of pressure, satisfying the system boundary conditions. The modes corresponding to vertical index $k = 0$ are called barotropic modes, whereas those corresponding to $k \geq 1$ are called baroclinic modes (see section A.3.4).

Horizontal structure equation

Applying the vertical transform (2.53) to (2.46)-(2.48), a dimensionless equation is obtained in the following vector form:

$$\frac{\partial}{\partial \hat{t}}\mathbf{W}_k + \mathbf{L}\,\mathbf{W}_k = \mathbf{B}_k + \mathbf{C}_k + \mathbf{D}_k, \tag{2.54}$$

where

$$\hat{t} = 2\,\Omega\,t, \tag{2.55}$$

$$\mathbf{W}_k = \mathbf{X}_k^{-1}\begin{bmatrix} u \\ v \\ \phi \end{bmatrix}_k, \tag{2.56}$$

$$\mathbf{B}_k = \mathbf{Y}_k^{-1}\begin{bmatrix} -\vec{V}\cdot\nabla u - \omega\frac{\partial u}{\partial p} + \frac{\tan\theta}{a}uv \\ -\vec{V}\cdot\nabla v - \omega\frac{\partial v}{\partial p} - \frac{\tan\theta}{a}u^2 \\ 0 \end{bmatrix}_k, \tag{2.57}$$

$$\mathbf{C}_k = \mathbf{Y}_k^{-1}\begin{bmatrix} 0 \\ 0 \\ \frac{\partial}{\partial p}\left[\frac{R}{pS_0}\left(-\vec{V}\cdot\nabla T - \omega\frac{\partial T}{\partial p}\right)\right] \end{bmatrix}_k, \tag{2.58}$$

$$\mathbf{D}_k = \mathbf{Y}_k^{-1}\begin{bmatrix} F_u \\ F_v \\ \frac{\partial}{\partial p}\left(\frac{q\,R}{p\,c_p\,S_0}\right) \end{bmatrix}_k. \tag{2.59}$$

The subscript k denotes the k^{th} component of the vertical transform. The vectors are made dimensionless by the scaling matrices $\mathbf{X}_k$ and $\mathbf{Y}_k$, involving the equivalent height, h_k, and $2\,\Omega$ for time, and are given by

$$\mathbf{X}_k = \begin{bmatrix} \sqrt{g h_k} & 0 & 0 \\ 0 & \sqrt{g h_k} & \\ 0 & 0 & g h_k \end{bmatrix}, \tag{2.60}$$

$$\mathbf{Y}_k = \begin{bmatrix} 2\,\Omega\sqrt{g h_k} & 0 & 0 \\ 0 & 2\,\Omega\sqrt{g h_k} & \\ 0 & 0 & 2\,\Omega \end{bmatrix}. \tag{2.61}$$

The linear operator $\mathbf{L}$ is given by

$$\begin{bmatrix} 0 & -\sin\theta & \frac{\alpha_k}{\cos\theta}\frac{\partial}{\partial\lambda} \\ \sin\theta & 0 & \alpha_k\frac{\partial}{\partial\theta} \\ \frac{\alpha_k}{\cos\theta}\frac{\partial}{\partial\lambda} & \frac{\alpha_k}{\cos\theta}\frac{\partial}{\partial\theta}\left(\cos\theta\,(\cdot)\right) & 0 \end{bmatrix}, \tag{2.62}$$

where the dimensionless coefficient, α_k, is defined as

$$\alpha_k = \frac{\sqrt{g\,h_k}}{2\,\Omega\,a}. \tag{2.63}$$

The *horizontal structure equations* corresponds to the homogeneous part of (2.54), by setting the right-hand side to zero, and are usually called as Laplace's tidal equations (e.g. Longuet-Higgins, 1968). This system describes small-amplitude motions of an incompressible, homogeneous, hydrostatic and inviscid fluid over a rotating sphere (Kasahara, 1976). The solutions of the Laplace tidal equations are called Hough harmonics, $\mathbf{H}_{nlk}$, after Hough (1898), and are obtained as eigensolutions of (e.g. Longuet-Higgins, 1968; Swarztrauber and Kasahara, 1985):

$$-\,i\,\sigma_{nlk}\,\mathbf{H}_{nlk} + \mathbf{L}\,\mathbf{H}_{nlk} = 0, \tag{2.64}$$

where σ_{nlk} are the eigenfrequencies for the free waves, the Hough harmonics $\mathbf{H}_{nlk}$ are given by

$$\mathbf{H}_{nlk}\,(\lambda,\theta) = \mathbf{\Theta}_{nlk}\,(\theta)\,e^{i\,n\,\lambda}, \tag{2.65}$$

and the Hough vector functions $\mathbf{\Theta}_{nlk}(\theta)$ are given by

$$\mathbf{\Theta}_{nlk}(\theta) = \begin{bmatrix} \mathrm{U}_{nlk}(\theta) \\ i\,\mathrm{V}_{nlk}(\theta) \\ \Phi_{nlk}(\theta) \end{bmatrix}. \tag{2.66}$$

The Hough vector functions components, i.e. U_{nlk},V_{nlk}, and Φ_{nlk}, are the vertical and Fourier-Hough transforms (see below) of zonal and meridional wind, (u, v), and perturbation geopotential, ϕ, respectively. The factor i in front of $\mathrm{V}_{nlk}(\theta)$ is introduced to account for a phase shift of $\pi/2$ (Kasahara, 1977). The subscripts n, l and k denote zonal wavenumber, meridional mode number and vertical mode number, respectively. In order to distinguish each wave type, the westward propagating Rossby wave and the westward and eastward propagating gravity waves, the meridional index l is defined as a sequence of three distinct modes, l_r, l_w and l_e, respectively (see section A.3.3 in Appendix A).

The Hough harmonics satisfy the orthonormal condition given by

$$\frac{1}{2\,\pi}\int_{-\frac{\pi}{2}}^{\frac{\pi}{2}}\int_{0}^{2\,\pi}\mathbf{H}^{\star}_{nlk}\cdot\mathbf{H}_{n'l'k}\cos\theta\mathrm{d}\lambda\mathrm{d}\theta = \delta_{nn'}\,\delta_{ll'}, \tag{2.67}$$

where the star, $\star$, denotes a conjugate transpose and the right-hand side is unity if $n = n^{'}$ and $l = l^{'}$, and zero otherwise.

Using orthonormal condition (2.67), a set of Fourier-Hough transforms may be written as

$$\mathbf{W}_k(\lambda,\theta,t) = \sum_{l=0}^{\infty}\sum_{n=-\infty}^{\infty} w_{nlk}(t)\,\mathbf{H}_{nlk}(\lambda,\theta), \tag{2.68}$$

$$w_{nlk}(t) = \int_{-\frac{\pi}{2}}^{\frac{\pi}{2}}\int_{0}^{2\,\pi}\mathbf{H}^{\star}_{nlk}(\lambda,\theta)\cdot\mathbf{W}_k(\lambda,\theta,t)\cos\theta\mathrm{d}\lambda\mathrm{d}\theta. \tag{2.69}$$

Applying the Fourier-Hough transforms to (2.54), yields

$$\frac{\mathrm{d}}{\mathrm{d}t}w_{nlk} + i\,\sigma_{nlk}\,w_{nlk} = b_{nlk} + c_{nlk} + d_{nlk}, \tag{2.70}$$

where the complex variables w_{nlk}, b_{nlk}, c_{nlk} and d_{nlk} are the Fourier-Hough transforms of the vector variables (2.56)-(2.59), respectively. According to (2.70), the time change

of the expansion coefficient of a normal mode, w_{nlk}, depends on a linear term related with phase change of the wave, nonlinear terms due to the wind and mass fields, and a diabatic process. The linear term do not contributes to the amplitude change of the wave because the eigenfrequencies, σ_{nlk}, are always real (Swarztrauber and Kasahara, 1985).

Energy balance equations for the normal modes

Multiplying the linearised versions of (2.46), (2.47) and (2.48) by u, v and $-\phi$, respectively, summing the three resulting equations, integrating over the whole atmospheric mass and using upper boundary condition A.89 given in Appendix A, the equation of energy conservation is obtained as

$$\frac{\mathrm{d}}{\mathrm{d}t}\left[\frac{1}{g\,S}\int_S\left(\int_0^{p_s} E\,\mathrm{d}p + \frac{1}{2}\frac{p_s}{R\,T_s}\phi_s^2\right)\,\mathrm{d}s\right] = 0, \tag{2.71}$$

where

$$E = K + A, \tag{2.72}$$

$$K = \frac{1}{2}\left(u^2 + v^2\right), \tag{2.73}$$

$$A = \frac{1}{2\,S_0}\left(\frac{\partial\phi}{\partial p}\right)^2, \tag{2.74}$$

and the subscript s denotes the variables at $p = p_s$. The available potential energy in the normal mode energetics involves contributions from geopotential flux across the lower boundary, which is expressed by the surface integral in (2.71). However, the observed variance of ϕ_s is only 1% of $K + A$ in the first term of (2.71), and therefore negligible (Tanaka and Kung, 1988). By expanding the dependent variables onto the vertical normal modes using (2.52), equation (2.71) takes the form

$$\frac{\mathrm{d}}{\mathrm{d}t}\left[\sum_{k=0}^{\infty}\frac{p_s\,h_k}{2\,S}\int_S\left(u_k^2 + v_k^2 + \phi_k^2\right)\,\mathrm{d}s\right] = 0. \tag{2.75}$$

Expanding (2.75) onto the Fourier-Hough harmonics using (2.68), the energy conservation is finally expressed in terms of a summation of energies associated with each mode,

i.e.

$$\frac{\mathrm{d}}{\mathrm{d}t}\sum_{k=0}^{\infty}\sum_{l=0}^{\infty}\sum_{n=0}^{\infty}E_{nlk}=0, \tag{2.76}$$

where

$$E_{0lk} = \frac{1}{4}\,p_s\,h_k|w_{0lk}|^2, \tag{2.77}$$

$$E_{nlk} = \frac{1}{2}\,p_s\,h_k|w_{nlk}|^2. \tag{2.78}$$

Substituting (2.70) into the time derivatives of (2.77) and (2.78), the energy balance equations for the normal modes are finally obtained as

$$\frac{\mathrm{d}}{\mathrm{d}t}E_{nlk}=\mathrm{B}_{nlk}+\mathrm{C}_{nlk}+\mathrm{D}_{nlk}, \tag{2.79}$$

where

$$\mathrm{B}_{nlk} = p_s\,\Omega\,h_k\left[w^{\star}_{nlk}\,b_{nlk}+w_{nlk}\,b^{\star}_{nlk}\right], \tag{2.80}$$

$$\mathrm{C}_{nlk} = p_s\,\Omega\,h_k\left[w^{\star}_{nlk}\,c_{nlk}+w_{nlk}\,c^{\star}_{nlk}\right], \tag{2.81}$$

$$\mathrm{D}_{nlk} = p_s\,\Omega\,h_k\left[w^{\star}_{nlk}\,d_{nlk}+w_{nlk}\,d^{\star}_{nlk}\right]. \tag{2.82}$$

Equations (2.80)-(2.82) should be multiplied by 1/2 for $n=0$ as in (2.77). The terms B_{nlk}, C_{nlk}, and D_{nlk} that contribute to the time change of E_{nlk} are respectively associated with nonlinear interactions of kinetic and available potential energies and with an energy source or sink due to diabatic processes which includes dissipation.

By summing up the 3-D normal mode energetics terms within the same physical categories, the energetics characteristics can be assessed separately, not only for the zonal mean and eddy components, but also for the barotropic and baroclinic modes, and for the Rossby and gravity waves. However, it should be noted that, the total energy associated with each mode, E_{nlk}, cannot be separated into the available potential and

kinetic energies of each mode, A_{nlk} and K_{nlk}, because U_{nlk}, V_{nlk} and Φ_{nlk} are not orthogonal to one another. It is for this reason that the wavenumber energetics terms $(L(n) - M(n))$ and $(R(n) + S(n))$ of the Saltzman scheme, may be obtained from terms B_{nlk} and C_{nlk}, respectively, by summing over all meridional and vertical indices, i.e.

$$\sum_{k=0}^{\infty}\sum_{l=0}^{\infty}\mathrm{B}_{nlk} = L(n) - M(n), \tag{2.83}$$

$$\sum_{k=0}^{\infty}\sum_{l=0}^{\infty}\mathrm{C}_{nlk} = R(n) + S(n), \tag{2.84}$$

whereas, the conversion between available potential energy and kinetic energy cannot be explicitly shown in the 3-D normal mode energetics scheme. On the other hand, A and K may be correctly separated in the vertical and zonal wavenumber domains, and thence it is possible to obtain explicitly the energy conversion term as a function of both the vertical mode and zonal wavenumber. As shown bellow, this energy conversion term may be obtained by combining the balance equations for A and K in both the vertical and zonal wavenumber domains, with the energy balance equation for the 3-D normal modes (2.79). This approach is different to that used by Terasaki and Tanaka (2008) for the analysis of the spectral energetics of the atmosphere in the vertical wavenumber domain. They have used the analytical vertical structure functions as a basis function for the vertical direction, which can be obtained by assuming the static stability parameter, γ, to be a constant value. Therefore, the formulation for the energy conversion term as a function of both the vertical mode and zonal wavenumber may constitute a new result since, apparently, it hasn't been described in the literature so far, and is obtained as follows:

The first two components of (2.54), may be written as

$$\frac{\partial \hat{u}_k}{\partial \hat{t}} - \sin\theta\,\hat{v}_k + \frac{\alpha_k}{\cos\theta}\frac{\partial \hat{\phi}_k}{\partial \lambda} = \hat{b}1_k + \left(\hat{F}_u\right)_k, \tag{2.85}$$

$$\frac{\partial \hat{v}_k}{\partial \hat{t}} + \sin\theta\,\hat{u}_k + \alpha_k\frac{\partial \hat{\phi}_k}{\partial \theta} = \hat{b}2_k + \left(\hat{F}_v\right)_k, \tag{2.86}$$

where

$$\hat{u}_k = \frac{u_k}{\sqrt{g\,h_k}}, \quad \hat{v}_k = \frac{v_k}{\sqrt{g\,h_k}}, \quad \hat{\phi}_k = \frac{\phi_k}{g\,h_k}, \tag{2.87}$$

$$\left(\hat{F}_u\right)_k = \frac{(F_u)_k}{2\,\Omega\,\sqrt{g\,h_k}}, \quad \left(\hat{F}_v\right)_k = \frac{(F_v)_k}{2\,\Omega\,\sqrt{g\,h_k}}, \tag{2.88}$$

$$\hat{b}1_k = \frac{1}{2\,\Omega\,\sqrt{g\,h_k}}\left[-\vec{V}\cdot\nabla u - \omega\frac{\partial u}{\partial p} + \frac{\tan\theta}{a}\right]_k, \tag{2.89}$$

$$\hat{b}2_k = \frac{1}{2\,\Omega\,\sqrt{g\,h_k}}\left[-\vec{V}\cdot\nabla v - \omega\frac{\partial v}{\partial p} - \frac{\tan\theta}{a}u^2\right]_k. \tag{2.90}$$

By applying the Fourier transform to (2.85) and (2.86), yields

$$\frac{\partial \hat{u}_{nk}}{\partial \hat{t}} = \sin\theta\,\hat{v}_{nk} - \frac{i\,n\,\alpha_k}{\cos\theta}\hat{\phi}_{nk} + \hat{b}1_{nk} + \left(\hat{F}_u\right)_{nk}, \tag{2.91}$$

$$\frac{\partial \hat{v}_{nk}}{\partial \hat{t}} = -\sin\theta\,\hat{u}_{nk} - \alpha_k\frac{\partial \hat{\phi}_{nk}}{\partial\theta} + \hat{b}2_{nk} + \left(\hat{F}_v\right)_{nk}. \tag{2.92}$$

Multiplying (2.91) and (2.92) by $\hat{u}^\star_{nk}$ and $\hat{v}^\star_{nk}$, respectively, and adding to each resulting equation the corresponding complex conjugate equation, gives

$$\begin{aligned}\frac{\partial}{\partial \hat{t}}\left(\hat{u}^\star_{nk}\,\hat{u}_{nk}\right) &= \sin\theta\left(\hat{u}^\star_{nk}\,\hat{v}_{nk} + \hat{u}_{nk}\,\hat{v}^\star_{nk}\right) + \frac{i\,n\,\alpha_k}{\cos\theta}\left(\hat{u}_{nk}\,\hat{\phi}^\star_{nk} - \hat{u}^\star_{nk}\,\hat{\phi}_{nk}\right)\\ &\quad + \left(\hat{u}^\star_{nk}\,\hat{b}1_{nk} + \hat{u}_{nk}\,\hat{b}1^\star_{nk}\right) + \left(\hat{u}^\star_{nk}\,\left(\hat{F}_u\right)_{nk} + \hat{u}_{nk}\,\left(\hat{F}_u\right)^\star_{nk}\right),\end{aligned} \tag{2.93}$$

$$\begin{aligned}\frac{\partial}{\partial \hat{t}}\left(\hat{v}^\star_{nk}\,\hat{v}_{nk}\right) &= -\sin\theta\left(\hat{v}^\star_{nk}\,\hat{u}_{nk} + \hat{v}_{nk}\,\hat{u}^\star_{nk}\right) - \alpha_k\left(\hat{v}^\star_{nk}\,\frac{\partial \hat{\phi}_{nk}}{\partial\theta} + \hat{v}_{nk}\,\frac{\partial \hat{\phi}^\star_{nk}}{\partial\theta}\right)\\ &\quad + \left(\hat{v}^\star_{nk}\,\hat{b}2_{nk} + \hat{v}_{nk}\,\hat{b}2^\star_{nk}\right) + \left(\hat{v}^\star_{nk}\,\left(\hat{F}_v\right)_{nk} + \hat{v}_{nk}\,\left(\hat{F}_v\right)^\star_{nk}\right).\end{aligned} \tag{2.94}$$

Summing equations (2.93) and (2.94), multiplying the resulting equation by $p_s h_k/2$, integrating over the latitude and recalling that $\hat{t} = 2\,\Omega\,t$, the rate of change of kinetic energy in the zonal wavenumber and vertical mode number domains, i.e. K_{nk}, may be written as

$$\frac{\partial}{\partial t}K_{nk} = \mathrm{B}_{nk} + \mathrm{D}_{nk}, \tag{2.95}$$

where

$$K_{nk} = \frac{p_s\, h_k}{2} \int_{-\frac{\pi}{2}}^{\frac{\pi}{2}} (\hat{u}^{\star}_{nk}\, \hat{u}_{nk} + \hat{v}^{\star}_{nk}\, \hat{v}_{nk}) \cos\theta \mathrm{d}\theta, , \tag{2.96}$$

$$\begin{aligned} \mathrm{B}_{nk} &= p_s\, \Omega\, h_k \int_{-\frac{\pi}{2}}^{\frac{\pi}{2}} \left\{ \frac{i\, n\, \alpha_k}{\cos\theta} \left(\hat{u}_{nk}\, \hat{\phi}^{\star}_{nk} - \hat{u}^{\star}_{nk}\, \hat{\phi}_{nk} \right) - \alpha_k \left(\hat{v}^{\star}_{nk}\, \frac{\partial \hat{\phi}_{nk}}{\partial \theta} + \hat{v}_{nk}\, \frac{\partial \hat{\phi}^{\star}_{nk}}{\partial \theta} \right) \right. \\ &\quad \left. + \left(\hat{u}^{\star}_{nk}\, \hat{b}1_{nk} + \hat{u}_{nk}\, \hat{b}1^{\star}_{nk} \right) + \left(\hat{v}^{\star}_{nk}\, \hat{b}2_{nk} + \hat{v}_{nk}\, \hat{b}2^{\star}_{nk} \right) \right\} \cos\theta\, \mathrm{d}\theta, \end{aligned} \tag{2.97}$$

$$\begin{aligned} \mathrm{D}_{nk} &= p_s\, \Omega\, h_k \int_{-\frac{\pi}{2}}^{\frac{\pi}{2}} \left\{ \left(\hat{u}^{\star}_{nk} \left(\hat{F}_u \right)_{nk} + \hat{u}_{nk} \left(\hat{F}_u \right)^{\star}_{nk} \right) \right. \\ &\quad \left. + \left(\hat{v}^{\star}_{nk} \left(\hat{F}_v \right)_{nk} + \hat{v}_{nk} \left(\hat{F}_v \right)^{\star}_{nk} \right) \right\} \cos\theta\, \mathrm{d}\theta. \end{aligned} \tag{2.98}$$

Equation (2.95) summed over all vertical modes, k, is equivalent to equation (2.43). That is,

$$\sum_{k=0}^{\infty} \frac{\partial}{\partial t} K_{nk} = \frac{\partial}{\partial t} K(n), \tag{2.99}$$

$$\tag{2.100}$$

from which it may be concluded that

$$\sum_{k=0}^{\infty} \mathrm{B}_{nk} = -M(n) + L(n) + C(n), \tag{2.101}$$

$$\sum_{k=0}^{\infty} \mathrm{D}_{nk} = -D(n). \tag{2.102}$$

Therefore, the terms for the energy conversion from available potential energy into kinetic energy, $C(n)$ and $C(0)$, of the Saltzman scheme, may be obtained from equations (2.83) and (2.101) as

$$C(n) = \sum_{k=0}^{\infty} \mathrm{B}_{nk} - \sum_{k=0}^{\infty} \sum_{l=0}^{\infty} \mathrm{B}_{nlk}, \tag{2.103}$$

$$C(0) = \sum_{k=0}^{\infty} \mathrm{B}_{0k} - \sum_{k=0}^{\infty} \sum_{l=0}^{\infty} \mathrm{B}_{0lk}. \tag{2.104}$$

In addition, the conversion rates from eddy available potential energy into eddy kinetic energy, and from zonal mean available potential energy into zonal mean kinetic energy in

the vertical mode domain, denoted as $C_E(k)$ and $C_Z(k)$, respectively, may be obtained as

$$C_E(k) = \sum_{n=1}^{\infty} \mathrm{B}_{nk} - \sum_{n=1}^{\infty}\sum_{l=0}^{\infty} \mathrm{B}_{nlk}, \tag{2.105}$$

$$C_Z(k) = \mathrm{B}_{0k} - \sum_{l=0}^{\infty} \mathrm{B}_{0lk}. \tag{2.106}$$

Following a similar procedure for the third component of (2.54), the rate of change of available potential energy in the zonal wavenumber and vertical mode number domains, i.e. A_{nk}, may be written as

$$\frac{\partial}{\partial t} A_{nk} = \mathrm{C}_{nk} + \mathrm{G}_{nk}, \tag{2.107}$$

where

$$A_{nk} = \frac{p_s\, h_k}{2} \int_{-\frac{\pi}{2}}^{\frac{\pi}{2}} \left(\hat{\phi}^{\star}_{nk}\, \hat{\phi}_{nk} \right) \cos\theta \, \mathrm{d}\theta, \tag{2.108}$$

$$\begin{aligned} \mathrm{C}_{nk} = {} & p_s\, \Omega\, h_k \int_{-\frac{\pi}{2}}^{\frac{\pi}{2}} \left\{ \frac{i\, n\, \alpha_k}{\cos\theta} \left(\hat{\phi}_{nk}\, \hat{u}^{\star}_{nk} - \hat{\phi}^{\star}_{nk}\, \hat{u}_{nk} \right) \right. \\ & - \frac{\alpha_k}{\cos\theta} \left(\hat{\phi}^{\star}_{nk} \frac{\partial \hat{v}_{nk}\, \cos\theta}{\partial\theta} + \hat{\phi}_{nk} \frac{\partial \hat{v}^{\star}_{nk}\, \cos\theta}{\partial\theta} \right) \\ & \left. + \left(\hat{\phi}^{\star}_{nk}\, \hat{c}3_{nk} + \hat{\phi}_{nk}\, \hat{c}3^{\star}_{nk} \right) \right\} \cos\theta \, \mathrm{d}\theta, \end{aligned} \tag{2.109}$$

$$\mathrm{G}_{nk} = p_s\, \Omega\, h_k \int_{-\frac{\pi}{2}}^{\frac{\pi}{2}} \left(\hat{\phi}^{\star}_{nk}\, \hat{d}3_{nk} + \hat{\phi}_{nk}\, \hat{d}3^{\star}_{nk} \right) \cos\theta \, \mathrm{d}\theta, \tag{2.110}$$

and

$$\hat{c}3_{nk} = \frac{1}{2\,\Omega} \left(\frac{\partial}{\partial p} \left[\frac{R}{p S_0} \left(-\vec{V} \cdot \nabla T - \omega \frac{\partial T}{\partial p} \right) \right] \right)_{nk}, \tag{2.111}$$

$$\hat{d}3_{nk} = \frac{1}{2\,\Omega} \left[\frac{\partial}{\partial p} \left(\frac{q\, R}{p\, c_p\, S_0} \right) \right]_{nk}. \tag{2.112}$$

Therefore, the terms for the conversion rates of available potential energy into kinetic energy given by (2.103)-(2.106), may be obtained alternatively as

$$C(n) = \sum_{k=0}^{\infty}\sum_{l=0}^{\infty} \mathrm{C}_{nlk} - \sum_{k=0}^{\infty} \mathrm{C}_{nk}, \tag{2.113}$$

$$C(0) = \sum_{k=0}^{\infty}\sum_{l=0}^{\infty} \mathrm{C}_{0lk} - \sum_{k=0}^{\infty} \mathrm{C}_{0k}, \tag{2.114}$$

$$C_E(k) = \sum_{n=1}^{\infty}\sum_{l=0}^{\infty} \mathrm{C}_{nlk} - \sum_{n=1}^{\infty} \mathrm{C}_{nk}, \tag{2.115}$$

$$C_Z(k) = \sum_{l=0}^{\infty} \mathrm{C}_{0lk} - \mathrm{C}_{0k}. \tag{2.116}$$

Moreover, the expressions for the energy generation and dissipation terms may be obtained explicitly in the zonal wavenumber and vertical mode domains, from the balance equations (2.95) and (2.107). The expressions in the zonal wavenumber domain may be written as

$$G(n) = \sum_{k=0}^{\infty} \frac{\partial}{\partial t} A_{nk} - \sum_{k=0}^{\infty} \mathrm{C}_{nk}, \tag{2.117}$$

$$G(0) = \sum_{k=0}^{\infty} \frac{\partial}{\partial t} A_{0k} - \sum_{k=0}^{\infty} \mathrm{C}_{0k}, \tag{2.118}$$

$$D(n) = \sum_{k=0}^{\infty} \mathrm{B}_{nk} - \sum_{k=0}^{\infty} \frac{\partial}{\partial t} K_{nk}, \tag{2.119}$$

$$D(0) = \sum_{k=0}^{\infty} \mathrm{B}_{0k} - \sum_{k=0}^{\infty} \frac{\partial}{\partial t} K_{0k}, \tag{2.120}$$

and the expressions in the vertical mode domain may be written as

$$G_E(k) = \sum_{n=1}^{\infty} \frac{\partial}{\partial t} A_{nk} - \sum_{n=1}^{\infty} \mathrm{C}_{nk}, \tag{2.121}$$

$$G_Z(k) = \frac{\partial}{\partial t} A_{0k} - \mathrm{C}_{0k}, \tag{2.122}$$

$$D_E(k) = \sum_{n=1}^{\infty} \mathrm{B}_{nk} - \sum_{n=1}^{\infty} \frac{\partial}{\partial t} K_{nk}, \tag{2.123}$$

$$D_Z(k) = \mathrm{B}_{0k} - \frac{\partial}{\partial t} K_{0k}. \tag{2.124}$$

Chapter 3

Datasets and Methodology

3.1 Reanalysis data

The NCEP and the NCAR produced their first reanalysis (NCEP/NCAR-R1) covering the period from 1948 to present. The prognostic variables are represented, in the horizontal, by spherical harmonic series triangularly truncated at wavenumber 62 and, in the vertical, by 28 vertical levels, i.e. T62 L28 (Kalnay et al., 1996). NCEP and the DOE completed their NCEP/DOE Atmospheric Model Intercomparison Project (AMIP)-II Reanalysis (NCEP-R2 hereafter) using an improved forecast model and data assimilation system of NCEP/NCAR-R1 (NCEP-R1 hereafter) (Kanamitsu et al., 2002). The ECMWF produced their ECMWF 15-year Re-Analysis (ERA-15) from 1979 to 1993 with resolution T106 L31 (Gibson et al., 1997). ECMWF completed their second reanalysis, ERA-40 (Uppala et al., 2005), spanning the period from September 1957 to August 2002 with a higher resolution of TL159 L60, and using an improved system from ERA-15. More recently, the JMA and Central Research Institute of Electric Power Industry (CRIEPI) produced the JRA-25, covering the period 1979 to present and with a resolution of T106 L40 (Onogi et al., 2007).

Since the first generation reanalysis, NCEP-R1 and ERA-15, became available, several diagnostic/comparative studies have been performed (e.g. Mo and Higgins, 1996; Stendel and Arpe, 1997; Trenberth et al., 2002; Trenberth and Stepaniak, 2002, among

others) which uncovered substantial problems that limit their use. NCEP-R2 is a second limited version of NCEP-R1, that was generated to handle some problems and should be regarded as an updated and human error-fixed version of NCEP-R1 (Kanamitsu et al., 2002). Besides fixing the human processing errors, upgrades to the forecast model and a new diagnostic package were incorporated into NCEP-R2, which is still considered a first generation reanalysis. Two second generation reanalysis, ERA-40 and JRA-25, have addressed some of the shortcomings of the earlier reanalysis (Uppala et al., 2005; Onogi et al., 2007), but many of the problems remain, which can be attributed to changes in the observing system, the different model biases and different assimilated observational data (e.g. Chen and Bosilovich, 2007; Trenberth et al., 2010).

In spite of their shortcomings, the reanalysis products have proven to be among the most valuable and widely used in the history of climate science. The NCEP-R2, ERA-40 and JRA-25 reanalysis datasets are included in this study as representing the observed atmosphere.

The NCEP-R2 reanalysis have been extracted from the NOAA/OAR/ESRL PSD website at `http://www.cdc.noaa.gov`. The ERA-40 datasets have been obtained from the ECMWF data server (`http://data-portal.ecmwf.int/data/d/era40_daily/`). The JRA-25 datasets are provided in the framework of the cooperative research project of the JRA-25 long-term reanalysis by the JMA/CRIEPI from it's website at `http://jra.kishou.go.jp`. The variables used in the energetics computation are temperature (T), the three wind components (u, v, ω) and the geopotential height (z) (or geopotential $(\Phi = \phi + \phi_0)$ for ERA-40). For NCEP-R2, 6-hourly values of these variables at 17 pressure levels (1000, 925, 850, 700, 600, 500, 400, 300, 250, 200, 150, 100, 70, 50, 30, 20, 10 hPa) with an horizontal resolution of 2.5 ° Longitude by 2.5 ° Latitude, are used. The same resolutions were considered for the other two datasets, except for ERA-40, for which 23 pressure levels (the same as NCEP-R2 plus 750, 7, 5, 3, 2 and 1 hPa) are used, and JRA-25 for which 23 pressure levels (the same as NCEP-R2 plus 7, 5, 3, 2, 1 and 0.4 hPa) are used. The period 1979 to 2001 is selected for JRA-25 and NCEP-R2, since these datasets are only available from 1979 onwards, while for ERA-40 the period

1970-2001 is considered.

3.2 Models data

The simulated atmosphere is represented by five state-of-the-art climate models, which have participated in the Coupled Model Intercomparison Project, phase three (CMIP3) and Intergovernmental Panel on Climate Change - Fourth Assessment Report (IPCC-AR4). The choice of the five climate models used in this study was only determined by the availability of high temporal resolution data, i.e. 6-hourly. The datasets from all these models are for the 20th Century Climate in Coupled Models (20C3M) experiment (20C hereafter) of CMIP3/IPCC-AR4, which run with greenhouse gases increasing as observed through the 20th Century. From this experiment, which represents the present climate, the period 1970 to 1999 was selected for all models.

Datasets representing a future climate were taken from IPCC's new SRES. The SRES scenarios, which are images of the future or alternative futures, cover a wide range of the main driving forces of future emissions, from demographic to technological and economic developments. The SRES approach involved the development of a set of four alternative scenario "families". Each family of SRES scenarios (A1, A2, B1 and B2) includes a descriptive part (called a "storyline") and a number of alternative interpretations and quantification of each storyline developed by six different modeling approaches (A1FI, A1T, A1B, A2, B1 and B2). Each storyline describes a demographic, social, economic, technological, and policy future for each of the scenario families. Within each family different scenarios explore variations of global and regional developments and their implications for greenhouse gas (GHG), ozone precursors, and sulphur emissions. Each of these scenarios is consistent with the broad framework specified by the storyline of the scenario family, and all are equally sound. Details concerning this SRES may be found at `http://www.ipcc.ch/ipccreports/sres/emission/index.php?idp=0`. The 6-hourly data from the above five climate models where only available for the SRES-A1B experiment. Therefore, this experiment was chosen to represent the future climate, and

the period 2070 to 2099 was selected for all models. A brief description of the climate models and their datasets used here will follow.

Data from the Third generation Coupled Global Climate Model (CGCM3.1) has been obtained from the Canadian Centre for Climate Modelling and Analysis (CCCma) website at `http://www.cccma.bc.ec.gc.ca/data/cgcm3/cgcm3.shtml`. The data used are for its medium-resolution version, in which the atmospheric component was run with a horizontal resolution of 47 waves triangular spectral truncated (T47) and 31 levels in the vertical (Model top at 1 hPa). Gridded output fields of CGCM3.1 occur on the reduced "linear" Gaussian grid associated with the chosen spectral truncation, with a size of 96 × 48 that corresponds approximately to 3.75° × 3.75° (Lon × Lat). Details for the atmospheric component of CGCM3.1 may be found in McFarlane et al. (2005). The other components are described in the CCCma website at `http://www.cccma.bc.ec.gc.ca/models/cgcm3.shtml` and references therein. The atmospheric variables T, u, v, ω and z are provided on the reduced Gaussian grid (96×48) at the 31 model levels.

The Community Climate System Model, version 3.0 (CCSM3), from NCAR, run an atmospheric component with T85 horizontal resolution, corresponding to a Gaussian grid of size 256 × 128 (approximately 1.4° × 1.4° (Lon × Lat)), and 26 levels in the vertical (Model top at 2.2 hPa). An overview of CCSM3 is given by Collins et al. (2006). Data from CCSM3 have been obtained from the Earth System Grid (ESG) data portal at `http://www.earthsystemgrid.org/`. The atmospheric variables T, u, v, and z of CCSM3 are available on the 256 × 128 grid and 26 model levels from the ESG data portal. The vertical p-velocity, ω, isn't available at 6-hourly interval for this model and had to be computed offline.

Data from the Centre National de Recherches Météorologiques Coupled global climate Model, version 3 (CNRM-CM3) were supplied by Meteo France. The atmospheric component run with T63 horizontal resolution, with "linear" reduced Gaussian grid equivalent to T42 quadratic grid, and 45 vertical levels (Model top at 0.05 hPa). Output data

of CNRM-CM3 are therefore on a grid size of 128 × 64, corresponding approximately to 2.8° × 2.8° (Lon × Lat). Details for the CNRM-CM3 climate model may be found in Salas-Mélia et al. (2003). The datasets with the atmospheric variables T, u, v, ω and z from CNRM-CM3, were provided on the 128 × 64 Gaussian grid at nine pressure levels (1000, 925, 850, 700, 500, 300, 200, 100, and 50 hPa).

The datasets from the Model for Interdisciplinary Research on Climate (MIROC3.2) were supplied by the National Institute for Environmental Studies, the Center for Climate System Research of University of Tokyo, the Frontier Research Center for Global Change, and the Ministry of Education, Culture, Sports, Science and Technology of Japan. The MIROC3.2 data used in this study are from the medium-resolution version, which run an atmospheric component with T42 horizontal resolution and 20 vertical levels (The height of model top is $\sim$ 30 km). An application of the MIROC3.2 climate model may be seen in Nozawa et al. (2005) and a technical description in Nozawa et al. (2007). The variables T, u, v, ω and z were provided on the grid size of 128 × 64 (Lon × Lat) at 18 pressure levels (1000, 925, 850, 775, 700, 600, 500, 400, 300, 250, 200, 150, 100, 70, 50, 30, 20, 10 hPa).

The fifth-generation atmospheric general circulation model (ECHAM5) developed at the Max Planck Institute for Meteorology (MPIM) is the most recent version in a series of ECHAM models evolving originally from the spectral weather prediction model of the ECMWF. The ECHAM5/MPI-OM climate model (ECHAM5 hereafter) run an atmospheric component with resolution T63 in the horizontal and 31 levels in the vertical (Model top at 10 hPa). A detailed description of the atmospheric model is given by Roeckner et al. (2003). A study evaluating the sensitivity of the model to horizontal and vertical resolution was performed by Roeckner et al. (2006). The variables T, u, v, ω and z from ECHAM5, have been obtained on the Gaussian grid of size 192 × 96 (approximately 1.875° × 1.875° (Lon × Lat)), and at 17 pressure levels (the same as for MIROC3.2 excluding the 20 hPa level) from the Climate and Environmental Retrieval and Archive (CERA) database of World Data Center for Climate (WDCC) maintained by Model and Data (M&D), which is hosted at the MPIM, in cooperation

with the German Climate Computing Centre (DKRZ).

A list with documentation, references and links for the above models (and other CMIP3 climate models) may be found in the Program for Climate Model Diagnosis and Intercomparison (PCMDI) website at `http://www-pcmdi.llnl.gov/ipcc/model_documentation/ipcc_model_documentation.php`.

3.2.1 Pre-processing of models data

Since the vertical p-velocity, ω, needed for the energetics, wasn't available at 6-hourly interval for CCSM3 model, it had to be computed for this model. The computation was accomplished via the same routine used in the CCSM3 model. Datasets from models CGCM3.1 and CCSM3 were interpolated from model levels to 17 pressure levels (the same as NCEP-R2). The interpolation method uses the ECMWF formulation, as described by Trenberth et al. (1993), to extrapolate to the parts of the pressure levels that are eventually below the surface (i.e. when a given pressure level is greater than the surface pressure at some point in a given time). The pressure levels data provided from model MIROC3.2 had "gaps" (i.e. missing values) at some points in the lower levels, which correspond to points belowground. These missing values were filled by solving Poisson's equation via relaxation. The tasks abovementioned were performed with the NCAR Command Language (NCL) software, freely available at `http://www.ncl.ucar.edu/`.

Finally, all model data were interpolated from their Gaussian grids to the same regular grid as the reanalysis data (2.5 ° Longitude × 2.5 ° Latitude). The interpolation method uses a conservative remapping scheme, as described by Jones (1999). This was accomplished with the Climate Data Operators (CDO) software developed at MPIM, and is freely available at `https://code.zmaw.de/projects/cdo`.

3.3 Methodology

The global wavenumber energetics was computed using the detailed expressions for the terms in the balance equations (2.42)-(2.45), which are given in Appendix A. The dissipation, $D(0)$ and $D(n)$, and generation terms, $G(0)$ and $G(n)$, were indirectly obtained as residuals from the respective balance equation. The maximum wavenumber for the analysis was set to $N = 72$ to fulfil the Nyquist frequency, which is half the sampling frequency. In the case of a 2.5 degree grid the sampling frequency is equal to 144. It is worth to mention that, for the case of those models with a coarser native horizontal resolution than that of a 2.5 degree grid (i.e. models CGCM3.1 (T47) and MIROC3.2 (T42)), the values of their energetics spectra are meaningless for the wavenumbers beyond their native resolution. The zonal mean and eddy energetics were obtained from the same equations, by summing the contributions from wavenumbers 1 to N in equations (2.43) and (2.45) and noting that $\sum_{n=1}^{\infty} S(n) = \sum_{n=1}^{\infty} L(n) = 0$ (see section 2.2.3)

For the computation of the rate of conversion of zonal available potential energy to zonal kinetic energy, $C(0)$, and the rate of conversion of available potential energy of wavenumber n to eddy kinetic energy of wavenumber n, $C(n)$, there are two possible formulations (see Equations (2.35) and (A.52) (or (2.37)), usually referred to as "$\mathbf{v} \cdot \nabla z$" and "$\omega\alpha$" (e.g. Peixoto and Oort, 1974), which correspond to different physical processes. For example, formulation "$\omega\alpha$" for $C(0)$ (second equality in Equation (2.35)) shows that zonal kinetic energy, $K(0)$, can be produced through the ascent of warm air relative to the descent of cool air in the mean meridional circulation. On the other hand, formulation "$\mathbf{v} \cdot \nabla z$" for $C(0)$ (first equality in Equation (2.35)) shows that $K(0)$ can be produced by horizontal cross isobaric flow down the north-south pressure gradient.

Although the integrands for the two formulations are locally different, their integrals should be, in theory, equal, provided that global integrals are considered (e.g. Peixoto and Oort, 1992). However, the expected (approximate) equality of the global integrals computed with both formulations, may not be found in practice. This is essentially a

consequence of neglecting the topography in the derivation of the energy cycle equations (Lorenz, 1955; Saltzman, 1957), while the data used in energetics computations is usually given on pressure levels even when these pressure levels are pierced by topography. Data in these "underground" regions are unphysical, and as such, shouldn't enter the calculations. The integrands for the two formulations may have different local contributions from the regions of unphysical (i.e. underground) data. Hence, their integrals may be different even if global integrals are considered, depending also on the way data is interpolated/extrapolated to pressure levels crossing the topography. Nonetheless, the "$\omega\alpha$" formula for $C(n)$ is less sensitive to the inclusion or exclusion of unphysical data in pressure levels (i.e. underground data) than the "$\mathbf{v} \cdot \nabla z$" formula, because its contribution to the integral is not concentrated near the surface (e.g. Marques et al., 2009). On the other hand, data in underground regions have less impact on the global integral of $C\,(0)$, when computed with the "$\mathbf{v} \cdot \nabla z$" formula, than when computed with the "$\omega\alpha$" formula. Additionally, using the "$\mathbf{v} \cdot \nabla z$" formula removes the direct dependence of $C(0)$ on the zonal mean field of ω, which seems overly influenced by the data assimilation processes (Kung and Tanaka, 1983).

In this study the terms $C(0)$ and $C(n)$ were computed using both the "$\mathbf{v} \cdot \nabla z$" and "$\omega\alpha$" formulae. However, for quantitative purposes the "$\mathbf{v} \cdot \nabla z$" formula is used for $C(0)$, and the "$\omega\alpha$" formula is used for $C(n)$, which are expected to give more accurate estimates of "reality", although both formulations may be used in the qualitative sense. The effects of data in underground regions are less problematic to the other directly computable energetics terms, because their contributions are either small relative to the contributions of the remaining data in the atmosphere ($\sim$10% for $A\,(0)$, $A\,(n)$ and $R\,(n)$) or negligible ($<$1% for $K\,(0)$, $K\,(n)$ and $M\,(n)$).

For the 3-D Normal Mode Energetics, the same periods were considered. First, the vertical structure functions were computed, using a reference state of the global mean temperature averaged over the periods considered for each dataset. The vertical structure equation was solved by a spectral method as in Kasahara (1984) (see also Castanheira et al., 1999), which has the advantage, over the finite difference method,

that the derivatives of the vertical structure function can be calculated by analytical differentiation. In the spectral method the solution of (2.50) is approximated by a series expansion of Legendre polynomials, where the expansion coefficients are determined by a Galerkin procedure. In this study, 23 Legendre polynomials were used to approximate the solution of (2.50) and 15 vertical modes were retained. It should be noted that, by adopting this spectral method for the solution of (2.50), an extra factor of $\frac{1}{2}$ must be taken into account in the computation of the normal mode energetics terms (equations (2.77),(2.78) and (2.80)-(2.82)).

Second, the Hough vector functions were computed following the method described in the paper of Swarztrauber and Kasahara (1985), being truncated by 30 Rossby modes, 20 eastward and 20 westward gravity modes. The zonal wavenumber has been truncated at $n = 42$. The modes for $n = 0$ were determined following the approach suggested by Shigehisa (1983), which is also described in Swarztrauber and Kasahara (1985). Finally, the normal mode energetics are computed by applying the three-dimensional data expansion into the normal mode functions, following the analysis scheme of Tanaka (1985). The assumption of vanishing surface wind at the lower boundary of the atmosphere has been adopted as in Tanaka and Kung (1988), in order to obtain an energetically consistent set of equations.

The energetics terms were computed at each time step (6-hourly) for all datasets and then averaged over selected periods to obtain the corresponding mean values in each season of the year. First, the time averages were computed over 1979-2001 for ERA-40, JRA-25 and NCEP-R2, in order to evaluate the differences and similarities between the three reanalysis (Chapter 4, section 4.1). The mean values of energetics terms for the present climate were obtained by averaging over the period 1979-1999 for JRA-25 and NCEP-R2, since these datasets are only available from 1979 onwards, and over 1970-1999 for ERA-40 and the climate models (Chapter 4, section 4.2). Finally, the energetics terms were computed at each time step for the models' datasets corresponding to experiment SRES-A1B. The time averages were then taken over the period 2070-2099 to obtain the corresponding mean values for the future climate in each season of the

year (Chapter 5). The seasons are defined as usual, namely DJF (northern winter), MAM (northern spring), JJA (northern summer) and SON (northern autumn). Model CNRM-CM3 was excluded from the normal mode energetics because the data from this model was only available at nine pressure levels, which is insufficient for a reliable normal mode energetics analysis in the present setup compared to the other datasets.

Chapter 4

Energetics in the Present Climate

Atmospheric energetics is analysed first from the viewpoint of the energy cycle of Lorenz (1955), within its basic resolution of zonal mean and eddy components. It will be followed by the energy cycle of Saltzman (1957), which allows for the analysis of energy forms and energy conversion rates in eddies of given wavenumber as well as the interaction between the eddies. Finally, the normal mode energetics is discussed, which can diagnose the 3-D spectral distribution of energy and energy interactions/conversions, the energetics characteristics of Rossby waves and gravity waves, and the energy conversion between the barotropic and baroclinic modes.

4.1 Energetics in the reanalysis

4.1.1 Lorenz energy cycle

Diagrams for the zonal mean and eddy components of the Lorenz energy cycle from ERA-40, JRA-25 and NCEP-R2, are illustrated in Figure 4.1. Values surrounding energetics symbols are averages over 1979-2001, each standing for a different season, DJF (upper left), MAM (upper right), JJA (bottom left) and SON (bottom right). Values for the time derivatives of available potential and kinetic energies are omitted.

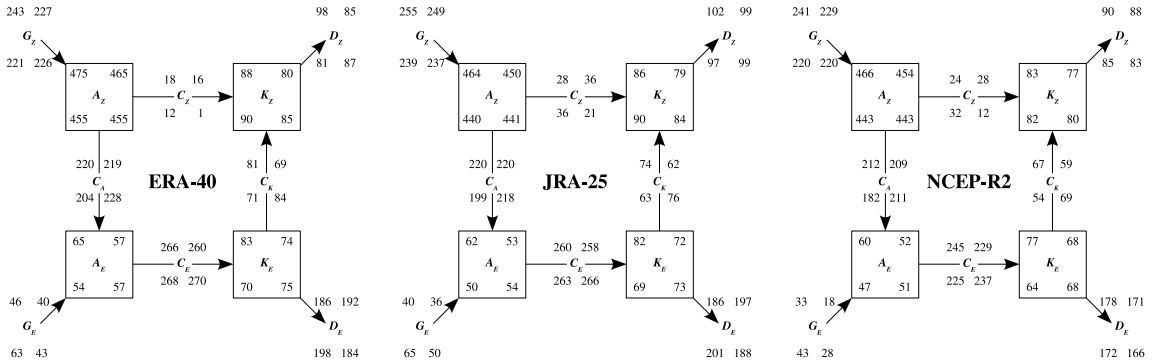

Figure 4.1: Lorenz energy cycle diagram from ERA-40 (left), JRA25 (middle) and NCEP-R2 (right) averaged over 1979-2001. The four values surrounding each symbol correspond to a different season: DJF (upper left), MAM (upper right), JJA (bottom left) and SON (bottom right). Units are 10^4 J m^{-2} for energy levels and 10^{-2} W m^{-2} for conversion rates.

Overall, the global energy cycles from the three reanalysis datasets are similar to each other (Figure 4.1). The direction of the energy flow is consistent among the three datasets. Nevertheless, there are differences in the magnitude of some energy and energy conversion/transfer rates between the datasets, which varies from season to season. In general, the magnitude of energetics is larger for ERA-40, followed by JRA-25 and finally by NCEP-R2. The cross-sections of the various energetics terms directly computed from the reanalysis and for all seasons are displayed in Figures 4.2 to 4.11, and the stability parameter (γ) in Figure 4.12. In Figures 4.2 to 4.11, the quantities (A_Z, A_E, K_Z, etc.) are plotted as black contours, and the differences between each reanalysis and the composite mean reanalysis are shaded with a distinct colour pallet.

Energy levels

Figure 4.2 shows the main tropospheric contributions to zonal mean available potential energy, A_Z, at high latitudes related to the rapid decrease of temperature with latitude. There is a secondary maximum at 100 hPa, while the contributions around level 200 hPa and from the mid-latitudes of both hemispheres at all levels are small. All these features are shared by the three datasets. The differences between the three datasets for the global integrated values of A_Z are quite small ($\leq$3%) for all seasons.

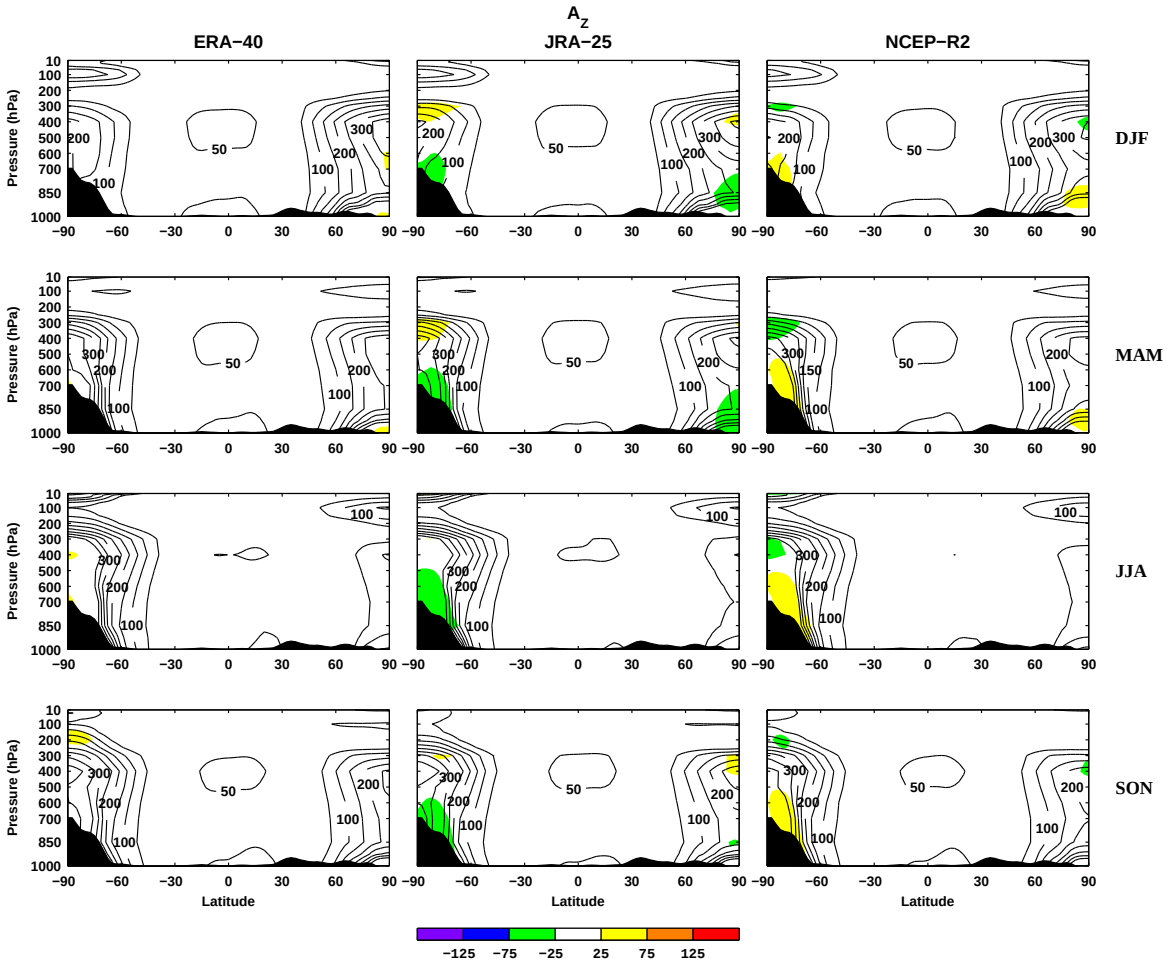

Figure 4.2: Mean cross-sections of zonal mean available potential energy, A_Z, for ERA-40 (Left column), JRA-25 (Middle column) and NCEP-R2 (Right column). Averages are over 1979-2001 for all seasons: DJF (Top row), MAM (Second row), JJA (Third row) and SON (Bottom row). The A_Z quantities are contoured (black) and the differences between each reanalysis and the composite mean reanalysis are shaded (colour). Units are J m^{-2} Pa^{-1} (10^5 J m^{-2} bar^{-1}). The zero contour is omitted and the contour interval is 50. The zonal mean topography is shaded in black.

The cross-sections of eddy available potential energy, A_E, in Figure 4.3, show all levels contributing importantly to the global integral at the high latitudes of both hemispheres (displaced to the equator compared to those in A_Z), reflecting the greater zonal variability in the temperature field at these latitudes. Overall, the distributions of the A_E integrands agree among the three reanalysis, with the integrated values reasonably close to each other. The greatest difference is of about 15% between ERA-40 and NCEP-R2 in JJA ($\lesssim$10% in the other seasons). It is also noticeable that the

contributions from the mid troposphere upwards of Southern Hemisphere (SH) are somewhat smaller in NCEP-R2 as compared to the others datasets, while those over the Antarctica region are somewhat larger.

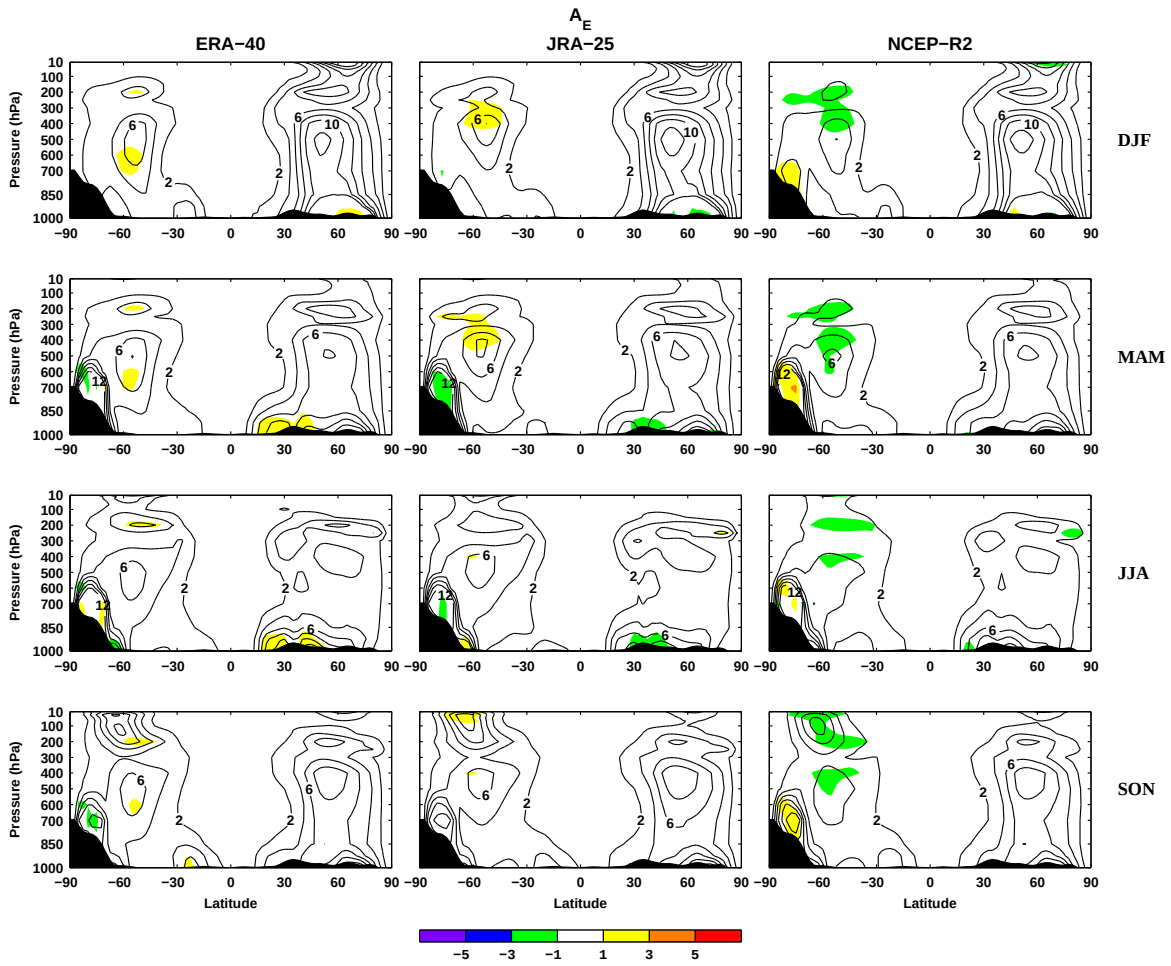

Figure 4.3: The same as in Figure 4.2, but for eddy available potential energy, A_E. The contour interval is 2.

Despite some local differences in magnitude, Figure 4.4 show an almost perfect match in the shape of the cross-sections of zonal mean kinetic energy, K_Z, among the three datasets. Differences between the integrated values are always less than 10%. The integrand of K_Z is dominated by the tropospheric jets, peaking at 200 hPa, with secondary contributions from the stratospheric polar night jets and low latitude easterlies.

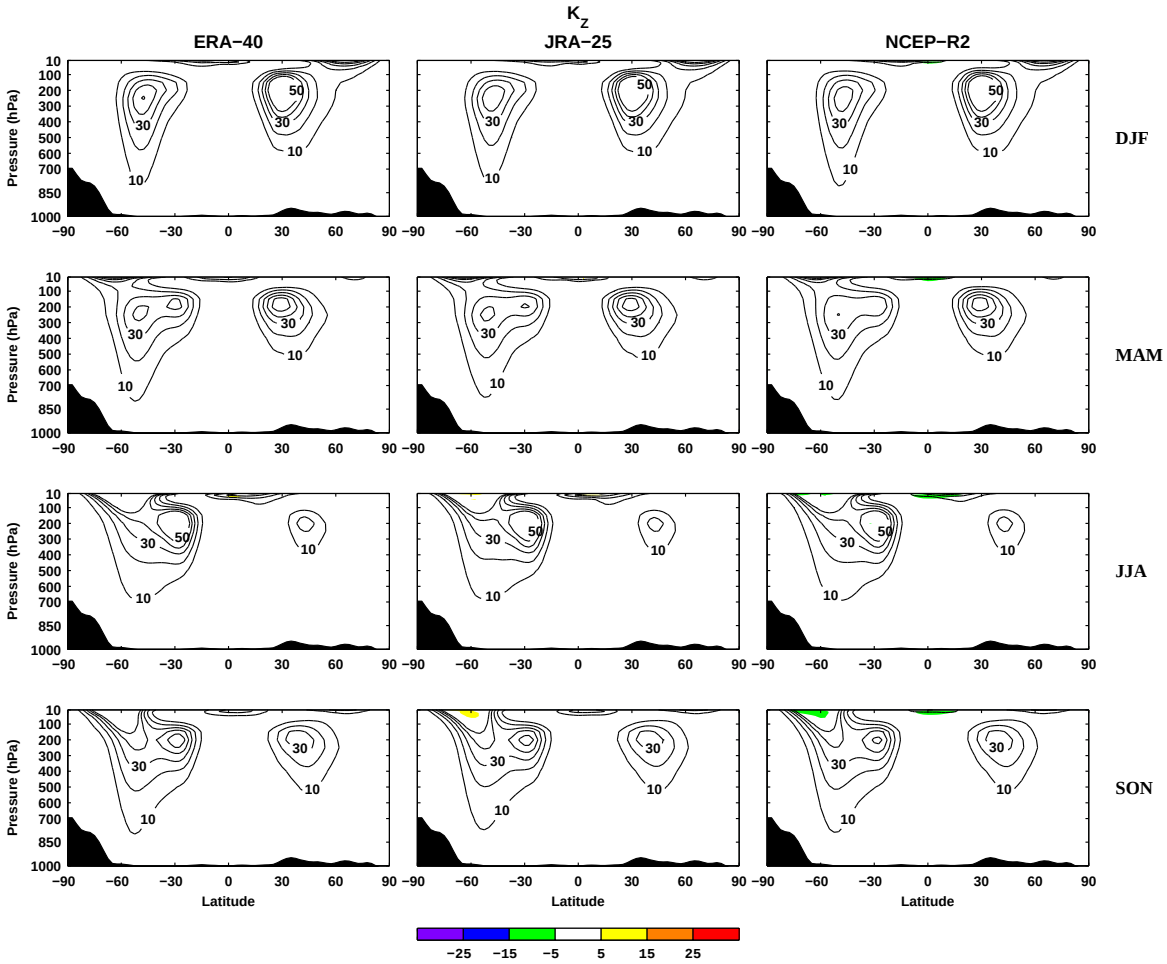

Figure 4.4: The same as in Figure 4.2, but for zonal mean kinetic energy, K_Z. The contour interval is 10.

The cross-sections for the eddy kinetic energy, K_E, are displayed in Figure 4.5. The main contribution to K_E, is associated with the tropospheric jet stream and its meanders, peaking at 250 hPa for all seasons. Additional contributions associated with the stratospheric polar night jets are also found, specially during DJF in the Northern Hemisphere (NH) and throughout JJA and SON in the SH. Although the NCEP-R2 values are again somewhat smaller than those from ERA-40 and JRA-25 near the SH jet stream, the cross-sections of K_E are similar between the three reanalysis and the differences in the global integrals of K_E do not exceed 10%.

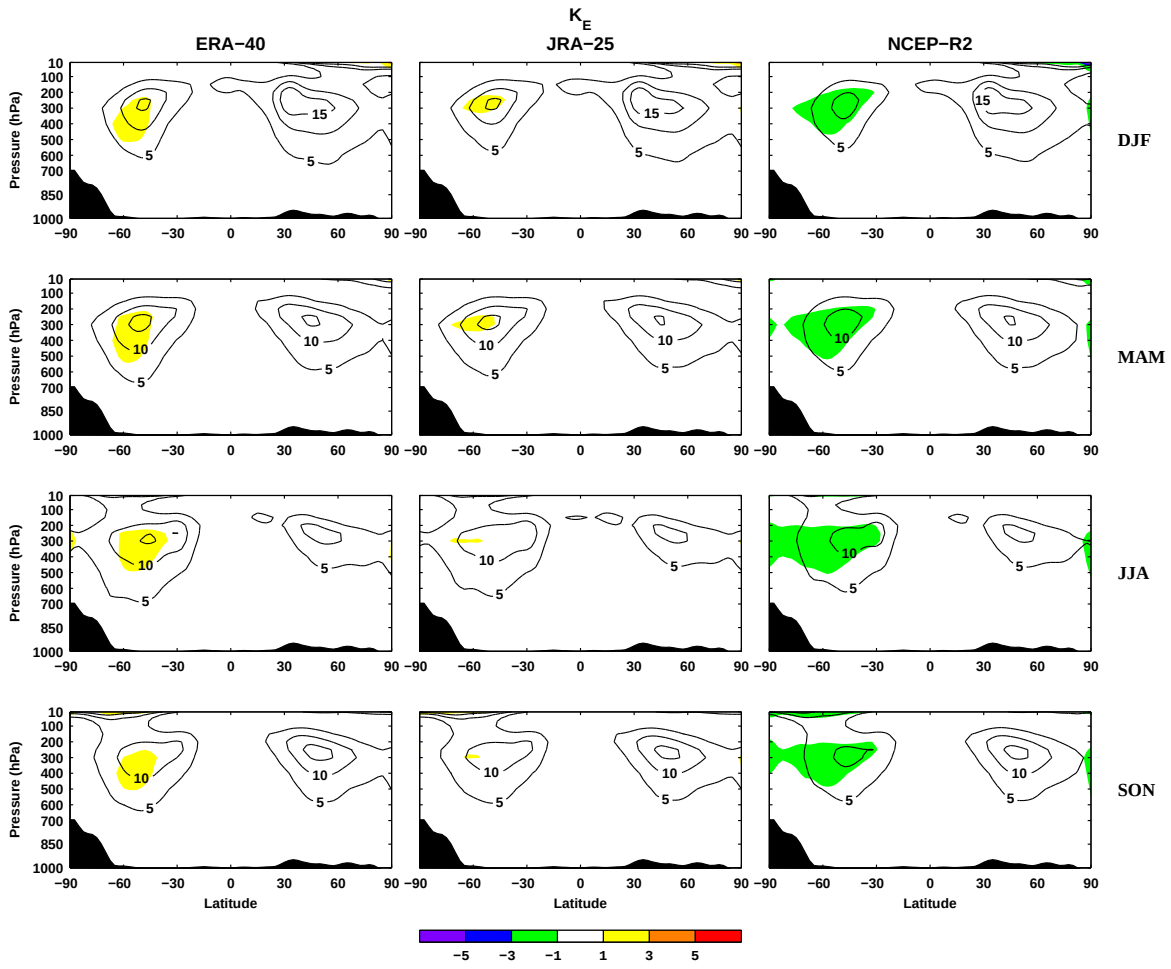

Figure 4.5: The same as in Figure 4.2, but for eddy kinetic energy, K_E. The contour interval is 5.

Energy conversion/transfer rates

Figure 4.6 shows all tropospheric levels contributing positively to the integral of the rate of transfer of zonal mean to eddy available potential energy, C_A, at the extratropical latitudes of both hemispheres in all seasons. Additional positive contributions come from the high latitudes in the upper levels, while small negative contributions are found at middle latitudes in the lower stratosphere centred around 100-150 hPa. These patterns in the integrands of C_A agree well between the datasets, although local differences in their magnitude are also apparent. The values of the C_A integrand from JRA-25 are typically lower than those of ERA-40 and NCEP-R2 at low levels (700-925 hPa) and larger at the upper troposphere (∼200-400 hPa). The largest difference in

the global integrals of C_A is between ERA-40 and NCEP-R2 in JJA (∼12%), and hence tracked in the SH, while for the other seasons those differences are less than 8%.

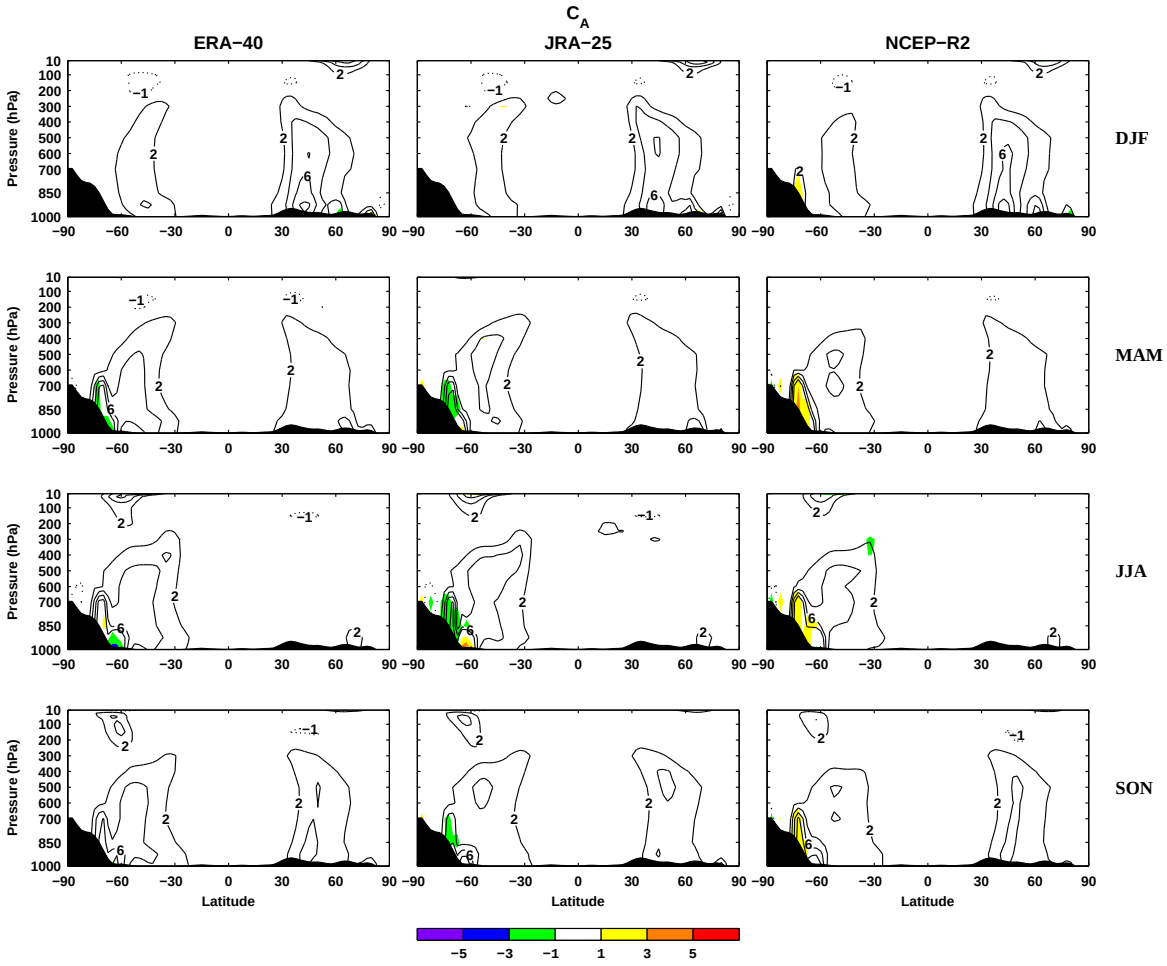

Figure 4.6: The same as in Figure 4.2, but for the transfer rate of zonal mean to eddy available potential energy, C_A. Positive (Negative) values of C_A are represented by continuous (dotted) contours. Units are 10^5 W m^{-2} Pa^{-1} (W m^{-2} bar^{-1}).

The conversion rate from eddy available potential energy to eddy kinetic energy, C_E, computed with the "$\omega\alpha$" formulation, is displayed in Figure 4.7. The three reanalysis have in common the positive contributions in the extratropical troposphere, with additional positive contributions at the winter hemisphere upper levels, and small negative values in the lower stratosphere. NCEP-R2 values are typically lower in the SH than those of ERA-40 and JRA-25 for all seasons, and also in the upper troposphere of NH for JJA. These facts lead to the differences between the global integrals of C_E

for NCEP-R2 and ERA-40 (JRA-25) that reach 19% (17%) in JJA, and 14% (12-13%) in SON and MAM. In DJF the same difference is 9% (6%). The same conversion rate computed with the "$\mathbf{v} \cdot \nabla z$" formulation is in Figure 4.8. It is evident that the stronger contributions for C_E with the "$\mathbf{v} \cdot \nabla z$" formula is concentrated near the surface. According to the discussion in section 3.3, the global integral of C_E, computed with the "$\mathbf{v} \cdot \nabla z$" formula, is therefore strongly dependent on the contributions from underground (i.e. unphysical) data and the way it is interpolated/extrapolated to the pressure levels crossing the topography. Hence, the global integral of C_E should be more accurately estimated by using the "$\omega\alpha$" formula.

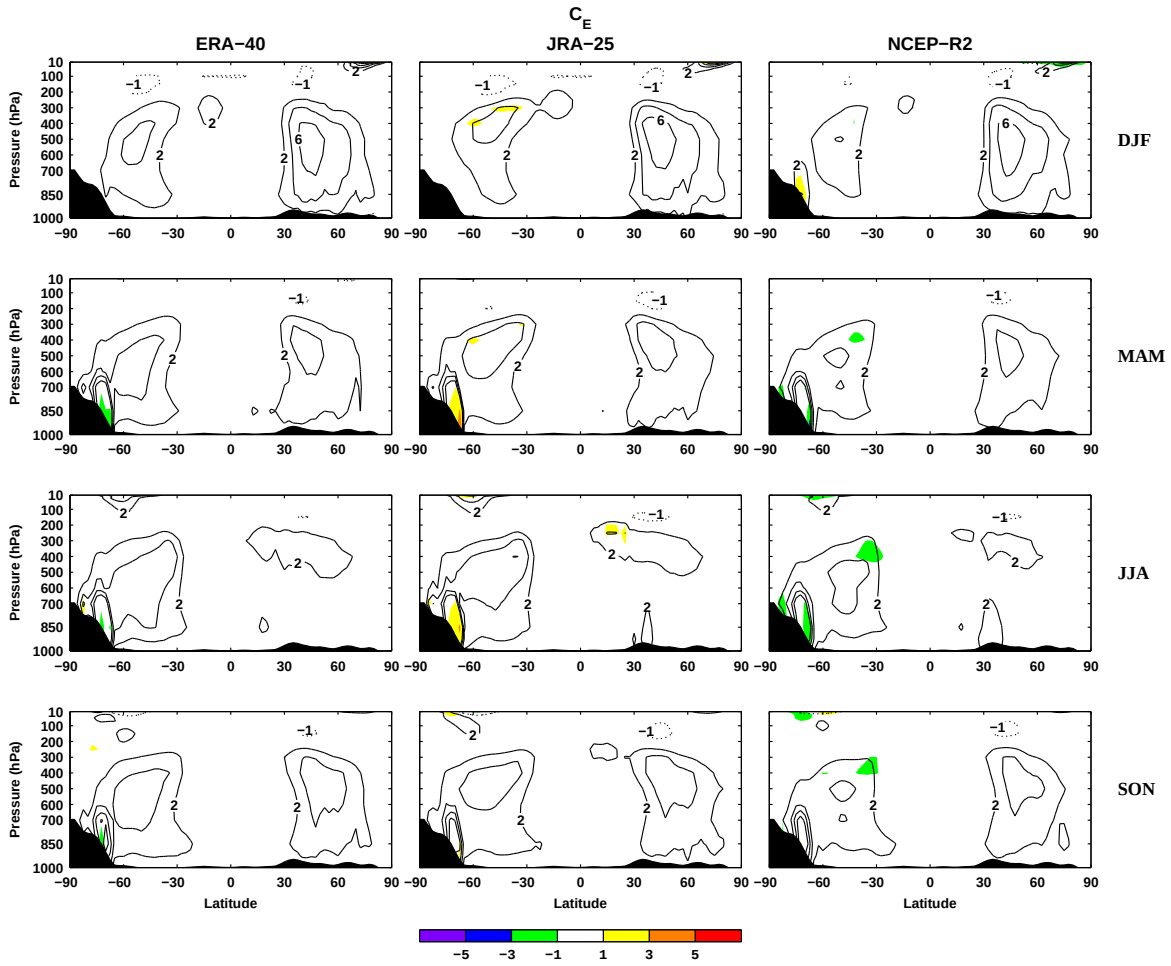

Figure 4.7: The same as in Figure 4.6, but for the conversion rate of eddy available potential energy to eddy kinetic energy, C_E, computed with the "$\omega\alpha$" formulation.

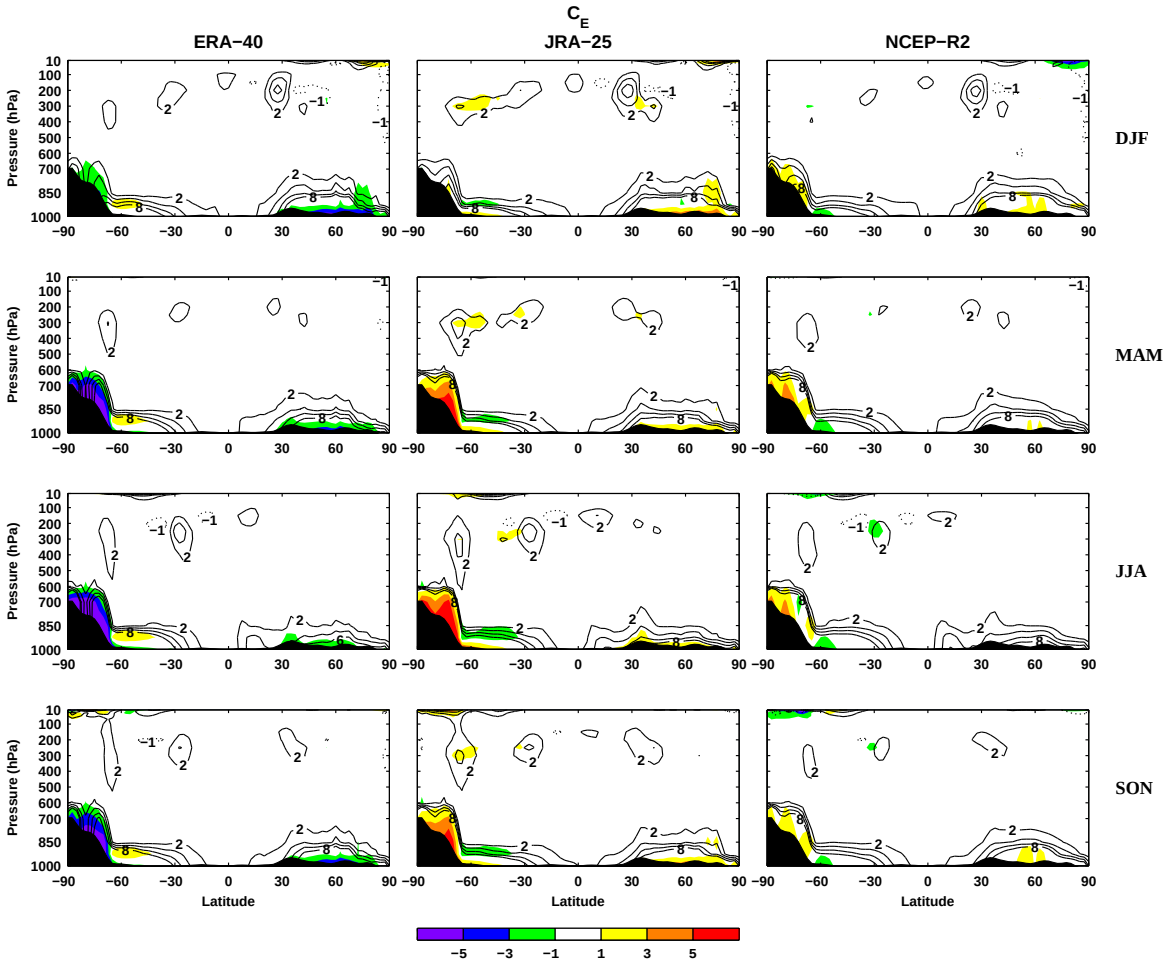

Figure 4.8: The same as in Figure 4.7, but computed with the "$\mathbf{v} \cdot \nabla z$" formulation.

In Figure 4.9, the cross-sections for the rate of transfer of eddy to zonal mean kinetic energy, C_K, show maximum positive contributions just equatorward the tropospheric jets, surrounded by smaller negative contributions in the winter hemisphere. Secondary positive contributions are seen equatorward the stratospheric polar night jets. These features are in good qualitative agreement among the three datasets, but quantitative differences are also detected, which are located mostly in the SH. Since this term is approximately one third of term C_A, the differences in the global integral of C_K between ERA-40 and NCEP-R2 (JRA-25) is about 31% (13%) in JJA and 17-22% (11%) in MAM and SON. In DJF, this difference is 5% (9%).

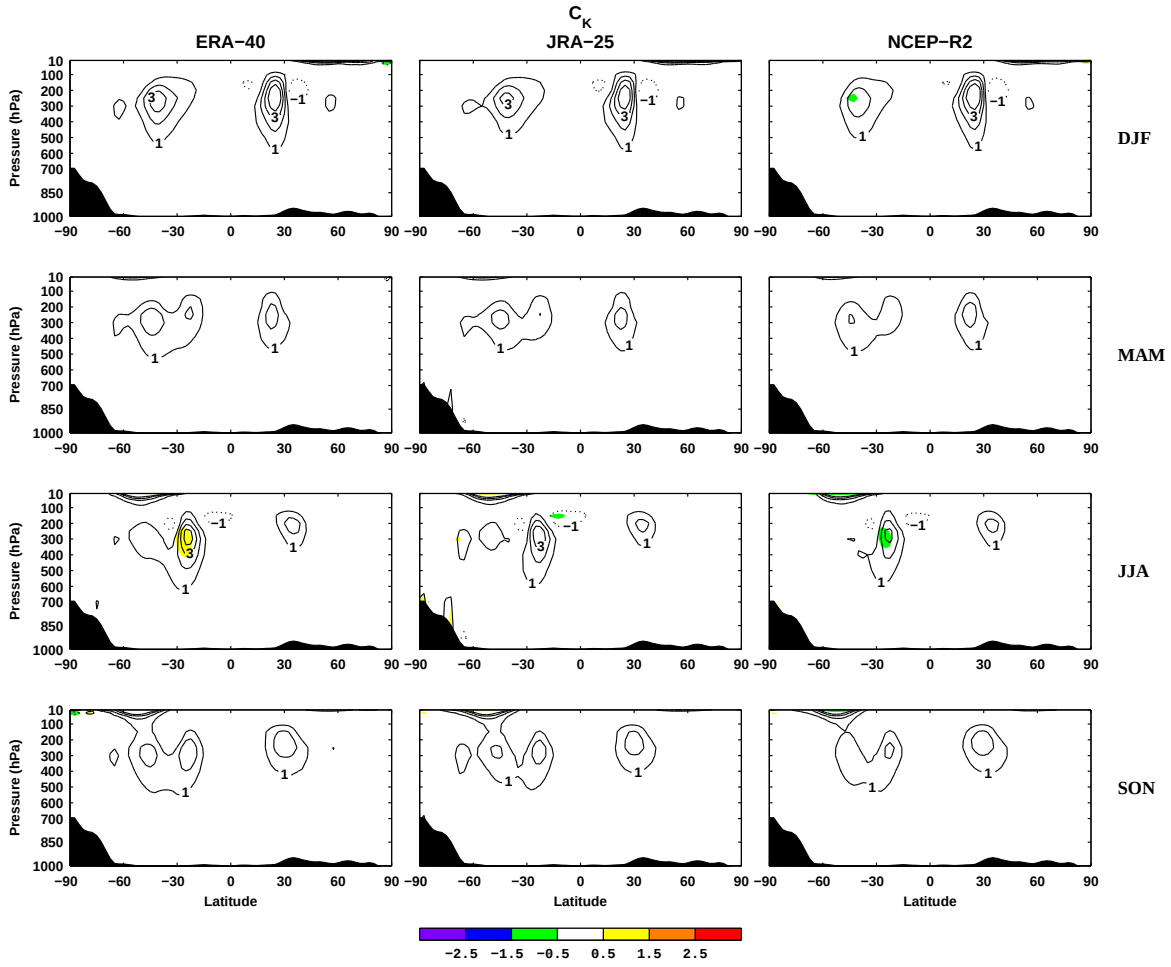

Figure 4.9: The same as in Figure 4.6, but for the transfer rate of eddy to zonal mean kinetic energy, C_K. Both positive and negative contour intervals is 1.

Figures 4.10 and 4.11 show the cross-sections for the conversion rate of zonal mean available potential energy to zonal mean kinetic energy, C_Z, computed with formulations "$\omega\alpha$" and "$\mathbf{v}\cdot\nabla z$", respectively. Both formulae yield positive and negative contributions in the integrand of C_Z. These contributions of opposite signs tend to cancel each other in the global integral of C_Z, leading this term to be the smallest in the global energy cycle. It may be seen that C_Z computed with formula "$\omega\alpha$" has a strong positive contribution from the underground region of Antarctica, which may erroneously imbalance the cancel effect towards the positive side. Positive contributions from the same region to the integrand of C_Z still exist when using formula "$\mathbf{v}\cdot\nabla z$", but their weight to the global integral of C_Z is less important. Consequently, term C_Z should be more accurately

evaluated with formula "$\mathbf{v} \cdot \nabla z$", for quantitative purposes.

Positive values of C_Z computed with formula "$\omega\alpha$", are usually associated with a thermodynamically direct circulation and negative values with an indirect circulation (e.g. Oriol, 1982). The positive and negative values alternating in the vertical are associated with the thermally direct Hadley cells, the indirect Ferrel cells and to some extent with the also direct Polar cells.

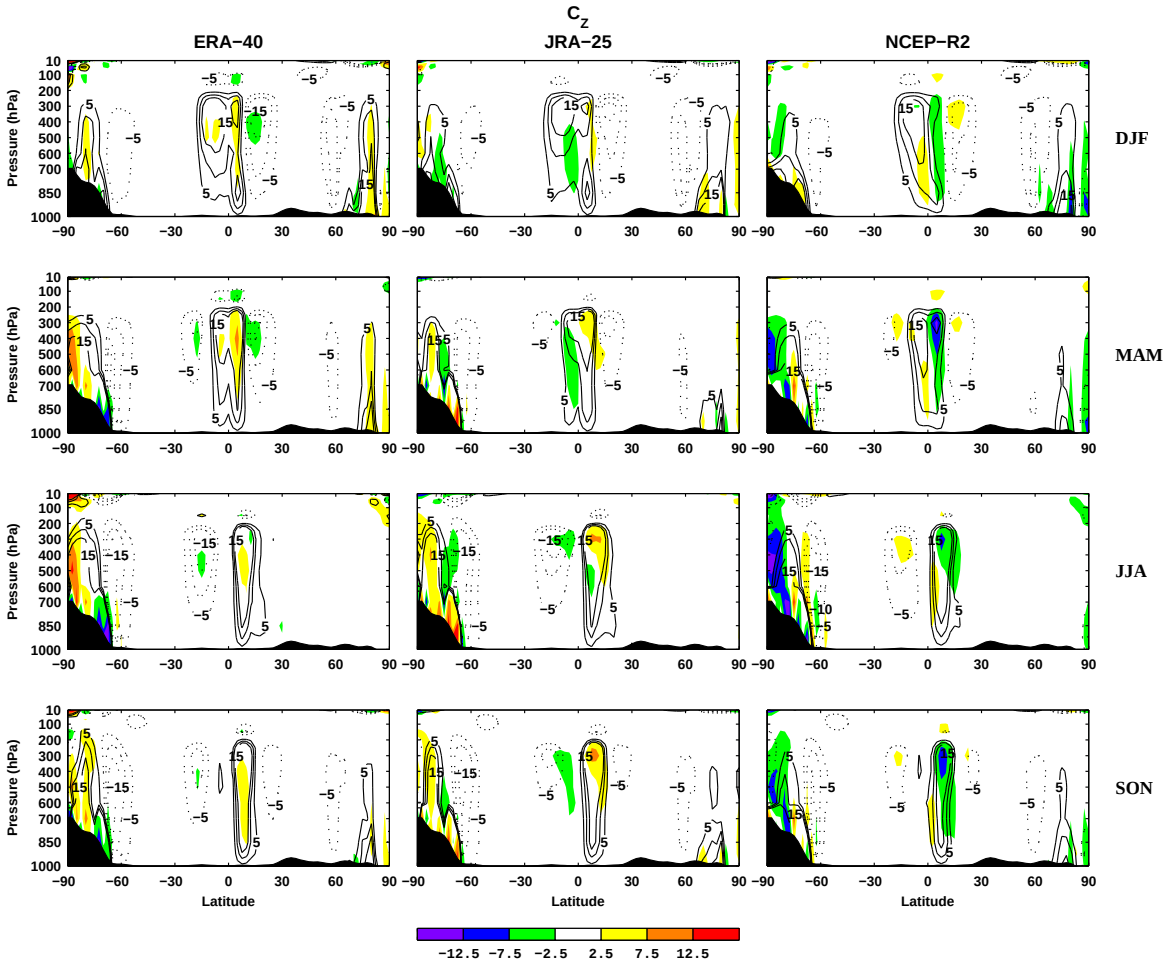

Figure 4.10: The same as in Figure 4.6, but for the conversion rate of zonal mean available potential energy to zonal mean kinetic energy, C_Z, computed with the "$\omega\alpha$" formulation. Both positive and negative contour intervals is 5.

For C_Z computed with formula "$\mathbf{v} \cdot \nabla z$", there are negative contributions in the upper troposphere just poleward of the tropospheric jets and positive contributions

equatorward the same jets in the upper troposphere/lower stratosphere. Additionally positive contributions are also found mainly at mid to high latitudes near the surface in the SH.

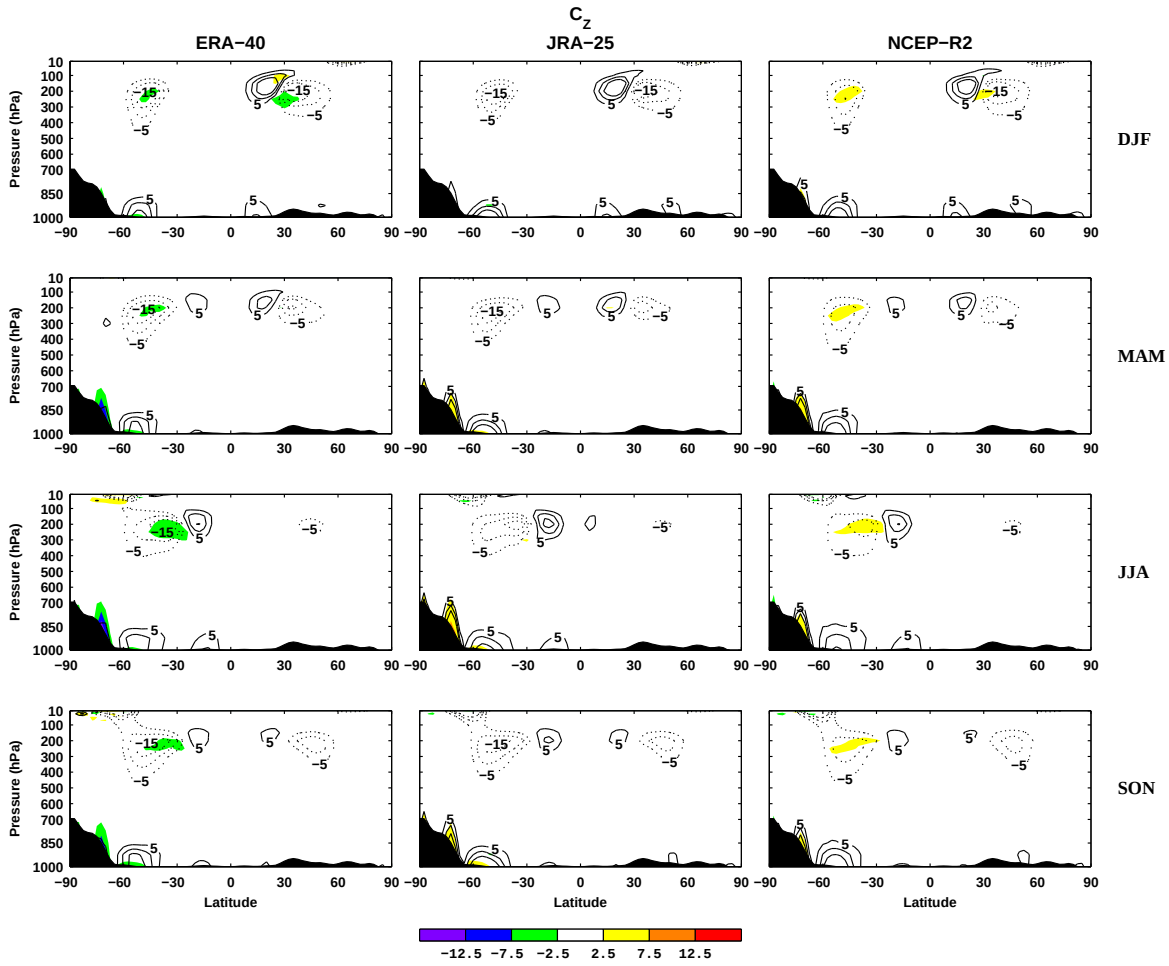

Figure 4.11: The same as in Figure 4.10, but computed with the "$\mathbf{v} \cdot \nabla z$" formulation.

Although the distributions of the C_Z integrands agree qualitatively between the three datasets, there are local differences in the magnitude of the contributions, which are once again stronger in the SH troughout the year. Despite these differences, the three datasets agree on the smallness of this conversion rate, which has little weight in the atmospheric energy cycle and, additionally, has an inter-annual variation comparable to its average value.

The comparison of the stability parameter (γ) in Figure 4.12, shows a close fitting between the three reanalysis in all seasons, peaking at the 400 hPa level and near the surface.

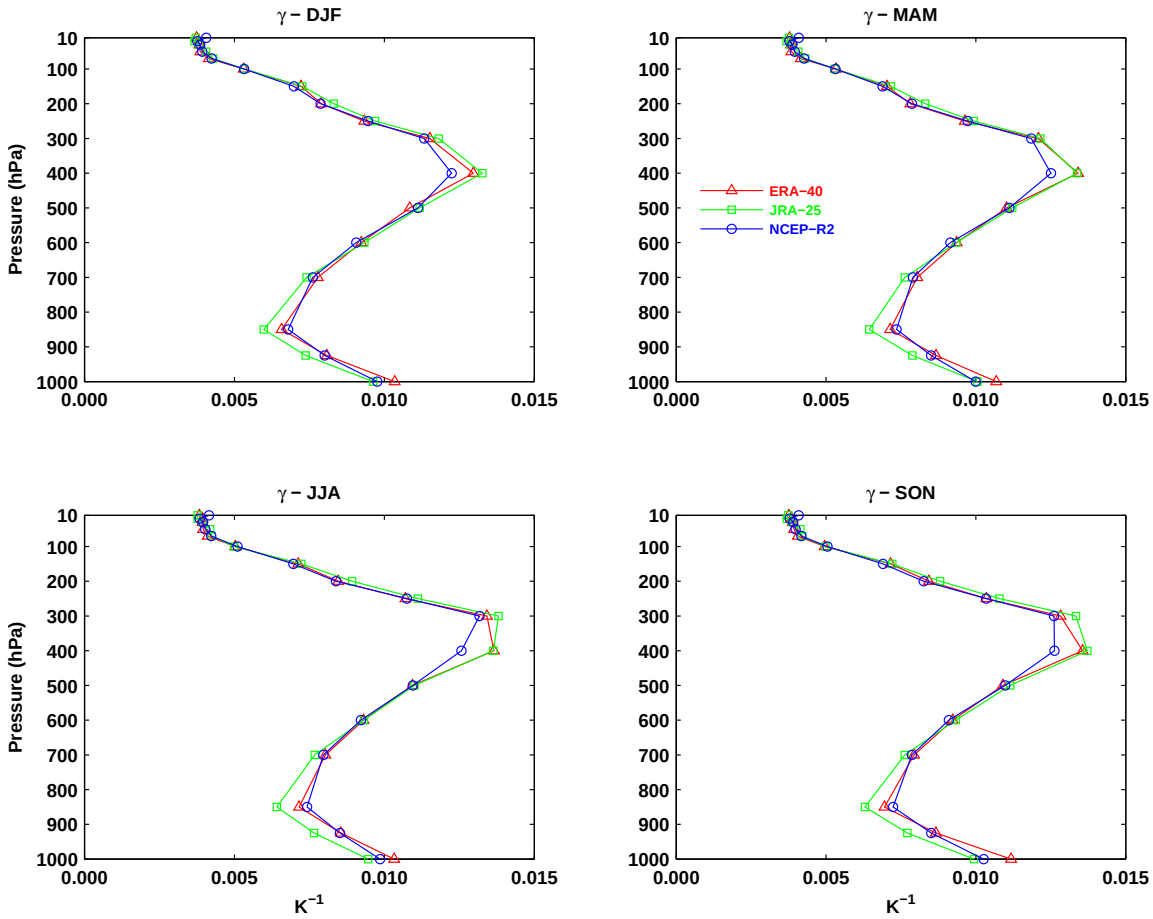

Figure 4.12: Mean vertical profile of the stability parameter, γ, for ERA-40 (△), JRA-25 (□) and NCEP-R2 (○). Averages are over 1979-2001 for all seasons: DJF (Top left), MAM (Top right), JJA (Bottom left) and SON (Bottom right). Units are K^{-1}.

This analysis was performed for the period after 1979, when the Television Infrared Observation Satellite Operational Vertical Sounder (TOVS) data are available, which is regarded as the most substantial change in the observing system. Since these satellite observations are used in all three assimilation systems, eventual discrepancies between the three reanalysis cannot be attributed to this change in the observing system "*per se*". However, the TOVS data are assimilated differently among the reanalysis sys-

tems, which may account for some of the differences between ERA-40, JRA-25 and NCEP-R2. The ERA-40 and JRA-25 systems assimilate satellite radiances directly in a variational scheme, while NCEP-R2 (and NCEP-R1) assimilates radiance retrievals produced by the National Environmental Satellite, Data and Information Service (NESDIS). Additionally, the Special Sensor Microwave/Imager (SSM/I), 1987 onwards, and the Advanced Microwave Sounding Unit (AMSU) from Advanced TOVS (ATOVS), replacing TOVS from 1998 onwards, are assimilated only in the ERA40 and JRA-25 reanalysis (Kanamitsu et al., 2002; Uppala et al., 2005; Onogi et al., 2007).

Time series of globally integrated terms of the Lorenz energy cycle are displayed in Figures 4.13 and 4.14 for DJF and JJA, respectively. The differences between the reanalysis are smaller for DJF and larger for JJA. The curves are generally in phase, which indicates consistency in the temporal variability of the energy cycle terms in the three reanalysis. It is also evident that the curves become closer to each other for the later years, which is probably due to the increase in the number of observations that are assimilated in the reanalysis (see Kistler et al., 2001, Figure 1), reducing therefore the influence of the models in the analysis and consequently their associated bias.

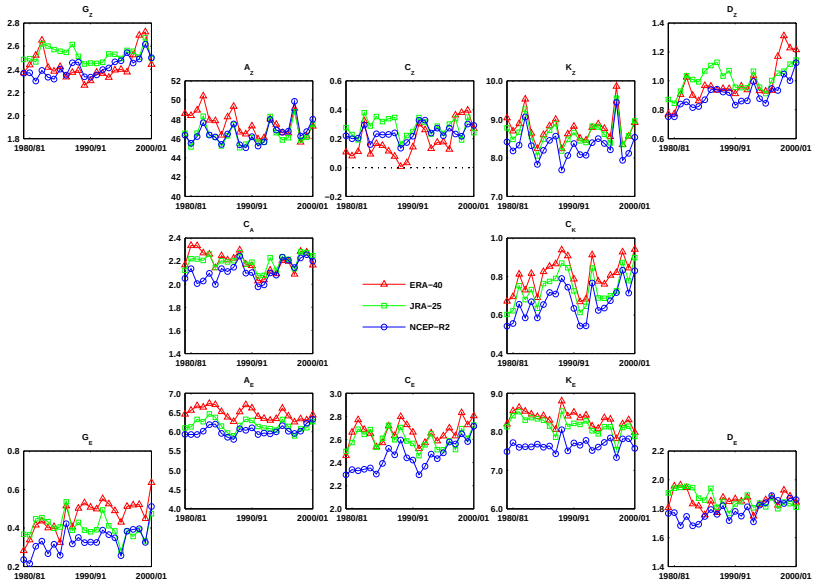

Figure 4.13: DJF time series of the Lorenz energy cycle terms for ERA-40, JRA-25 and NCEP-R2. Units are 10^5 J m^{-2} for energy levels and W m^{-2} for conversion/transfer rates.

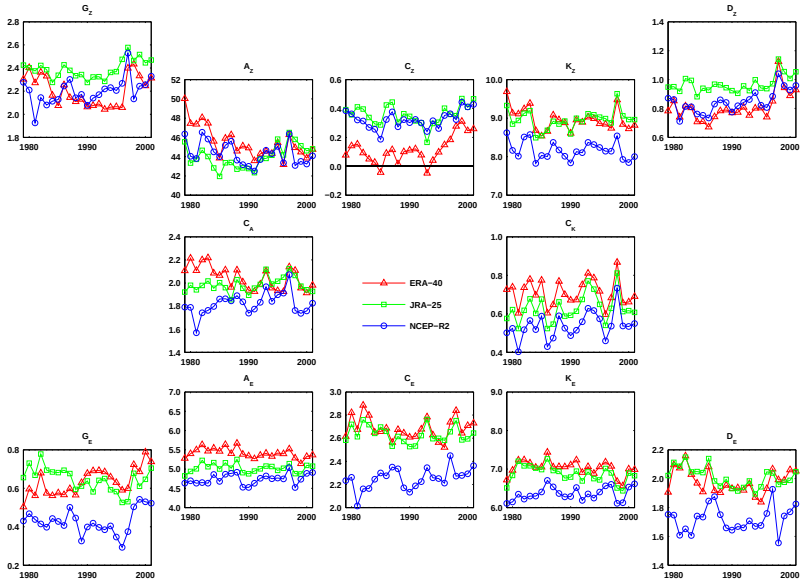

Figure 4.14: The same as in Figure 4.13, but for JJA.

Apparently, the assimilation of SSM/I data in ERA-40 and JRA-25 does not have a great impact on the energetics since, otherwise, its influence should have been noted only in ERA-40 and JRA-25, which isn't perceptible from Figures 4.13 and 4.14. The different horizontal and vertical resolutions of the models used for the reanalysis may be implied in some of the discrepancies between them. For example, Dell'Aquilla et al. (2005) argue that the spectral truncation can affect the horizontal convergence of momentum, which changes the horizontal wind shear that controls the growth of the baroclinically unstable eddies. In addition, the vertical resolution may influence the meridional and vertical heat fluxes associated with baroclinic perturbations.

In summary, it is clear from Figures 4.2 to 4.11 that the shape and location of the latitude-pressure distributions in the various integrands, are rather similar among the three reanalysis. Differences are mainly related to the magnitude of some of those distributions, which are typically weaker in NCEP-R2 and almost exclusively located in the SH. In general, the differences are fairly unimpressive and are likely due to the different model biases and resolutions, and the different data assimilation methods used in the reanalysis systems.

4.1.2 Saltzman energy cycle

The spectra of the various energetics terms averaged over 1979-2001 for all seasons, are represented in Figures 4.15 to 4.22. A linear-log scale is used to highlight the differences for the lowest order wavenumbers, that account for most of the energy flow. As expected from the previous analysis, some differences in the magnitudes of energy and energy conversion/transfer are found at each wavenumber, yet, overall, the peaks and slopes in the various spectra are coherent among the three datasets for all seasons.

Energy levels

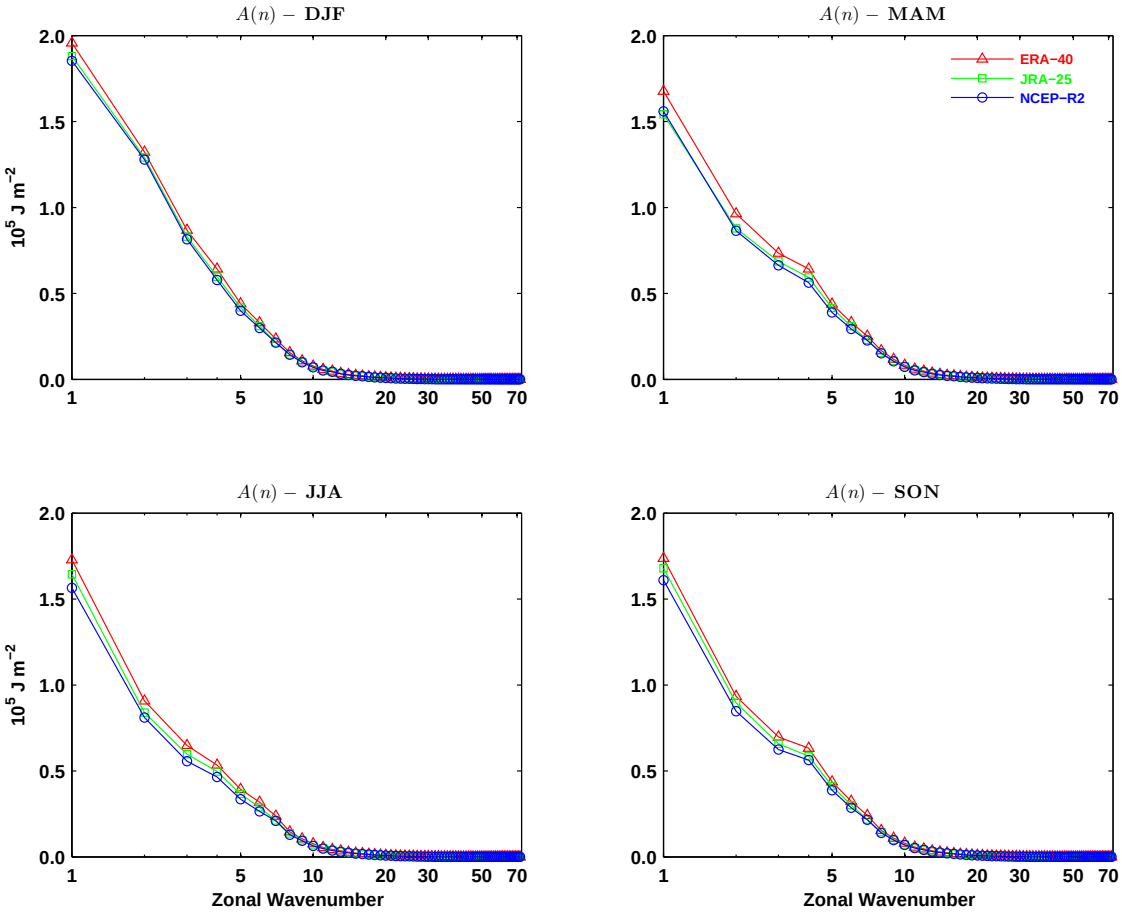

Figure 4.15: Mean wavenumber spectra of available potential energy, $A(n)$, for ERA-40, JRA-25 and NCEP-R2. Averages are over 1979-2001 for all seasons: DJF (Top left), MAM (Top right), JJA (Bottom left) and SON (Bottom right). Units are 10^5 J m^{-2}.

The shape of the available potential energy spectra, $A(n)$, is similar among the three datasets in all seasons, with the JRA-25 values closer to those of NCEP-R2 (Figure 4.15). Analogous features and similarities is seen in the spectra of kinetic energy, $K(n)$, represented in Figure 4.16, except that the JRA-25 values are closer to those of ERA-40. Using a log-log scale, both spectra, $A(n)$ and $K(n)$, follow a -3 power law beyond wavenumber 6 for all reanalysis (not shown), which is in agreement with previous studies (e.g. Hasegawa et al., 1997). A log-log scale can also emphasise the differences between the various datasets in the tail of the spectra, although it may obscure the differences for the first wavenumbers (say $n = 1$ to 15). This type of scale is used in section 4.1.3 for the energy spectra within the 3-D normal mode energetics scheme, becoming then evident the power law behaviour.

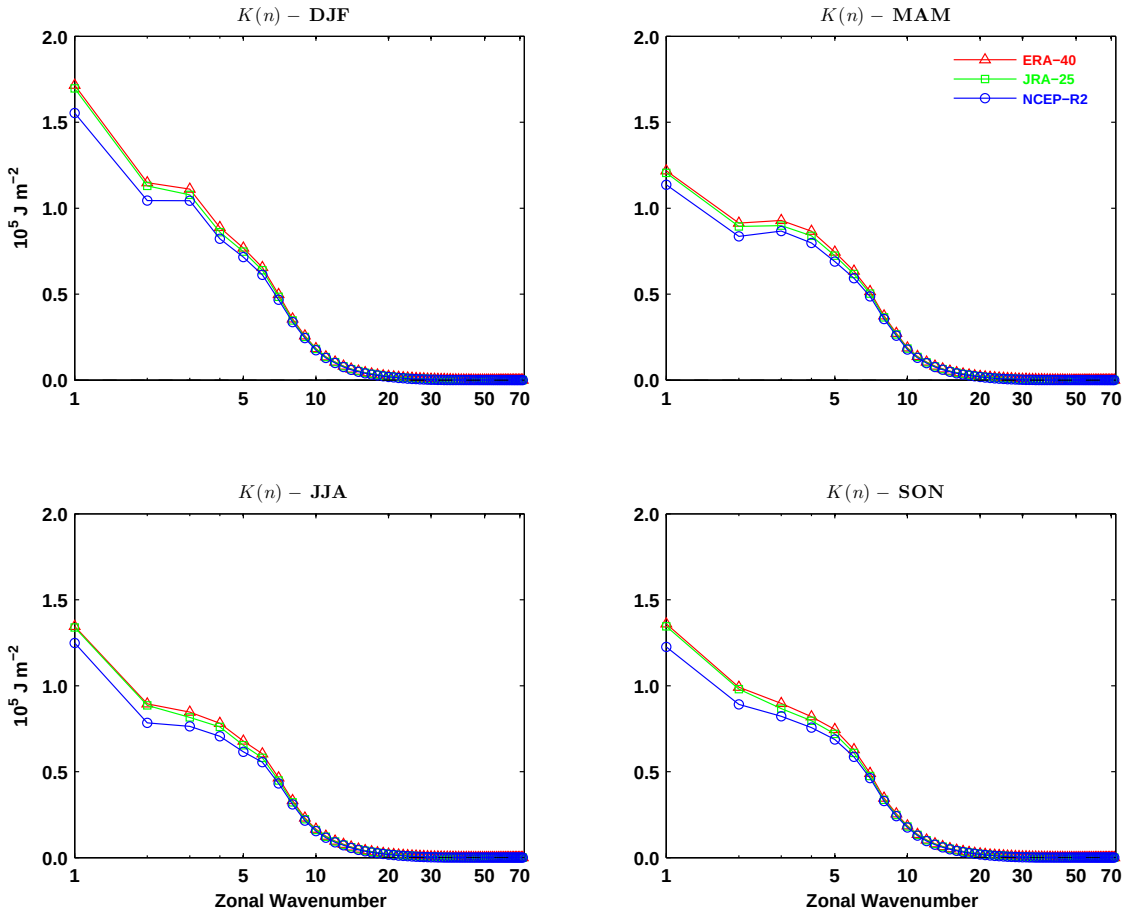

Figure 4.16: The same as in Figure 4.15, but for kinetic energy, $K(n)$.

Energy conversion/transfer rates

The spectra for the rate of transfer of zonal mean available potential energy to the eddy available potential energy in wavenumber n, $R(n)$, which may be denominated by zonal-wave interactions of available potential energy, are shown in Figure 4.17. In DJF, the $R(n)$ spectra peaks at the planetary-scale wavenumber $n = 3$ and secondarily at the synoptic-scale wavenumber $n = 6$. In the other seasons it has a characteristic broad maximum at synoptic-scale wavenumbers $n = 4$ to 6. These properties are present in the three datasets. At each wavenumber, the conversion values of JRA-25 are generally closer to those of ERA-40 for all seasons except for SON.

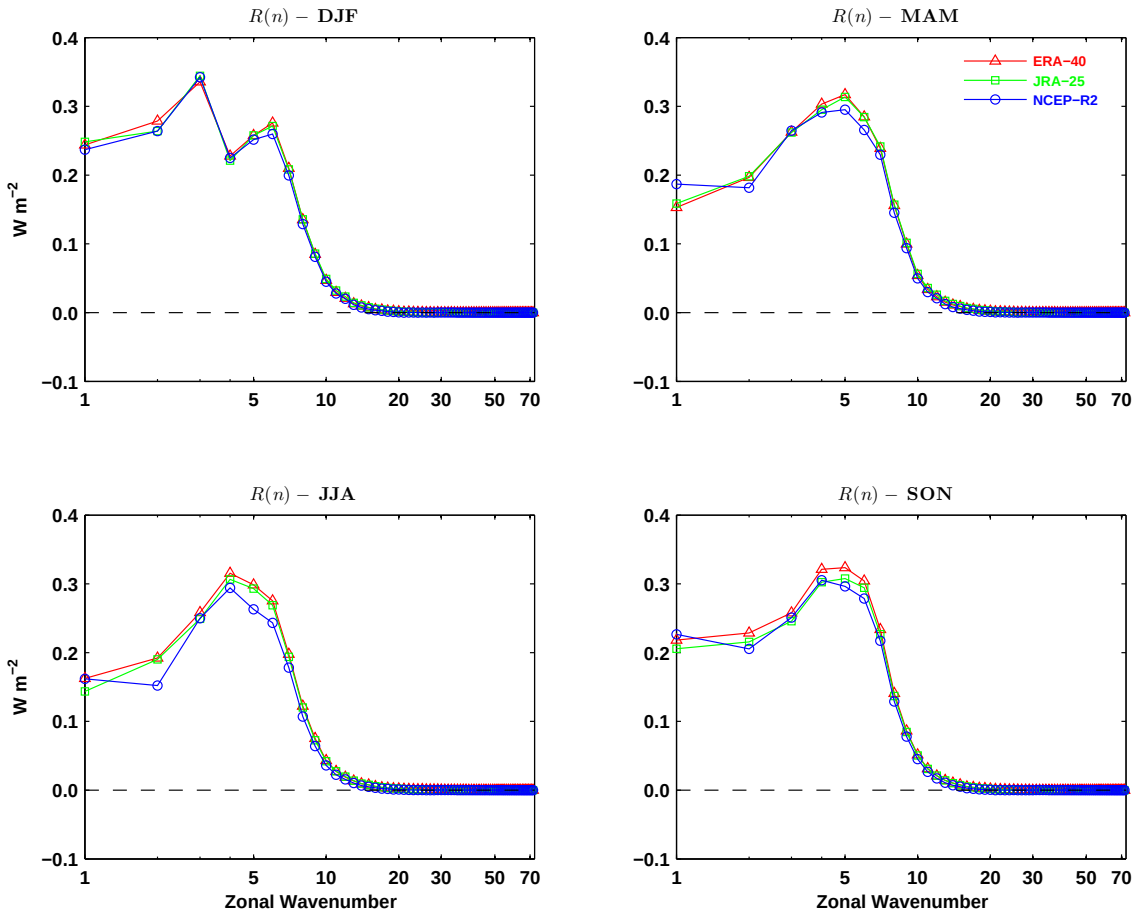

Figure 4.17: Mean wavenumber spectra of zonal-wave interactions of available potential energy, $R(n)$, for ERA-40, JRA-25 and NCEP-R2. Averages are over 1979-2001 for all seasons: DJF (Top left), MAM (Top right), JJA (Bottom left) and SON (Bottom right). Units are W m^{-2}.

Figures 4.18 and 4.19 contain the spectra for baroclinic conversion of available potential energy of wavenumber n to eddy kinetic energy of wavenumber n, $C(n)$, computed with the "$\omega\alpha$" and "$\mathbf{v} \cdot \nabla z$" formulae, respectively. The greater discrepancies between the estimates with formula "$\mathbf{v} \cdot \nabla z$" are associated to its strong dependence on the underground data (see Figure 4.8) and the way it is interpolated/extrapolated to the pressure levels crossing the topography. Nevertheless, the shape of the spectra is similar among the three reanalysis. In DJF, these spectra have maxima at $n = 1$ to 3, and at $n = 6$. In the remaining seasons, the $C(n)$ spectra peak at $n = 1$ (most notable in JJA and MAM) and have a secondary broad maximum at about $n = 4$ to 6.

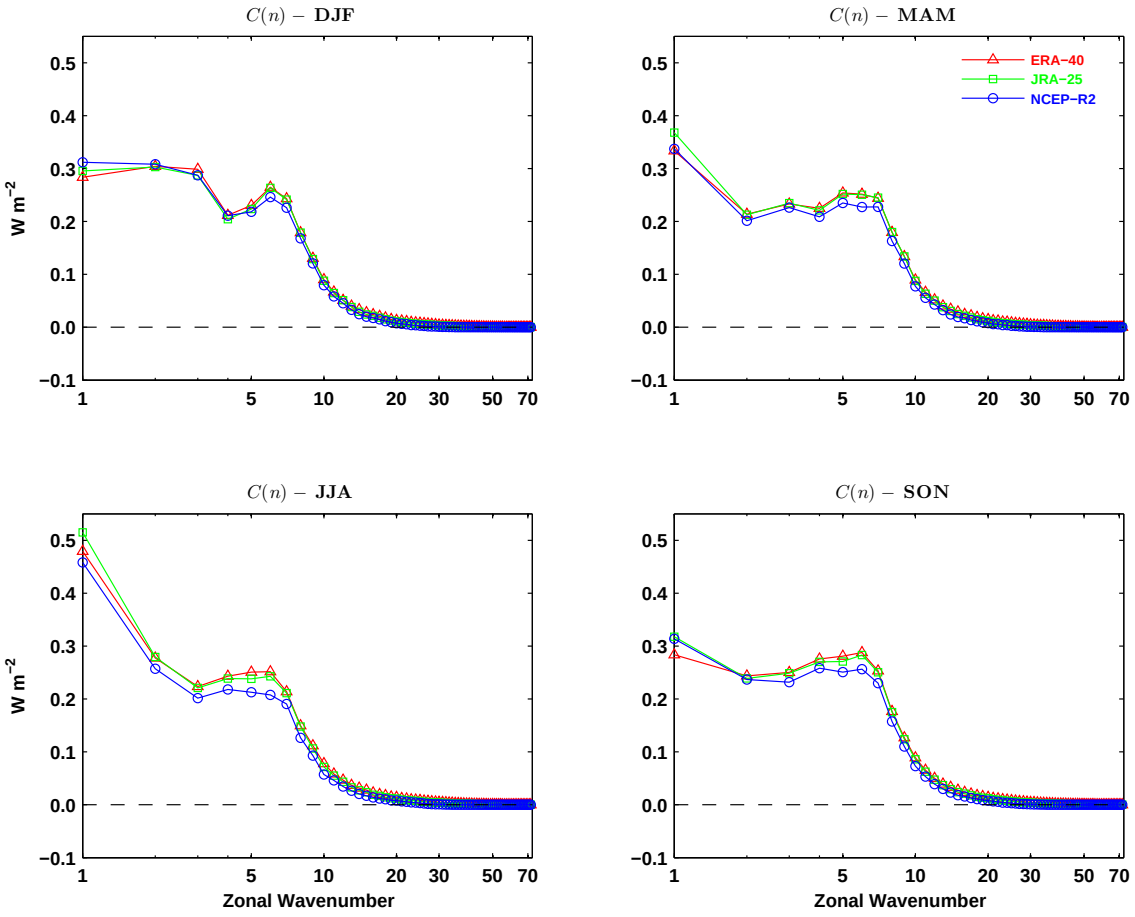

Figure 4.18: The same as in Figure 4.17, but for baroclinic conversion, $C(n)$, computed with the "$\omega\alpha$" formulation.

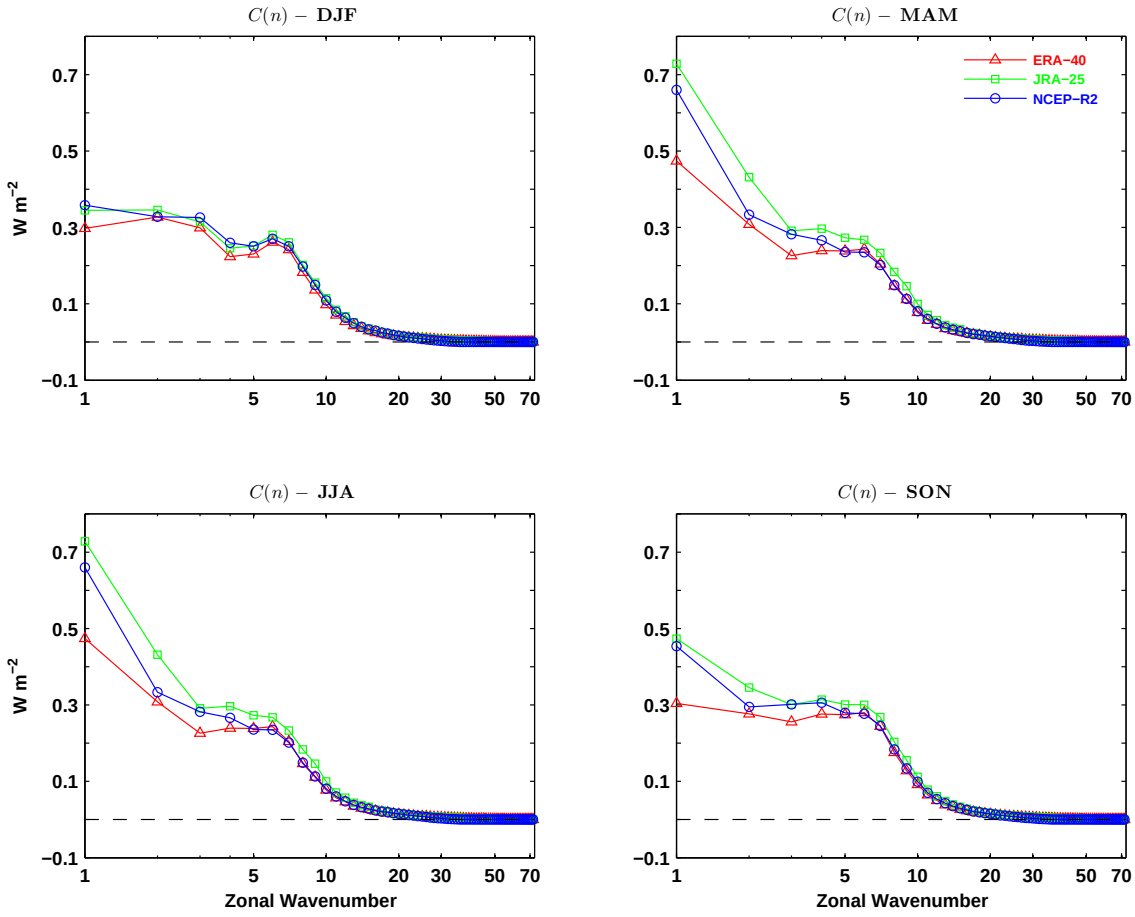

Figure 4.19: The same as in Figure 4.18, but computed with the "$\mathbf{v} \cdot \nabla z$" formulation.

Figure 4.20 illustrates the spectra of zonal-wave interactions of kinetic energy, $M(n)$. These spectra have maxima at $n = 3$ and 6 in all seasons. There is another maximum at $n = 1$ in MAM, SON and DJF (most prominent) for the three datasets (except for NCEP-R2 in SON). The $M(n)$ values in JRA-25 are closer to those in ERA-40 for planetary-scale wavenumbers and to those in NCEP-R2 at the synoptic-scale, in all seasons, and agrees with the estimates of Watarai and Tanaka (2007) for DJF. Most of the 31% (17%) difference between the $C_K = \sum_{n=1}^{N} M(n)$ of NCEP-R2 and that of ERA-40 (JRA-25) in JJA is reflected in the spectra of $M(n)$ at $n = 1$ to 3, the NCEP-R2 values being substantially lower than those of the other two datasets. Analysis of the cross-sections for $\sum_{n=1}^{3} M(n)$ (not shown) confirms that the smaller values of C_K

equatorward the SH tropospheric jet in NCEP-R2 (Figure 4.9), are mostly due to a smaller transfer rate from eddy to zonal mean kinetic energy, at these wavenumbers ($n = 1$ to 3), in all seasons (most prominent in JJA).

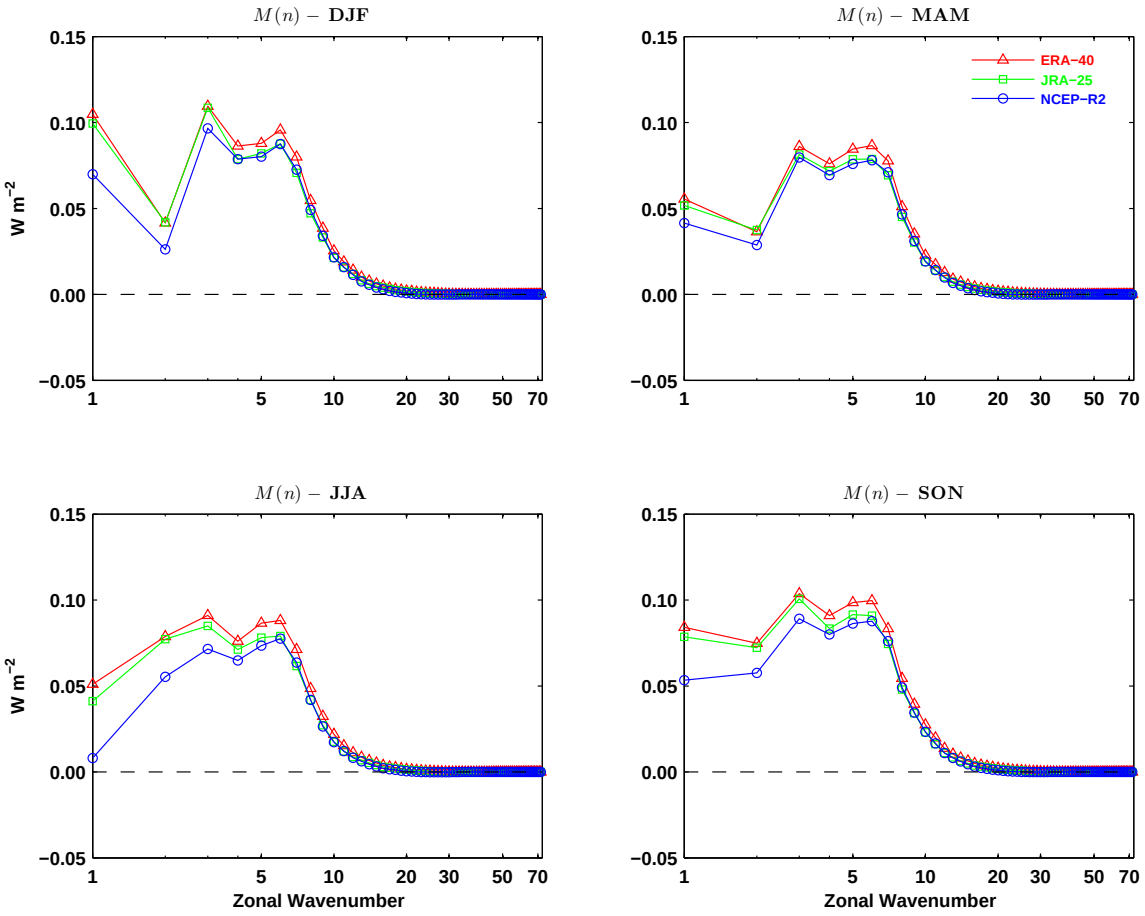

Figure 4.20: The same as in Figure 4.17, but for zonal-wave interactions of kinetic energy, $M(n)$.

Nonlinear wave-wave interactions

The spectra for the rate of transfer of available potential energy to the eddies of wavenumber n from eddies of all other wavenumbers, $S(n)$, which may be termed nonlinear wave-wave interactions of available potential energy, are shown in Figure 4.21. In all seasons, $S(n)$ is negative at wavenumbers in the range of about $n = 2$ to 7 (and also $n = 1$ in DJF), which indicates that the energy is transferred from the eddies in this range to smaller eddies, implying that the flux is associated with the downscale energy

cascade, and also to $n = 1$ (specially in MAM and SON), forming an upscale energy cascade. Throughout the year, the synoptic waves are an important source of available potential energy for smaller waves, which are dominant during MAM and SON.

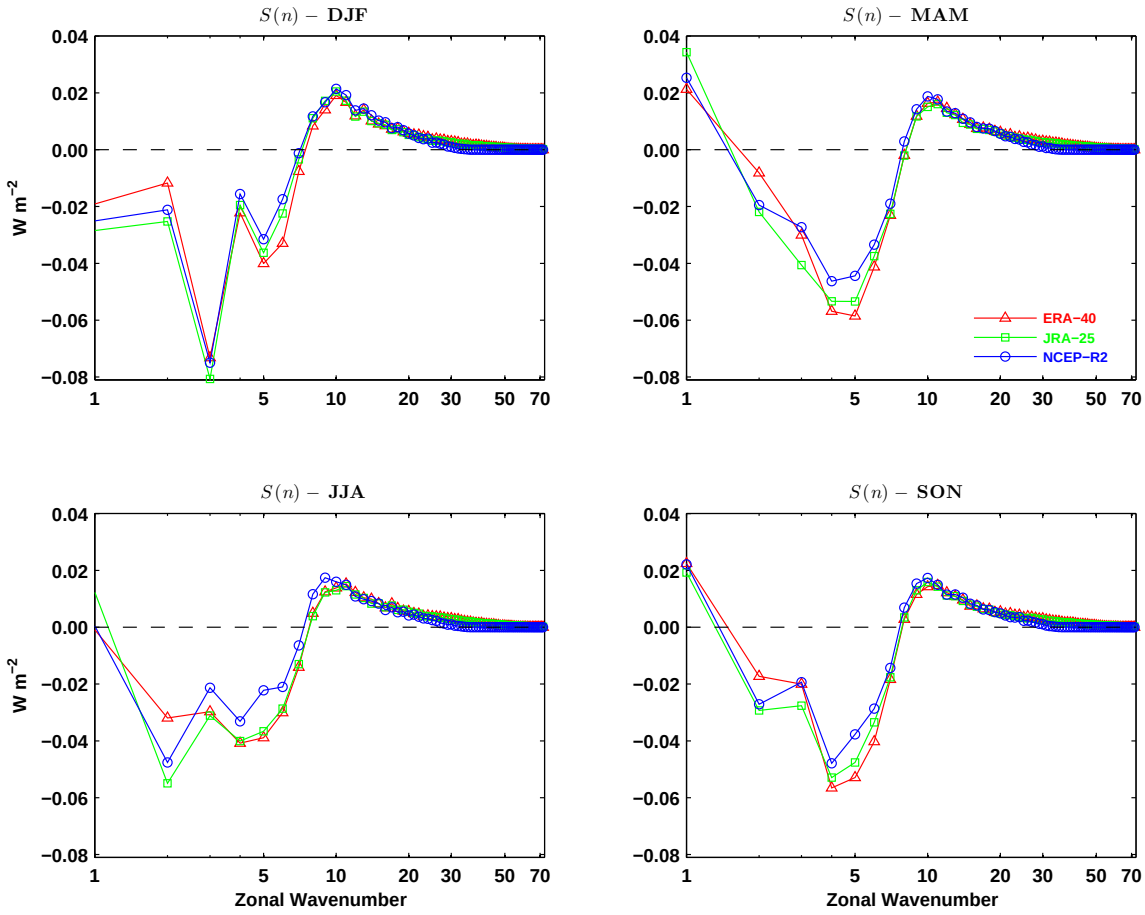

Figure 4.21: The same as in Figure 4.17, but for wave-wave interactions of available potential energy, $S(n)$.

Figure 4.22 illustrates the spectra of nonlinear wave-wave interactions of kinetic energy, $L(n)$. In all seasons, these spectra are generally positive at both the planetary-scale and short-scale wavenumbers, being negative at intermediate wavenumbers, including the synoptic-scale. This leads to the transfer of kinetic energy from the spectral region of negative $L(n)$ to the planetary waves, forming an upscale energy cascade, and to the short waves, forming a downscale energy cascade. In DJF, there is an exception at

wavenumber 2, where $L(n)$ is negative in the three reanalysis. Hence, an orographic forcing in response to the variation of zonal background flow may be the source of energy at wavenumber 2, instead of the synoptic waves, during DJF. The $L(n)$ spectra agree qualitatively well among the three reanalysis, despite some differences in the magnitude of the spectra at each wavenumber, which are smaller in DJF. Another difference in the $L(n)$ spectra between the three datasets, is observed in the spectral range of the energy source region. This region extends from about $n = 5$ to 12 in NCEP-R2, while in ERA-40 and JRA-25 the same region is wider, extending from about $n = 5$ to 16. This implies that waves at the scale of wavenumbers $n = 13$ to 16 receive energy from the source range in NCEP-R2, while the same waves supply energy to the planetary and short waves in both ERA-40 and JRA-25.

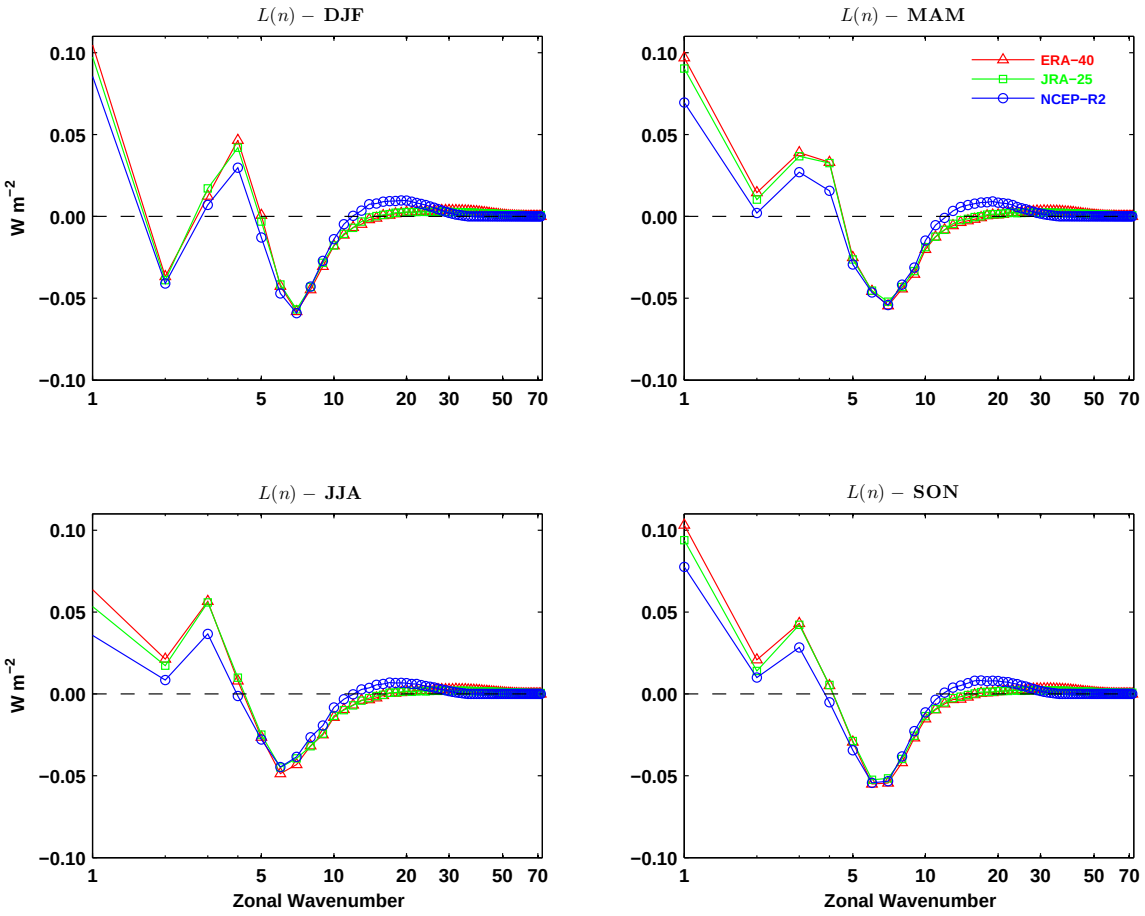

Figure 4.22: The same as in Figure 4.17, but for wave-wave interactions of kinetic energy, $L(n)$.

The shorter range in the $L(n)$ energy source region of NCEP-R2 may be attributed most likely to one or both of the following characteristics. The first is the lower horizontal resolution of the model (T62 for NCEP-R2, TL159 for ERA-40 and T106 for JRA-25) and the second is a consequence of filtering/smoothing when converting data from model levels to pressure levels, which is the case for NCEP-R2 (and also ERA-40, although with much less smoothing), as discussed further below. These two aspects should influence the important downscale cascade of kinetic energy, which must be reproduced, if possible, within the available spectral resolution. Therefore, with lower horizontal resolution it may be expected that the downscale energy cascade starts at lower wavenumbers.

Wavenumber energetics were recently calculated by Watarai and Tanaka (2007) for the DJF case, using ERA-40, JRA-25 and NCEP-R1 reanalysis over the 1979-2001 period. Their estimates are in good agreement with those in this study for DJF. Small numerical differences between both estimates are certainly related to some discrepancies in the variables used for computing the energy cycle terms. For example, they didn't used the vertical velocity (ω) provided by the reanalysis datasets, as being done here, but computed it by integrating the continuity equation from the top of the atmosphere. In Watarai and Tanaka (2007), the energy cycle term for generation of eddy available potential energy, G_E, is an energy output for NCEP-R1, while here the same term is an energy input for NCEP-R2, which agrees with both ERA-40 and JRA-25. A rapid decrease in the spectra of NCEP-R1 and ERA-40 for short waves was reported by Watarai and Tanaka (2007), while such decrease is absent in JRA-25. This is supported in this study as it was also found a rapid decrease for short waves in the spectra of both NCEP-R2 ($n = 36$) and ERA-40 ($n = 63$) in all seasons, which should be a consequence of filtering/smoothing when converting data from model levels to pressure levels. The smoothing is done by transforming the data to spectral space, and truncating the spectrum at T36 for NCEP-R2 (see Roman et al., 2004, for NCEP-R1) and at T63 for ERA-40 (e.g. Trenberth et al., 2002), and then transforming back to grid.

4.1.3 Normal mode energetics

The summation of the normal mode energetics terms over all the normal modes is equivalent to the integration over the entire mass of the atmosphere. If a term is summed over all meridional and vertical modes, becomes a function only of the zonal wavenumber (see section 2.2.4), and, therefore, may be compared with the standard energetics in the wavenumber domain. It should be recalled that, the separation of K and A cannot be performed within the 3-D normal mode energetics. Tanaka (1994) has argued that, the separation in K and A obtained trough multiplication of E_{nlk} by coefficients (β_u, β_v, β_ϕ) representing energy ratios of U_{nlk}, V_{nlk} and Φ_{nlk}, although it is not correct, may be a good approximation to the reality. Nevertheless, this separation of K and A was not performed in this study, for correctness. However, K and A may be correctly separated in the vertical and zonal wavenumber domains, and this has been included in this study.

A comparison of the normal mode energetics with the standard energetics in the wavenumber domain is illustrated in Figure 4.23, for ERA-40 in DJF. The spectra of $K(n)$ and $A(n)$ were obtained by projecting the data only in the vertical and zonal domains, and summing over all vertical modes. The nonlinear interactions terms, B_{nlk} and C_{nlk}, were summed over all vertical and meridional modes. The conversion term, $C(n)$, was computed with both equivalent formulae (2.103) and (2.113), in the left and right panels, respectively. Despite the discrepancies in the magnitude of some spectra at each wavenumber, the results obtained with the two schemes agree reasonably well with each other. The discrepancies may be attributed to the assumptions and the specific computational procedures involved in the normal mode energetics scheme, such as the non-slip lower boundary condition for the horizontal wind (see section 3.3), the approximations discussed in section 2.2.4, and the truncations in the 3-D normal modes (see also Tanaka and Kung, 1988). As expected, these assumptions and computational procedures impact the normal mode energetics differently among the reanalysis, varying also with the season. For example, Figure 4.24 shows, overall, a better agreement between the two energetics schemes, for NCEP-R2 in MAM.

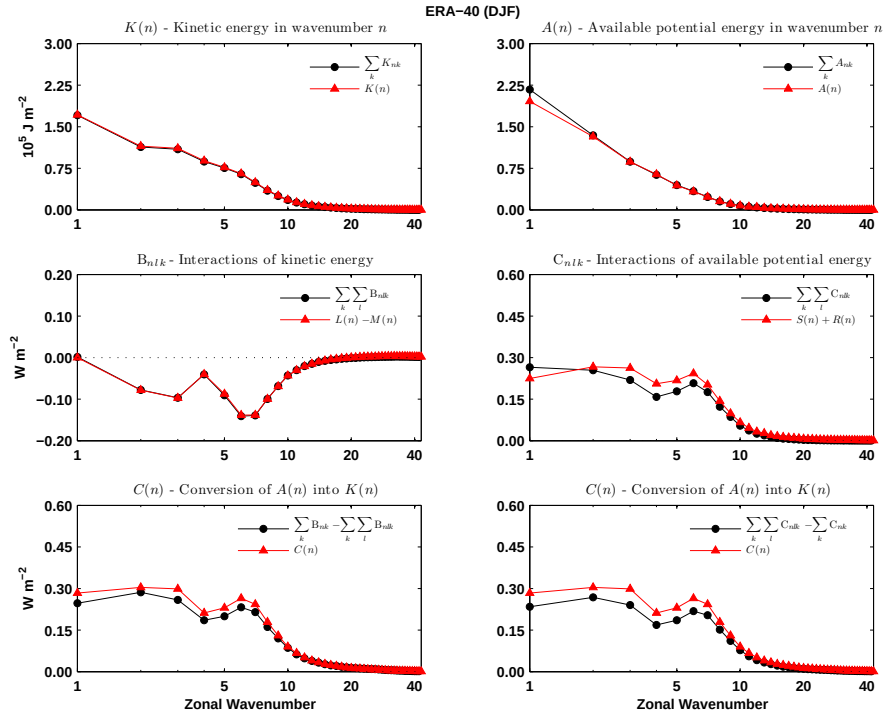

Figure 4.23: Comparison of the normal mode energetics (black circles) with the standard energetics in the wavenumber domain (red triangles), for ERA-40 in DJF.

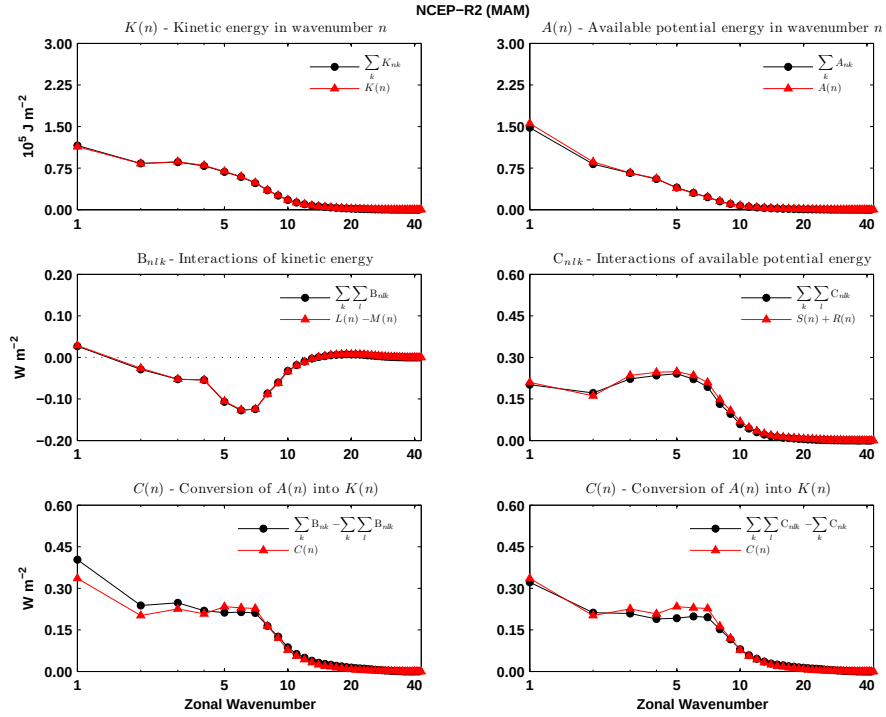

Figure 4.24: The same as in Figure 4.23, but for NCEP-R2 in MAM.

The vertical structure functions, $G_k(p)$, for the first nine vertical modes, $k = 0 - 8$, are represented in Figure 4.25. The first vertical mode $k = 0$ is called a barotropic (or external) mode because has no node in the vertical and its values are almost constant throughout the troposphere. The vertical structures of the baroclinic (or internal) modes, $k \geq 1$, show increased variations with pressure for increasing k. The functions $G_k(p)$ are rather similar among the three reanalysis, because they depend only on the vertical profile of the reference temperature, T_0, and have been obtained with the same number of Legendre polynomials approximating the solution of (2.50).

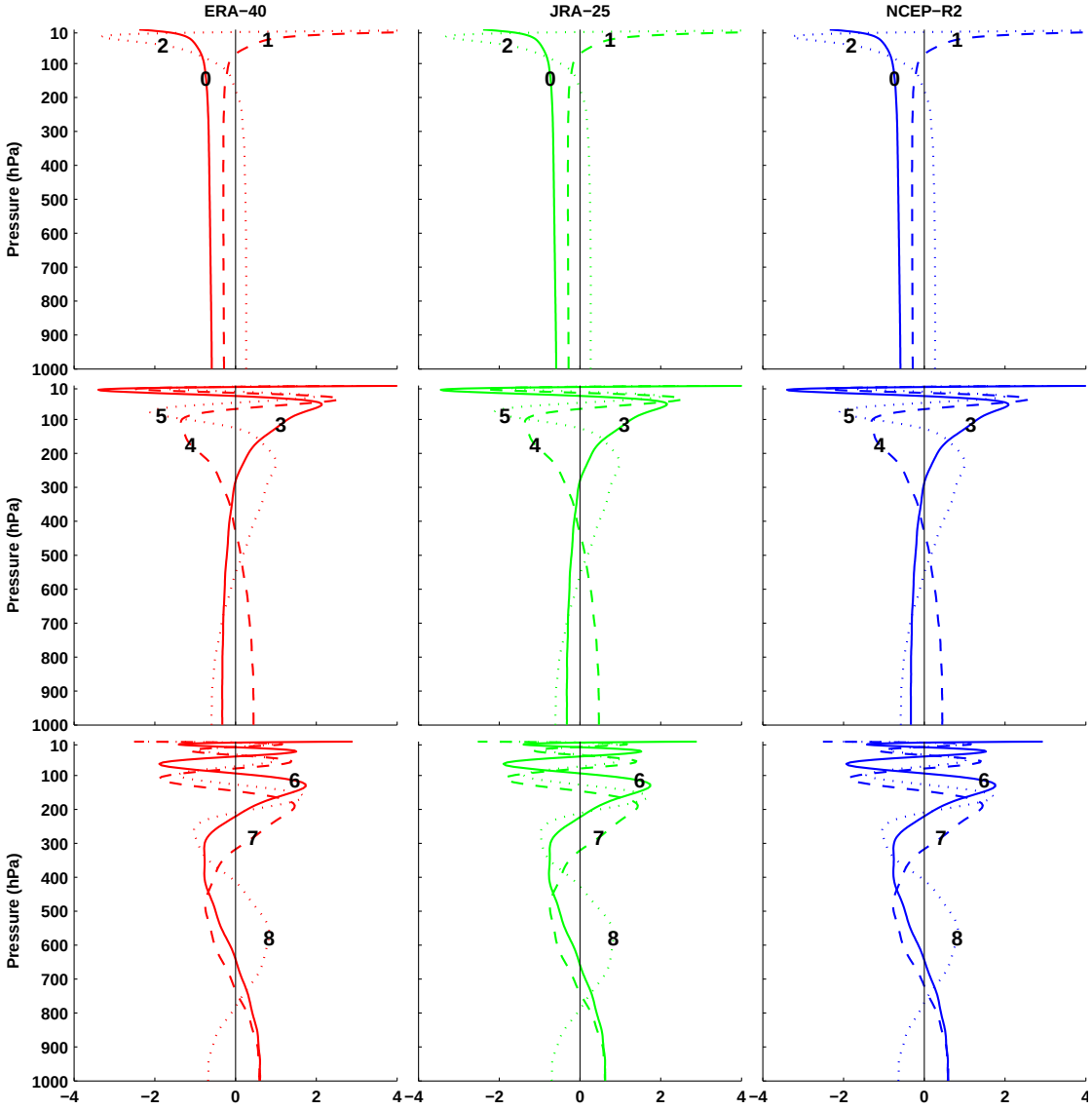

Figure 4.25: Vertical structure functions for the first nine vertical modes, $k = 0 - 8$.

Energy levels

In this section, only the spectra in DJF will be presented, for compactness. Other seasons (e.g. JJA) may also be included if justified. A log-log scale is used to display the energy spectra in the wavenumber domain in order to assess their power law behaviour. In addition, the log-log scale emphasises the differences in the tail of the spectra, complementing therefore the linear-log scale used for the spectra in section 4.1.2.

Figure 4.26 shows the wavenumber spectra of total energy, E_{nlk}, for ERA-40, JRA-25 and NCEP-R2 in DJF. The contributions from the barotropic and baroclinic vertical modes are presented separately in the left and right panels, respectively. Within each column of panels, the contributions from all meridional modes are presented in the top row, while the contributions from the gravity modes, with both the westward (dashed lines) and eastward (dotted lines) propagating gravity modes, have been separated from those of the Rossby modes in the middle and bottom rows, respectively.

Most of the energy is included in the Rossby modes for both barotropic and baroclinic modes. For the baroclinic modes, the energy spectrum of the gravity modes is an order of magnitude smaller than that of the Rossby modes at the lower zonal wavenumbers, but it becomes comparable at higher wavenumbers. For the barotropic mode, the energy of the gravity modes is about two orders of magnitude smaller than that of the Rossby modes at all wavenumbers. Within the baroclinic components, the wavenumber spectra of E_{nlk} follows the -3 power law for the Rossby modes in the range of $7 \lesssim n \lesssim 30$, which is in line with several results reported in the literature (e.g. Charney, 1971; Nastrom and Gage, 1985; Tanaka, 1985; Tanaka et al., 1986; Terasaki and Tanaka, 2007a), and has been regarded as an inertial subrange for two-dimensional isotropic turbulence in the atmosphere. The energy spectrum for the gravity modes follows approximately the $-5/3$ power law for $7 \lesssim n \lesssim 20$, which is regarded as three-dimensional isotropic turbulence in the atmosphere (Tanaka, 1985). On the other hand, E_{nlk} follows the -4 power law for the Rossby modes of the barotropic component, which agrees with Terasaki and Tanaka (2007b), and can be explained with the Rossby wave saturation

theory according to Tanaka et al. (2004). Nevertheless, a complete understanding of the atmospheric energy spectrum remains elusive (e.g. Tung and Orlando, 2003). The higher levels of the eastward gravity modes for the long waves of the baroclinic modes are attributable to the first eastward gravity meridional mode (Tanaka and Kung, 1988), referred to as a Kelvin wave, which is clearly evident below in Figure 4.27. The three reanalysis show identical energy spectra in the zonal wavenumber domain, appart from a few exceptions, which are worth to mention. On the one hand, there is a rapid decrease in the spectra of NCEP-R2 at $n \gtrsim 36$, previously discussed at the end of section 4.1.2, which is clearly evident now by using a log-log scale. In addition, it may be seen that the energy spectra for NCEP-R2 starts to decrease more rapidly than those for ERA-40 and JRA-25 at wavenumbers $n \gtrsim 25$ (Figure 4.26). On the other hand, the spectra of NCEP-R2 for the gravity modes decays more slowly for wavenumbers $n \lesssim 25$, and for this reason it follows more closely the $-5/3$ power law in the range $7 \lesssim n \lesssim 20$ than the same spectra of ERA-40 and JRA-25.

The energy distributions for the Kelvin mode ($l_e = 0$) and for the first Rossby mode ($l_r = 0$), which is referred to as a mixed Rossby-gravity wave, because it behaves like a Rossby mode for small values of ε (see Appendix A), but behaves more like a gravity mode for large values of ε (Swarztrauber and Kasahara, 1985), are shown in Figure 4.27. The spectra are presented separately for the zonal wavenumber domain (left panel) and for the vertical domain (right panel). Most of the energy is included in the planetary waves for the Kelvin mode, whereas for the mixed Rossby-gravity mode the spectrum peaks at the cyclone-scale waves ($n = 5 - 7$). These features are similar among the three reanalysis data, but both the Kelvin and Rossby-gravity modes of NCEP-R2 have higher levels of energy than those of ERA-40 and JRA-25 for wavenumbers $n \gtrsim 10$. In the vertical domain, most of the energy is included in the barotropic mode ($k = 0$) for the mixed Rossby-gravity mode. The Kelvin mode has a maximum at the baroclinic mode $k = 4$, and little energy in the barotropic mode. The minimum at the first baroclinic mode ($k = 1$) in the Kelvin mode of ERA-40 and JRA-25, is not present in NCEP-R2 which agrees with Tanaka (1985) using the FGGE data of GFDL. The Kelvin

mode value at $k = 1$ for ERA-40 and JRA-25 is almost an order of magnitude smaller than the same value in NCEP-R2, and therefore accounts for some of the difference in the wavenumber spectra between NCEP-R2 and the other two reanalysis.

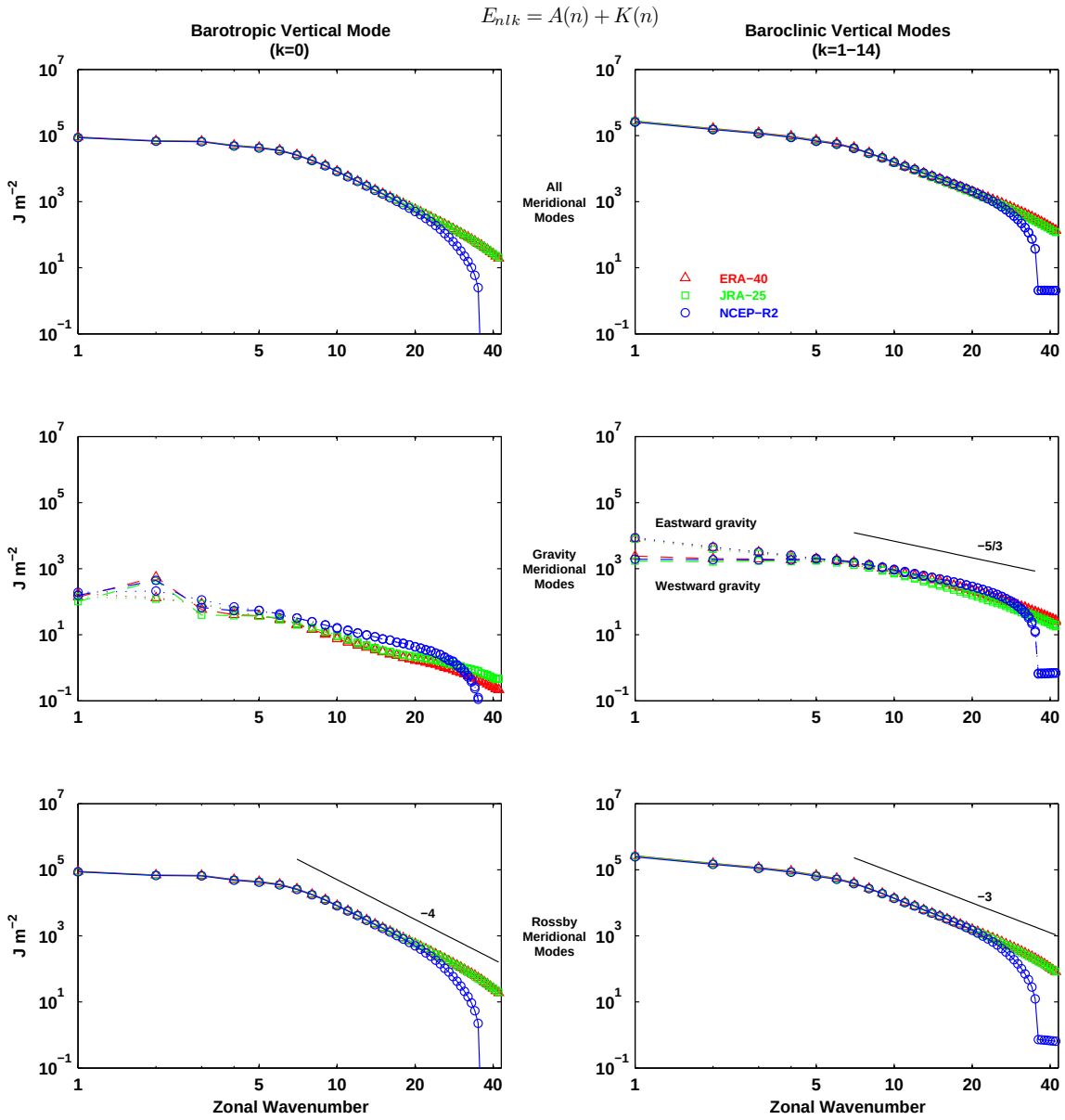

Figure 4.26: Total energy spectra in the wavenumber domain for ERA-40, JRA-25 and NCEP-R2 in DJF. The barotropic (left panels) and baroclinic (right panels) modes are presented separately. For each column of panels, the spectra is presented for all meridional modes (top row), only for the gravity modes (middle row), with the westward gravity (dashed lines) distinguished from the eastward gravity (dotted lines), and only for the Rossby modes (bottom row). Units are J m^{-2}.

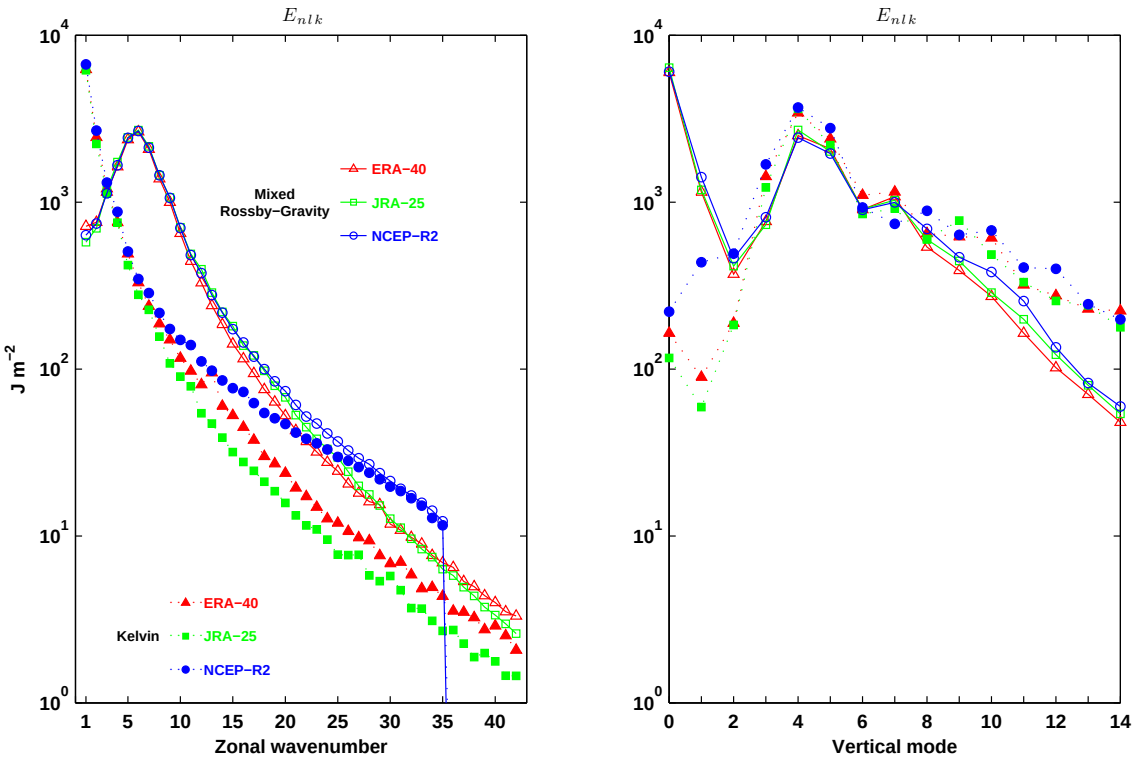

Figure 4.27: Energy distributions for Kelvin (dotted line) and mixed Rossby-Gravity (continuous line) modes in the zonal wavenumber domain (left) and vertical mode domain (right), for ERA-40, JRA-25 and NCEP-R2 in DJF (1979-2001). Units are J m^{-2}.

The wavenumber spectra of available potential energy, $A(n)$, and kinetic energy, $K(n)$, are depicted in the left and right panels of Figure 4.28, respectively, for ERA-40, JRA-25 and NCEP-R2 in DJF. The contributions from all vertical modes are presented in the top rows, while the separated contributions from the barotropic and baroclinic modes are presented in the middle and bottom rows, respectively. Again, the three reanalysis show identical spectra for $A(n)$ and $K(n)$ in the zonal wavenumber domain, except at wavenumbers $n \gtrsim 25$ for NCEP-R2 as discussed above. Most of $A(n)$ resides in the baroclinic modes, whereas for $K(n)$ there are comparable amounts of energy among the barotropic and baroclinic modes. Both energy spectra follows the -3 power law for the baroclinic modes, in agreement with the spectra of Figure 4.26. For the barotropic mode, the spectra of $K(n)$ follows the -4 power law, agreeing also with Figure 4.26, but the slope for the spectra of $A(n)$ is steeper following approximately a -5 power law. This -5 power law behaviour of the spectra of $A(n)$ has been observed in

the work of Steinberg (1971). Additionally, Merilees and Warn (1972) argues that any numerical model which has a much finer resolution in the horizontal than the vertical, would ultimately have a section of the spectrum where $A(n)$ would follow the -5 power law.

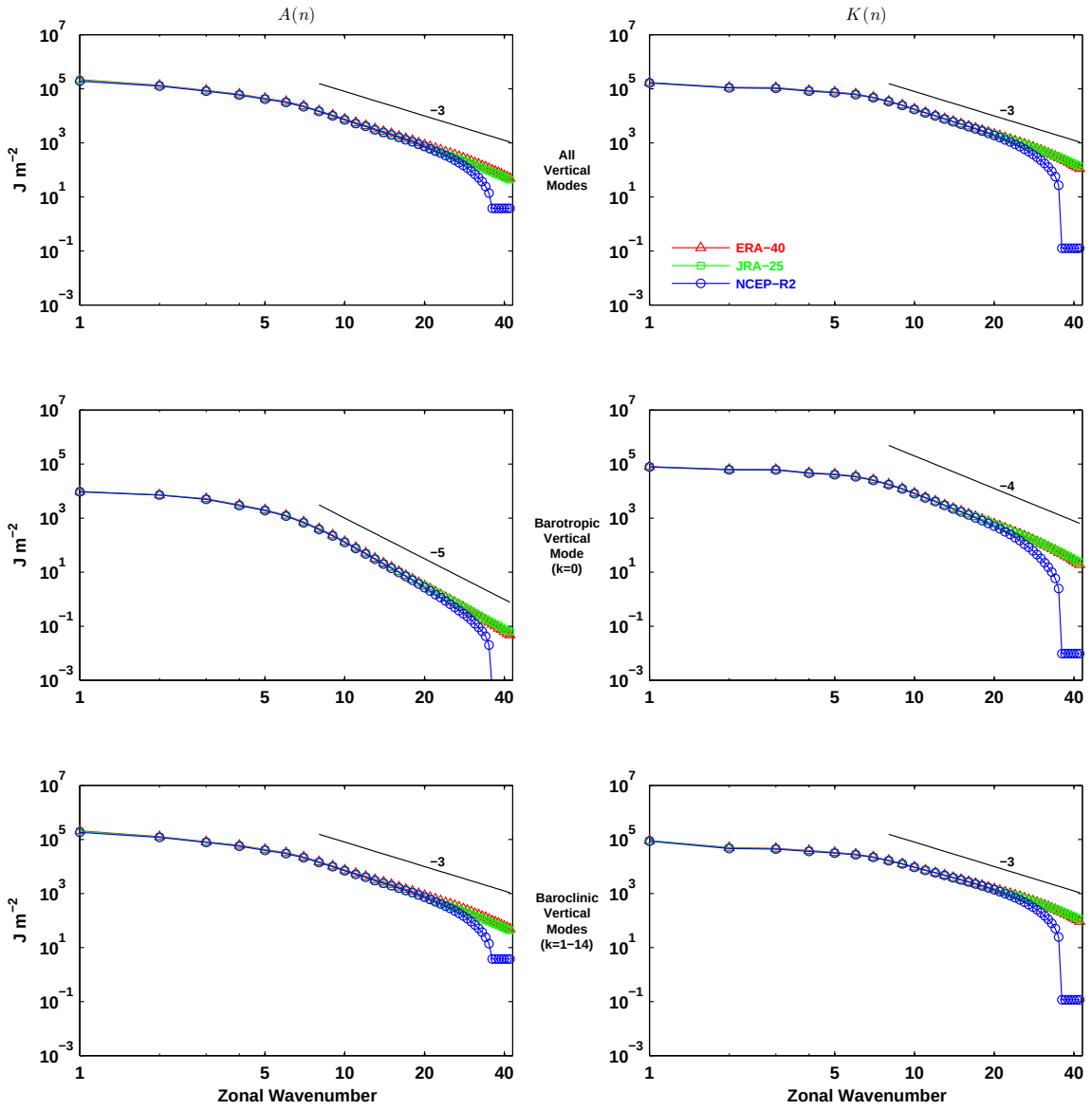

Figure 4.28: Zonal wavenumber spectra of available potential energy (left panels), $A(n)$, and kinetic energy (right panels), $K(n)$, for ERA-40, JRA-25 and NCEP-R2 in DJF. Within each energy form, the spectra is presented for all vertical modes (top row), for the barotropic mode (middle row), and for the baroclinic modes (bottom row). Units are J m^{-2}.

The total energy spectra in the vertical mode domain are illustrated in Figure 4.29. The contributions from the zonal mean component ($n = 0$) are presented separately from that of the eddy component ($n = 1 - 42$) in the left and right panels, respectively. Within each component, the contributions from all meridional modes are in the top row, those from the gravity modes, with both the westward gravity (dashed lines) and eastward gravity (dotted lines), in the middle row, and those from the Rossby modes in the bottom row. The energy distribution of the zonal mean component shows a maximum at $k = 5$ for both the Rossby and gravity modes (both eastward and westward propagating), with the energy levels in the Rossby modes about five to ten times larger than that of the eastward gravity modes, which in turn is about two orders of magnitude higher than that of the westward gravity modes at most vertical modes. Another energy peak is seen at the barotropic mode ($k = 0$). Almost all eddy energy is included in the Rossby modes, peaking at the barotropic mode, with another energy peak at the baroclinic mode $k = 5$. The gravity modes show an energy peak at $k = 4 - 5$, which is about an order of magnitude smaller than that of the Rossby mode. These spectra are similar among the three reanalysis, appart for a few differences in magnitude at the higher vertical modes (specially for the zonal mean), and for the first two baroclinic modes ($k = 1$ and 2) of the gravity modes in the eddy component, where NCEP-R2 $>$ ERA-40 $\gtrsim$ JRA-25.

The total energy spectra in the vertical mode domain may be presented separately for the available potential energy, A, and kinetic energy, K, but the additional separation of these two forms of energy into Rossby and gravity modes is not correct, as stated earlier in this section. Therefore, Figure 4.30 shows the spectra of A and K in the vertical mode domain for the zonal mean and eddy components, i.e. $A_Z(k)$, $A_E(k)$, $K_Z(k)$ and $K_E(k)$. The distribution of available potential energy shows a maximum at $k = 5$ for both the zonal mean and eddy components, with the $A_E(k)$ maximum an order of magnitude smaller than that of $A_Z(k)$. In $A_Z(k)$, there is another peak of energy at $k = 0$, while for $A_E(k)$ the energy level is small at the barotropic mode. A large amount of kinetic energy is included at the barotropic mode for both the zonal

mean and eddy components, with comparable magnitudes. In both $K_Z(k)$ and $K_E(k)$, there is another energy peak at $k = 4 - 5$, which may be caused by the tropospheric jet near 250 hPa (e.g. Tanaka, 1985), where $G_5(p)$ has a maximum (Figure 4.25).

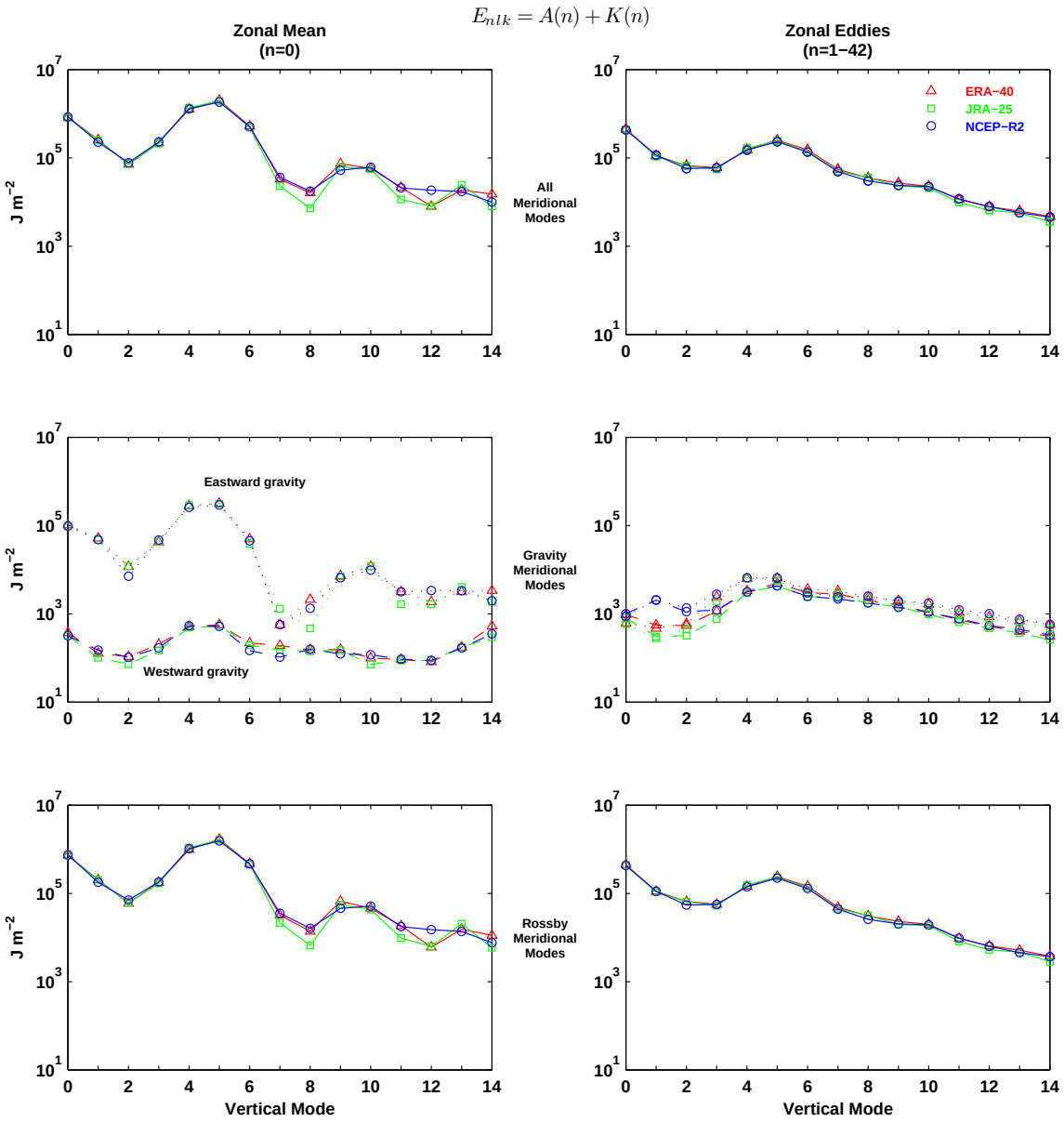

Figure 4.29: Total energy spectra in the vertical mode domain for ERA-40, JRA-25 and NCEP-R2 in DJF. The spectra are presented separately for the zonal mean (left panels) and eddy (right panels) components, and for all meridional modes (top row), only for the gravity modes (middle row), with the westward gravity (dashed lines) distinguished from the eastward gravity (dotted lines), and only for the Rossby modes (bottom row). Units are J m^{-2}.

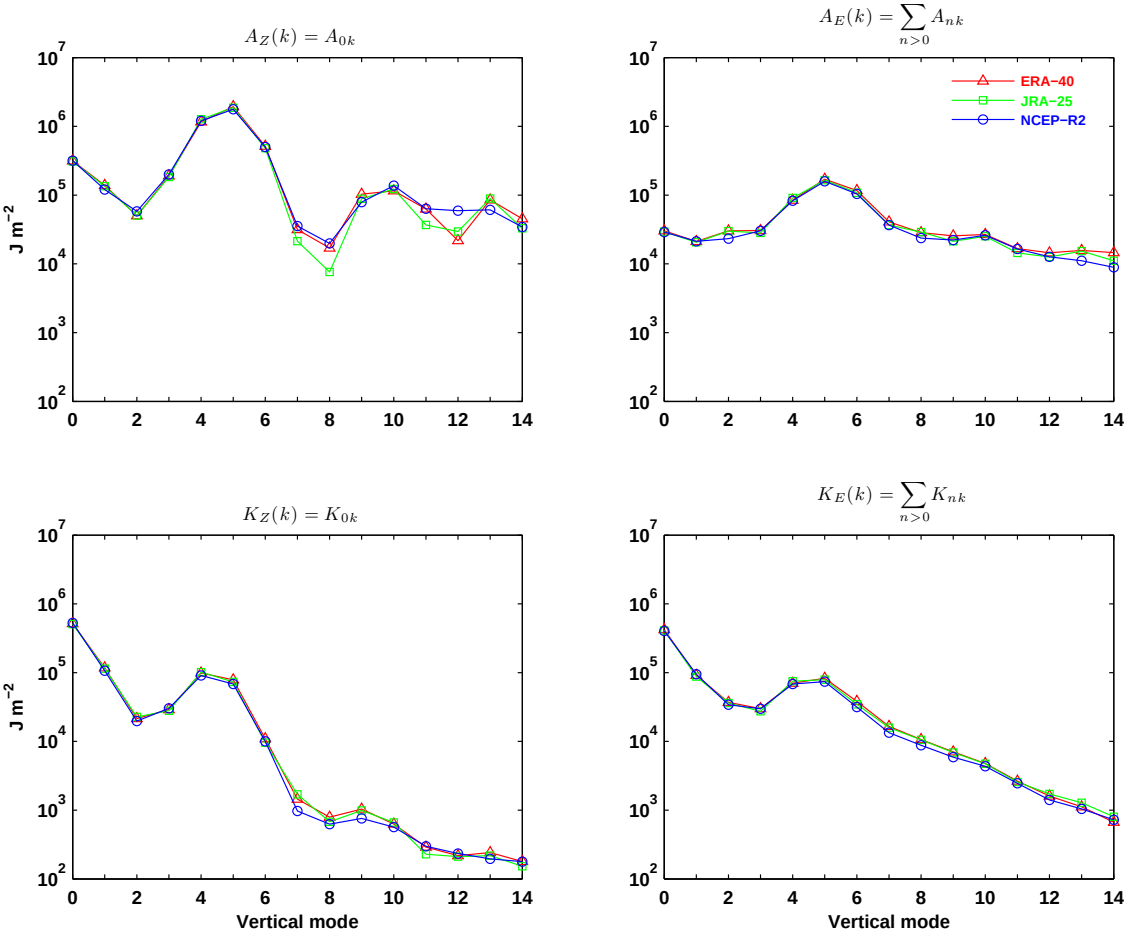

Figure 4.30: Spectra of available potential energy (top row) and kinetic energy (bottom row) in the vertical mode domain, for the zonal mean (left panels) and eddy (right panels) components of ERA-40, JRA-25 and NCEP-R2 in DJF. Units are J m^{-2}.

By separating the available potential energy from the kinetic energy in the vertical mode domain, it is concluded that the energy peak at $k = 0$ in zonal mean E_{nlk} has comparable contributions from $A_Z(k)$ and $K_Z(k)$, with that of $K_Z(k)$ somewhat larger, while the same peak at $k = 0$ in eddy E_{nlk} is due to $K_E(k)$. On the other hand, the energy peak at $k = 5$ in zonal mean E_{nlk} is due to $A_Z(k)$, while the same peak at $k = 5$ in eddy E_{nlk} has comparable contributions from $A_E(k)$ and $K_E(k)$, although the contribution of $A_E(k)$ is somewhat larger.

The total eddy energy spectra in the meridional mode domain are shown in Figure 4.31, for the barotropic (left) and baroclinic components (right). The spectra are also decomposed into Rossby, eastward gravity and westward gravity modes. Within the barotropic mode, the energy distribution for the Rossby modes peaks at $l = 3 - 4$. According to Tanaka (1985, 1994), the wave energy started to propagate vertically when the energy peak reached $l = 3 - 4$, which is a critical meridional scale for the vertical propagation. The range $l \lesssim 4$ is therefore regarded as pertaining to the propagative mode, whereas the range of larger meridional mode is the trapped mode. The spectra for the baroclinic modes show energy peaks at $l = 4 - 6$, associated with the characteristic meridional scale of the cyclone-scale waves (Tanaka, 1994). The energy spectra for both the westward and eastward gravity modes peaks at the first meridional mode ($l = 0$), decreasing for the higher meridional modes, first slowly in the range $2 \leqslant l \lesssim 5$ and then more rapidly for $l \gtrsim 6$, within both barotropic and baroclinic modes. The energy levels for the eastward gravity modes are larger than those for the westward gravity modes, at the meridional modes $l \geqslant 1$ of the barotropic mode, and at $0 \leqslant l \leqslant 5$ of the baroclinic modes. The spectra for the Rossby modes are rather similar among the three reanalysis, with the exception for the higher meridional modes ($l \geqslant 20$) where the energy spectra decreases somewhat more rapidly in NCEP-R2. The shape of the spectra for both the westward and eastward gravity modes is also similar among the reanalysis, but show typically higher levels of energy in NCEP-R2, specially in the barotropic mode, which is consistent with Figure 4.26. As have been pointed by Tanaka and Kung (1988), the energy level of the gravity modes is very sensitive to the atmospheric ageostrophic components, and therefore may be influenced by the assimilation process applied to the dataset.

The features in the energy spectra for DJF, presented and discussed above in this section, remain essentially the same for the other seasons. For this reason and for compactness, the various energy spectra within the normal mode energetics scheme were not shown for the other seasons.

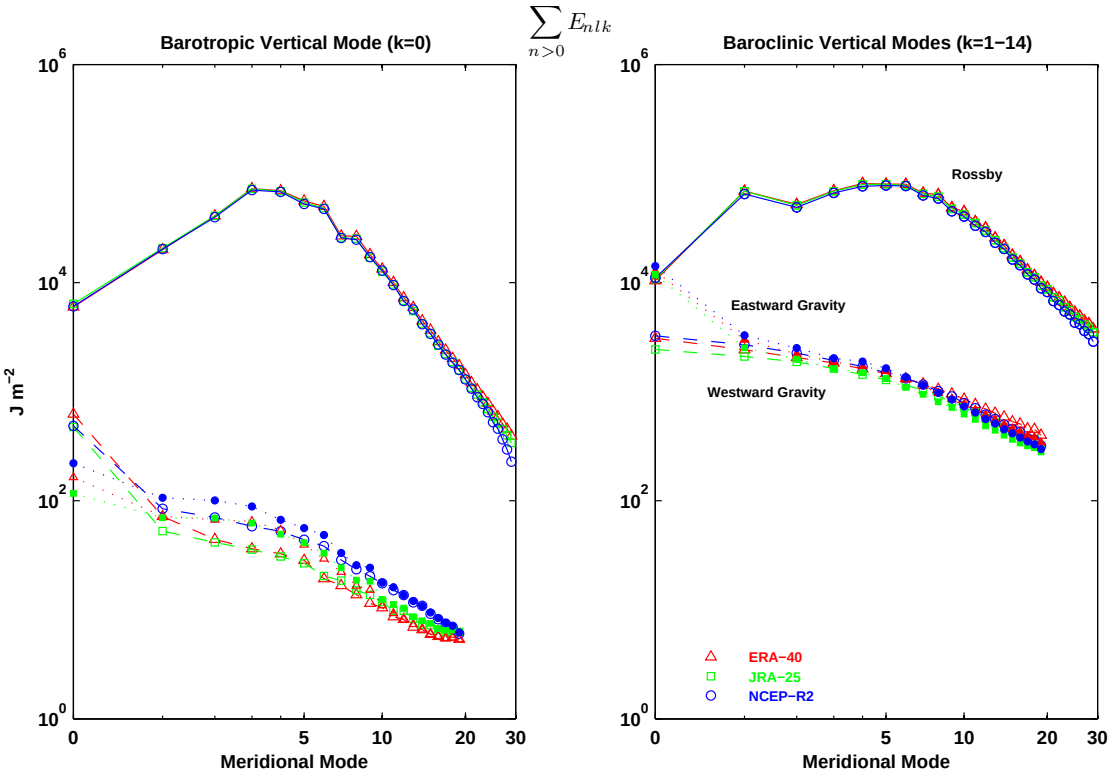

Figure 4.31: Energy distributions in the meridional mode domain for the barotropic mode (left) and baroclinic modes (right). The spectra for the westward (dashed lines) and eastward (dotted lines) propagating gravity modes, and for the Rossby modes (continuous lines) are presented in each panel, for ERA-40, JRA-25 and NCEP-R2 in DJF. Units are J m^{-2}

Energy interactions

The spectra for the interactions of available potential energy, C_{nlk}, in the wavenumber domain are illustrated in Figure 4.32 for ERA-40, JRA-25 and NCEP-R2 in DJF. The separation into barotropic ($k = 0$) and baroclinic modes ($k = 1 - 14$) is shown in the left and right panels, respectively, while the separation into all meridional modes, only gravity modes, and only Rossby modes is shown in the top, middle and bottom rows, respectively. The positive values of C_{nlk} means that the zonal mean available potential energy is transferred into the eddy available potential energy. Most of this interaction takes place within the baroclinic modes, and almost all interaction is included in the Rossby modes. There is also a significant interaction in the barotropic Rossby modes of JRA-25 and NCEP-R2, whereas in the same modes of ERA-40 the interaction has

the same sign but is considerably smaller. These spectra remain essentially the same in the other seasons, appart for a small reduction in the interaction for the barotropic Rossby modes and the changes in the shape of the spectra for the baroclinic component of C_{nlk}, which are coherent with the changes in the shape of spectra $R(n)$ and $S(n)$ troughout the seasons (see Figures 4.17 and 4.21).

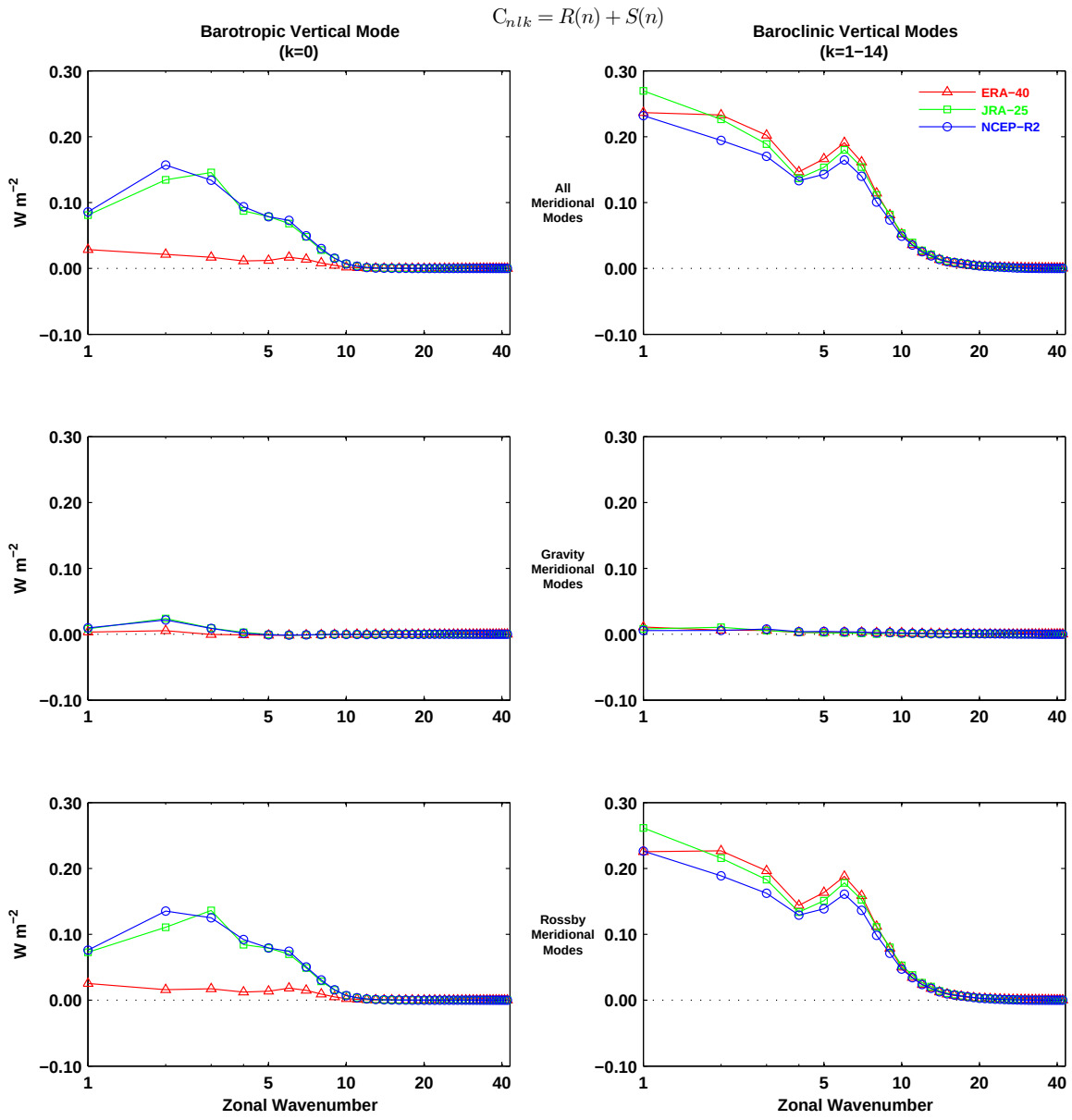

Figure 4.32: As in Figure 4.26, but for interactions of available potential energy. Units are W m^{-2}.

The above results are in relative contradiction with those of Tanaka (1985), for the Rossby modes, in which most of the interaction is included in the barotropic mode, instead of the baroclinic modes. The discrepancy is explained by the treatment of the lower surface wind. By assuming the vanishing wind at the lower surface, as done here and in Tanaka and Kung (1988) and Terasaki and Tanaka (2007a), the barotropic component of C_{nlk} is greatly reduced. It seems therefore that, the barotropic component of C_{nlk} is very sensitive to the treatment of the lower boundary. The treatment of vanishing surface wind seems a reasonable and physically correct assumption for the normal mode energetics (e.g. Tanaka and Kung, 1988; Tanaka, 1994). Part of the discrepancies in the barotropic interaction between ERA-40 and the other two reanalysis, may be related to the treatment of data at the lower levels, namely in those regions of the pressure levels pierced by topography. It has become apparent by now that the treatment (interpolations/extrapolations) of this pressure levels data is different among the reanalysis, as inferred from the results in Figures 4.8 or 4.10, for example.

On the other hand, the interactions of kinetic energy in the wavenumber domain, B_{nlk}, depicted in Figure 4.33, show negative values for the baroclinic modes, considering the contributions of all meridional modes, which means that the eddy kinetic energy is transformed into the zonal mean kinetic energy. However, this is only valid for the Rossby modes, since the separation into gravity and Rossby modes shows an opposite flow of baroclinic kinetic energy for the gravity modes. The same opposite flow of kinetic energy is found for the Rossby modes of the barotropic component, indicating an energy flow from the zonal mean kinetic energy to the eddy kinetic energy. As have been pointed by Tanaka (1994), this would suggest for an investigation of barotropic instability, but both zonal and eddy kinetic energy of the barotropic mode seems to be supplied by the eddy kinetic energy of the baroclinic modes, as shown below (Figure 4.35). Again, the analysis remains basically unaltered for the other seasons, appart for the changes in the shape of B_{nlk} spectra, in agreement with the changes in the spectra of $M(n)$ and $L(n)$ troughout the seasons (see Figures 4.20 and 4.22). The absolute values of B_{nlk} are generally smaller in NCEP-R2, which is also coherent to its

smaller values for the spectra $M(n)$ in Figure 4.20.

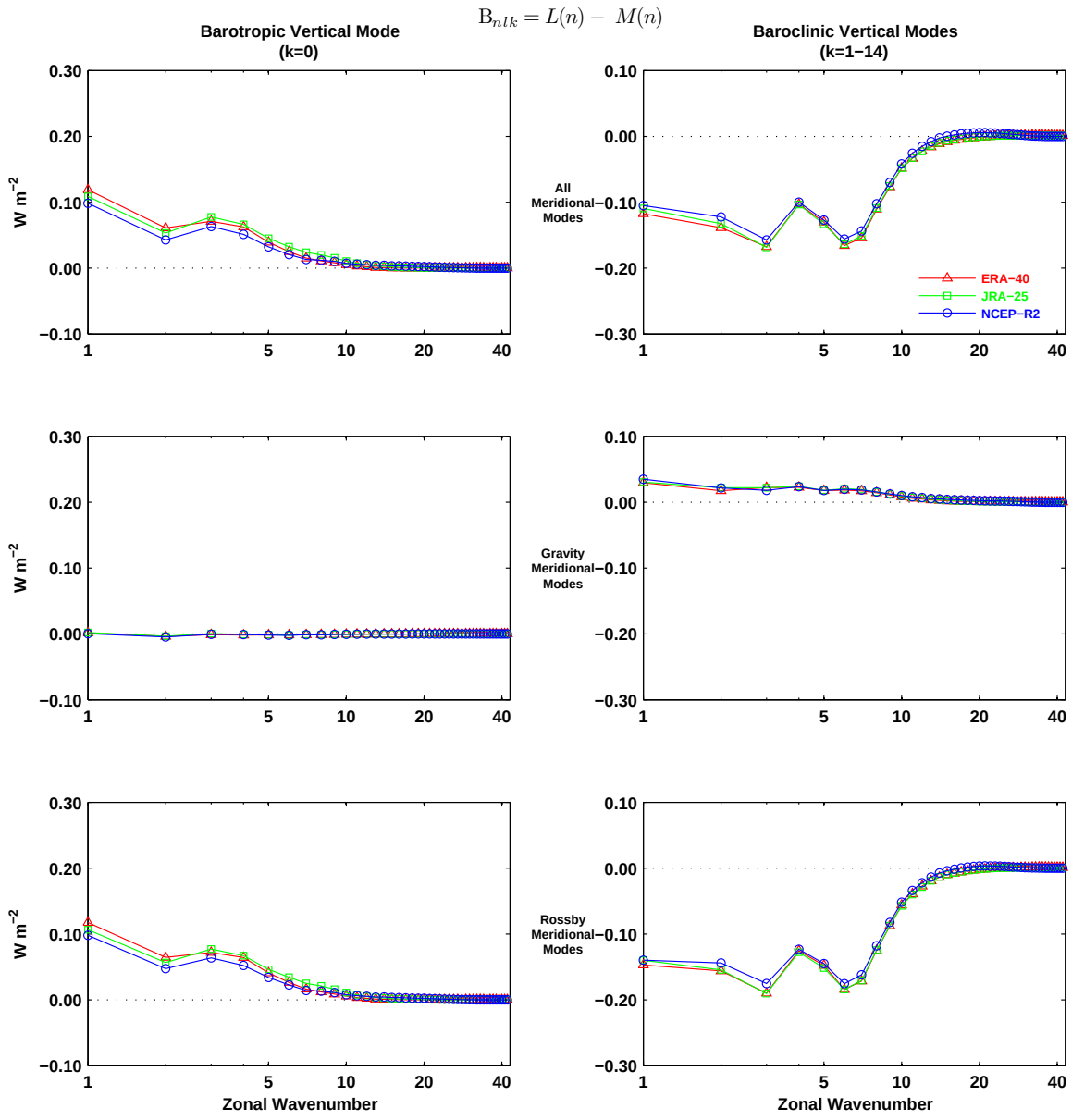

Figure 4.33: As in Figure 4.26, but for interactions of kinetic energy. Units are W m^{-2}.

Figure 4.34 shows the interactions of available potential energy in the vertical mode domain for the three reanalysis in DJF. The zonal mean and eddy components are separated in the left and right panels, respectively, and the meridional modes have been separated as in Figure 4.32. The top row of Figure 4.34 shows negative values of

C_{nlk} at both the barotropic ($k = 0$) and baroclinic modes (peaking at $k = 5$) of the zonal mean component, whereas for the eddy component both the barotropic and baroclinic modes (peaking at $k = 4$) have positive values. This means that A_Z is transformed into A_E at both the barotropic and baroclinic modes, but not necessarily in a barotropic-to-barotropic and baroclinic-to-baroclinic correspondence. It is also possible, for example, that the A_Z contained in the barotropic mode is transformed into A_E of both the barotropic and baroclinic modes. The transformation of A_Z into A_E, as mentioned above, is valid only for the Rossby modes, since, on the one hand, the interaction C_{nlk} is neglegible for the gravity modes of the eddy component, and, on the other hand, it is positive for the gravity baroclinic modes ($k = 3-5$) of the zonal mean component. The value of C_{nlk} in ERA-40 is substantially smaller than that in JRA-25 and NCEP-R2 for the barotropic Rossby modes of the eddy component, which is coherent to Figure 4.32, and also for the barotropic gravity modes of the zonal mean component, where it has even an opposite sign. The same is found in NCEP-R2 for the barotropic Rossby modes of the zonal mean component. Since the energy level is very small for the eddy available potential energy of the barotropic mode (see Figure 4.30), the energy must be either converted immediately to eddy kinetic energy or dissipated radiatively. However, as it will be shown later on, the A_E is in fact dissipated radiatively at the barotropic mode (Figure 4.39), whereas its conversion into K_E occurs in the baroclinic modes, mostly in $k = 3 - 6$ (Figure 4.38). This explains the low levels of A_E in the barotropic mode, and seems that it hasn't been described in the literature so far.

Figure 4.35 illustrates the interactions of kinetic energy, B_{nlk}, in the vertical mode domain for the three reanalysis in DJF. The interactions are dominated by the Rossby modes, where the negative values at the baroclinic modes ($k = 3 - 7$) of the eddy component, are balanced by positive values at the barotropic mode of both the zonal mean and eddy components, and also at the baroclinic modes ($k = 4 - 5$) of the zonal mean component. This means that the K_E contained in the baroclinic component of the Rossby modes is transferred into the barotropic component of both K_Z and K_E, which agrees with previous studies (e.g. Tanaka, 1985; Tanaka and Kung, 1988; Terasaki and

Tanaka, 2007a). A small amount of baroclinic eddy kinetic energy is also transformed into baroclinic zonal mean kinetic energy. The interactions of kinetic energy for the gravity modes are relatively small and the flow of energy is in the opposite direction compared to that for the Rossby modes. This is seen by positive B_{nlk} in the baroclinic modes ($k = 4 - 6$) of the eddy component and by negative B_{nlk} in the barotropic and baroclinic modes ($k = 3 - 5$) of the zonal mean component.

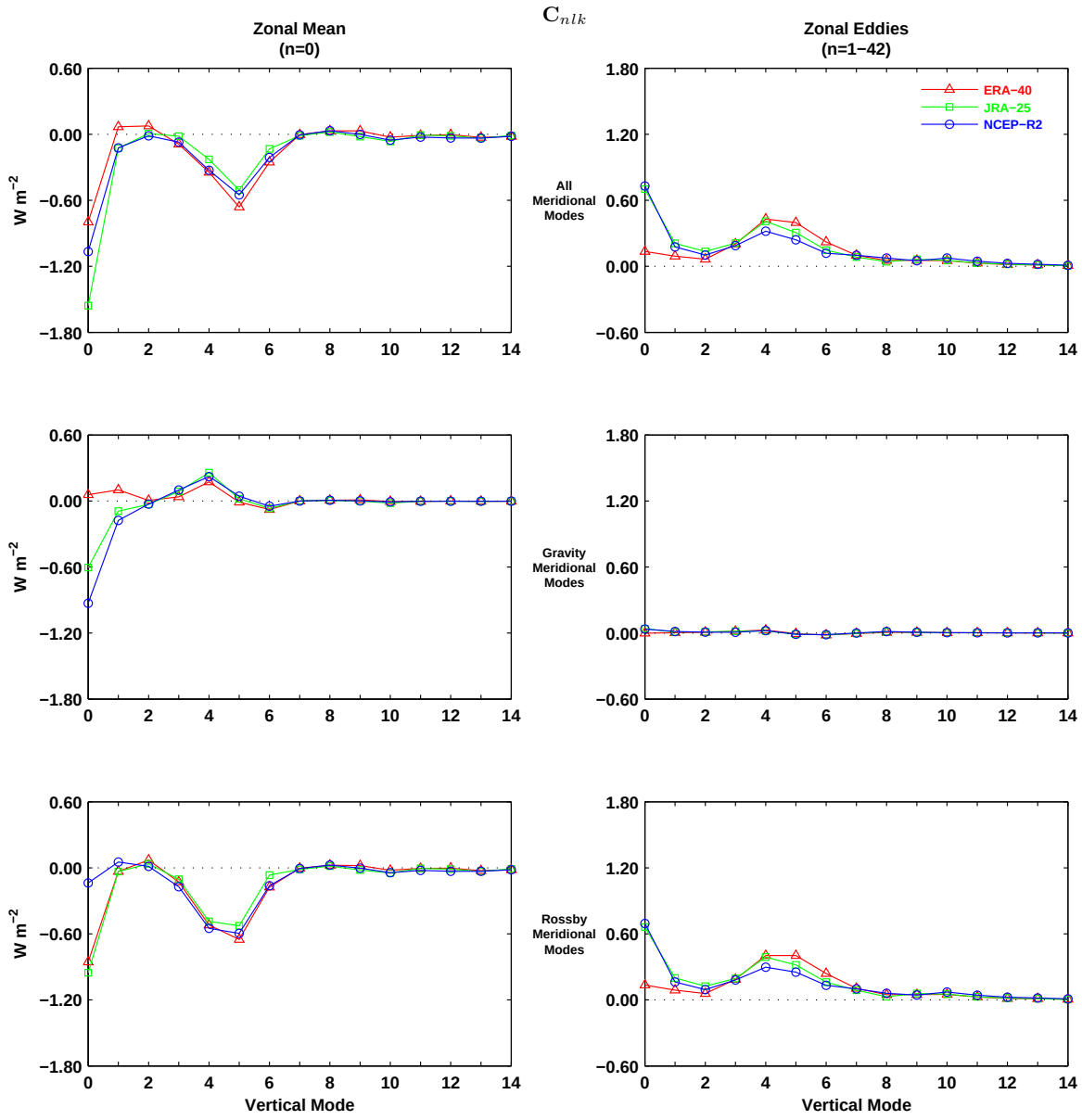

Figure 4.34: As in Figure 4.29, but for interactions of available potential energy. Units are W m^{-2}.

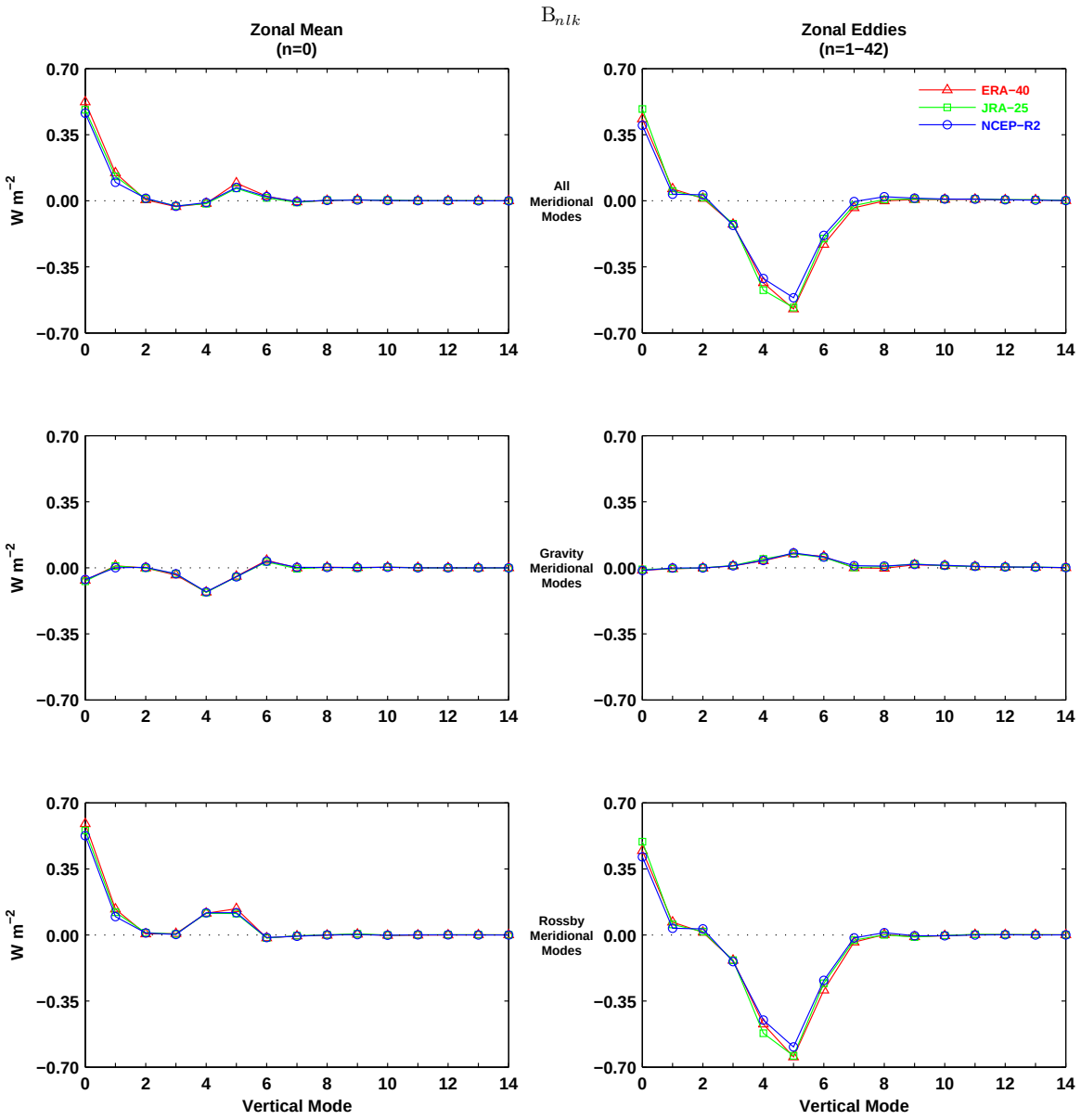

Figure 4.35: As in Figure 4.29, but for interactions of kinetic energy. Units are W m^{-2}.

Interactions of A_E and K_E in the meridional mode domain are depicted in Figure 4.36. It is seen that the A_E supplied into the barotropic mode is mostly accomplished by the Rossby modes in the range of $l = 2 - 8$, with the values for ERA-40 substantially lower than those for the other two reanalysis. The A_E is supplied similarly to the baroclinic modes, except that the contributions from the higher Rossby modes are still appreciable, and the agreement among the three reanalysis is much better. The K_E is transferred

from almost all baroclinic Rossby modes, excluding the mixed Rossby-gravity mode, into the barotropic Rossby modes mostly in the range of $l = 2-10$. On the other hand, K_E is supplied at the baroclinic gravity modes, with the maximum at $l = 0$, which is due to the first eastward gravity mode (the Kelvin mode), and secondary maxima in the range of about $l = 3-10$, which are due to westward gravity modes.

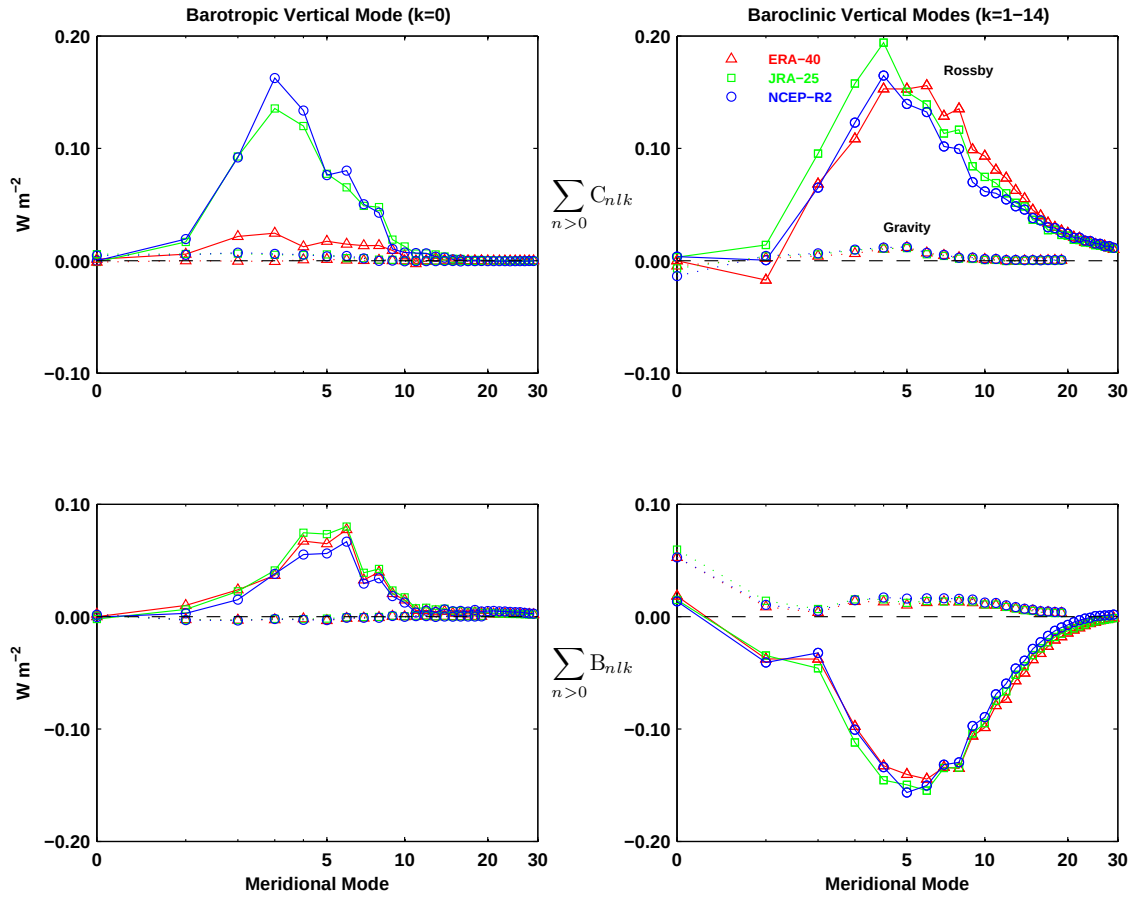

Figure 4.36: Interactions of eddy available potential energy (top row) and eddy kinetic energy (bottom row) in the meridional mode domain for ERA-40, JRA-25 and NCEP-R2 in DJF. The barotropic and baroclinic modes are presented separately in the left and right panels, respectively. Units are W m^{-2}.

Energy conversion

As mentioned previously, the conversion rate between available potential energy and kinetic energy cannot be explicitly shown in the 3-D normal mode framework. Nev-

ertheless, using the appropriate formulae derived in section 2.2.4, the spectra for this energy conversion rate can be computed explicitly in both the zonal wavenumber and vertical mode domains. These spectra, which are to be presented below, haven't been described in the literature so far, and therefore it may constitute a new result on this subject.

Figure 4.37 shows the spectra for the conversion of eddy available potential energy into eddy kinetic energy in the zonal wavenumber domain, $C(n)$, for the three reanalysis in DJF. Two theoretically equivalent formulae were used for the computation of $C(n)$, which have yielded nearly identical spectra, as seen in the left and right panels. The contributions from the barotropic mode are neglegible, which confirms the baroclinic nature of conversion $C(n)$. It may be seen that the spectra have maxima at the planetary-scale wavenumbers $n = 1 - 3$, and at the sinoptic-scale wavenumber $n = 6$, which agree with the spectra of Figures 4.18 and 4.19 in DJF.

The spectra for the conversion of available potential energy into kinetic energy in the vertical mode domain, are illustrated in Figure 4.38 for the three reanalysis in DJF. Two equivalent formulae were also used for each zonal mean and eddy components (see figure caption). The conversion between the zonal mean components of available potential and kinetic energies is relatively small for all reanalysis, as seen in the left panels. It seems that zonal mean available potential energy is converted into zonal mean kinetic energy in the barotropic mode $k = 0$, and in the baroclinic modes $k = 3$ and 4, whereas in the baroclinic modes $k = 1$ and 5 the conversion is in the opposite direction. However, since these values are relatively small, their reliability may be doubtful. Nevertheless, there is consistency among the three reanalysis, and when the contributions from all vertical modes are summed, a small positive conversion is obtained, which agrees with the small positive values for C_Z in Figure 4.1. The spectra for the conversion between the eddy components of available potential and kinetic energies are shown in the right panels of Figure 4.38. Despite the nonzero values at $k = 0$ (specially for JRA-25 and NCEP-R2), it is seen that this conversion is essentially accomplished at the baroclinic modes, mainly at $k = 3 - 6$ with maximum at $k = 5$.

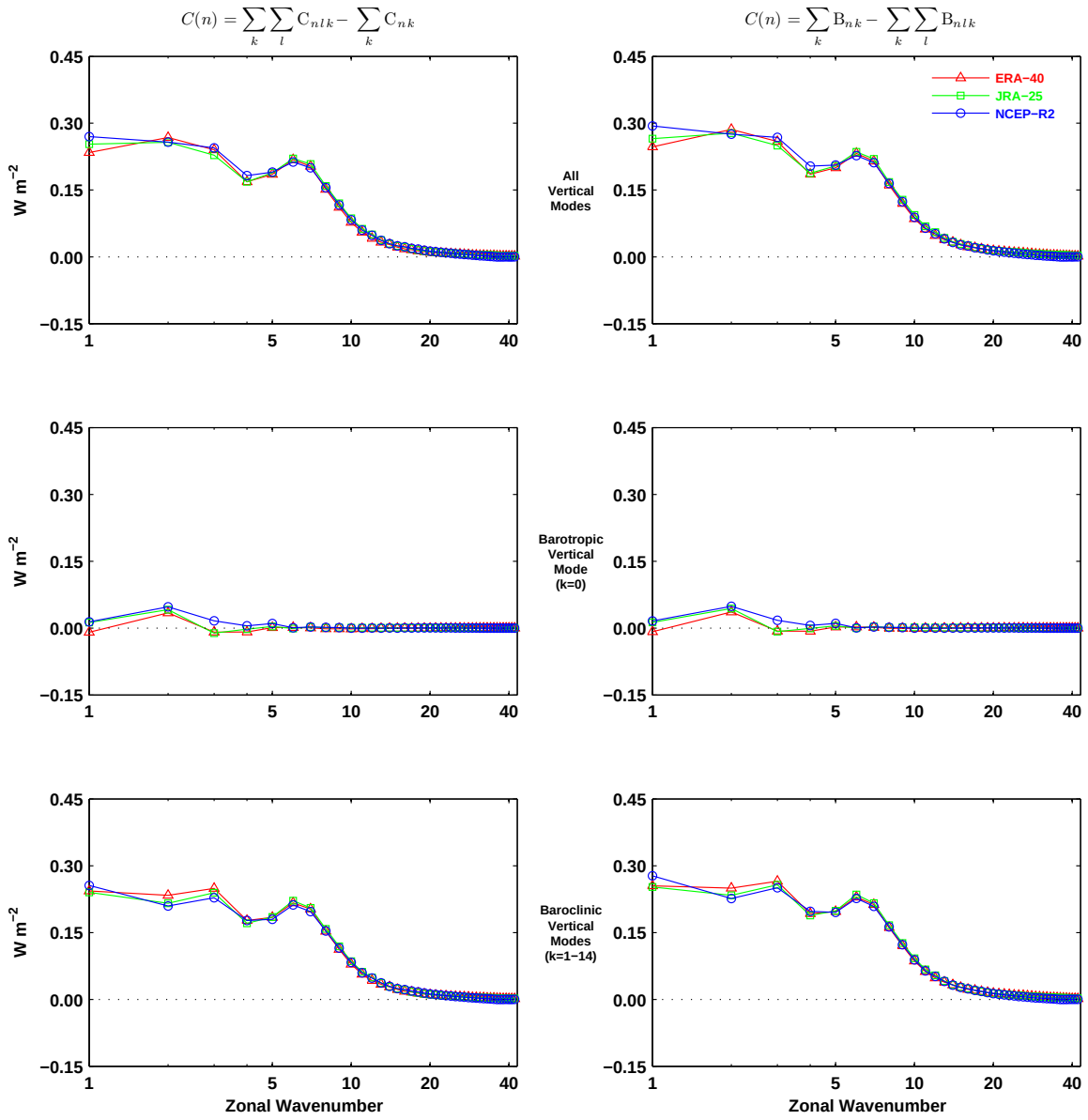

Figure 4.37: Conversion of eddy available potential energy into eddy kinetic energy in the wavenumber domain, $C(n)$, for ERA-40, JRA-25 and NCEP-R2 in DJF. The two equivalent formulae (2.113) and (2.103) were used in the computations, corresponding to the left and right panels, respectively. The barotropic and baroclinic modes are presented separately in the middle and bottom rows, respectively, and their sum in the top row. Units are W m^{-2}.

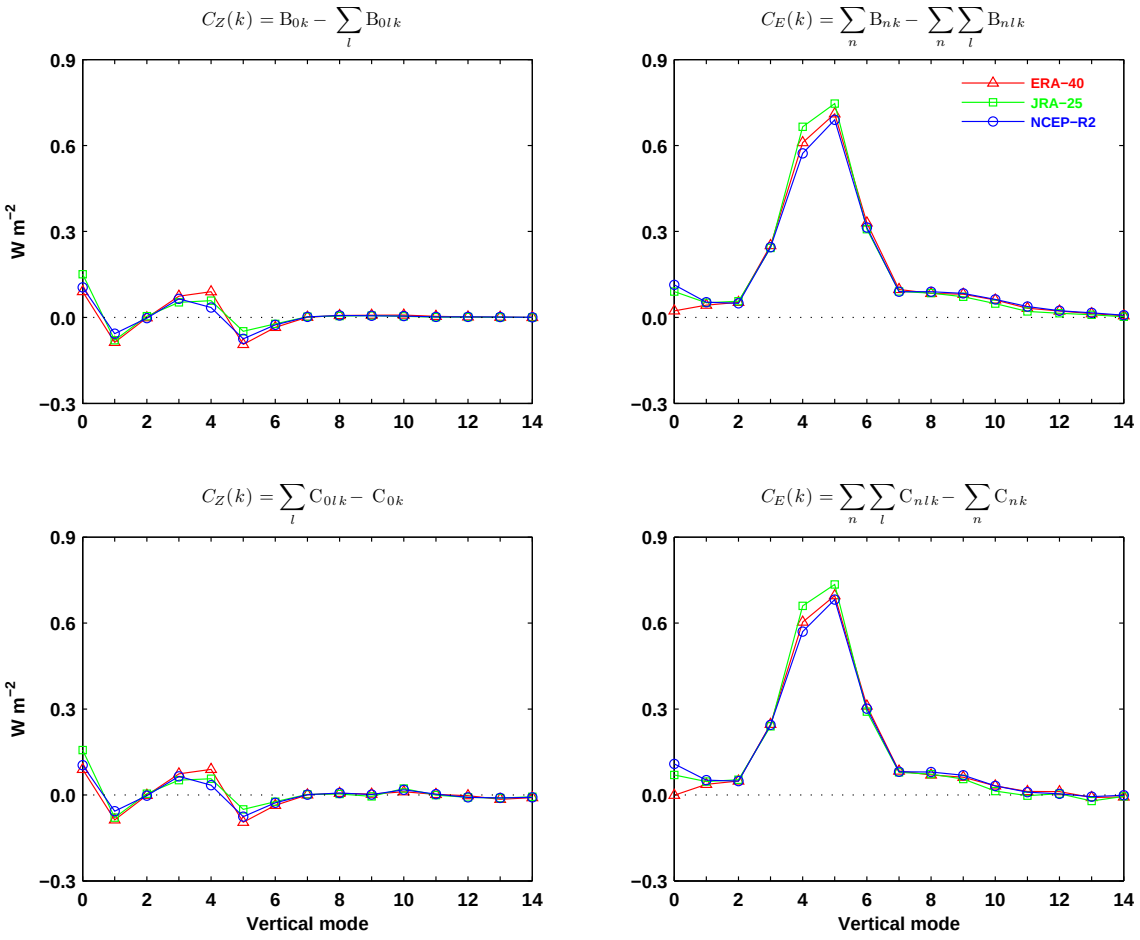

Figure 4.38: Conversion of available potential energy into kinetic energy in the vertical mode domain, for ERA-40, JRA-25 and NCEP-R2 in DJF. The zonal mean and eddy components are presented separately in the left and right panels, respectively. The computations are according to formulae (2.106), (2.105), (2.116) and (2.115), from left to right and top to bottom, respectively. Units are W m^{-2}.

Energy generation and dissipation

Figure 4.39 shows the spectra for the generation and dissipation terms of the zonal mean and eddy components of available potential energy and kinetic energy in the vertical mode domain, i.e. $G_Z(k)$, $G_E(k)$, $D_Z(k)$ and $D_E(k)$, respectively. These terms were computed as residuals from the balance equations (2.95) and (2.107), accounting for the time change of available potential energy and kinetic energy. The spectra of $G_E(k)$ shows that eddy available potential energy is generated at the baroclinic modes

($G_E(k) > 0$ at $k = 3-6$), peaking at $k = 5$, but it is dissipated at the barotropic mode ($G_E(k) < 0$ at $k = 0$). The energy dissipated is approximately of the same amount as the energy supplied from the zonal mean available potential energy into the barotropic component of eddy available potential energy (Figure 4.34), explaining therefore the low levels of barotropic A_E.

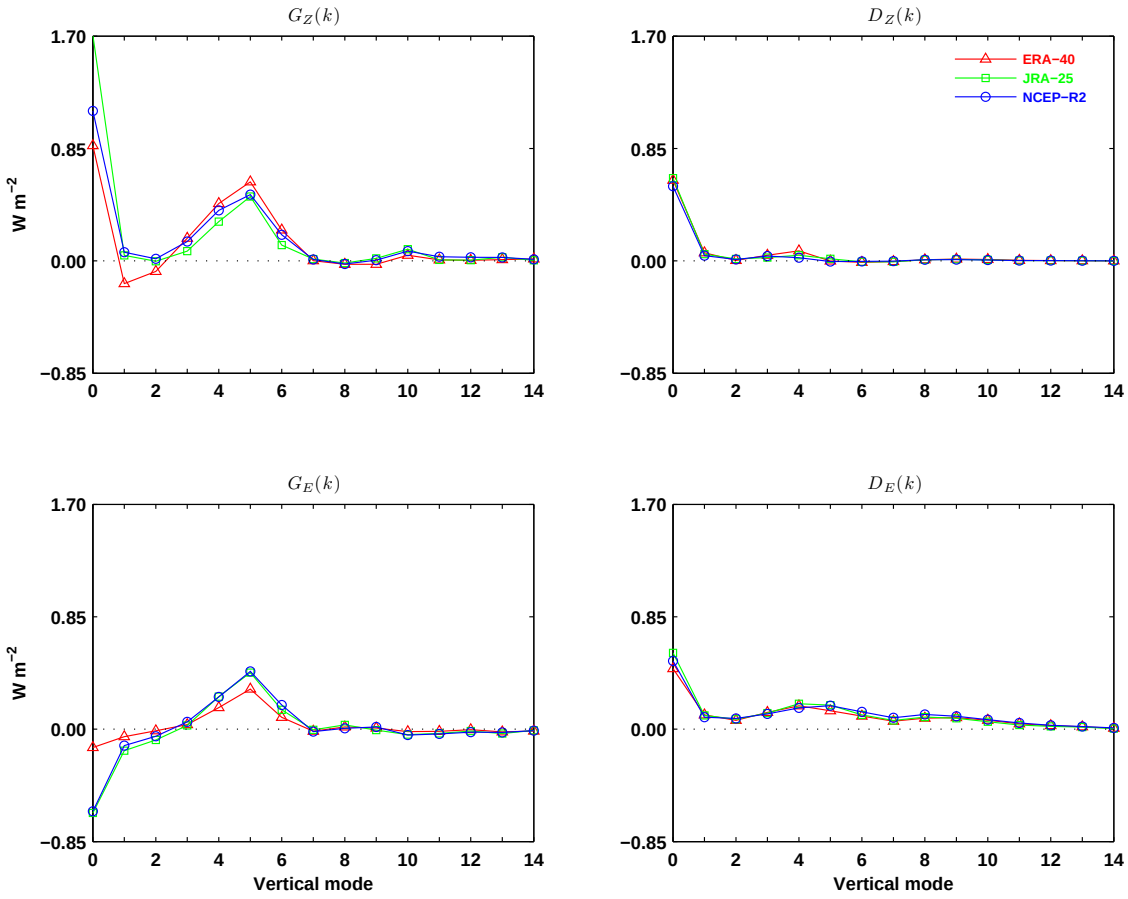

Figure 4.39: Generation of zonal and eddy available potential energy (left panels) and dissipation of zonal and eddy kinetic energy (right panels) in the vertical mode domain for ERA-40, JRA-25 and NCEP-R2 in DJF. Units are W m^{-2}.

According to the results presented troughout this section, it is evident that the basic characteristics of the flow of energy in the atmosphere are determined by the Rossby modes, whereas the contributions from the gravity modes are relatively small. Most of the energy of the atmospheric general circulation is generated at both the barotropic and

baroclinic components of zonal mean available potential energy, A_Z, by the differential heating of solar radiation, as seen by the positive values of $G_Z(k)$ in Figure 4.39. Almost all the energy generated in A_Z is transformed into eddy available potential energy, A_E, at the planetary and synoptic-scale eddies of both the barotropic and baroclinic components, as seen by the positive values of interaction C_{nlk} in Figure 4.32, and by the negative values of the zonal mean component of C_{nlk} in Figure 4.34, which are balanced by the positive values of the eddy component. Both A_Z and A_E are contained mainly in the baroclinic component of the atmosphere, because the energy generated at the barotropic component of A_Z is transformed into both the barotropic and baroclinic components of A_E, and the energy supplied into the barotropic component of A_E is dissipated radiatively, probably by the warming of cold air masses and the cooling of warm air masses in middle latitudes (Lorenz, 1955), as seen by the negative values of $G_E(k)$ at $k = 0$ in Figure 4.39. Some energy is also generated in the baroclinic components of A_E, as seen by the positive values of $G_E(k)$ in Figure 4.39. This energy, together with the energy supplied from A_Z into the baroclinic component of A_E, is converted into the eddy kinetic energy, K_E, of the baroclinic component, mostly by the planetary and synoptic-scale eddies, as seen by the positive values of $C(n)$ and $C_E(k)$ in Figures 4.37 and 4.38, respectively. Part of the energy supplied into the baroclinic K_E is dissipated by surface friction and viscosity, as seen by positive $D_E(k)$ for $k > 0$ in Figure 4.39, whereas the remainder part is transformed by the synoptic to planetary waves into barotropic kinetic energy of both the zonal mean and eddy components, K_Z and K_E, and also into zonal mean kinetic energy of the baroclinic component, as seen by positive B_{nlk} in Figures 4.33 and 4.35. The kinetic energy supplied to the barotropic component of both K_Z and K_E is also dissipated by surface friction and viscosity, as seen by positive $D_Z(k)$ and $D_E(k)$ at $k = 0$ in Figure 4.39. Some dissipation also takes place in the baroclinic K_Z (Figure 4.39), and the remainder small part of energy generated in A_Z, seems to be converted into K_Z, as seen by the net positive values of $C_Z(k)$ over all vertical modes in Figure 4.38.

4.2 Energetics in the climate models

4.2.1 Lorenz energy cycle

Table 4.1 displays the numerical values of energy cycle terms averaged over 1979-1999 for JRA-25 and NCEP-R2, and over 1970-1999 for ERA-40 and the climate models. The percentage differences between the climate models and the reanalysis, calculated with respect to the average energy cycle of the three reanalysis, are represented in parentheses. Due to its smallness, the term C_Z is only indicated as having the same (S) or different (D) sign from that of the reanalysis average. Values for the time derivatives (left hand sides in (2.26)-(2.29)) of available potential and kinetic energies are omitted. A comparison of the global energy cycle between the three reanalysis and the five models, is illustrated in Figure 4.40, for all seasons. In both Table 4.1 and Figure 4.40, the values of C_E were computed with the "$\omega\alpha$" formula while those of C_Z were computed with the "$\mathbf{v} \cdot \nabla z$" formula.

The direction of the energy flow is generally consistent among the datasets, with the exception for conversion C_Z, which, depending on the season and the dataset considered, has opposite signs among the various estimates (Table 4.1). However, this conversion is the smallest among the energy cycle terms and has, therefore, little weight in the global energy cycle. Additionally, the smallness of C_Z is a characteristic shared by all datasets, despite the somewhat larger C_Z for JRA-25, NCEP-R2 and CNRM-CM3. Nevertheless, the global energy cycle is generally too strong in the models compared to that in the reanalysis (Figure 4.40, Table 4.1). The contributions for the global integrals are represented in Figures 4.41 to 4.50, as a function of latitude and pressure, for the reanalysis and models averages, and for each model. These cross-sections are shown only for DJF and JJA, for compactness. The differences between the models' integrands and those of the reanalysis average are shaded with a distinct colour pallet. The zonal mean topography is represented, for displaying purposes, by the time mean of the zonal average surface pressure, shown as the black filled portions in the cross-sections. The stability parameter, γ, is displayed in Figure 4.51 for all seasons.

Table 4.1: Global integrated energetics for the reanalysis and the climate models. Percentage differences between the energy cycle in the climate models and those in the reanalysis, calculated with respect to the average energy cycle of the three reanalysis, are represented in parentheses. Due to its smallness, the term C_Z is only indicated in the percentage differences as having the same (S) or different (D) sign from that of the average reanalysis. Units are 10^5 J m^{-2} for energy levels and W m^{-2} for conversion/transfer rates.

Dataset	A_Z	A_E	K_Z	K_E	C_A	C_E	C_K	C_Z	G_Z	G_E	D_Z	D_E	Season
ERA-40	**47.8**	**6.40**	**8.74**	**8.15**	**2.19**	**2.65**	**0.80**	**0.14**	**2.39**	**0.46**	**0.93**	**1.85**	DJF
JRA-25	**46.4**	**6.16**	**8.63**	**8.18**	**2.19**	**2.59**	**0.73**	**0.28**	**2.52**	**0.40**	**1.00**	**1.86**	
NCEP-R2	**46.5**	**6.00**	**8.32**	**7.64**	**2.11**	**2.43**	**0.66**	**0.23**	**2.40**	**0.32**	**0.88**	**1.77**	
CGCM3.1	**51.5** (10)	**6.18** (0)	**8.96** (5)	**7.49** (-6)	**2.47** (14)	**2.83** (11)	**0.77** (5)	**0.07** (S)	**2.60** (7)	**0.36** (-8)	**0.83** (-11)	**2.06** (13)	
CCSM3	**52.2** (11)	**6.14** (-1)	**10.7** (25)	**8.29** (4)	**2.69** (24)	**2.98** (17)	**0.93** (27)	**0.09** (S)	**2.84** (16)	**0.29** (-25)	**1.01** (8)	**2.05** (12)	
CNRM-CM3	**54.3** (16)	**4.54** (-27)	**8.51** (-1)	**5.54** (-31)	**2.37** (10)	**2.82** (10)	**0.75** (3)	**0.32** (S)	**2.73** (12)	**0.45** (15)	**1.07** (14)	**2.07** (13)	
MIROC3.2	**48.4** (3)	**5.53** (-11)	**9.38** (10)	**7.25** (-9)	**2.45** (13)	**2.84** (11)	**1.01** (38)	**-0.12** (D)	**2.40** (-2)	**0.39** (-1)	**0.88** (-6)	**1.83** (0)	
ECHAM5	**49.3** (5)	**6.48** (5)	**8.80** (3)	**8.72** (9)	**2.57** (19)	**3.17** (24)	**0.82** (12)	**0.10** (S)	**2.72** (11)	**0.60** (54)	**0.92** (-5)	**2.35** (26)	
ERA-40	**46.7**	**5.67**	**7.93**	**7.21**	**2.18**	**2.58**	**0.67**	**0.12**	**2.23**	**0.39**	**0.80**	**1.92**	MAM
JRA-25	**45.0**	**5.31**	**7.89**	**7.25**	**2.20**	**2.57**	**0.62**	**0.36**	**2.48**	**0.36**	**0.99**	**1.96**	
NCEP-R2	**45.5**	**5.16**	**7.67**	**6.82**	**2.09**	**2.27**	**0.58**	**0.27**	**2.28**	**0.16**	**0.86**	**1.70**	
CGCM3.1	**50.6** (11)	**5.67** (5)	**8.61** (10)	**7.20** (2)	**2.65** (23)	**2.97** (20)	**0.79** (27)	**-0.09** (D)	**2.50** (7)	**0.31** (3)	**0.71** (-19)	**2.18** (17)	
CCSM3	**52.8** (15)	**5.90** (10)	**10.2** (30)	**7.86** (11)	**2.86** (33)	**3.13** (27)	**0.97** (56)	**0.02** (S)	**2.82** (21)	**0.27** (-12)	**1.00** (14)	**2.17** (16)	
CNRM-CM3	**50.0** (9)	**3.82** (-29)	**7.08** (-10)	**4.90** (-31)	**2.16** (0)	**2.71** (10)	**0.60** (-4)	**0.26** (S)	**2.29** (-2)	**0.55** (81)	**0.89** (1)	**2.12** (14)	
MIROC3.2	**47.1** (3)	**4.91** (-9)	**8.98** (15)	**6.77** (-5)	**2.42** (12)	**2.71** (10)	**0.79** (27)	**-0.05** (D)	**2.28** (-2)	**0.28** (-6)	**0.75** (-15)	**1.93** (4)	
ECHAM5	**47.8** (5)	**6.11** (14)	**8.10** (3)	**8.12** (14)	**2.65** (23)	**3.30** (33)	**0.84** (35)	**-0.01** (D)	**2.57** (10)	**0.64** (112)	**0.84** (-5)	**2.46** (32)	
ERA-40	**45.9**	**5.38**	**8.96**	**6.85**	**2.03**	**2.66**	**0.70**	**0.10**	**2.18**	**0.63**	**0.78**	**1.97**	JJA
JRA-25	**43.9**	**5.03**	**8.94**	**6.89**	**1.99**	**2.64**	**0.63**	**0.35**	**2.38**	**0.65**	**0.96**	**2.02**	
NCEP-R2	**44.3**	**4.73**	**8.17**	**6.35**	**1.82**	**2.24**	**0.54**	**0.31**	**2.18**	**0.42**	**0.83**	**1.71**	
CGCM3.1	**51.2** (15)	**5.80** (15)	**9.01** (4)	**7.06** (5)	**2.44** (25)	**2.94** (17)	**0.68** (9)	**-0.01** (D)	**2.50** (11)	**0.50** (-12)	**0.66** (-24)	**2.27** (20)	
CCSM3	**53.1** (19)	**6.06** (20)	**10.5** (21)	**7.52** (12)	**2.55** (31)	**3.12** (24)	**0.88** (41)	**-0.05** (D)	**2.56** (14)	**0.57** (1)	**0.81** (-6)	**2.25** (18)	
CNRM-CM3	**50.3** (13)	**4.42** (-12)	**6.82** (-22)	**5.08** (-24)	**1.93** (-1)	**2.79** (11)	**0.50** (-20)	**0.33** (S)	**2.37** (6)	**0.86** (53)	**0.81** (-5)	**2.29** (21)	
MIROC3.2	**46.5** (4)	**5.14** (2)	**9.05** (4)	**6.61** (-1)	**2.11** (8)	**2.78** (11)	**0.66** (6)	**0.03** (S)	**2.18** (-3)	**0.67** (18)	**0.68** (-21)	**2.13** (12)	
ECHAM5	**48.2** (8)	**5.83** (16)	**8.73** (0)	**8.04** (20)	**2.36** (21)	**3.18** (27)	**0.66** (6)	**0.20** (S)	**2.62** (13)	**0.82** (45)	**0.85** (-1)	**2.52** (33)	
ERA-40	**45.9**	**5.62**	**8.45**	**7.32**	**2.25**	**2.67**	**0.82**	**-0.01**	**2.20**	**0.44**	**0.83**	**1.83**	SON
JRA-25	**44.0**	**5.36**	**8.41**	**7.31**	**2.18**	**2.66**	**0.76**	**0.20**	**2.36**	**0.50**	**0.98**	**1.88**	
NCEP-R2	**44.3**	**5.09**	**8.01**	**6.79**	**2.11**	**2.36**	**0.69**	**0.12**	**2.20**	**0.27**	**0.82**	**1.65**	
CGCM3.1	**50.4** (13)	**5.78** (8)	**8.98** (8)	**7.28** (2)	**2.67** (22)	**3.01** (17)	**0.87** (15)	**-0.14** (D)	**2.46** (9)	**0.35** (-14)	**0.74** (-15)	**2.13** (19)	
CCSM3	**52.5** (17)	**5.89** (10)	**10.6** (28)	**7.83** (10)	**2.84** (30)	**3.17** (24)	**1.04** (37)	**-0.08** (D)	**2.70** (20)	**0.33** (-18)	**0.97** (11)	**2.12** (19)	
CNRM-CM3	**52.4** (17)	**3.99** (-26)	**7.67** (-7)	**5.12** (-28)	**2.25** (3)	**2.81** (10)	**0.68** (-10)	**0.26** (S)	**2.48** (10)	**0.56** (39)	**0.93** (6)	**2.13** (19)	
MIROC3.2	**46.5** (4)	**4.83** (-10)	**8.99** (8)	**6.74** (-6)	**2.37** (9)	**2.76** (8)	**0.87** (15)	**-0.14** (D)	**2.21** (-2)	**0.40** (0)	**0.73** (-16)	**1.88** (5)	
ECHAM5	**48.2** (8)	**5.92** (11)	**8.64** (4)	**8.10** (13)	**2.70** (24)	**3.33** (30)	**0.97** (28)	**-0.09** (D)	**2.57** (14)	**0.64** (59)	**0.89** (1)	**2.36** (32)	

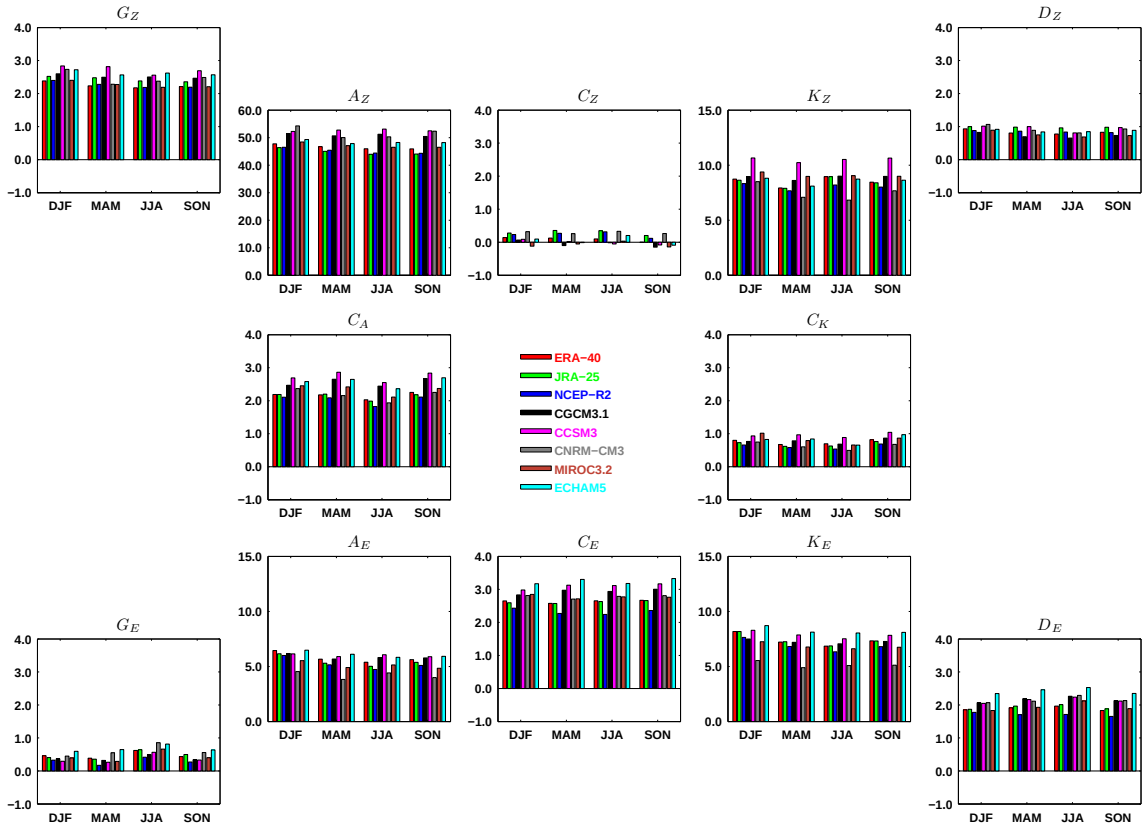

Figure 4.40: Lorenz energy cycle in the present climate, for ERA-40 (red), JRA-25 (green), NCEP-R2 (blue), CGCM3.1 (black), CCSM3 (pink), CNRM-CM3 (grey), MIROC3.2 (brown) and ECHAM5 (cyan) in the four seasons (DJF, MAM, JJA and SON). Averages are over 1970-1999 for ERA-40 and the five models, and over 1979-1999 for JRA-25 and NCEP-R2. Units are 10^5 J m^{-2} for energy levels and W m^{-2} for conversion/transfer rates.

Energy levels

The structure of the integrand of zonal mean available potential energy, A_Z, in the models agree generally well with that of the reanalysis average, as summarised in Figure 4.41. Nevertheless, the integral of A_Z for all models is greater than the corresponding value for the reanalysis average (Table 4.1). This may be seen as the energetics manifestation of the classical temperature cold bias in high latitudes of the models' atmosphere (specially in the middle and upper troposphere). Some deficit of A_Z in parts of the models' atmosphere is also present.

The cross-sections for A_E are illustrated in Figure 4.42. Overall, the structure of the A_E integrand in the models agrees with that of the reanalysis, but local excesses and/or deficits are also found. Globally, the models have less A_E than the average reanalysis in DJF, except for ECHAM5, typically in the NH high latitudes, particularly from the middle/upper troposphere upwards. In JJA there is an overall excess of A_E in the models, except for CNRM-CM3. The deficit of A_E is rather prominent in CNRM-CM3 throughout all levels, although much less pronounced in JJA.

Figure 4.43 shows the cross-sections for the integrand of zonal mean kinetic energy, K_Z. In general, the models and reanalysis agree on the fact that the distributions in the K_Z integrand are dominated by the tropospheric jets, peaking at 200 hPa, and, secondarily, by the stratospheric polar night jets and low latitude easterlies, specially in JJA. Overall, there is too much K_Z in the models, most notably in CCSM3, which is mainly related to the tropospheric jets being too strong in the models. In models CGCM3.1, MIROC3.2 and CNRM-CM3, the SH tropospheric jet is also somewhat displaced to the equator in DJF.

The cross-sections of eddy kinetic energy, K_E, are obtained from the spatial variance of the horizontal wind field, and are displayed in Figure 4.44. The main features in the structure of K_E, associated with the tropospheric and stratospheric jet streams and its meanders, are commun to reanalysis and models. Despite this general agreement, models CNRM-CM3 and MIROC3.2 have less K_E than the average reanalysis in all seasons, which is most remarkable in CNRM-CM3, while in MIROC3.2 it is relatively modest troughout the year (Table 4.1). Also modest is the deficit (excess) of K_E in DJF (JJA) for CGCM3.1. The SH maximum for models CGCM3.1, CNRM-CM3 and MIROC3.2, is displaced to the equator in DJF, and also in JJA for CNRM-CM3 and MIROC3.2. The NH maximum is somewhat weaker and less extended poleward in those three models, which may indicate less pronounced meanders in theirs NH tropospheric jets. Models CCSM3 and ECHAM5 have too much K_E near the tropospheric jet streams, being less prominent in DJF, in particular for CCSM3.

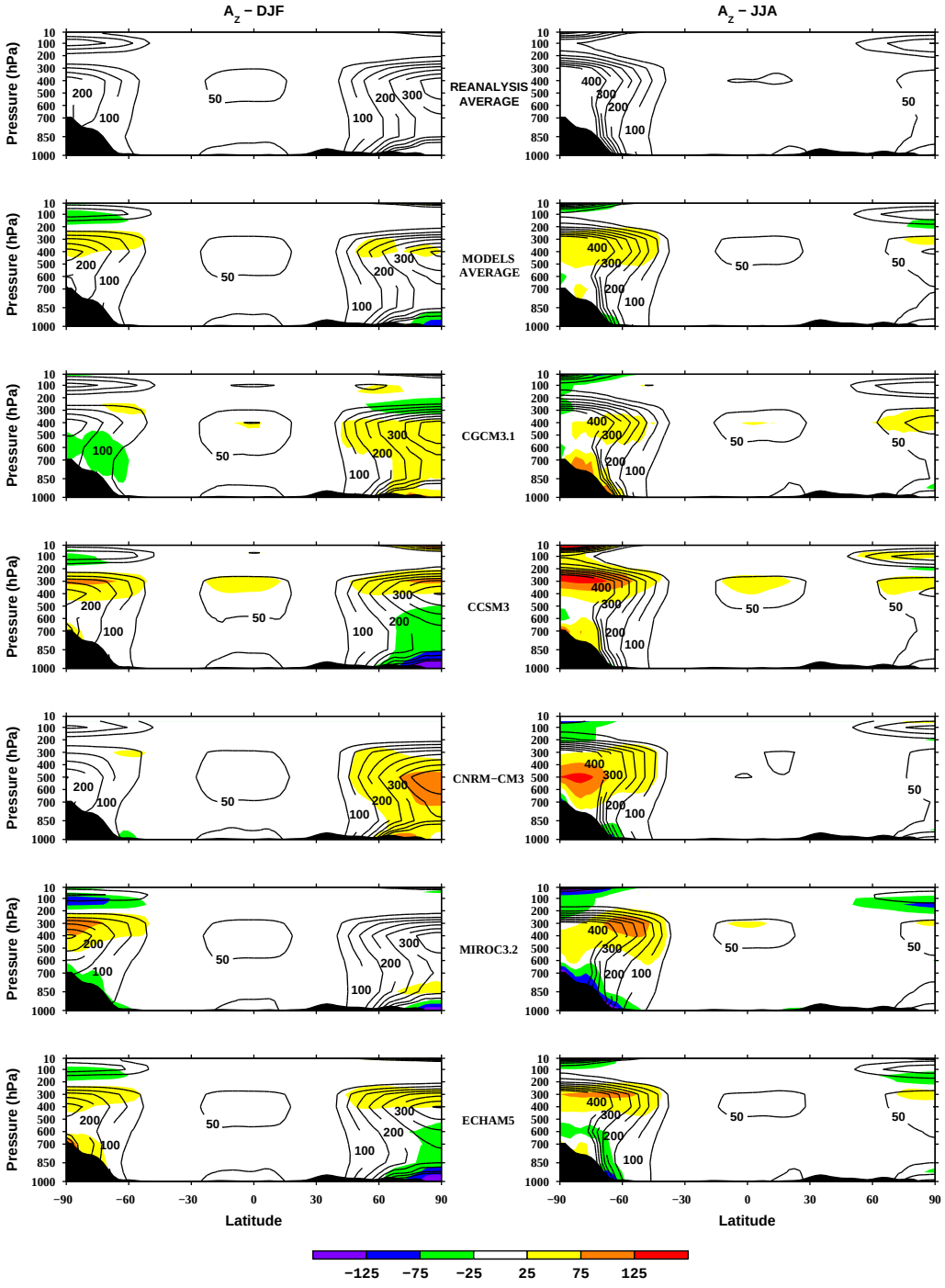

Figure 4.41: Mean cross-sections of zonal mean available potential energy, A_Z, for the reanalysis average, the models average and the five individual models, in DJF (left panels) and JJA (right panels). Averages are over 1970-1999 for ERA-40 and the five models, and over 1979-1999 for JRA-25 and NCEP-R2. The A_Z quantities are contoured (black) and the differences between the models and the reanalysis average are shaded (colour). Units are J m^{-2} Pa^{-1} (10^5 J m^{-2} bar^{-1}).

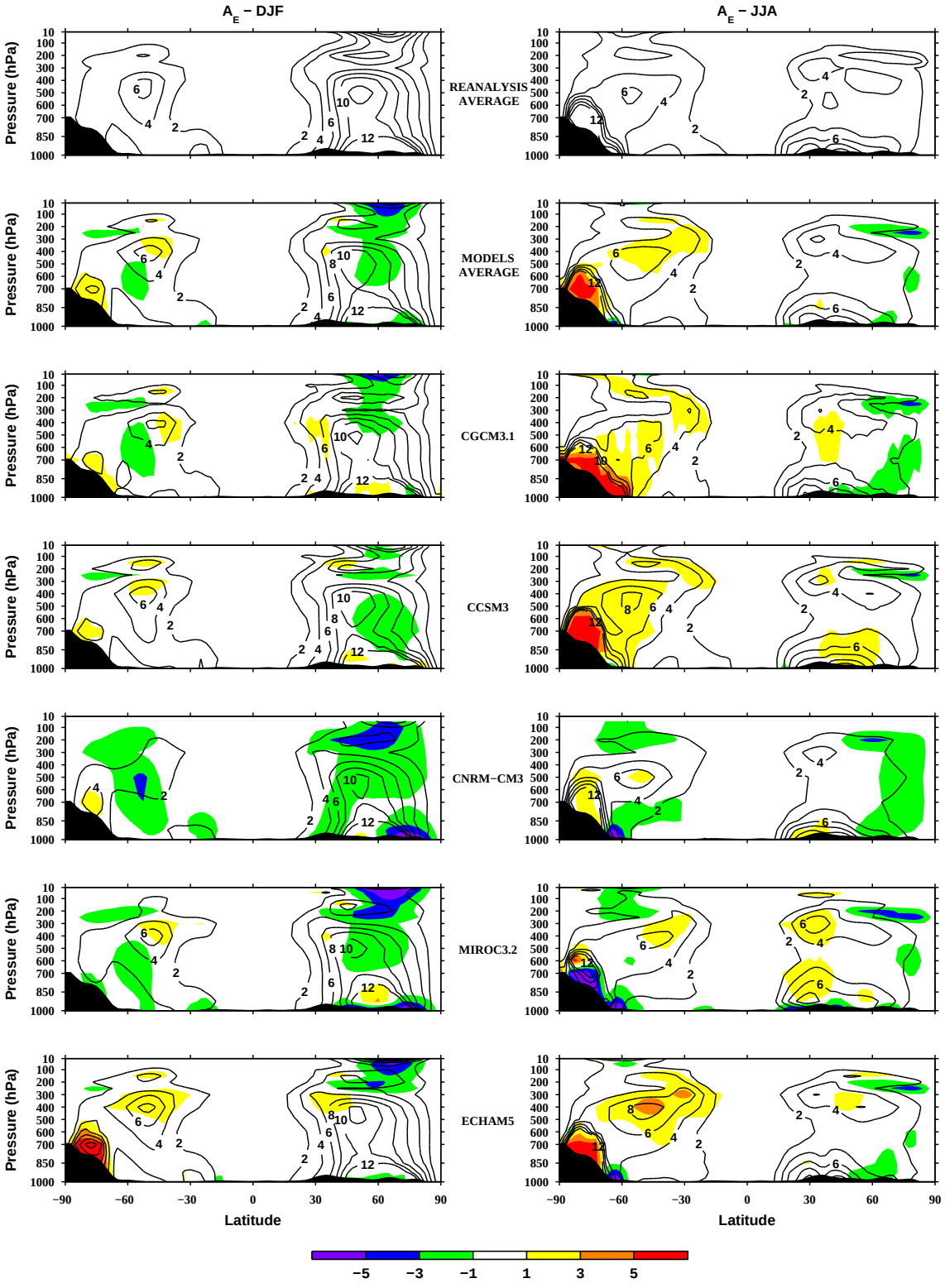

Figure 4.42: The same as in Figure 4.41, but for eddy available potential energy, A_E.

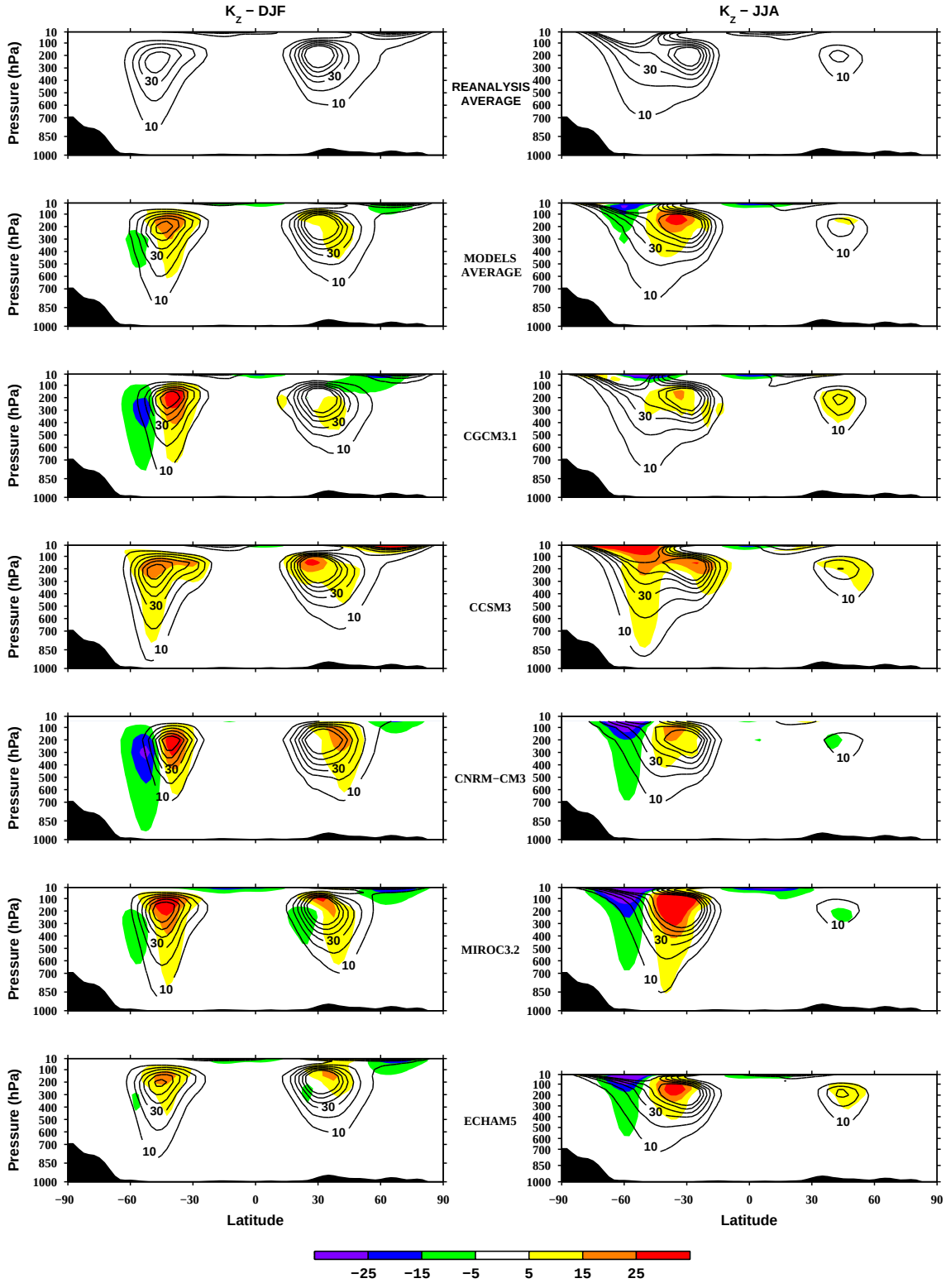

Figure 4.43: The same as in Figure 4.41, but for zonal mean kinetic energy, K_Z.

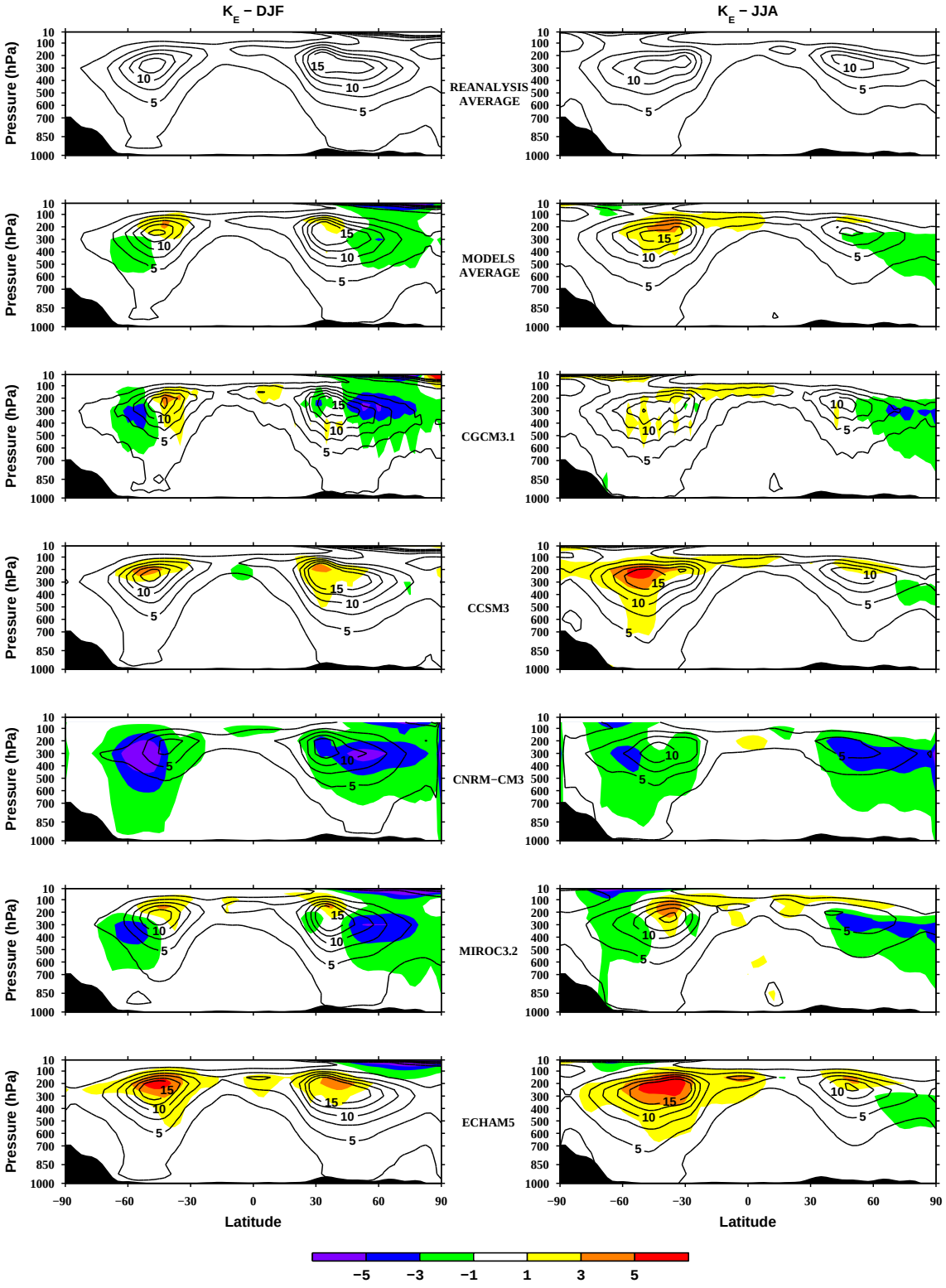

Figure 4.44: The same as in Figure 4.41, but for eddy kinetic energy, K_E.

Energy conversion/transfer rates

Cross-sections for the rate of transfer from zonal mean to eddy available potential energy, C_A, which depends upon the γ weighted horizontal and vertical transports of sensible heat up the temperature gradient, are shown in Figure 4.45. The structure of the main positive contributions to C_A, is similar between models and reanalysis. Negative contributions are mainly found in the lower stratosphere ($\sim$ 100-150 hPa) for both models and reanalysis, which reflect the known reverse conversion from A_E to A_Z (e.g. Oort and Peixoto, 1974), being most evident in DJF. However, there is generally too much C_A in the models, mostly at the tropospheric extratropical latitudes of the winter hemispheres and nearby Antarctica in JJA. The exception is in model CNRM-CM3, for which the excess of C_A is mainly found at the tropical upper troposphere in DJF and JJA, and also nearby Antarctica in JJA, while in the lower troposphere of the mid latitudes there is some deficit of C_A in this model.

The conversion rates from eddy available potential energy to eddy kinetic energy, C_E, computed with both "$\omega\alpha$" and "$\mathbf{v} \cdot \nabla z$" formulations, are displayed in Figures 4.46 and 4.47, respectively. As mentioned in section 4.1.1, the estimates of C_E should reflect "reality" more accurately when computed with the "$\omega\alpha$" formula. Therefore, the analysis of this term is based on the estimates with this formula, while the results with the "$\mathbf{v} \cdot \nabla z$" formula are only included for comparison and completeness. On the contrary, the estimate of C_Z is much less sensitive to the inclusion of underground data when the calculations are performed with the "$\mathbf{v} \cdot \nabla z$" formula (section 4.1.1), and hence, the comparative analysis between models and reanalysis for C_Z will be based on the estimates with this formula. Figure 4.46 shows, for both reanalysis and models, the principal positive contributions to C_E in the extratropical troposphere, peaking at mid latitudes of the middle troposphere in the winter hemispheres, and nearby Antarctica in JJA. Additional positive contributions are found at upper levels of the winter hemisphere, and negative values in the lower stratosphere. Once again, there is too much C_E in the models, most noticeable in ECHAM5 and CCSM3, and at similar regions as those for the excess of C_A.

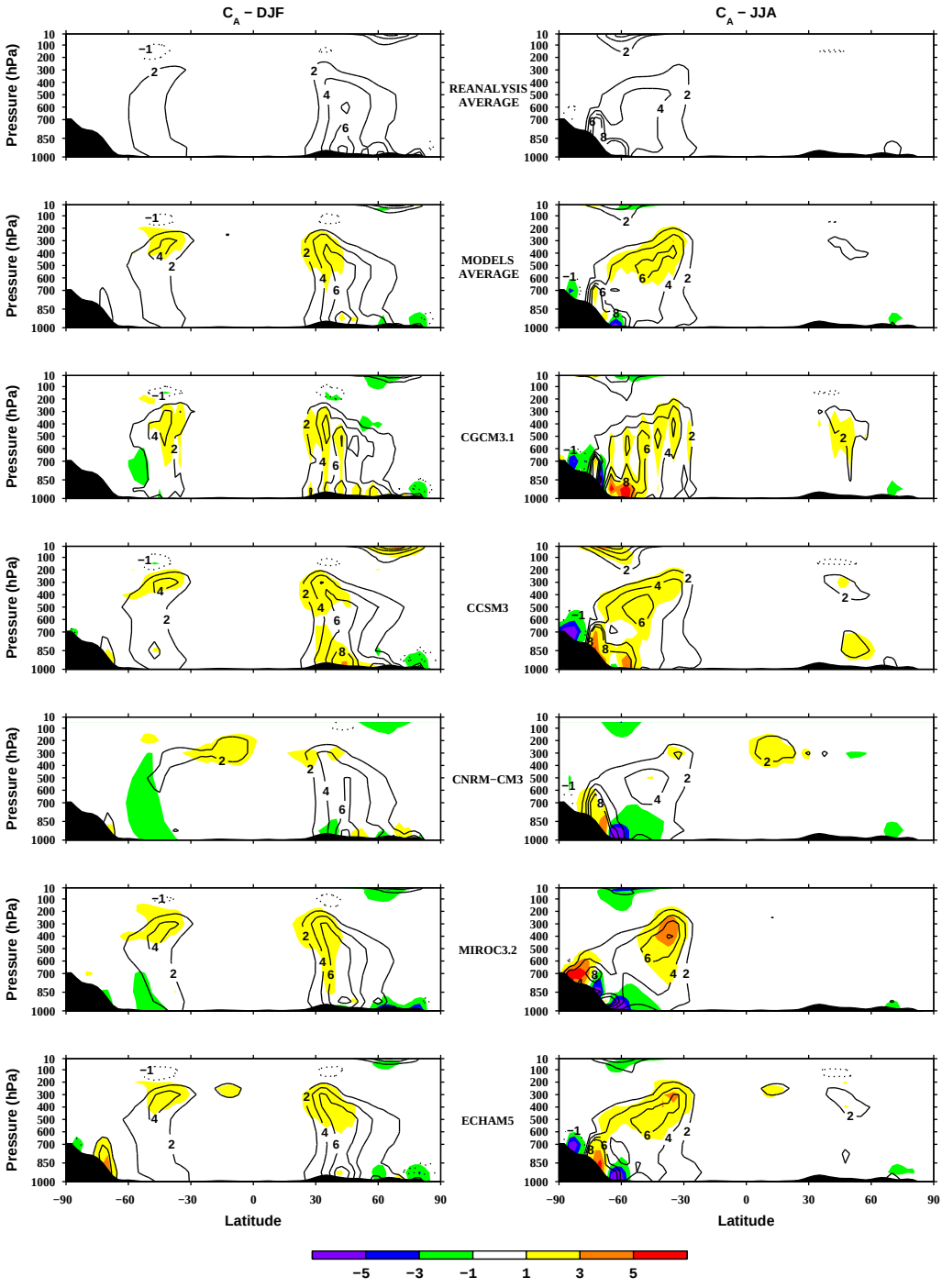

Figure 4.45: The same as in Figure 4.41, but for the rate of transfer from zonal mean to eddy available potential energy, C_A. Positive (Negative) values of C_A are represented by continuous (dotted) contours. Units are 10^5 W m^{-2} Pa^{-1} (W m^{-2} bar^{-1}).

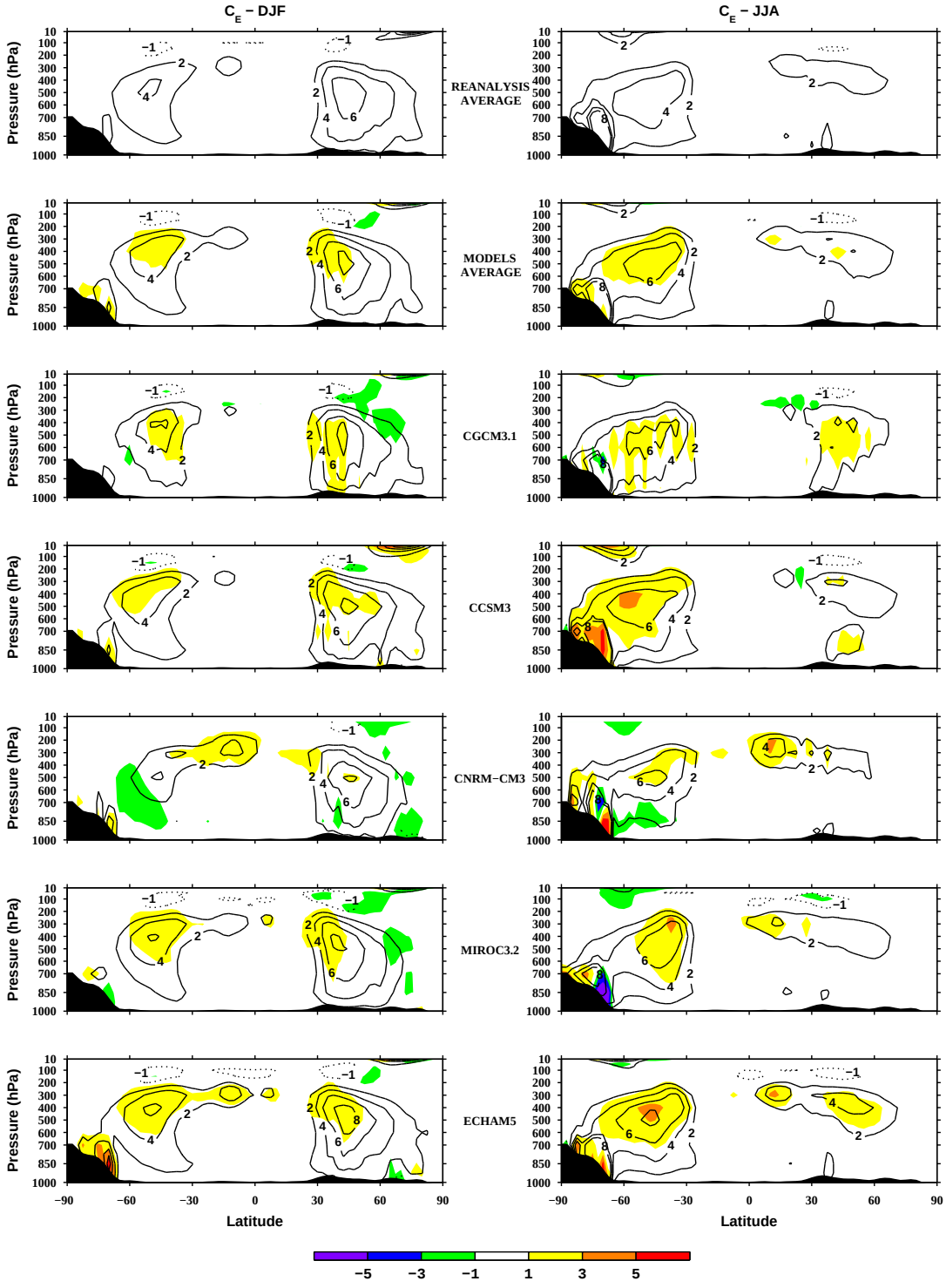

Figure 4.46: The same as in Figure 4.45, but for the conversion rate of eddy available potential energy to eddy kinetic energy, C_E, computed with the "$\omega\alpha$" formulation.

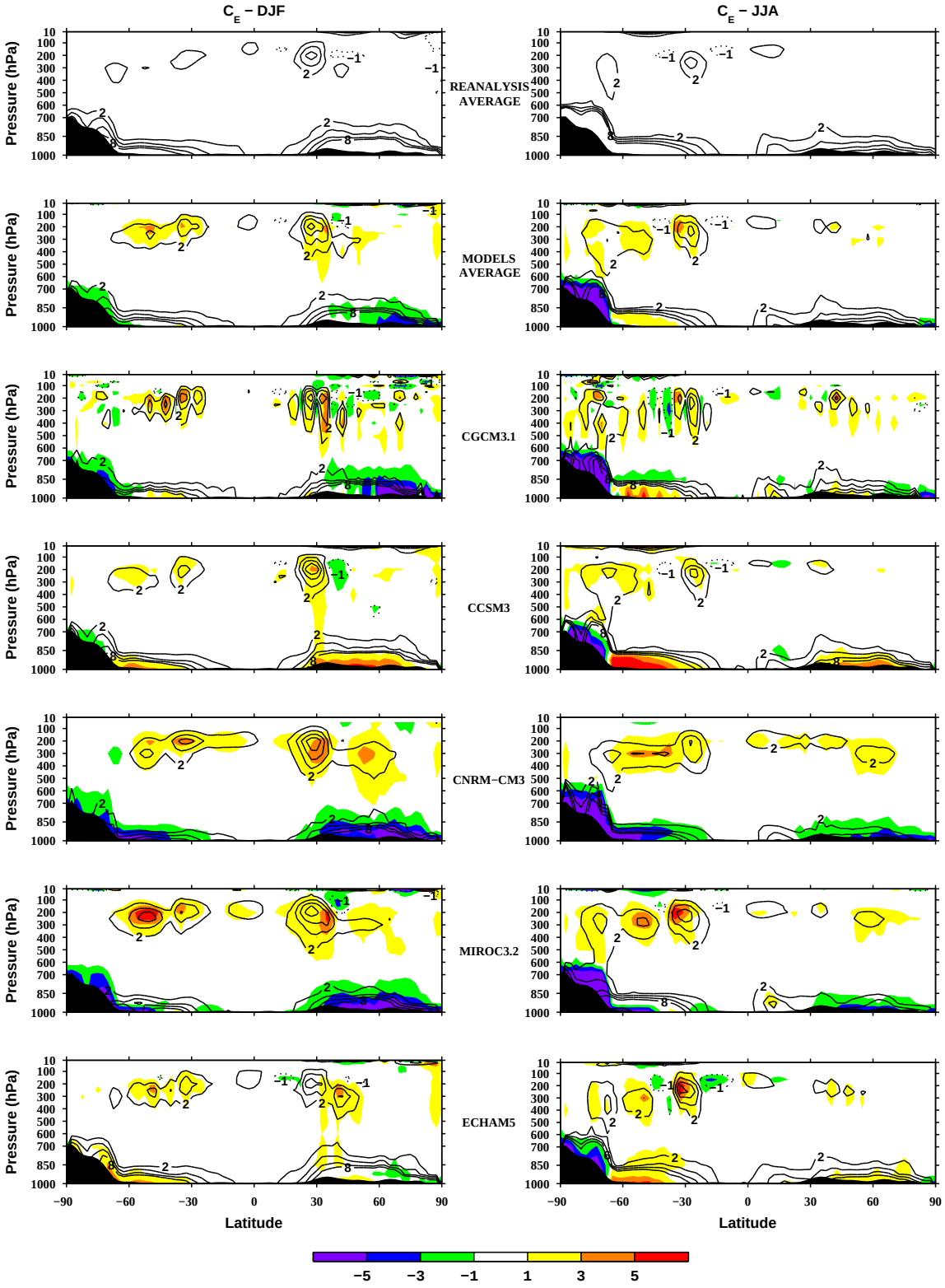

Figure 4.47: The same as in Figure 4.46, but computed with the "$\mathbf{v} \cdot \nabla z$" formulation.

Figure 4.48 shows the cross-sections for the rate of transfer of eddy to zonal mean kinetic energy, C_K, which depends upon the horizontal and vertical transports of angular momentum by the eddies along the gradient of relative angular velocity. Maximum positive contributions are found just equatorward the tropospheric jets, with that of the winter hemispheres between the main negative contributions, centred slightly upward the positive maximums. Secondary positive contributions are located just equatorward the stratospheric polar night jets. These features are generally common to reanalysis and models, but both qualitative and quantitative differences are also evident. Overall, there is too much C_K in the models, more evident for CCSM3 in all seasons, for MIROC3.2 in DJF and for ECHAM5 in MAM (Table 4.1). The CNRM-CM3 model is an exception, showing less C_K than the reanalysis average in all season, except for a modest excess in DJF, which is also the case for model CGCM3.1 in this season. In DJF, the SH positive contributions are displaced equatorward for models CGCM3.1, CNRM-CM3 and MIROC3.2.

The conversion rates from zonal mean available potential energy to zonal mean kinetic energy, C_Z, computed with the "$\omega\alpha$" and "$\mathbf{v}\cdot\nabla z$" formulae, are displayed in Figures 4.49 and 4.50, respectively. Depending on the season, the global integral of C_Z is negative for some models (Table 4.1), which disagrees with the positive values found for the reanalysis average. This difference is mainly due to stronger negative contributions in the upper troposphere (Figure 4.50), which seems typical in the models, except for CNRM-CM3. In DJF, the negative contributions of SH are also slightly displaced to the equator in CGCM3.1, CNRM-CM3 and MIROC3.2. Despite the above disagreements, the distributions of C_Z integrand are reasonably similar between models and reanalysis, which agree also on the smallness of this conversion rate.

The stability parameter, γ, is shown in Figure 4.51, generally peaking at 400 hPa and near the surface for the reanalysis. The models' main differences seem to be in CCSM3, MIROC3.2 and ECHAM5, which have somewhat larger values at 250 hPa and 300 hPa, the later being where γ peaks for these models instead at 400 hPa. At the remaining levels there is a reasonably close agreement between models and reanalysis.

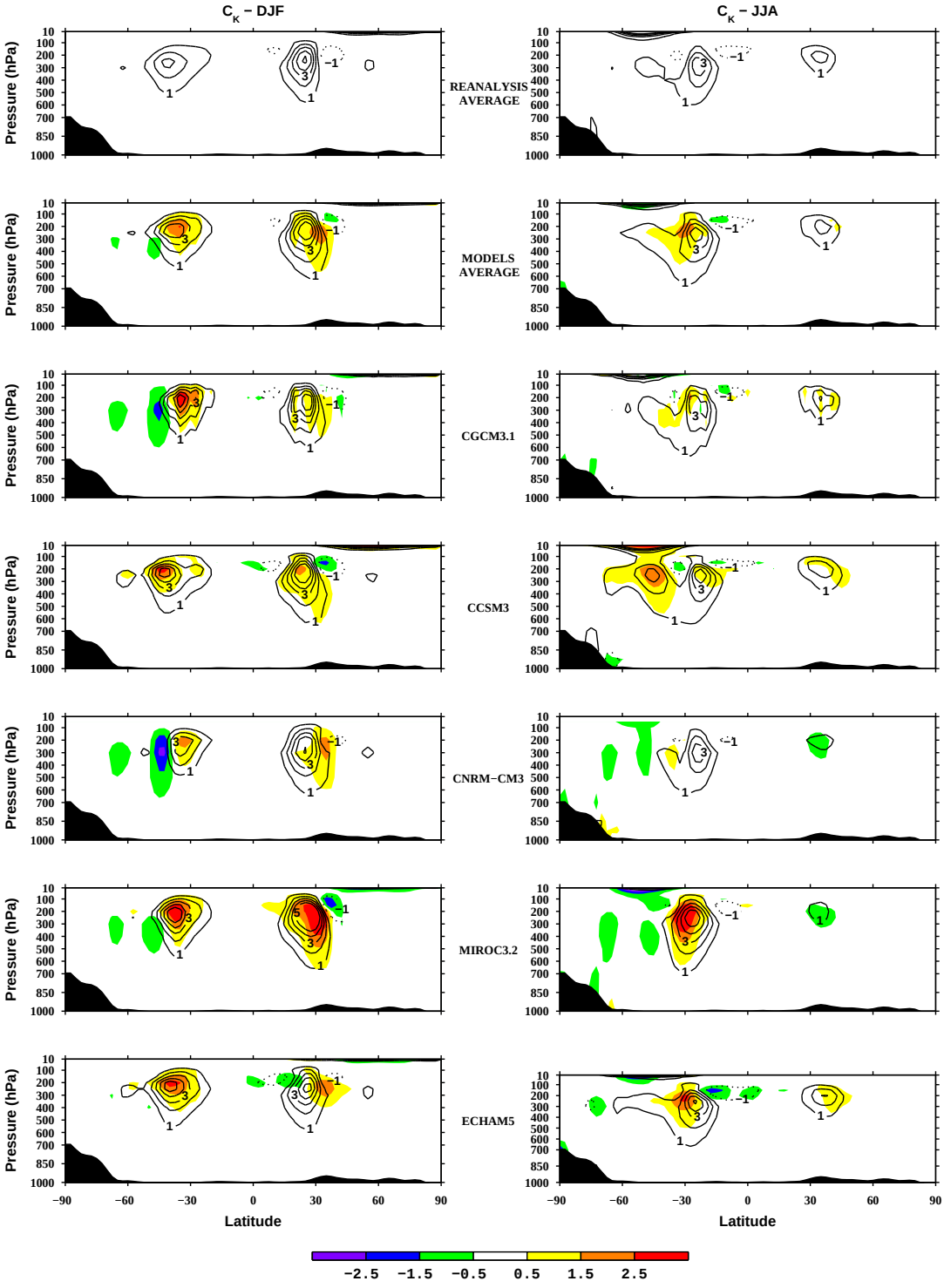

Figure 4.48: The same as in Figure 4.45, but for the rate of transfer from eddy to zonal mean kinetic energy, C_K.

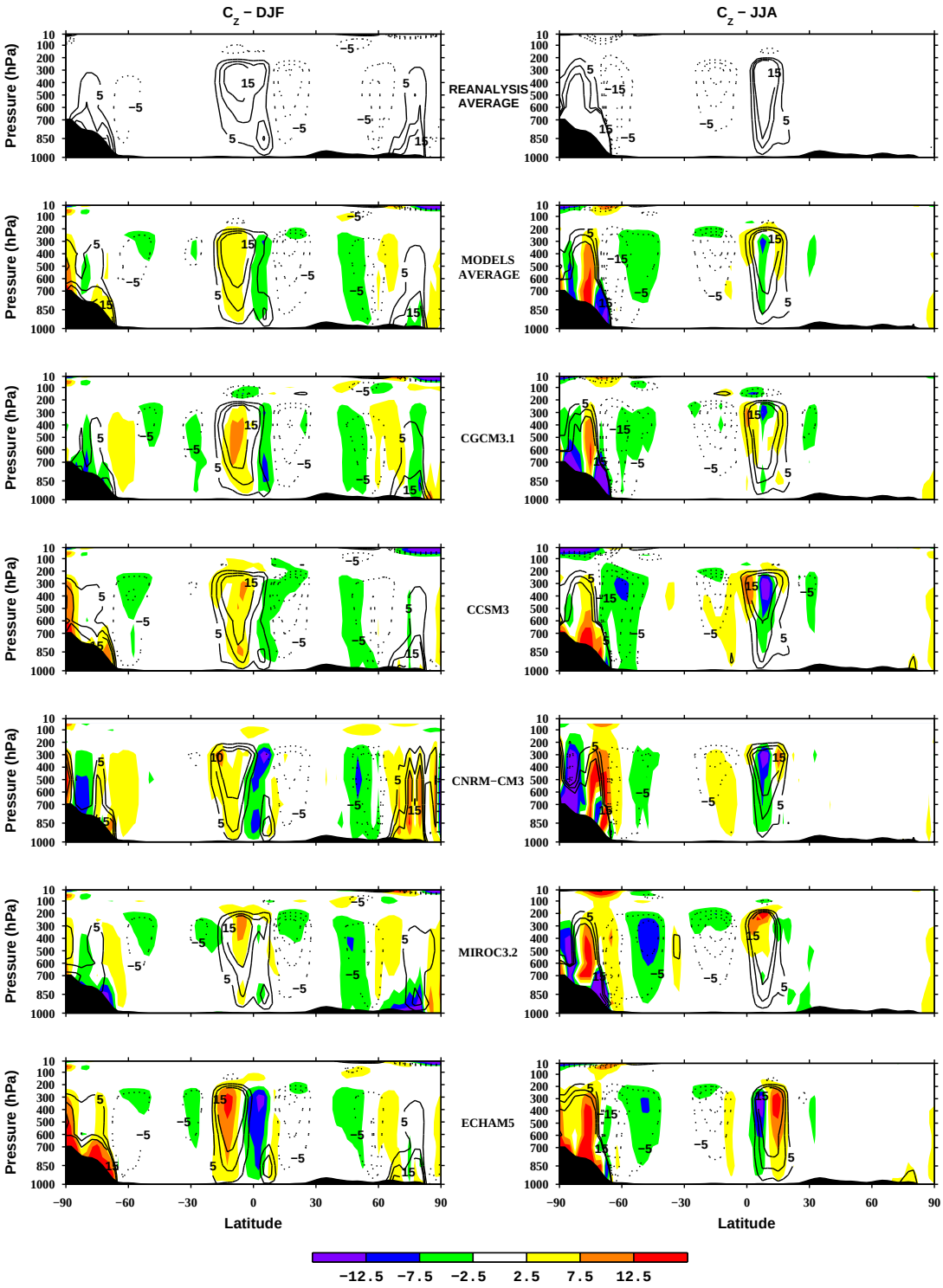

Figure 4.49: The same as in Figure 4.45, but for the conversion rate from zonal mean available potential energy to zonal mean kinetic energy, C_Z, computed with the "$\omega\alpha$" formulation.

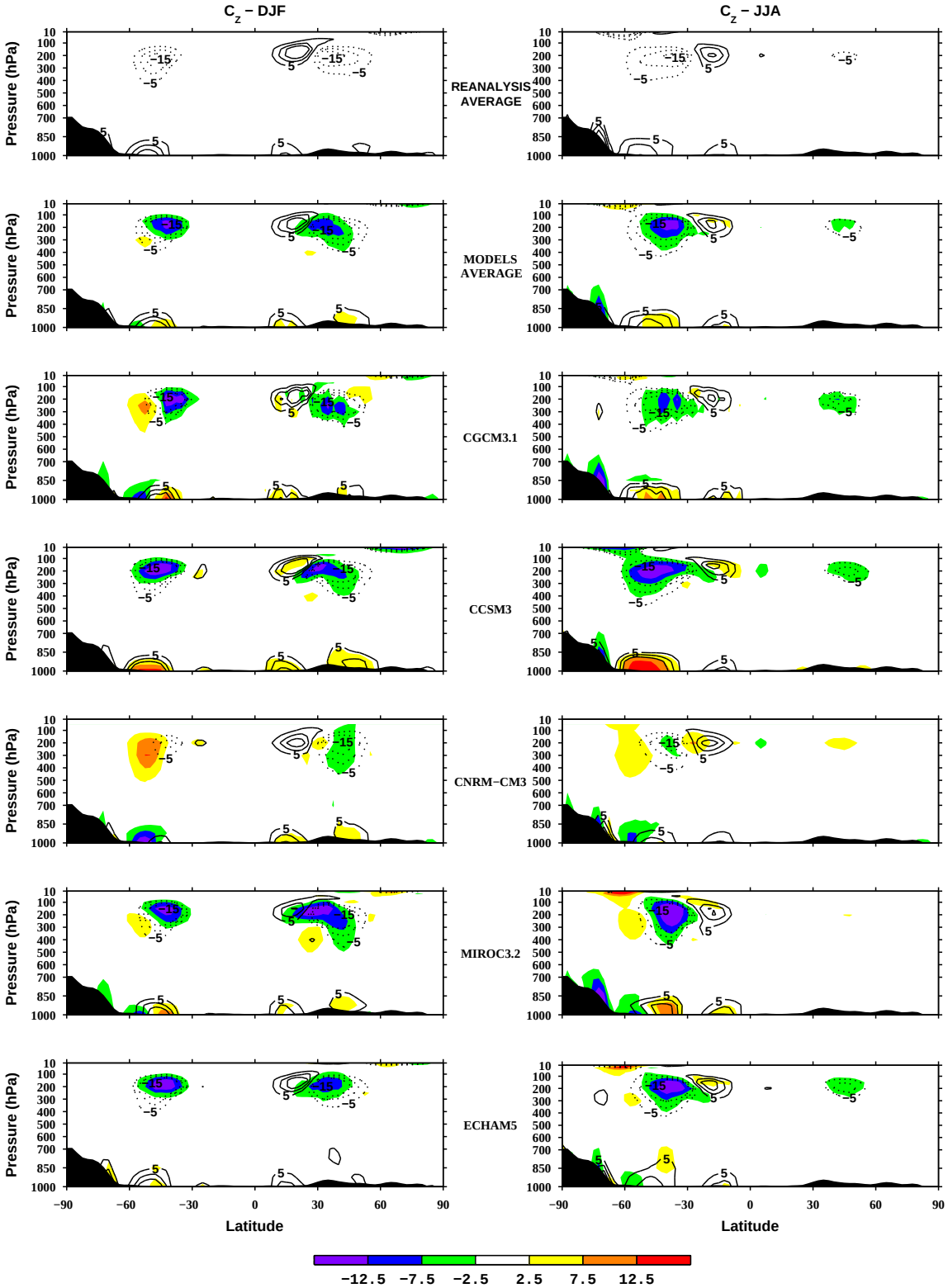

Figure 4.50: The same as in Figure 4.49, but computed with the "$\mathbf{v} \cdot \nabla z$" formulation.

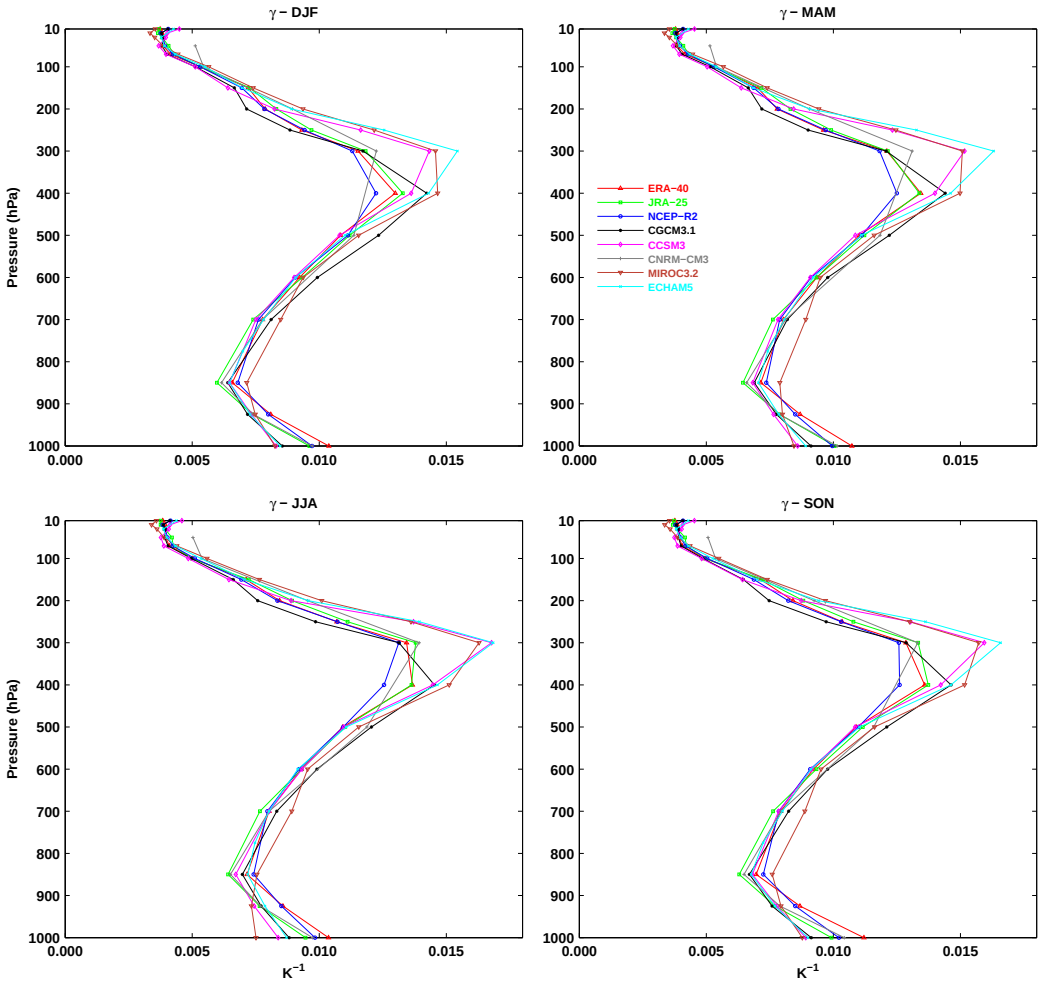

Figure 4.51: Mean vertical profile of the stability parameter, γ, for ERA-40 (red), JRA-25 (green), NCEP-R2 (blue), CGCM3.1 (black), CCSM3 (pink), CNRM-CM3 (grey), MIROC3.2 (brown) and ECHAM5 (cyan). Averages are over 1970-1999 for ERA-40 and the five models, and over 1979-1999 for JRA-25 and NCEP-R2, for all seasons: DJF (Top left), MAM (Top right), JJA (Bottom left) and SON (Bottom right). Units are K^{-1}.

4.2.2 Saltzman energy cycle

Energy levels

The shape of the available potential energy, $A(n)$, spectra is similar among the datasets in all seasons, with the CNRM-CM3 values clearly bellow those of the other datasets, although less pronounced in JJA (Figure 4.52).

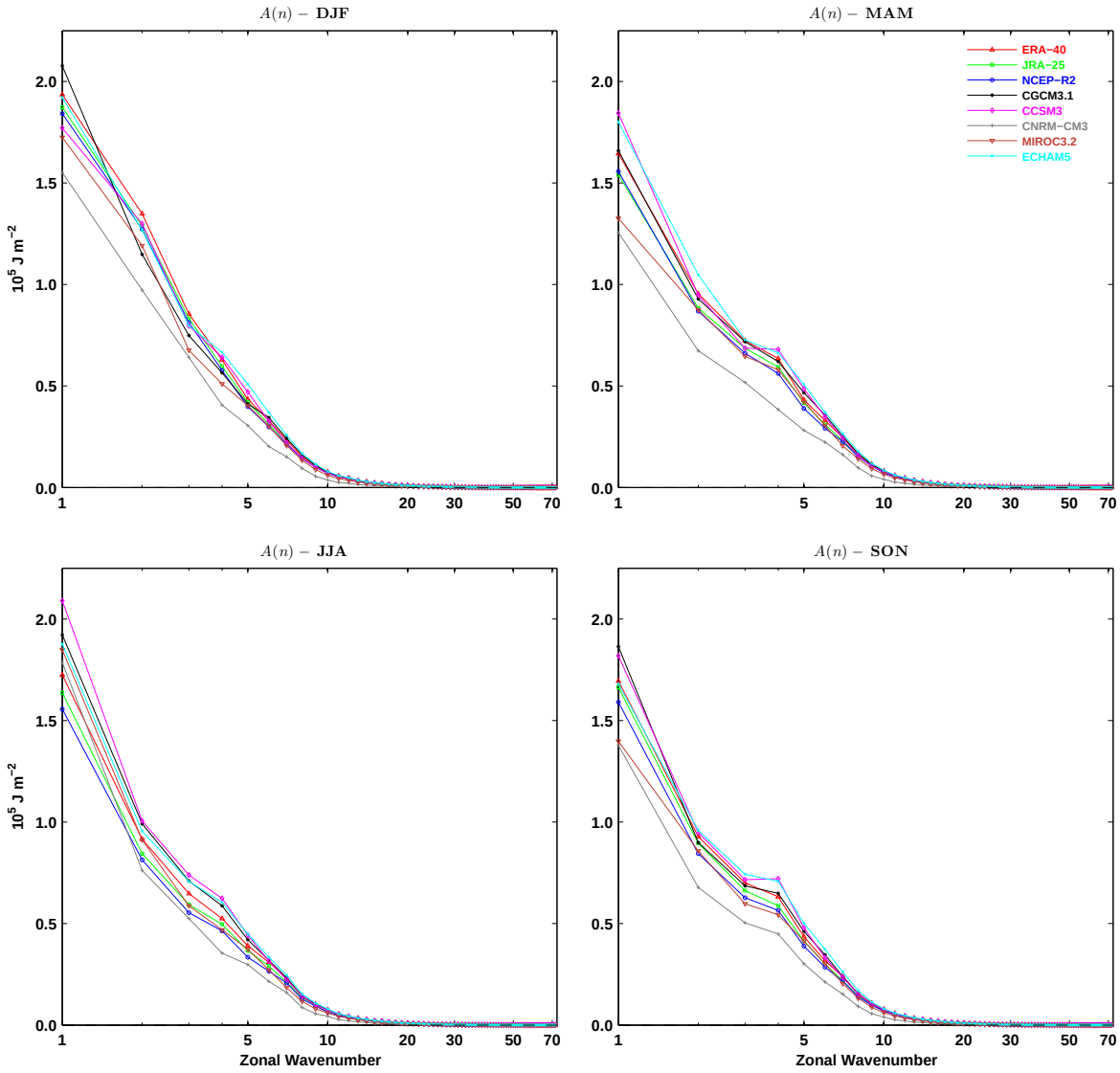

Figure 4.52: Mean wavenumber spectra of available potential energy, $A(n)$, for ERA-40 (red), JRA-25 (green), NCEP-R2 (blue), CGCM3.1 (black), CCSM3 (pink), CNRM-CM3 (grey), MIROC3.2 (brown) and ECHAM5 (cyan). Averages are over 1970-1999 for ERA-40 and the five models, and over 1979-1999 for JRA-25 and NCEP-R2, for all seasons: DJF (Top left), MAM (Top right), JJA (Bottom left) and SON (Bottom right). Units are 10^5 J m^{-2}.

Analogous features and similarities reported for the $A(n)$ spectra, may be seen in the spectra of kinetic energy, $K(n)$, represented in Figure 4.53. In a log-log scale, both spectra, $A(n)$ and $K(n)$, also follow a -3 power law beyond wavenumber 6 for reanalysis and models (not shown), in agreement with section 4.1.3.

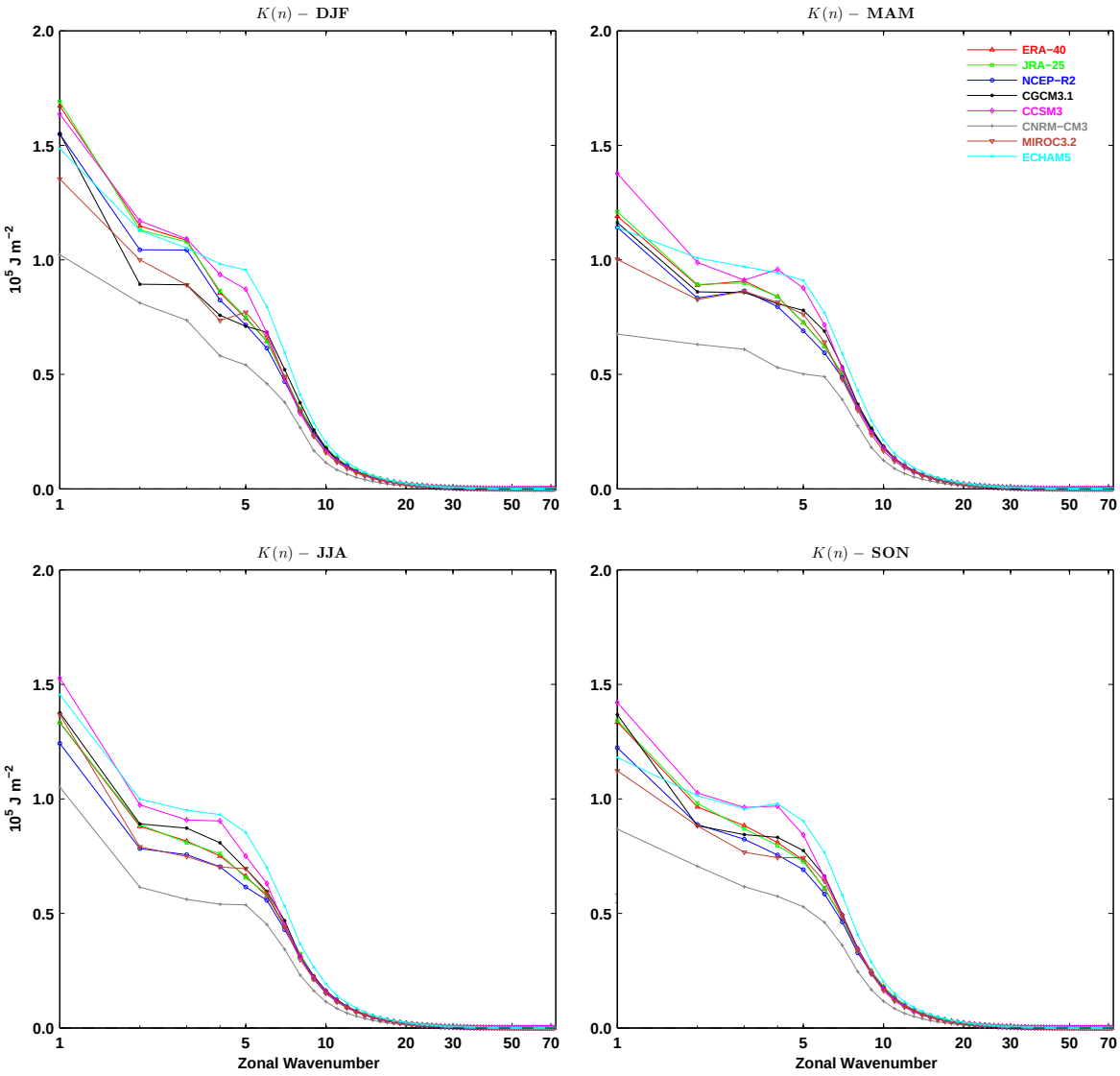

Figure 4.53: The same as in Figure 4.52, but for the spectra of kinetic energy, $K(n)$.

Energy conversion/transfer rates

The spectra for the rate of transfer of zonal mean available potential energy to the eddy available potential energy in wavenumber n, $R(n)$, are shown in Figure 4.54. Overall, the peaks and slops in these spectra of zonal-wave interactions of available potential energy agree between models and reanalysis, with just a few exceptions. In DJF, the $R(n)$ spectra peaks at the planetary-scale wavenumber $n = 3$ and secondarily at the synoptic-scale wavenumber $n = 6$, while in the other seasons it has a characteristic broad maximum at wavenumbers from about $n = 4$ to 6, included in the synoptic-scale.

On the other hand, the magnitude of $R(n)$ is generally larger in most models, specially at the synoptic-scale wavenumbers from about $n = 4$ to 10, with some exceptions in CNRM-CM3.

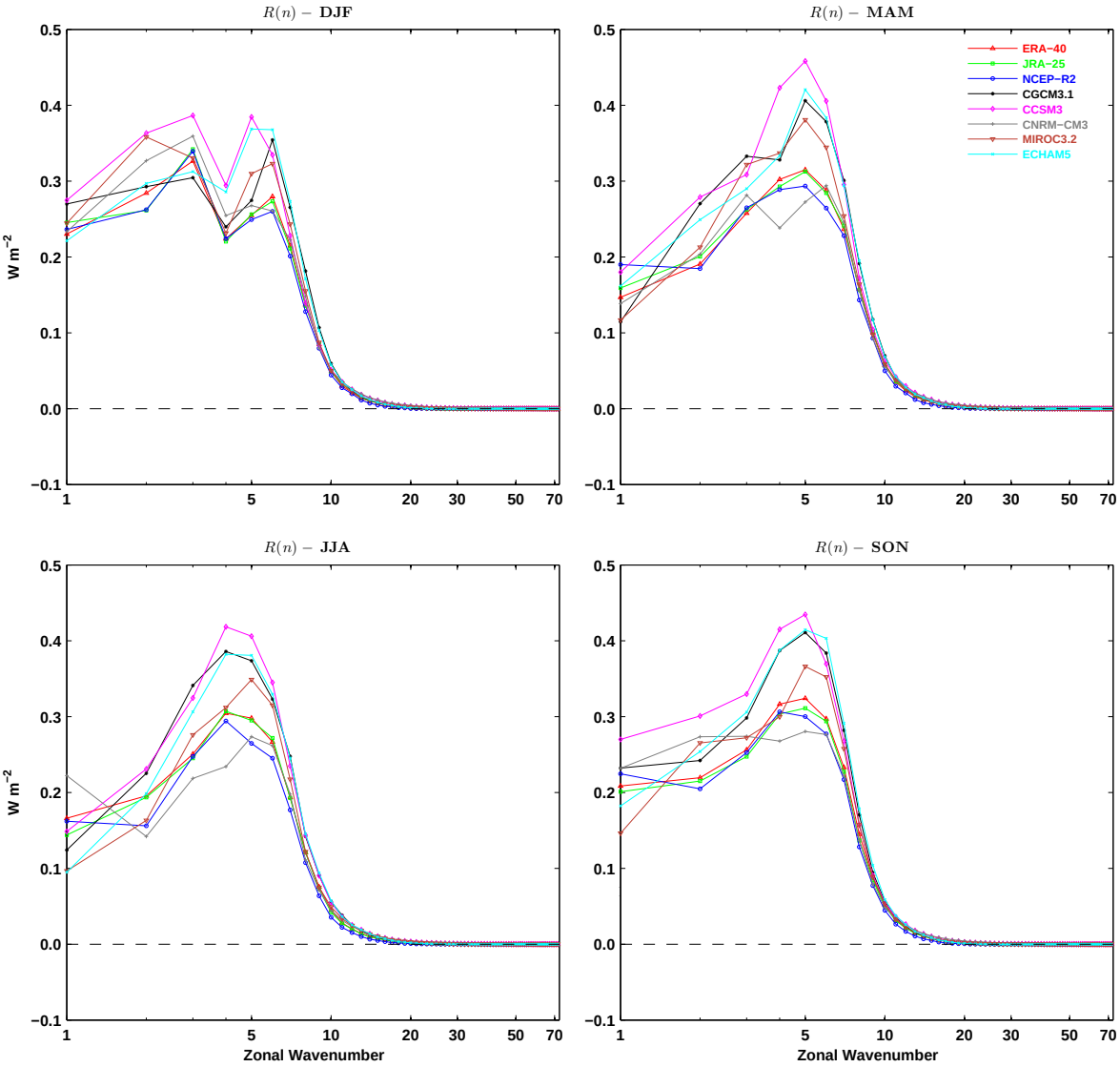

Figure 4.54: The same as in Figure 4.52, but for the spectra of zonal-wave interactions of available potential energy, $R(n)$. Units are W m^{-2}.

The spectra for baroclinic conversion of available potential energy of wavenumber n to eddy kinetic energy of wavenumber n, $C(n)$, are depicted in Figures 4.55 ("$\omega\alpha$") and 4.56 ("$\mathbf{v} \cdot \nabla z$") for all seasons. Their shape characteristics are in general common to reanalysis and models. In DJF, these spectra have maxima at $n = 1$ to 3, and at

$n = 6$, while in the remaining seasons, they peak at $n = 1$ (most notable in JJA) and have a secondary broad maximum at about $n = 4$ to 6 (Figure 4.55). Once again, the magnitude of $C(n)$ is typically larger in the models, at the synoptic-scale wavenumbers.

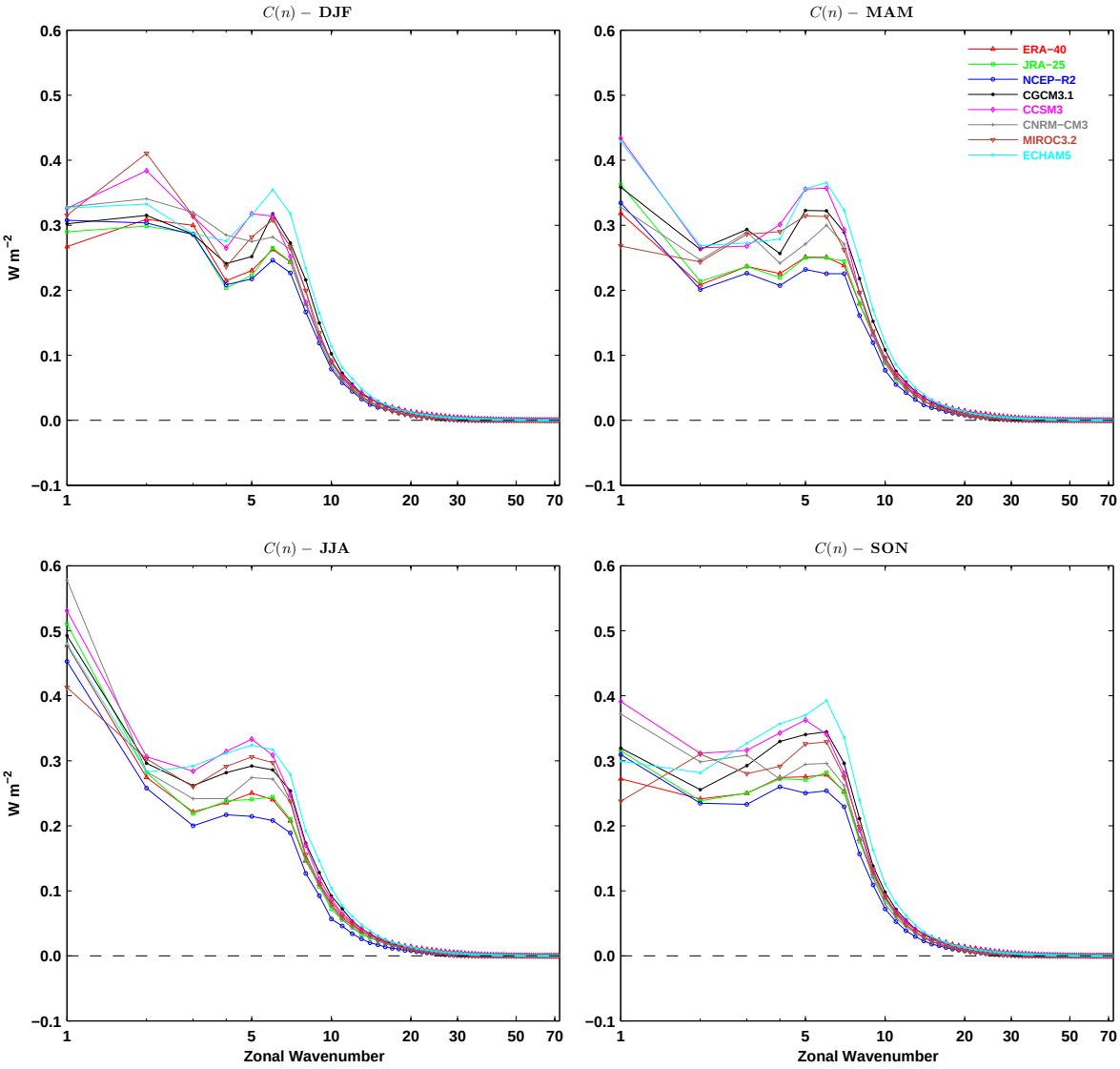

Figure 4.55: The same as in Figure 4.54, but for baroclinic conversion spectra, $C(n)$, computed with the "$\omega\alpha$" formulation.

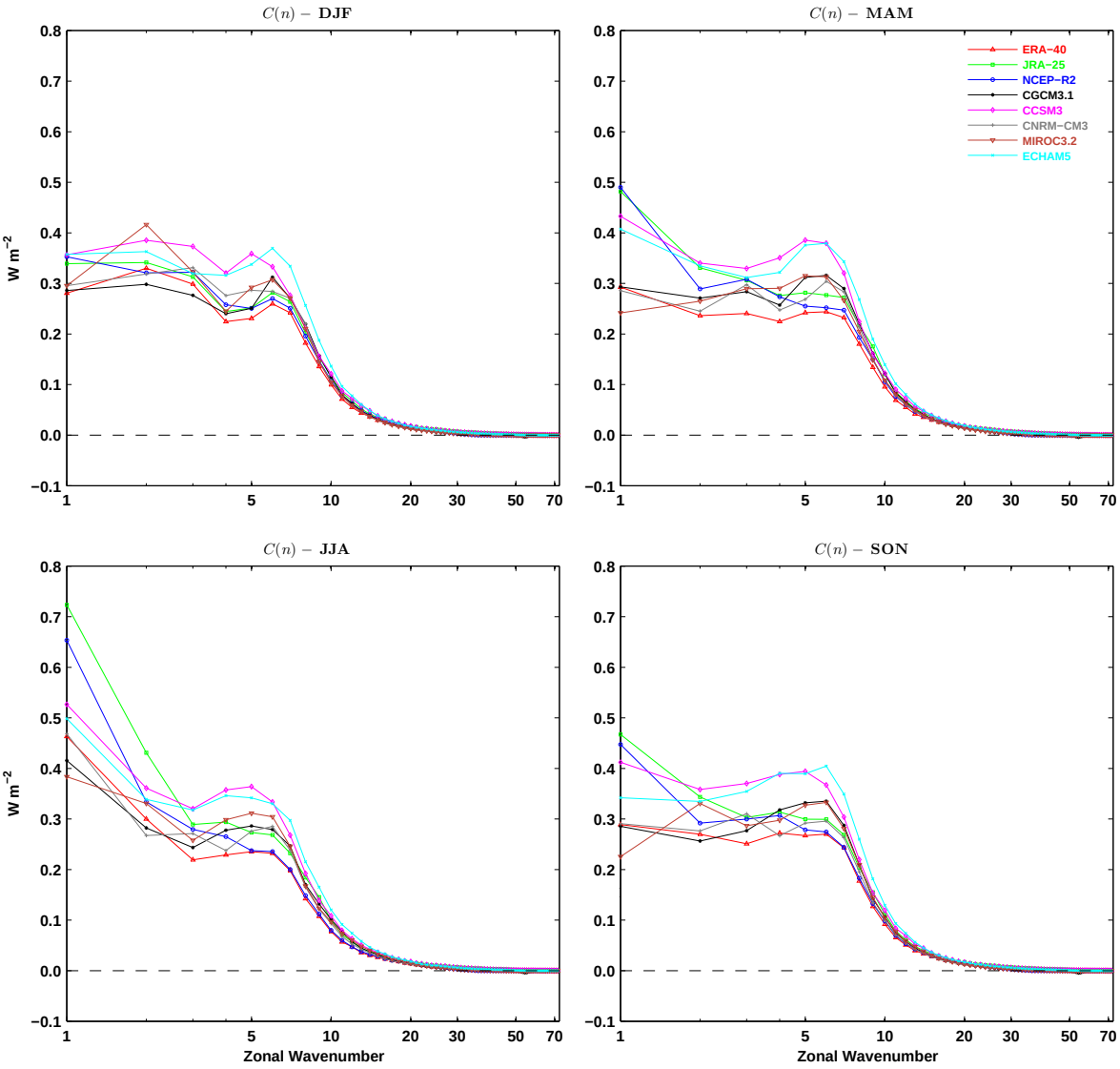

Figure 4.56: The same as in Figure 4.55, but computed with the "$\mathbf{v} \cdot \nabla z$" formulation.

Figure 4.57 illustrates the spectra of zonal-wave interactions of kinetic energy, $M(n)$. For the reanalysis, the $M(n)$ spectra have maxima at $n = 3$ and 6 in all seasons, and another maxima at $n = 1$ in MAM, SON (except for NCEP-R2) and DJF (most prominent). For the models, in addition to the generally larger magnitudes of $M(n)$ at the synoptic-scale wavenumber, again with exceptions for CNRM-CM3, the shape of these spectra seems also less well simulated. For example, the two distinct maxima in JJA are missing in all models, although this seems to improve in DJF.

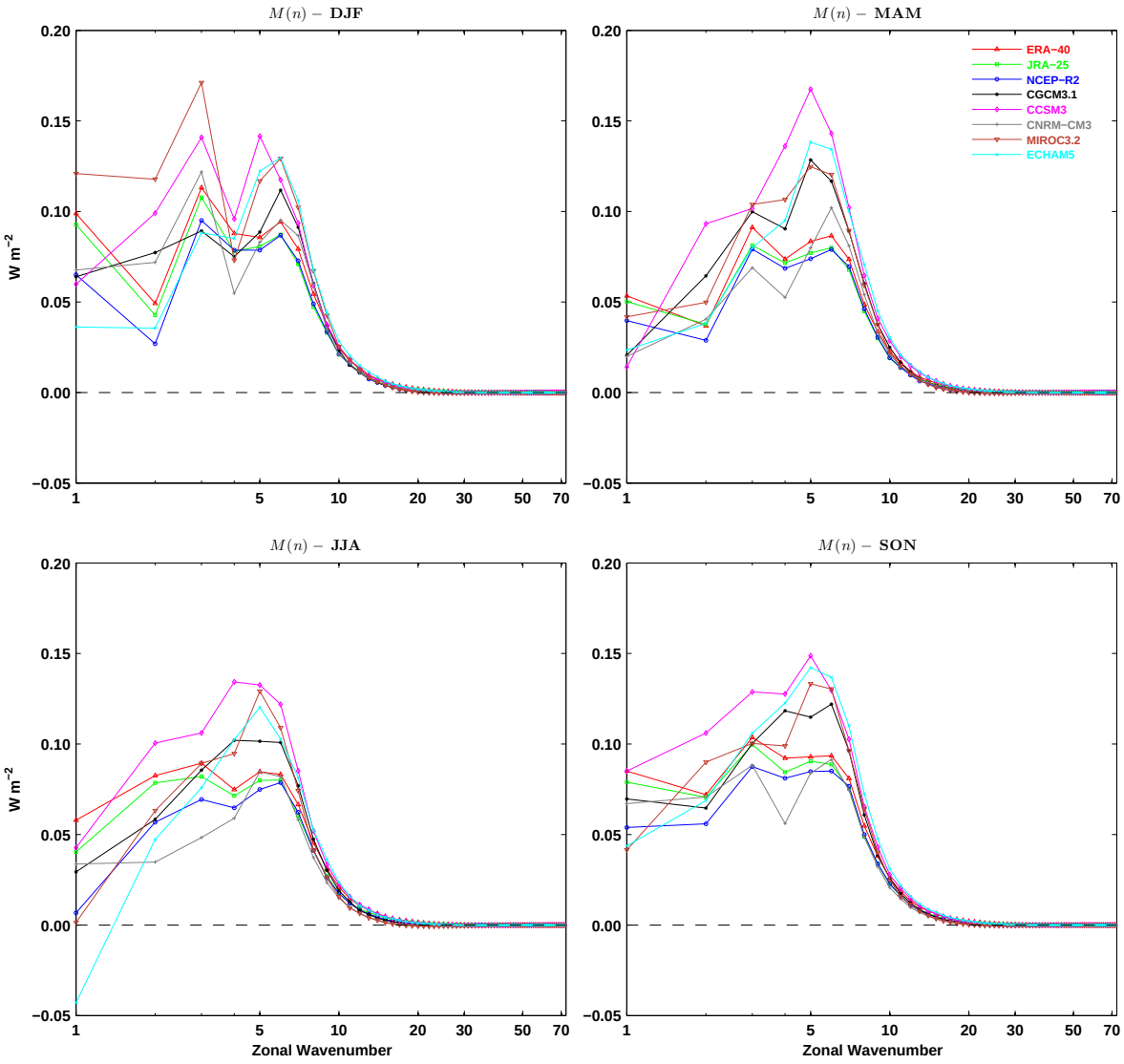

Figure 4.57: The same as in Figure 4.54, but for the spectra of zonal-wave interactions of kinetic energy, $M(n)$.

Nonlinear wave-wave interactions

The spectra for the nonlinear wave-wave interactions of available potential energy, $S(n)$, are shown in Figure 4.58. Despite the differences in the magnitude of $S(n)$ at each wavenumber, the main characteristics of these spectra in the reanalysis are also present in the models. In all seasons, $S(n)$ is negative at wavenumbers in the range of about $n = 2$ to 7 (and also $n = 1$ in DJF for all reanalysis and model CGCM3.1), indicating that energy is transferred from the eddies in this range to smaller eddies, prevailing the

flux associated with the downscale energy cascade, and also to $n = 1$ (specially in MAM and SON), forming an upscale energy cascade. The synoptic waves transfer important amounts of available potential energy for the smaller waves, particularly during MAM and SON, which is generally excessive in the models.

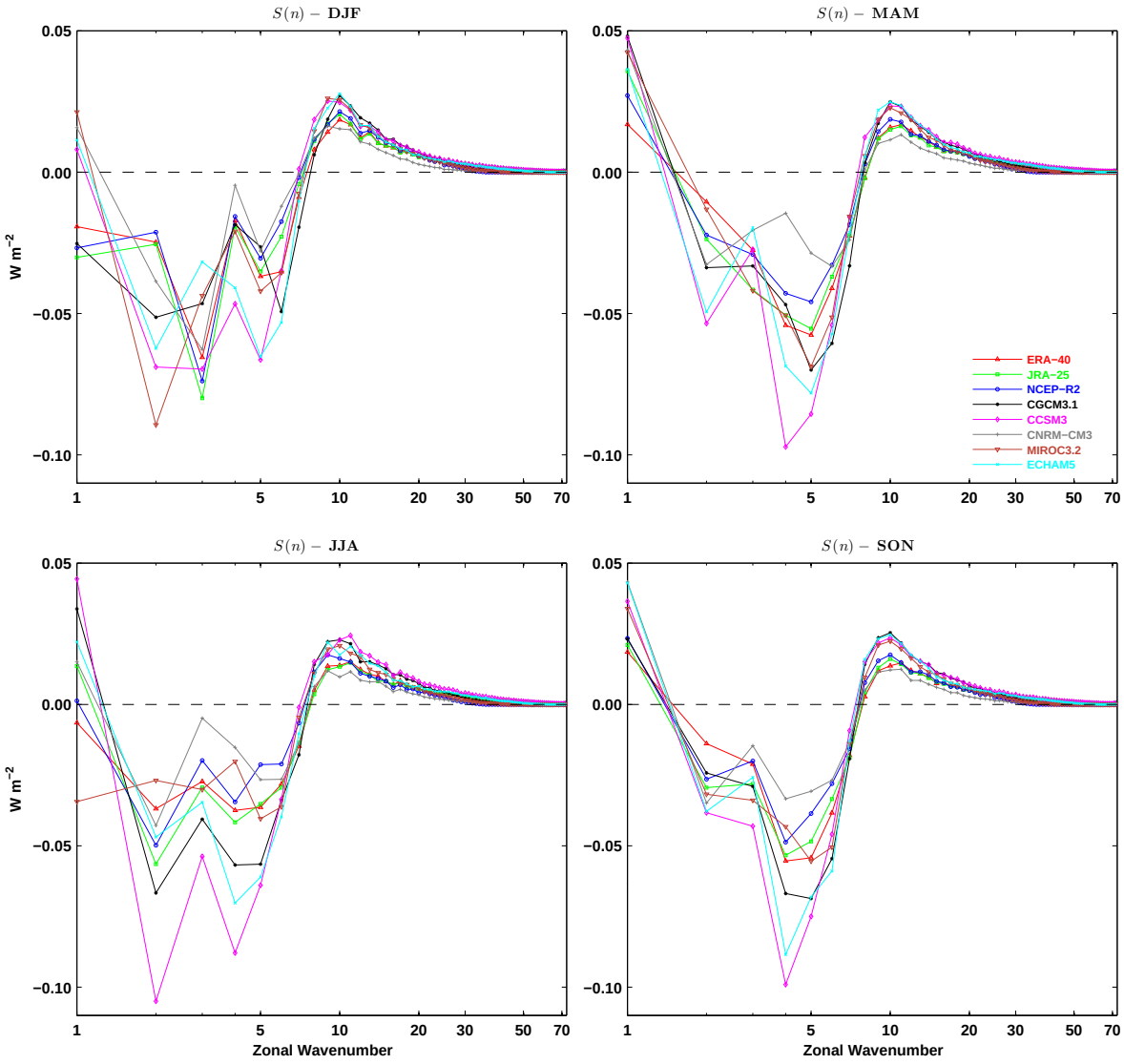

Figure 4.58: The same as in Figure 4.54, but for wave-wave interactions of available potential energy spectra, $S(n)$.

Figure 4.59 illustrates the spectra of nonlinear wave-wave interactions of kinetic energy, $L(n)$. Overall, the shape of this spectra is similar between models and reanalysis in all seasons. A few discrepancies are also evident such as those at wavenumbers 3 and

4 for CNRM-CM3. The $L(n)$ spectra is generally positive at both the planetary-scale and short-scale wavenumbers, being negative at intermediate wavenumbers, including the synoptic scale. Hence, the transfer of kinetic energy is from the spectral region of negative $L(n)$ to the planetary waves, forming an upscale energy cascade, and to the short waves, forming a downscale energy cascade. The spectral range of this energy source region is different among the various datasets, probably as a consequence of the different native horizontal and vertical resolutions.

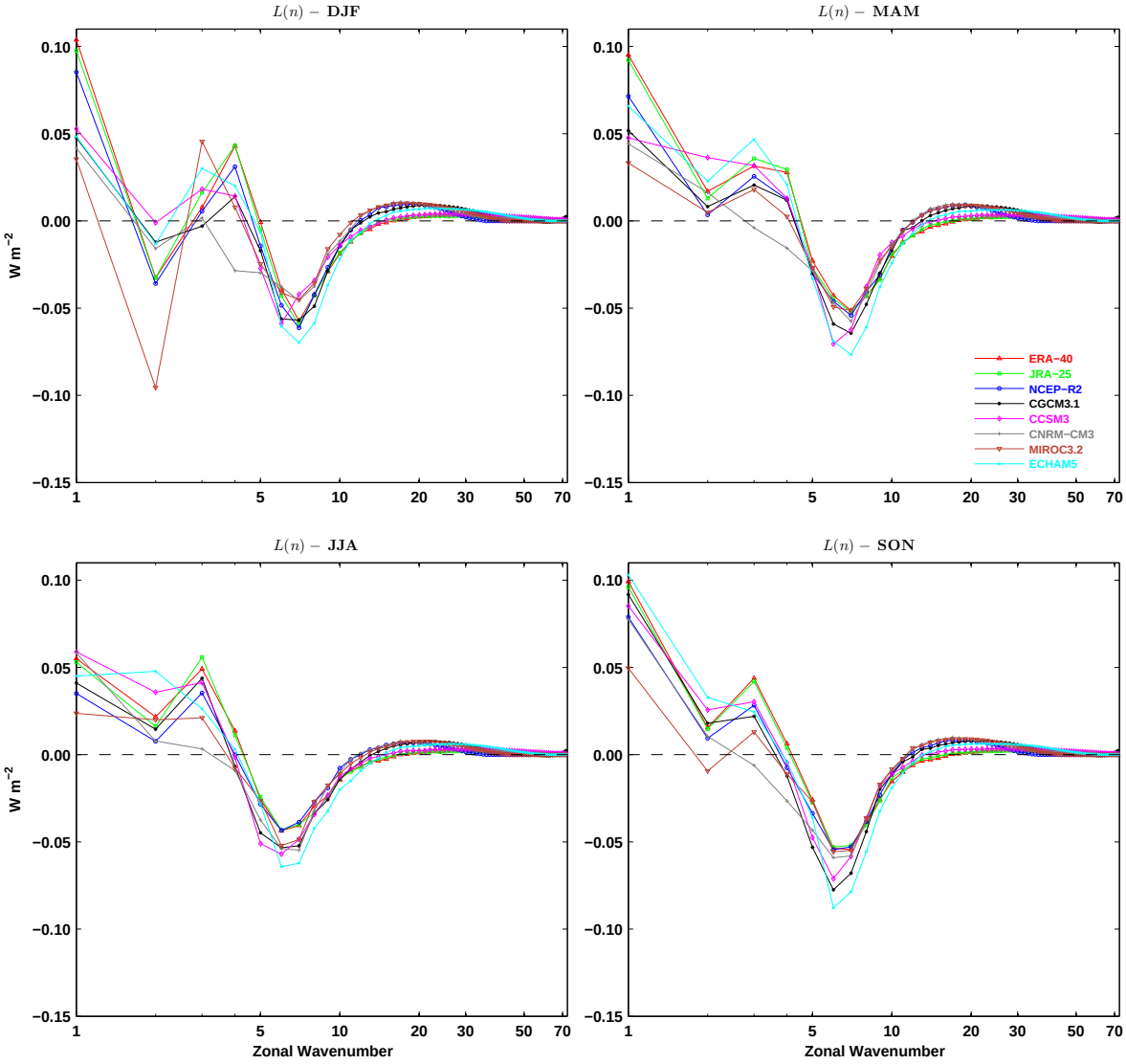

Figure 4.59: The same as in Figure 4.54, but for wave-wave interactions of kinetic energy spectra, $L(n)$.

It should be remarked that 6-hourly data for model CNRM-CM3 was only available at 9 pressure levels, and some of the unavailable pressure levels, as the 250 hPa and 400 hPa, have important contributions to the global integrals of some energetics quantities. Hence, the energy cycle computations for this model were restricted by a smaller number of pressure levels data compared to the other datasets. This may have influenced the results to be in "favour" of the model in some cases (i.e. leading to a smaller difference between the model-based estimates and those based in the reanalysis) and in other cases to be "against" the model (i.e. increasing the difference between the model and reanalysis energetics). For example, the stronger positive contributions for $L(3)$ in JJA and for $L(4)$ in DJF are found at 250 hPa for most models and reanalysis (not shown). This may explain part of the discrepancies in $L(n)$ at wavenumbers 3 and 4 for CNRM-CM3. On the other hand, the strong contributions for A_Z present in all other models and reanalysis at 400 hPa, would lead to even more excessive A_Z in CNRM-CM3 if the 400 hPa data was available and used.

Test experiments (not shown) have confirmed that all the conclusions based on the above results remain essentially the same if the analysis is restricted to the period 1979-1999, and also if the evaluation for the models is performed on the original Gaussian grid. The later couldn't be confirmed for the reanalysis, since the reanalysis data was not available on the native grid.

In general, the results presented here for the classic energy cycle of Lorenz show that the distributions in the integrands are reasonably well simulated by the models in a qualitative sense, when compared to the reanalysis. However, in addition to some contributions in the models' integrands being somewhat displaced, as is the case for those related to the tropospheric jets, the magnitude of the distributions in the integrands is generally greater in the models, resulting in larger quantities of energy and an overactive energy cycle. Accordingly, the magnitude of the various energy and energy conversion/transfer spectra is generally excessive in the models, specially at the synoptic-scale wavenumbers from about $n = 4$ to 10, although the shape of most spectra agree reasonably well between models and reanalysis.

The temperature cold bias and the too strong tropospheric jets, along with the jets' shifts in some cases, constitute some of the main deficiencies in the models simulations which are directly implicated in their excessive energy and too vigorous energy cycle. Improving these deficiencies should lead to significant benefits in the energy cycle of the models. Reducing the temperature cold bias should decrease A_Z and G_Z, leading also to a weaker meridional temperature gradient, that should reduce C_A. Weakening the jets and improving their position, should reduce both K_Z and C_K.

Various sensitive studies show that increasing horizontal resolution leads to a warming of the troposphere, predominantly at mid-latitudes, and to a poleward shift and intensification of the westerly jets (e.g. Déqué et al. (1994); Williamson et al. (1995); Stratton (1999); Pope and Stratton (2002); Roeckner et al. (2006)), while increasing vertical resolution leads to an increase in the upper-tropospheric and stratospheric temperatures and to a equatorward shift and weakening of the westerly jets (e.g. Pope et al. (2001); Stratton (2004); Roeckner et al. (2006)). High vertical resolution has also been shown to be specially important on the simulation of the tropical climate and its variability (Hamilton et al. (1999); Ruti et al. (2006)). The Hadley circulation can also be sensitive to resolution. Pope et al. (2001) reported a slight weakening of the Hadley circulation and less extending into the stratosphere with increased vertical resolution, and thus should be reflected in C_Z and C_E.

These results seem to indicate some improvements in the models' simulations as a result of refining both horizontal and vertical resolution, that is in agreement with the arguments of Lindzen and Fox-Rabinovitz (1989), which, on the basis of quasi-geostrophic theory, advocate a consistent choice of vertical and horizontal resolution for a proper representation of horizontal and vertical scales. However, it is also apparent that increasing the vertical resolution has the opposite effect to that of increasing the horizontal resolution (Roeckner et al., 2006), at least with respect to the tropospheric jets. For example, the cross-sections of A_Z and K_Z for models CCSM3 and ECHAM5 indicate a temperature bias in upper troposphere/lower stratosphere and too strong westerly jets. Therefore, according to the aforementioned sensitive stud-

ies, models CCSM3 and ECHAM5 can improve with increased vertical resolution, that should reduce the temperature bias and weaken the jets, but the consequent equatorward shift of the westerly jets can also deteriorate these models' simulations. On the other hand, the same cross-sections for models CGCM3.1 and CNRM-CM3 indicate a predominant temperature bias in the troposphere and also too strong jets shifted equatorwards. Hence, increasing horizontal resolution may help to improve the temperature bias and shift the jets poleward, but may also enhance the jets which are already too strong. As for model MIROC3.2, it is not clear that increasing both horizontal and vertical resolutions will improve its energetics, once more due to the opposite effects achieved by refining both spatial resolutions.

This suggest that improvements in the energy cycle of the models are not straightforward achieved by simple increasing their horizontal and vertical resolutions, unless there exists some optimal balance between the two resolutions that needs to be found, which is currently not evident. Therefore, it seems inevitable that attention should be given to improve fundamental aspects of the climate models, such as the numerical schemes, physics parameterisations and resolution dependence of parameterisations. For example, Pope et al. (2001) showed that the behaviour of the convection scheme in the Hadley Centre Atmospheric Climate Model version 3 (HadAM3) is sensitive to the position and number of model levels. In experiments with the same model, Pope and Stratton (2002) also report changes in the energetics of both the full and dynamical core models by increasing horizontal resolution, in line with the results of Boer and Denis (1997), in experiments with the CCCma second generation Coupled Global Climate Model (CGCM2), using the Held and Suarez forcing (Held and Suarez, 1994). Both these studies showed that the level of convergence in the models energetics may depend partly on the model physical parameterisations and not entirely on the model dynamics, implying that the simulated climate depend on the ability to correctly and consistently parameterise the physical processes in a climate model as a function of resolution.

By analysing the Lorenz energy cycle of 12 atmospheric models participating in AMIP2 (the second phase of AMIP1 (the first Atmospheric Model Intercomparison Project)), Boer and Lambert (2008) also reported an energy cycle too strong simulated by those models. They suggest that excessive generation of zonal mean available potential energy, G_Z, and excessive dissipation of eddy kinetic energy, D_E, in the models, are implicated on the overactive energy cycle, through what they termed as "generation push" and "dissipation pull", respectively. The basic reasoning is that too large G_Z "pushes" more energy into the available potential energy side of the energy cycle, increasing both A_Z and its transfer rate to A_E, while too large D_E weakens K_E which "pulls" more energy from A_E via C_E, being A_E maintained by too large G_E and C_A. Boer and Lambert (2008) suggest, therefore, that decreasing both G_Z and D_E would improve the models energy cycle, and hence, efforts should be made to improve the physical processes controlling G_Z and D_E in models. For example, the study of Kunz et al. (2008) show that the kinetic energy dissipation may be reduced by increasing the horizontal diffusivity which reduces the amplitude and efficiency of the large scale eddies.

Overall, the results in this study (see also Marques et al., 2010b) agree with those of Boer and Lambert (2008), and consequently seem to support their "generation push" and "dissipation pull" hypothesis. Moreover, the generation and dissipation terms have been computed indirectly as residuals from the balance equations and, hence, their values are strongly dependent on the estimates for the conversion/transfer rates terms (C_A, C_E, C_K and C_Z), which are computed directly from the atmospheric data. As the models are devised to conserve energy, the processes controlling the generation, dissipation and the conversion/transfer rates terms should be closely related. Therefore, since the models show excessive energy conversion/transfer rates typically at the synoptic-scale wavenumbers (Figures 4.54 to 4.59), the synoptic-scale processes should be of significant importance also for the generation and dissipation terms.

Global energetics analysis in the wavenumber domain has been performed by Hasegawa et al. (1997) for the NCAR CCM2 model with different horizontal resolutions

(R15, T42, T63 and T106) and 18 vertical levels. They found no evidence that a high resolution model is allways better than the low resolution model, although it was generally found a better agreement with the observationally based energetics for the higher resolution models. An important finding in Hasegawa et al. (1997) is the downscale energy transfer beyond wavenumber 30 for the zonal-wave interactions of kinetic energy, which led them to suggest T42 as the minimum resolution required for a sufficient two-way interaction between eddies and zonal motion. Accordingly, resolution R15 is clearly inadequate for climate simulations from the viewpoint of energetics. In JJA, the observed upscale energy cascade for the wave-wave interactions of kinetic energy was only reproduced in T106 model, being missing in both T42 and T63 models. There is also in JJA a double jet structure in the SH meridional distribution of zonal mean kinetic energy associated with the subtropical and polar frontal jets, which is totally missing in T42 model but improves in the higher resolution models, specially in the T106 model. This double jet structure observed in JJA also reflects that the stratospheric polar night jet of SH extends downward and is connected with the polar frontal jet, while its NH counterpart in DJF does not extend to low levels.

All models (and reanalysis) in this study show the downscale energy transfer for the zonal-wave interactions of kinetic energy, although the wavenumber beyond which this energy transfer occurs varies with the dataset. Most models also show the upscale energy cascade for the wave-wave interactions of kinetic energy, specially in JJA. The downward extension of the SH polar night jet in JJA is clearly seen only in models CCSM3 and CGCM3.1, although being too strong in CCSM3 (Fig. 4.43). Accordingly, the SH double jet structure in the meridional distribution of zonal mean kinetic energy (not shown) is only present in those two models.

4.2.3 Normal mode energetics

In this section, the energetics of the global atmosphere in the climate models is assessed against that in the three reanalysis, by using the normal mode energetics scheme. It is recalled that model CNRM-CM3 was excluded from the normal mode energetics analysis, due to the small number of pressure levels data available for this model. The results are displayed in analogous Figures to those of section 4.1.3, with the various spectra presented separately for the barotropic and baroclinic vertical modes, and for the Rossby and gravity meridional modes.

Energy levels

Figure 4.60 shows the wavenumber spectra of total energy, E_{nlk}, for the three reanalysis and four climate models in DJF, with the separations into barotropic-baroclinic and Rossby-gravity modes presented as in Figure 4.26. It is seen that the basic characteristics in the spectra of E_{nlk} for the models, such as their power law behaviour, agree to those for the reanalysis, excluding the higher wavenumbers, say $n \gtrsim 30$. Discrepancies are seen at the tail of the spectra, in which the energy decreases more rapidly for the lower horizontal resolution models, MIROC3.2 and CGCM3.1, than that for the higher resolution models, ECHAM5 and CCSM3. The rapid decrease at higher wavenumbers was found similarly for NCEP-R2, which has a native horizontal resolution (T62) close to that of ECHAM5 (T63), and should be due to data filtering/smoothing (see section 4.1.2).

The energy distributions for the Kelvin and mixed Rossby-gravity modes are shown in Figure 4.61. Overall, the spectral peaks of these two modes in the models agree with those in the reanalysis for both the zonal wavenumber and vertical mode domains. However, from zonal wavenumber $n \simeq 10$ onwards, the spectra of these two particular modes decrease slower in the models than in ERA-40 and JRA-25, and therefore have more energy, but decrease faster in the models than in NCEP-R2, and therefore have less energy. The energy level of the gravity modes is sensitive to the atmospheric ageostrophic components, while that of the (rotational) Rossby mode is sensitive to the

geostrophic components. It seems therefore that, the ageostrophic components in the models' atmosphere are stronger than those of ERA-40 and JRA-25 and weaker than those of NCEP-R2. The minimum seen in the first baroclinic mode ($k = 1$) of the Kelvin mode of ERA-40 and JRA-25, is not present in both the NCEP-R2 reanalysis and the climate models.

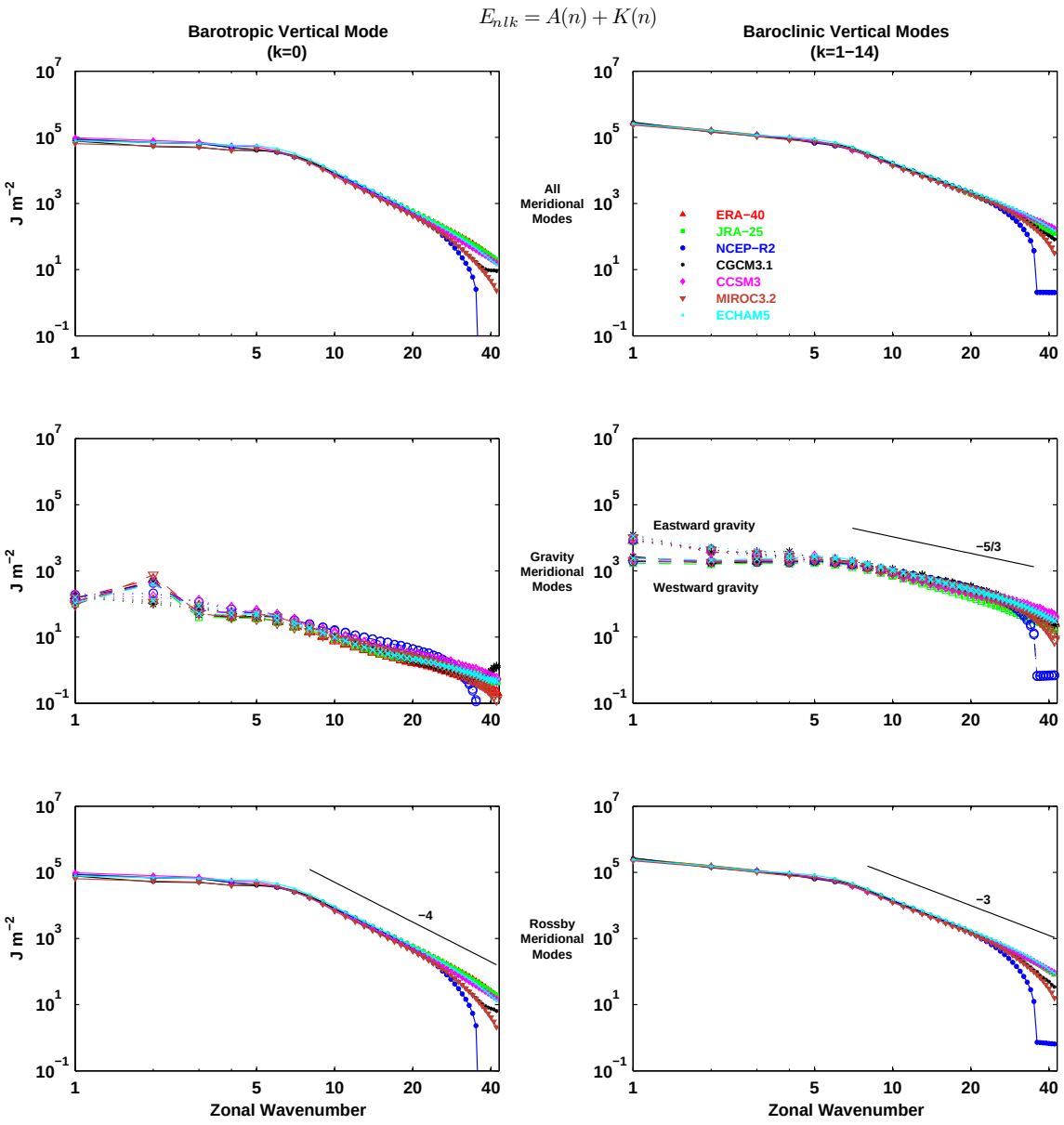

Figure 4.60: As in Figure 4.26, but for both the three reanalysis and four climate models.

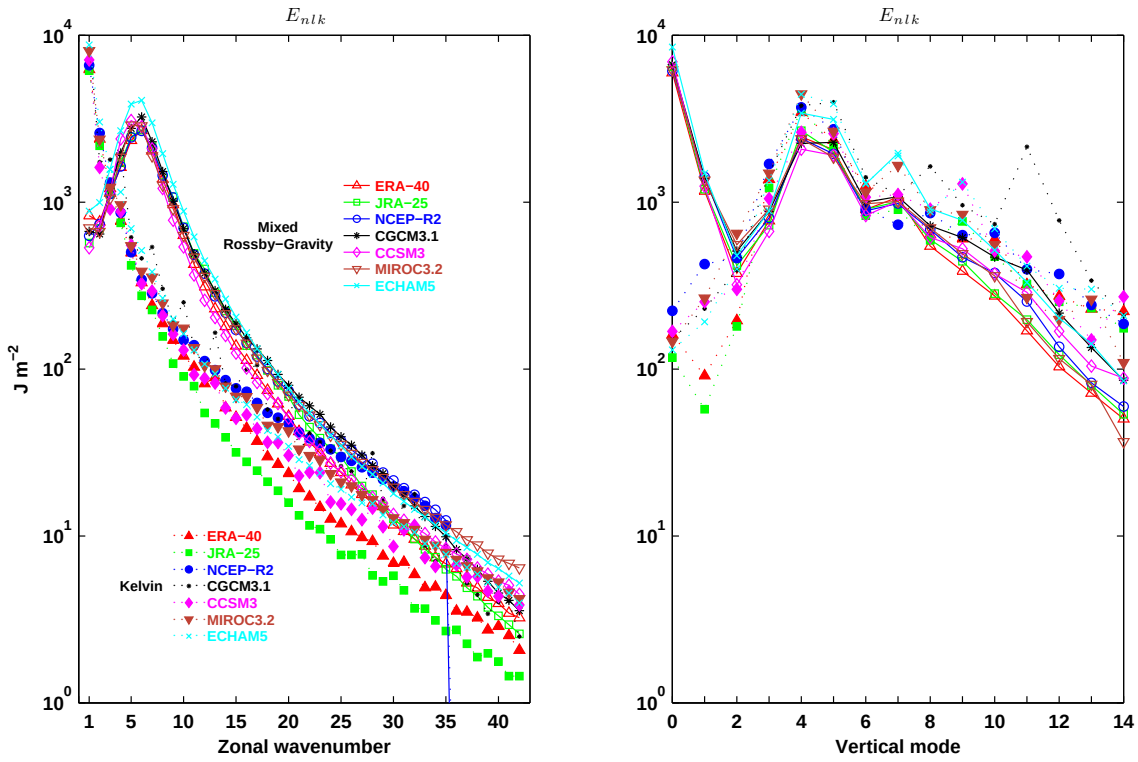

Figure 4.61: As in Figure 4.27, but for both the three reanalysis and four climate models.

The wavenumber spectra of available potential energy, $A(n)$, and kinetic energy, $K(n)$, are depicted in the left and right panels of Figure 4.62, respectively. As for the spectra of E_{nlk}, the basic characteristics of the $A(n)$ and $K(n)$ spectra are common to reanalysis and models, excluding the higher wavenumbers. Namely, both energy spectra follows the -3 power law for the baroclinic modes, whereas the spectra of $K(n)$ follows the -4 power law and the spectra of $A(n)$ follows approximately the -5 power law for the barotropic mode.

Figure 4.63 shows the total energy spectra in the vertical mode domain. The maximum at $k = 5$ and the secondary maximum at the barotropic mode ($k = 0$) found in the reanalysis (Figure 4.29) for both the Rossby and gravity modes of the zonal mean component, is also present in the climate models. For the Rossby modes of the eddy component, the energy spectra peaks at the barotropic mode, with another peak at the baroclinic mode $k = 5$, whereas for the gravity modes the maximum energy is found at $k = 4 - 5$, which is also in agreement between models and reanalysis. Therefore,

it may be concluded that the main features of the total energy spectra in the vertical mode domain are similar amongst the reanalysis and climate models for both the zonal mean and eddy components, and for the gravity and Rossby modes. The differences found are essentially related to the magnitude in these spectra at some vertical modes, and mainly for the zonal mean component, which shows a somewhat larger dispersion among the datasets than that for the eddy component.

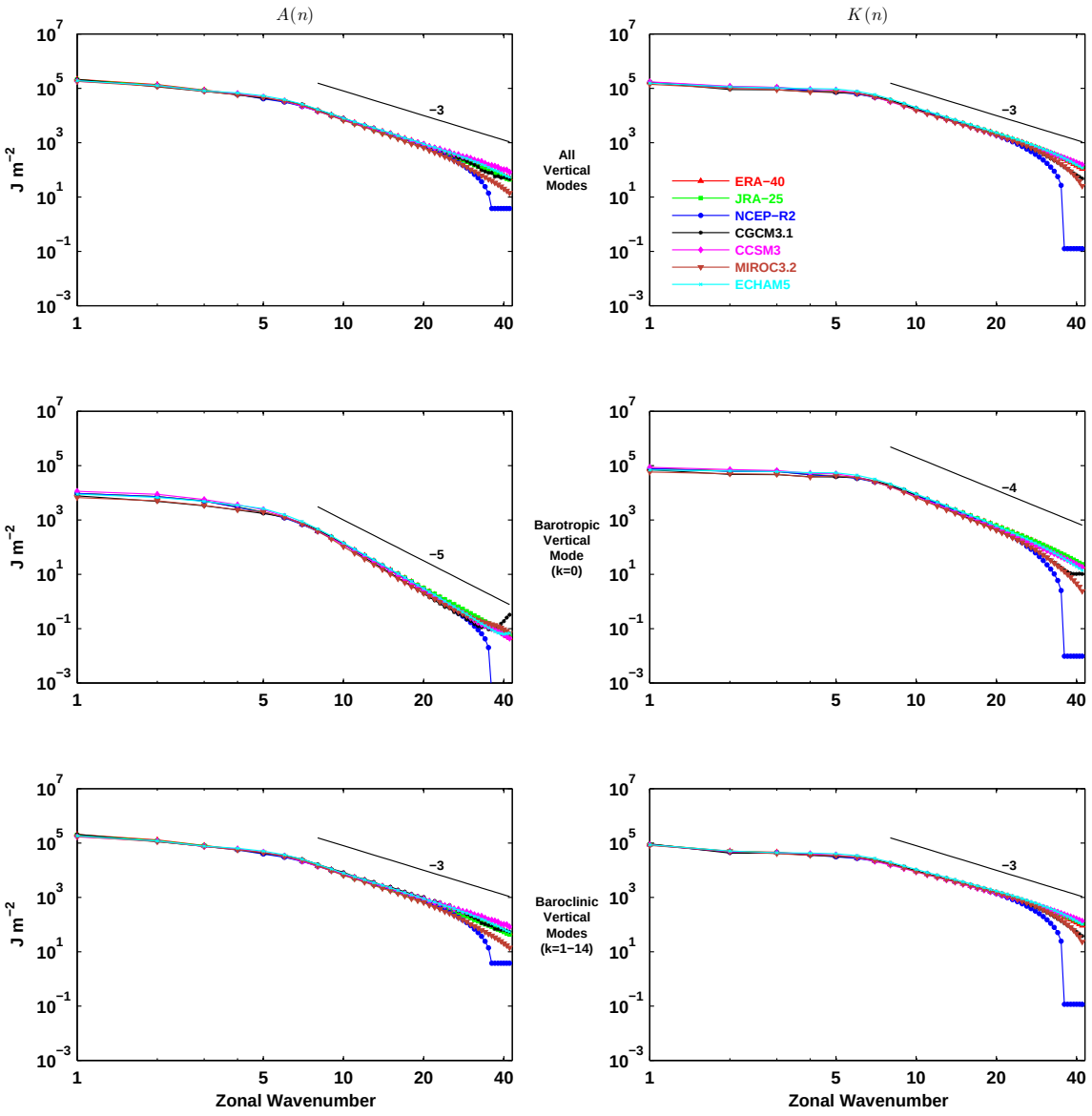

Figure 4.62: As in Figure 4.28, but for both the three reanalysis and four climate models.

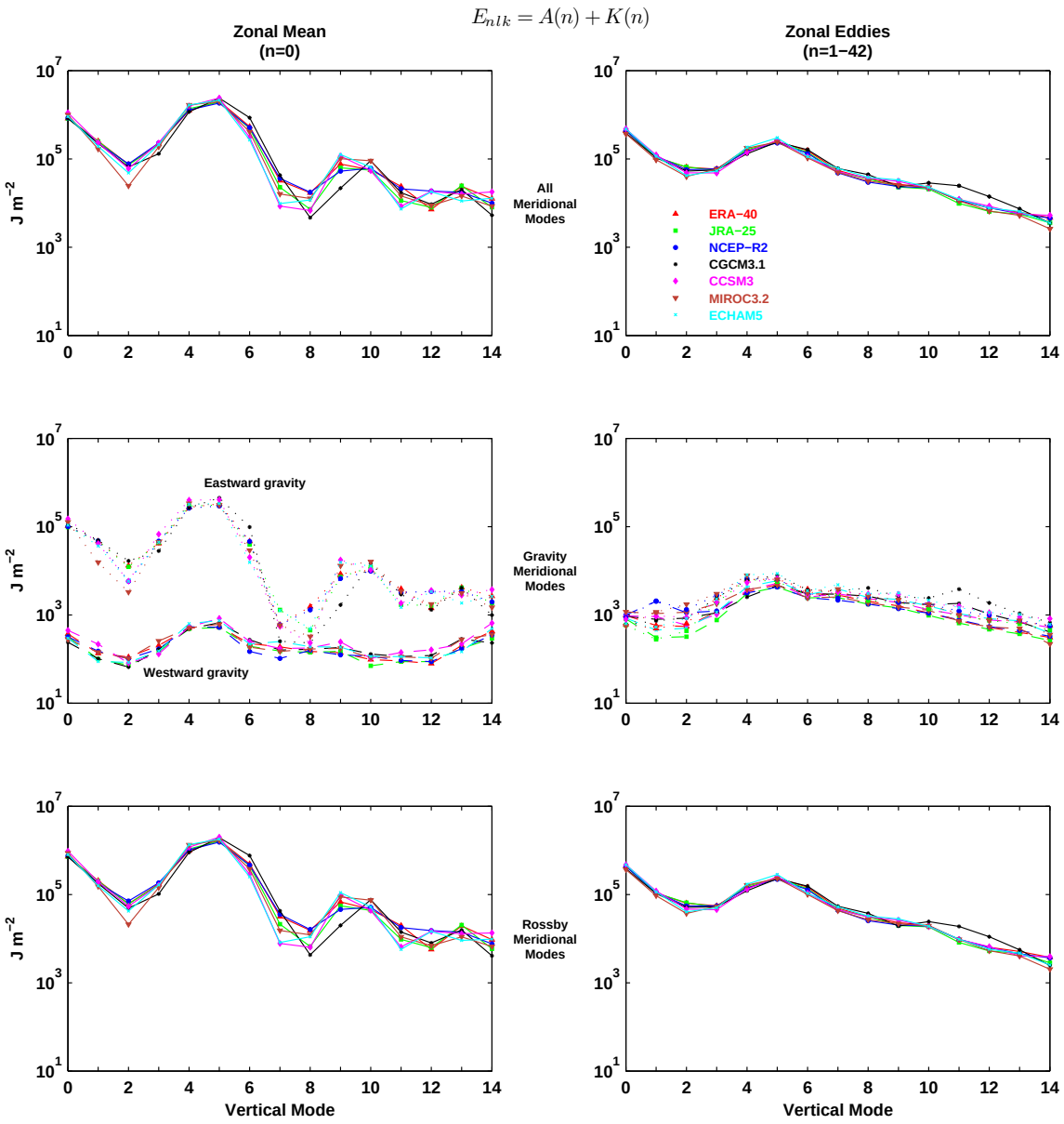

Figure 4.63: As in Figure 4.29, but for both the three reanalysis and four climate models.

Figure 4.64 shows the spectra of available potential and kinetic energies for the zonal mean and eddy components, $A_Z(k)$, $A_E(k)$, $K_Z(k)$ and $K_E(k)$. Once again these spectra are similar between the reanalysis and climate models. In all datasets, the spectra of available potential energy shows a maximum at $k = 5$ for both $A_Z(k)$ and $A_E(k)$, with the later an order of magnitude smaller than that of the former, and another peak at $k = 0$ for $A_Z(k)$. Most of the kinetic energy is included at the barotropic mode for both

the zonal mean and eddy components, with a secondary peak at $k = 4 - 5$.

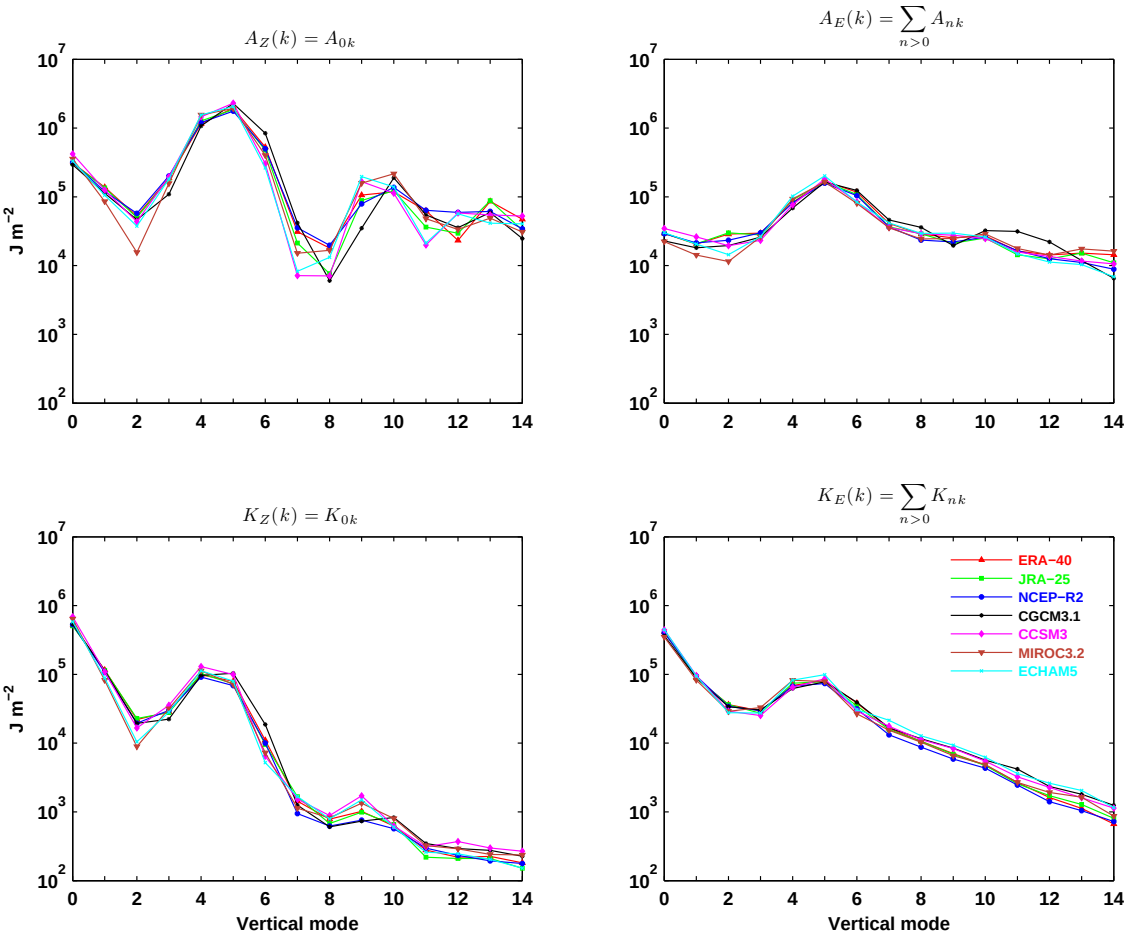

Figure 4.64: As in Figure 4.30, but for both the three reanalysis and four climate models.

Figure 4.65 illustrates the total eddy energy spectra in the meridional mode domain. The main characteristics found in these spectra for the reanalysis, as discussed in section 4.1 (Figure 4.31), such as, for example, the range $l \lesssim 4$ pertaining to the propagative mode for the barotropic Rossby waves, are also present in the climate models. The total eddy energy spectra of the models in the meridional mode domain, is therefore rather identical to that of the reanalysis, despite a few differences in the energy magnitude at some meridional modes.

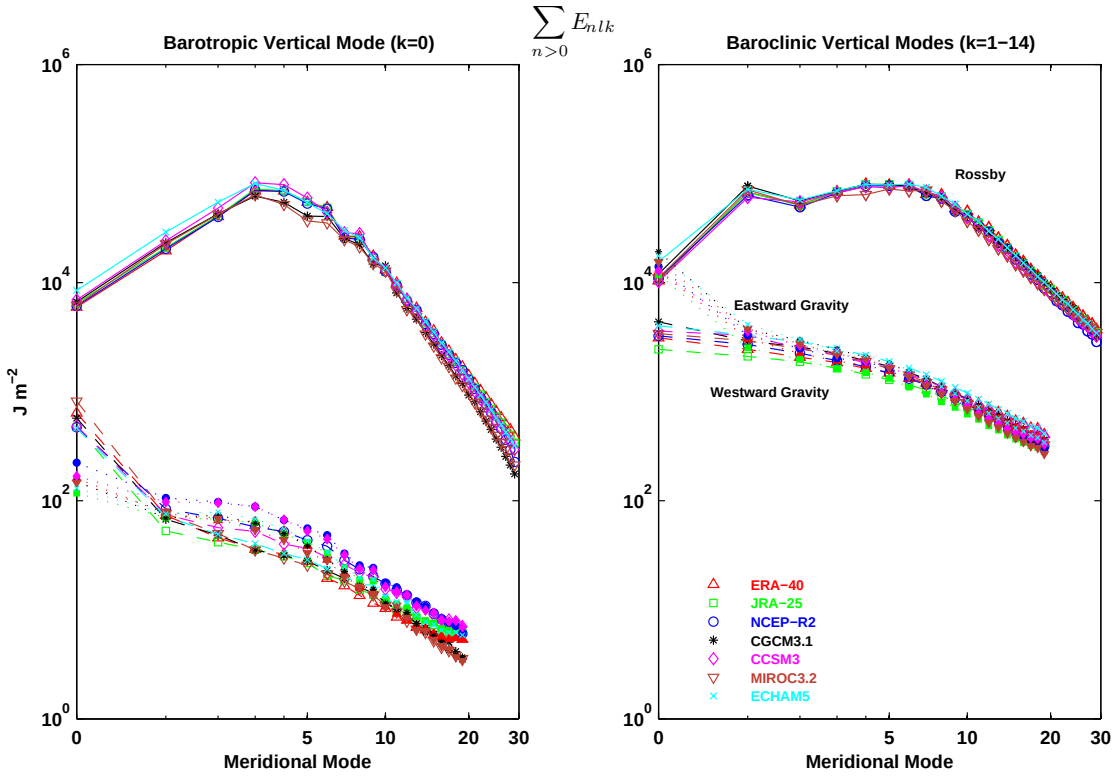

Figure 4.65: As in Figure 4.31, but for both the three reanalysis and four climate models.

Energy interactions

The spectra for the interactions of available potential energy, C_{nlk}, in the wavenumber domain are in Figure 4.66. Nearly all the zonal mean available potential energy transferred into the eddy available potential energy ($C_{nlk} > 0$) is included in the Rossby modes, and most of which in the baroclinic component. The shape of the spectra for the baroclinic Rossby modes in the models agrees to that of the reanalysis, but there is too much interaction in the models, typically at the synoptic-scale wavenumbers $n \simeq 4 - 8$, which is consistent to the excessive transfer rate $R(n)$ in the models, as found in section 4.2.2 (Figure 4.54). The spectra for the part of C_{nlk} taking place at the barotropic Rossby modes, shows that the models CGCM3.1 and CCSM3 are close to JRA-25 and NCEP-R2, with appreciable interactions at the lower wavenumbers, whereas model MIROC3.2 is close to ERA-40, with little interactions, and model ECHAM5 is in between these two groups.

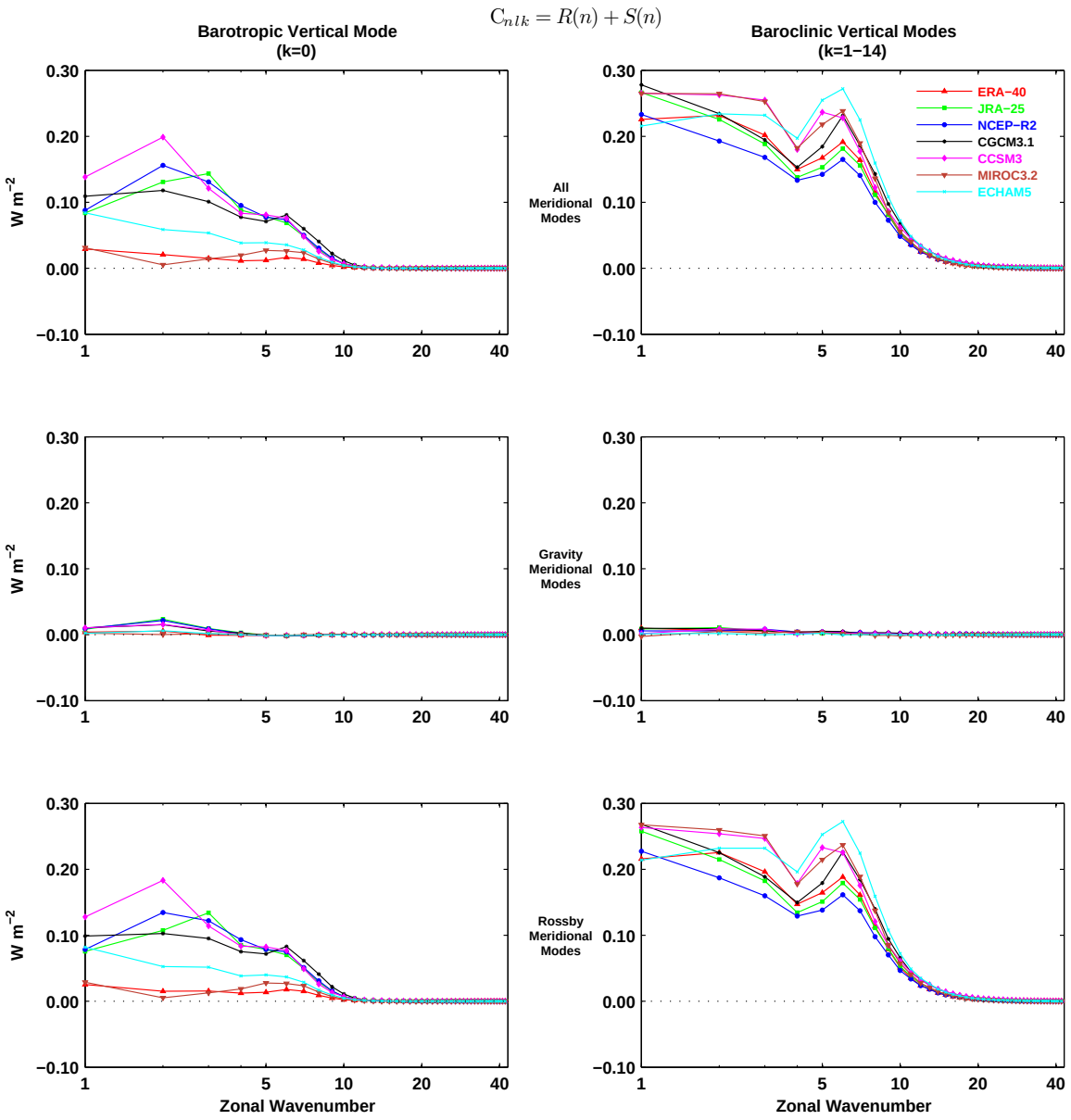

Figure 4.66: As in Figure 4.32, but for both the three reanalysis and four climate models.

Figure 4.67 shows the interactions of kinetic energy in the wavenumber domain, B_{nlk}. It is seen that the flow of kinetic energy is coherent among models and reanalysis, although B_{nlk} is generally excessive in the models. The excessive transfer rate of eddy to zonal mean kinetic energy, $M(n)$, specially at the synoptic-scale wavenumbers (Figure 4.57) is reflected in B_{nlk}, but somewhat differently among the models. Models CCSM3 and ECHAM5, have an excessive transfer of eddy to zonal mean kinetic energy

in the baroclinic Rossby modes, at $n \simeq 1-8$ and $n \simeq 4-8$, respectively. However, part of this excess, is balanced by an excessive transfer in the opposite direction at large scales ($n \simeq 2-8$) in the baroclinic gravity modes, and also in the barotropic Rossby modes for ECHAM5. For models CGCM3.1 and MIROC3.2, excessive transfer of eddy to zonal mean kinetic energy is found at $n \simeq 4-8$ and $n \simeq 1, 2, 4-8$, respectively, for the baroclinic Rossby modes, but not in the opposite direction.

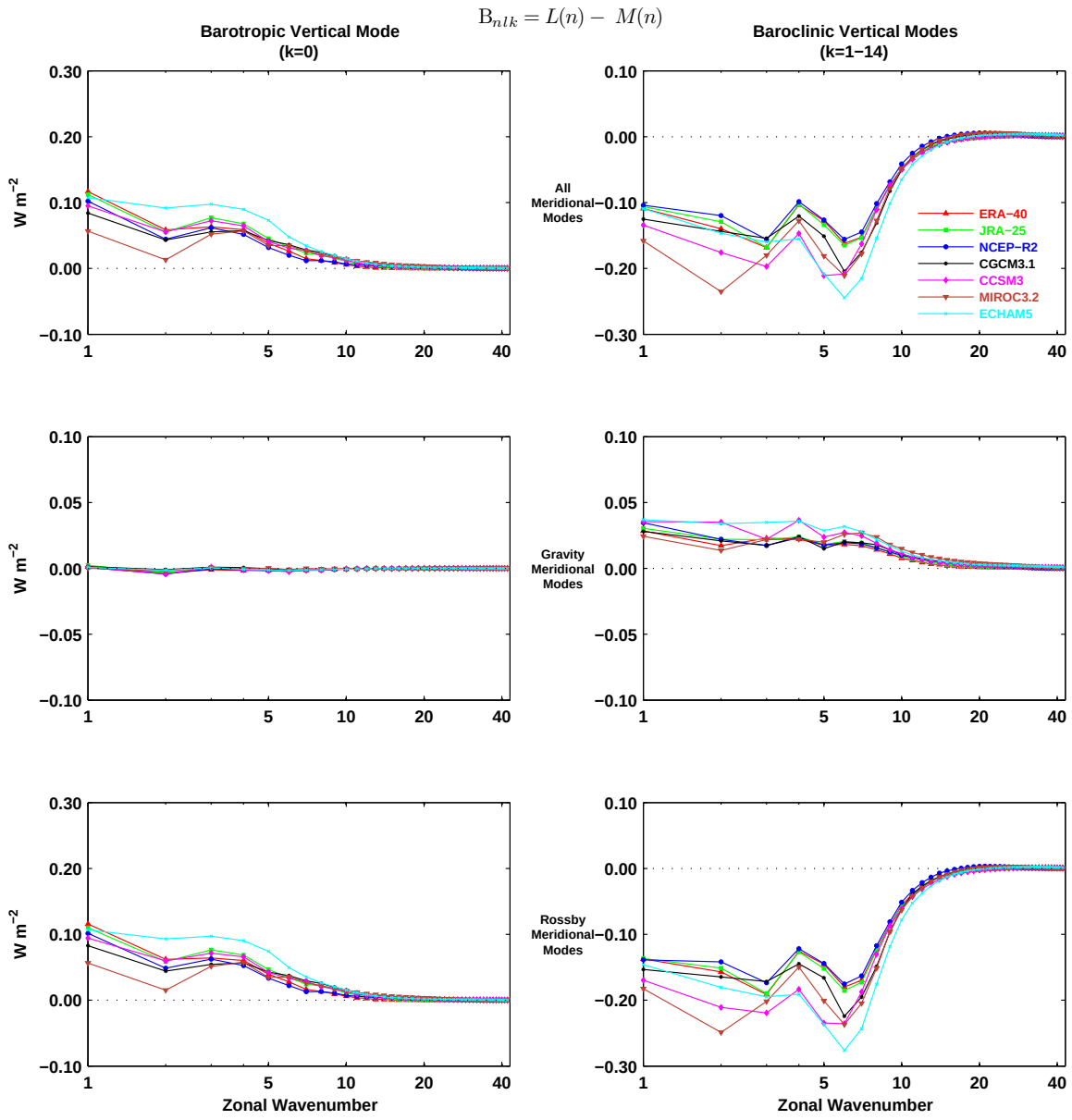

Figure 4.67: As in Figure 4.33, but for both the three reanalysis and four climate models.

Figure 4.68 shows the interactions of available potential energy in the vertical mode domain. The A_Z is transformed into A_E at both the barotropic and baroclinic Rossby modes, which is common to the reanalysis and climate models. There is an exception in the zonal mean component of the barotropic Rossby mode for model MIROC3.2, at which some A_Z seems to be suplied by the baroclinic Rossby modes of the same component. The transfer of energy from A_Z to A_E is typically too strong in the baroclinic Rossby modes of the models, specially at $k = 4$ and 5. For the barotropic Rossby modes, in addition to the different sign in the zonal mean component of MIROC3.2, the magnitude of C_{nlk} varies greatly among the datasets in both the zonal mean and eddy components. For the zonal mean component, the values of ERA-40 and JRA-25 are close to each other, with those of ECHAM5 somewhat stronger and those of CCSM3 somewhat weaker. The same values for CGCM3.1 and NCEP-R2 are small and close to each other. On the other hand, for the eddy component, the C_{nlk} values of CCSM3, CGCM3.1, JRA-25 and NCEP-R2 have the strongest magnitude and are close to each other, wheres those of ERA-40 and MIROC3.2 are the smallest, and the value in ECHAM5 is in between the strongest and the smallest ones. For the gravity modes, interaction C_{nlk} remains neglegible in the eddy component of the models, whereas in the zonal mean component it has a positive maximum at $k = 4$ for both models and reanalysis, and different signs at the barotropic mode, being positive for ECHAM5, MIROC3.2 and ERA-40, and strongly negative for the other models and reanalysis.

As mentioned previously, the barotropic mode of C_{nlk} seems sensitive to the treatment of the lower boundary. Although the vanishing surface wind was adopted as a lower boundary condition for all datasets, the treatment of the atmospheric data in the lower levels, such as the interpolation from model levels to pressure levels, is likely to be different among the datasets, and therefore may be implicated in the discrepancy between the various datasets for the barotropic mode of C_{nlk}. For example, for model MIROC3.2 the below ground data were filled by solving the Poisson equation, whereas the data for models CCSM3 and CGCM3.1 were interpolated from model levels to pressure levels using an ECMWF formulation to extrapolate geopotential and temperature

below ground.

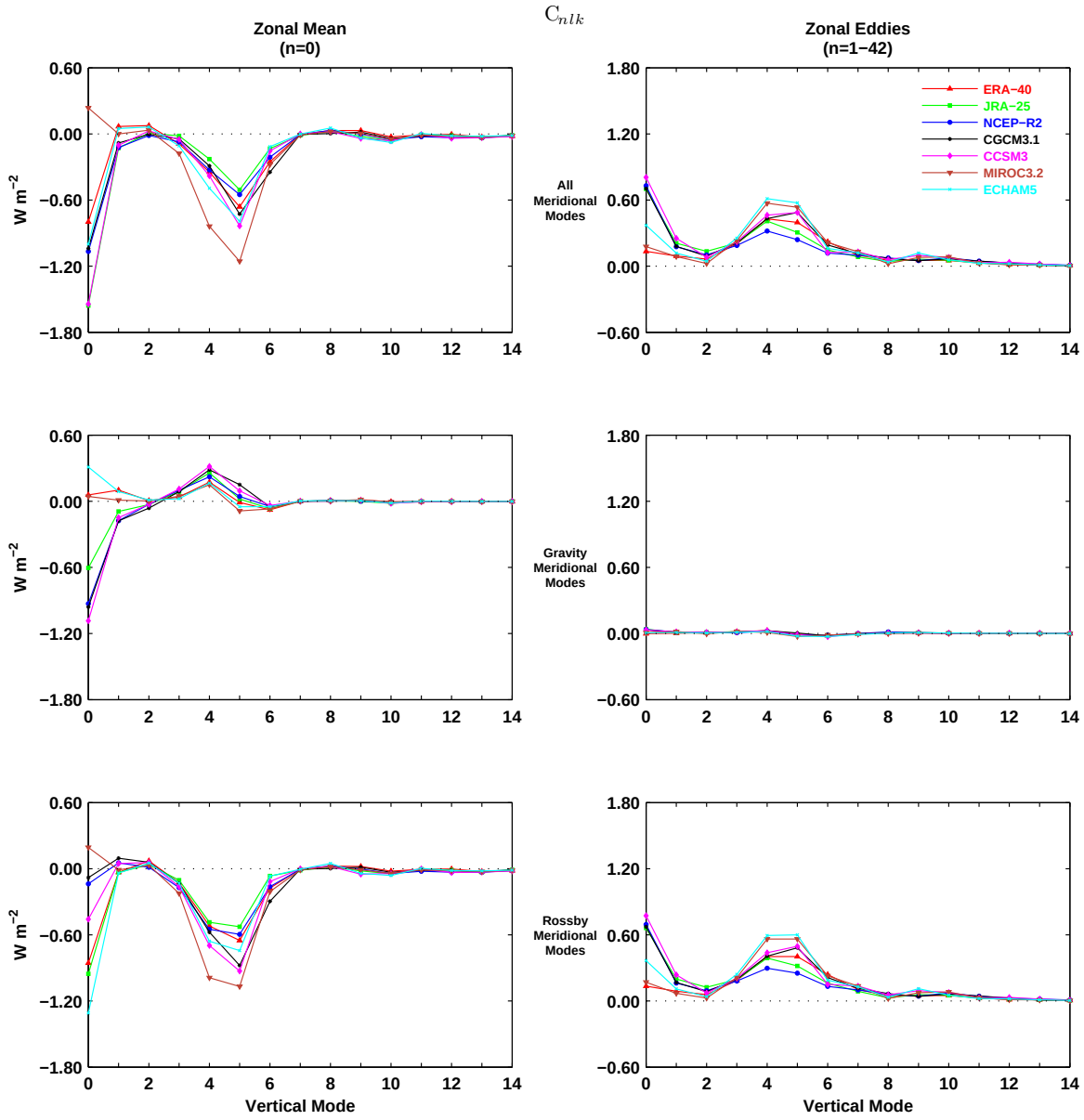

Figure 4.68: As in Figure 4.34, but for both the three reanalysis and four climate models.

Figure 4.69 illustrates the interactions of kinetic energy, B_{nlk}, in the vertical mode domain. For the models, these interactions are rather similar to those for the reanalysis, in a qualitative sense. The discrepancies between models and reanalysis are in the magnitude of B_{nlk}. The models transform too much eddy kinetic energy contained

in the baroclinic components $k = 4$ and 5 of the Rossby modes, into the barotropic component of both the zonal mean and eddy kinetic energy. In models CCSM3 and MIROC3.2, it seems that most of the excessive eddy kinetic energy transferred from the baroclinic Rossby modes goes into the barotropic mode of the zonal mean component, whereas in model ECHAM5 the excessive energy goes mostly into the barotropic mode of the eddy component.

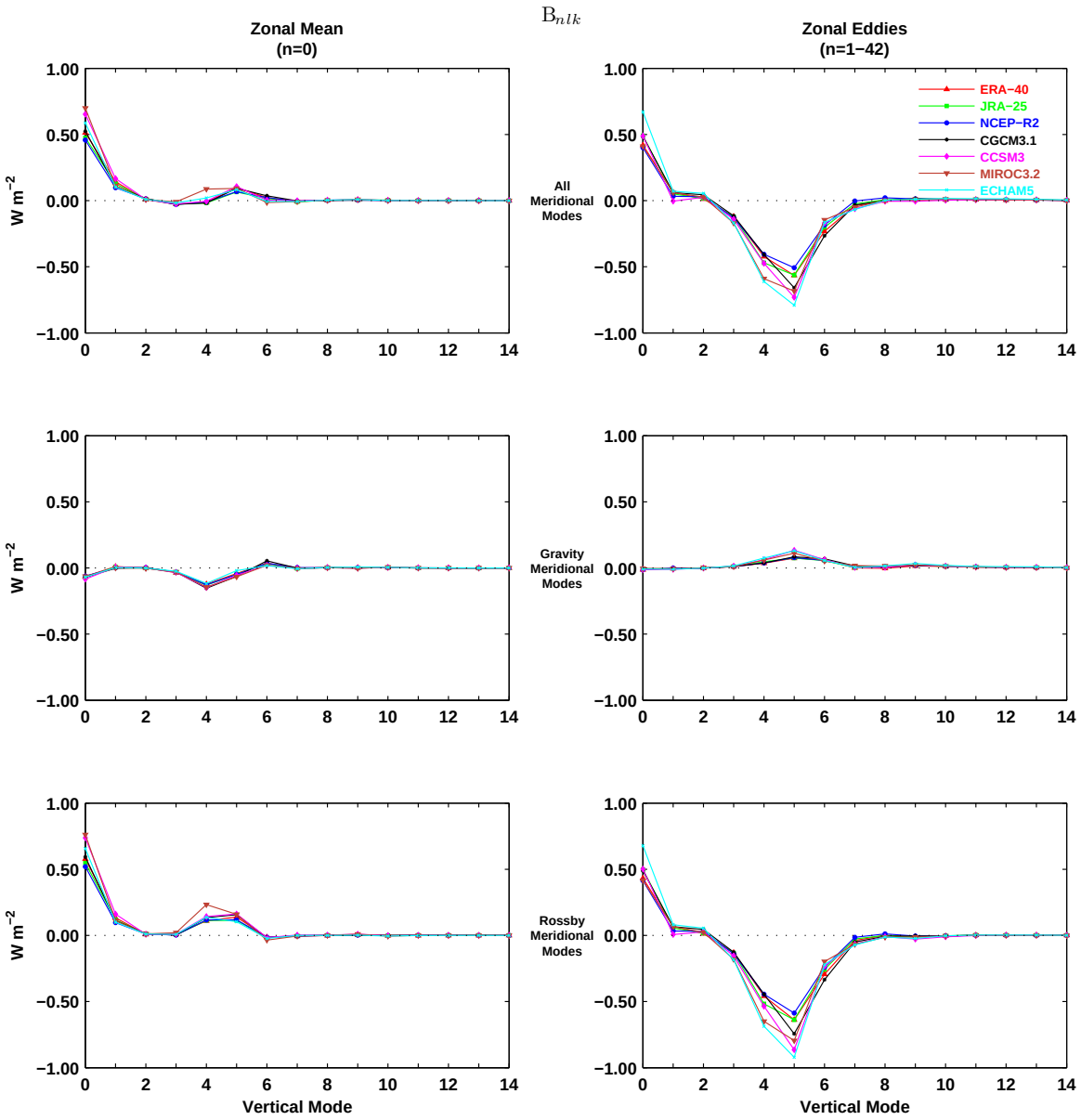

Figure 4.69: As in Figure 4.35, but for both the three reanalysis and four climate models.

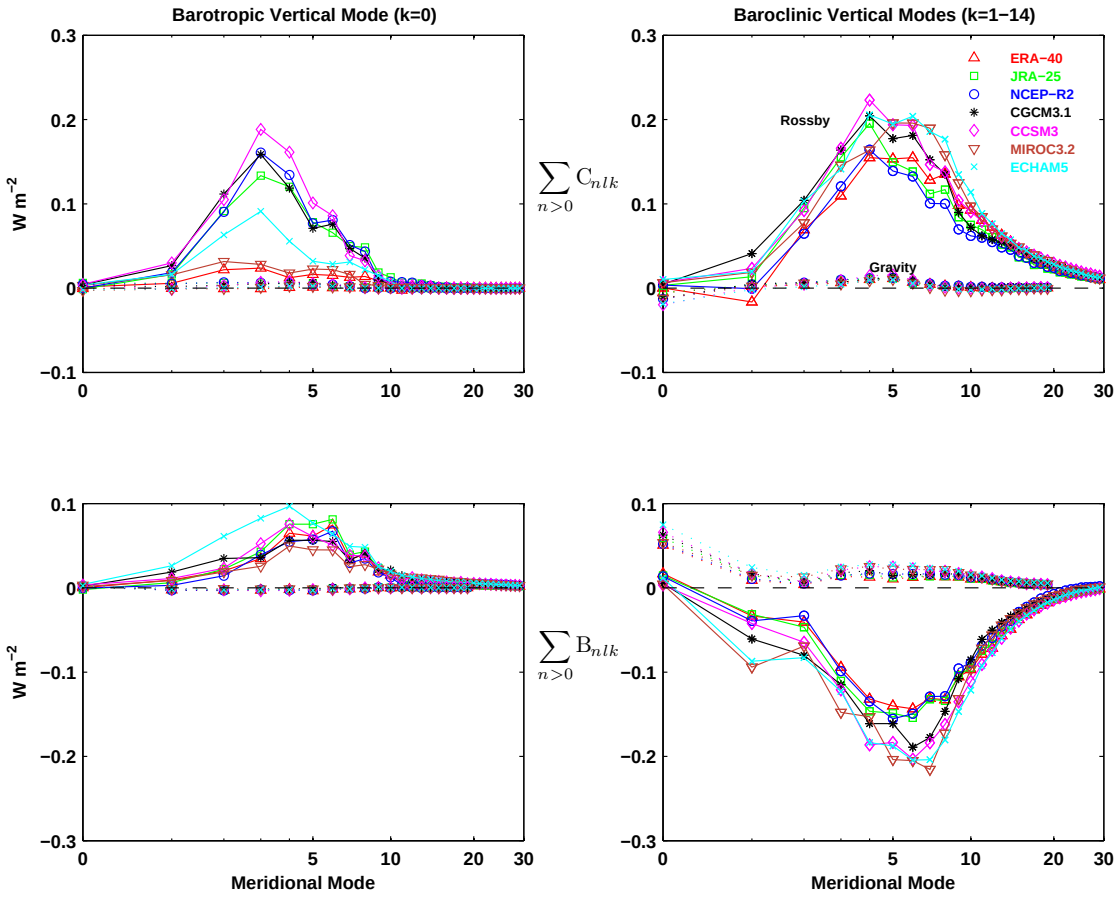

Figure 4.70: As in Figure 4.36, but for both the three reanalysis and four climate models.

Figure 4.70 shows the interactions of A_E and K_E in the meridional mode domain, i.e. C_{nlk} and B_{nlk}, respectively, for $n > 0$. For model MIROC3.2, the A_E supplied into the barotropic Rossby modes is close to that for ERA-40, and is substantially lower than that for CCSM3, NCEP-R2, CGCM3.1 and JRA-25, which are reasonable close to each other, except for CCSM3 at $l = 3 - 5$ which is somewhat too high. The A_E supplied into the same modes for ECHAM5 lays in between the lower and higher values. In the case of the A_E supplied into the baroclinic Rossby modes, the various datasets show identical spectra, although the energy supplied into these modes tends to be too high for the climate models, specially in the range $l \simeq 5 - 10$. The interactions of K_E show similar spectra among reanalysis and climate models. However, the K_E transferred from the baroclinic Rossby modes is too high in the models, specially in the range of

$l \simeq 2 - 10$. The K_E supplied into the barotropic Rossby modes is reasonable identical among the various datasets, excluding the values for ECHAM5 at $l \simeq 1 - 4$, which are too high. These results for the eddy componet of available potential and kinetic energies in the meridional mode domain, complements those obtained for the same component in the wavenumber and vertical mode domains.

Based on the above results, it is concluded that the excessive transfer rates of zonal mean to eddy available potential energy and of eddy to zonal mean kinetic energy in the models, which are compactly expressed by terms C_A and C_K, are mostly due to synoptic-scale Rossby waves in the baroclinic modes $k = 4$ and 5. This is seen by the too strong values in the $R(n)$ and $M(n)$ spectra, typically at the synoptic-scale wavenumbers $n \simeq 4 - 8$ for all models (Figures 4.54 and 4.57), being complemented further by the spectra of C_{nlk} and B_{nlk} in the zonal wavenumber domain (Figures 4.66 and 4.67), in which the excessive energy transfer rates in the models were typically found at the synoptic-scale wavenumbers $n \simeq 4 - 8$ for the Rossby modes of the baroclinic component. In addition, the vertical spectra of both C_{nlk} and B_{nlk} has revealed the baroclinic modes $k = 4$ and 5, as those vertical modes in the models with the most excessive interactions of both available potential and kinetic energies (Figures 4.68 and 4.69). The fact that the excessive energy transfer rates in the models is basically determined by the Rossby modes, is also expressed in the spectra of C_{nlk} and B_{nlk} in the meridional mode domain (Figure 4.70).

Energy conversion

The spectra for the conversion rate of eddy available potential energy into eddy kinetic energy in the zonal wavenumber domain, $C(n)$, are displayed in Figure 4.71. It is seen that this baroclinic conversion rate is too strong in the models, typically at the synoptic-scale wavenumbers, but also at the planetary-scale wavenumbers (specially at $n = 2$) for most models, excluding CGCM3.1. It is also seen that the results obtained with the Saltzman scheme, which are illustrated in Figure 4.55 (or Figure 4.56), and those obtained within the normal mode energetics scheme are similar to one another.

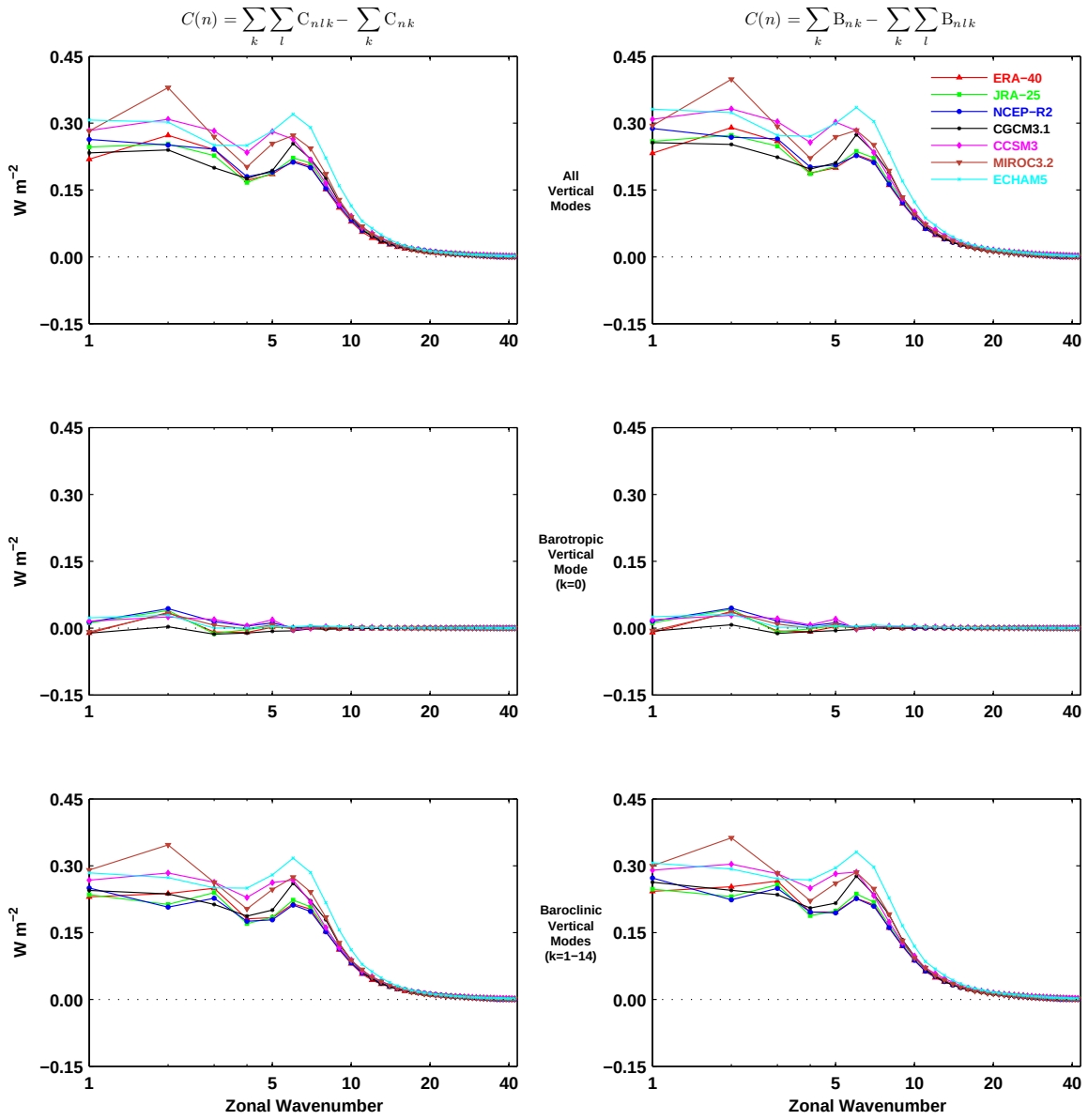

Figure 4.71: As in Figure 4.37, but for both the three reanalysis and four climate models.

The spectra for the conversion rate of available potential energy into kinetic energy in the vertical mode domain, are illustrated in Figure 4.72. The conversion between the zonal mean components of available potential and kinetic energies, $C_Z(k)$, is relatively small for both the reanalysis and climate models. At the barotropic mode $k = 0$, the conversion $C_Z(k)$ seems to be in the opposite direction for most models, excluding model ECHAM5, as compared to the reanalysis. The spectra for the conversion rate

between the eddy components of available potential and kinetic energies, $C_E(k)$, shows that the major contributions in both models and reanalysis are at the baroclinic modes, mainly at $k = 3-6$, with too strong values for the models at $k = 5$, where $C_E(k)$ peaks, and also at $k = 4$ for MIROC3.2 and ECHAM5.

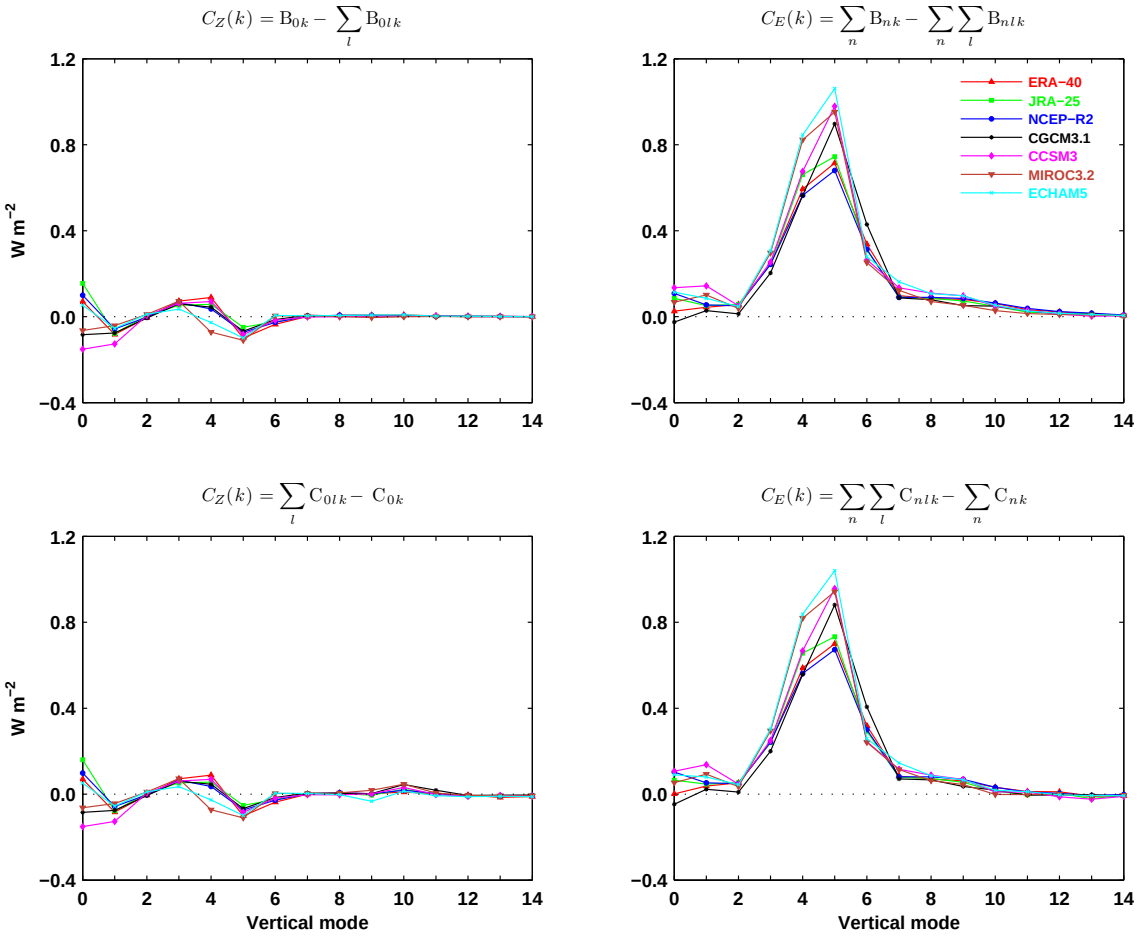

Figure 4.72: As in Figure 4.38, but for both the three reanalysis and four climate models.

Energy generation and dissipation

The vertical mode spectra for the generation and dissipation terms of the zonal mean and eddy components of available potential energy and kinetic energy are in Figure 4.73. Overall, it is seen that the inputs and outputs of energy in the models agree to those in the reanalysis, with an exception for model MIROC3.2 in the barotropic mode of G_Z. The other differences between models and reanalysis are related to the magnitude

in the energy generation and dissipation rates. These are seen mainly in the baroclinic modes of G_Z, where too much A_Z is generated in the models at $k = 4-5$, most notably for MIROC3.2, in which part of this energy is dissipated in the barotropic mode. In addition, the A_E is dissipated in the barotropic mode at a smaller rate for MIROC3.2, ECHAM5 and ERA-40 than that for the other datasets. Finally, the K_E is generally dissipated at a higher rate in the models at baroclinic modes $k = 4-5$ and at the barotropic mode for ECHAM5, whereas the K_Z is generally dissipated at a slightly lower rate in the barotropic mode of models CGCM3.1 and CCSM3.

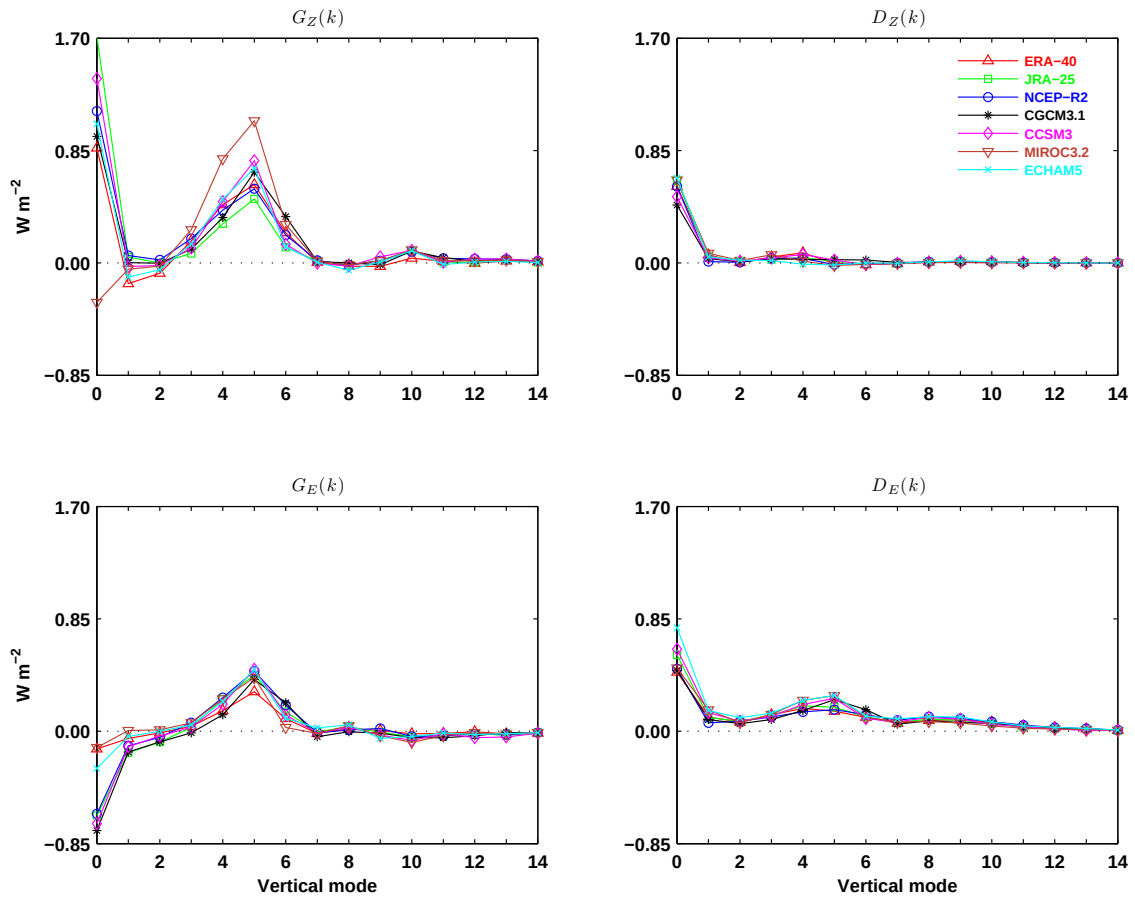

Figure 4.73: As in Figure 4.39, but for both the three reanalysis and four climate models.

Extended energy cycle diagram

Based on the results presented troughout this section, it is here proposed an extended energy cycle diagram describing the flow of energy among the zonal mean and eddy components, and also among the barotropic and baroclinic components. That is, the available potential and kinetic energies, A and K, are decomposed into the zonal mean and eddy components, A_Z, A_E, K_Z and K_E, and each of these components is also decomposed into the barotropic and baroclinic components, which are denoted by the extra subscripts B and b, respectively. Thus, for example, term A_{ZB} denotes the zonal mean available potential energy of the barotropic component. The other subscripts appearing in the terms for the energy conversion/transfer rates are the letters A and K, referring to available potential and kinetic energies, respectively. When these subscripts appear alone, it means that the term designates an energy conversion/transfer rate within that type of energy, A or K, with the origin and destination specified by an appropriate combination of letters Z, E, B and b between parenthesis. For example, $C_A(ZB, Eb)$ designates the transfer rate of available potential energy from the zonal mean barotropic component, A_{ZB}, to the eddy baroclinic component, A_{Eb}. When a subscript A or K is followed by the letters B or b, it means that the term designates an energy conversion/transfer rate between the zonal mean and eddy components of the energy type A or K contained in component B or b. For example, term C_{AB} refers to the transfer rate of available potential energy between the barotropic components, which are A_{ZB} and A_{EB}. When neither A nor K appears as a subscript in a term, it means that the term designates an energy conversion/transfer rate between the energies contained in the components identified by the two subscripts. For example, term C_{ZB} denotes the conversion rate between the energies contained in the zonal barotropic components, which are A_{ZB} and K_{ZB}. This extended energy cycle diagram is illustrated in Figure 4.74, in which the boxes represent the levels of energy and the arrows the energy generation/dissipation rates and the energy conversion/transfer rates. The estimates in the diagram are for the reanalysis average (top values) and the models average (bottom values) in the DJF climate. A negative value means that the energy flows in the opposite direction of that indicated by the arrow.

All the terms presented in the diagram of Figure 4.74 may be computed directly with the formulae given in section 2 and Appendix A, except the term $C_A(ZB, Eb)$. This term must exist to account for the part of the energy involved in the interactions of available potential energy, C_{nlk}, that is not supplied into the eddy available potential energy of the barotropic component, A_{EB}, but it can only be estimated indirectly from C_{nlk}. This is so because, on the one hand, the negative value of C_{nlk} obtained for $n = 0$, $k = 0$ and summing over all l, denoted for simplicity as C_{0l0}, gives the amount of energy that flows out of A_{ZB}, which, by definition, excludes both the conversion of available potential energy into kinetic energy and the generation (or dissipation) of available potential energy. Therefore, this energy flowing out of A_{ZB} can only be transferred into another component of available potential energy, but not to A_{Zb} because this component is supplying energy instead of receiving energy from elsewhere due to the nonlinear interactions, as seen by the negative value of C_{nlk} obtained for $n = 0$, and summing over all $k > 0$ and all l, denoted as $\mathrm{C}_{0l(k>0)}$. Hence, the energy from A_{ZB} can only be transferred into A_{EB} or A_{Eb}, or both. On the other hand, the positive value of C_{nlk} obtained for $k = 0$, and summing over all $n > 0$ and all l, denoted as $\mathrm{C}_{(n>0)l0}$, gives the amount of energy that flows into A_{EB}. Since $\mathrm{C}_{(n>0)l0}$ is less than the absolute value of C_{0l0}, then it means that part of the energy flowing out of A_{ZB} is transferred into A_{EB}, which is represented by C_{AB}, and the remainder energy must be transferred to A_{Eb}, which is represented by $C_A(ZB, Eb)$. Therefore, $C_A(ZB, Eb)$ must exit and may be computed as the difference between the absolute values of C_{0l0} and $\mathrm{C}_{(n>0)l0}$.

In addition, for an unstable perturbation to grow, by extracting available potential energy from the mean flow, it must tilt westward and therefore a baroclinic instability will result (Vallis, 2006). That is, the energetics of baroclinic waves require that they remove available potential energy from the mean flow (Holton, 2004). Thus, the baroclinic available potential energy of the zonal mean component, A_{Zb}, is transferred into the eddy baroclinic available potential energy, A_{Eb}, which is the energy source for the eddy baroclinic kinetic energy, K_{Eb}. This energy transferred from A_{Zb} to A_{Eb} is represented by C_{Ab} in Figure 4.74. As expected, by the existence of term $C_A(ZB, Eb)$

shown above, C_{Ab} is less than the positive value of C_{nlk} that is obtained by summing over all $n > 0$, $k > 0$ and all l, denoted as $\mathrm{C}_{(n>0)l(k>0)}$, and which represents the amount of energy flowing into A_{Eb}. Thus, the difference $\mathrm{C}_{(n>0)l(k>0)} - C_{Ab}$ gives another possible indirect estimation for term $C_A(ZB, Eb)$.

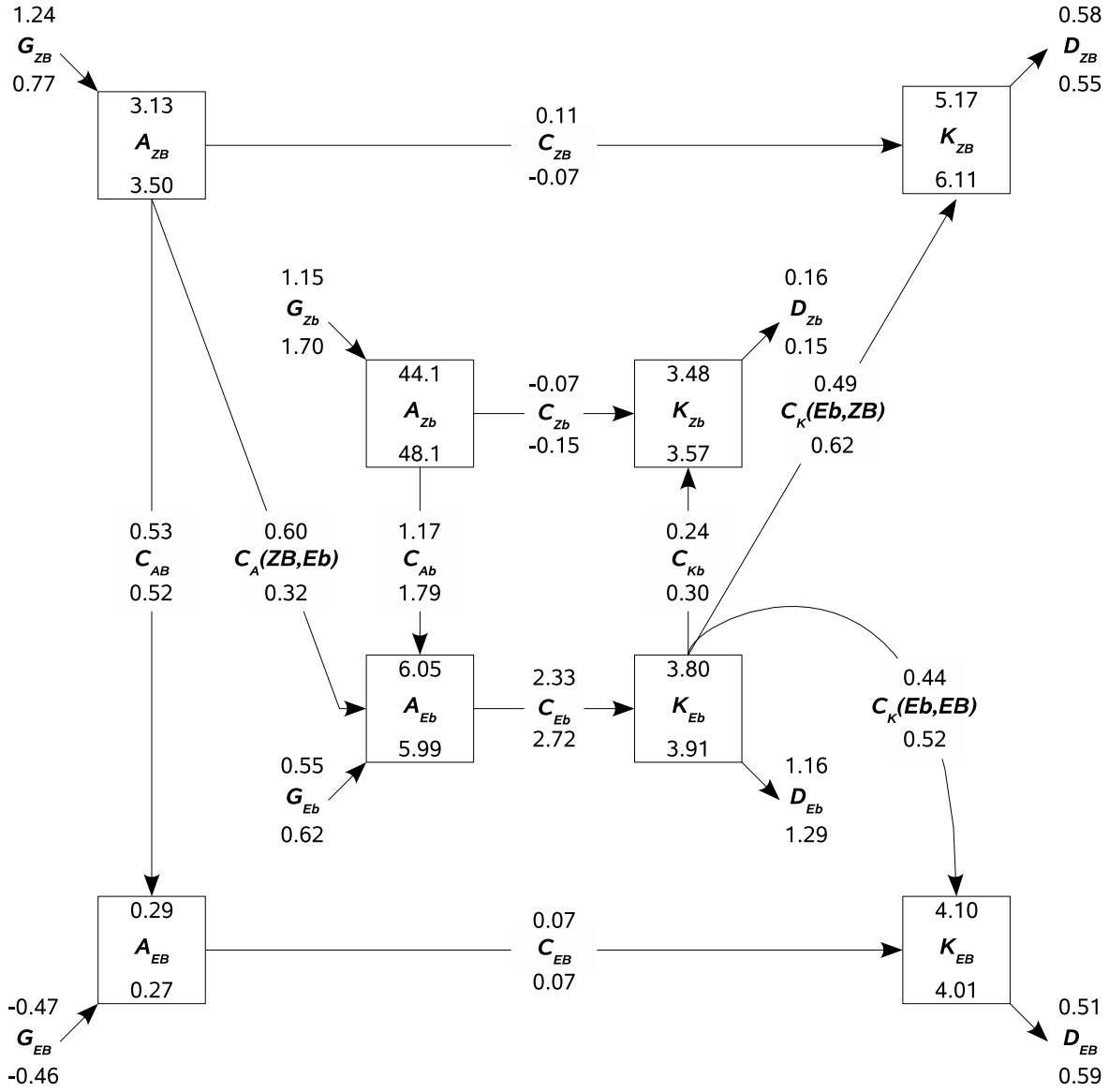

Figure 4.74: Energy cycle diagram for the reanalysis average (top values) and models average (bottom values) in DJF, separated into both the zonal mean and eddy components, and into barotropic and baroclinic components. Units are 10^5 J m^{-2} for energy levels and W m^{-2} for conversion rates.

Using either one or the other indirect estimations presented above for term $C_A(ZB, Eb)$, should yield the same value. However, the values obtained for $C_A(ZB, Eb)$ with the two indirect estimations were somewhat different, and the discrepancy is due to an imbalance in the nonlinear term C_{nlk}. The summations of C_{nlk}, B_{nlk} and D_{nlk} over all indices n, k, and l, should ideally be zero, but this condition was not met due to the assumptions and approximations discussed in sections 3.3 and 2.2.4, and the truncations in n, k, and l. When the imbalance in C_{nlk} is adjusted, by redistributing the error linearly among all indices, which is similar to the approach of Terasaki and Tanaka (2007a), the two indirect estimations for $C_A(ZB, Eb)$ are perfectly equal. This approach was adopted in the estimates presented in Figure 4.74, in order to adjust the imbalances of 0.23 (0.08) W m^{-2} in C_{nlk} and of 0.10 (0.12) W m^{-2} in B_{nlk}, for the reanalysis (models).

From Figure 4.74, it is seen that most of the energy is generated at both the barotropic and baroclinic components of zonal mean available potential energy, A_{ZB} and A_{Zb}, as seen by the positive values of G_{ZB} and G_{Zb}. Almost all the energy generated in A_{ZB} is transformed into both A_{EB}, and A_{Eb}, as indicated by positive values of terms C_{AB} and $C_A(ZB, Eb)$, respectively. Virtually all the energy supplied into A_{EB} is dissipated radiatively, as seen by the negative values of G_{EB}, although there is a residual conversion of energy from A_{EB} into K_{EB}, as seen by the positive C_{EB}. For the reanalysis, a small part of the energy generated in A_{ZB} is also converted into K_{ZB}, whereas for the models a small amount of energy is converted in the opposite direction, as seen by positive and negative C_{ZB}, respectively, which is the only discrepancy in the flow of energy between the models average and the reanalysis average. With the zonal wavenumber energetics scheme, the sum $C_{ZB} + C_{Zb}$ yields a small positive value for the models average (0.04 W m^{-2}), agreeing therefore qualitatively with the reanalysis average. Nevertheless, the sum $C_{ZB} + C_{Zb}$ is small, and has little weight in the energy cycle. All the energy generated in A_{Zb}, along with a small amount of energy converted from K_{Zb} into A_{Zb}, as seen by positive G_{Zb} and negative C_{Zb}, respectively, is transformed into A_{Eb}, as indicated by positive C_{Ab}. Some energy is also generated in A_{Eb}, as seen by the positive values of G_{Eb}. This energy, together with the energy supplied from both A_{ZB} and A_{Zb}

into A_{Eb}, is converted into the eddy kinetic energy of the baroclinic component, K_{Eb}, as seen by the positive values of C_{Eb}. Part of this energy is dissipated in K_{Eb}, and part is transferred into the eddy kinetic energy of the barotropic component, K_{EB}, being afterwards dissipated, as indicated by positive values of D_{Eb}, $C_K(Eb, EB)$ and D_{EB}. The remainder part of the energy converted from A_{Eb} into K_{Eb} is transformed into the zonal mean kinetic energy of both the barotropic and baroclinic components, K_{ZB} and K_{Zb}, as seen by positive values of $C_K(Eb, ZB)$ and C_{Kb}, respectively, being afterwards dissipated in each component of the zonal mean kinetic energy, as indicated by positive values of D_{ZB} and D_{Zb}.

Chapter 5

Energetics in a Future Climate Scenario

According to section 3.3, the energetics terms for the future climate were computed, at each time step, from the models' datasets for experiment SRES-A1B. The climatological mean values correspond to the averages taken over the period 2070-2099. The energetics for the SRES-A1B climate are compared to that for the present climate (20C). In the same manner as that for Chapter 4, the zonal mean and eddy components of the Lorenz energy cycle, are discussed first, followed by the energetics in the domain of zonal wavenumber, and finally by the normal modes energetics.

5.1 Lorenz energy cycle

One way to assess how the energetics of the atmosphere may be affected by the increase in global mean temperature, which is implied by higher greenhouse gas concentrations, is through the Lorenz energy cycle. In its simpler form, the Lorenz energy cycle characterises the maintenance of the general circulation in terms of the generation of available potential energy A, its conversion into kinetic energy K, and its further frictional dissipation. The terms of the more detailed Lorenz energy cycle, which is obtained by the decomposition of A and K into zonal mean and eddy components, are related to specific processes as described in section 1.

Recently, Hernández-Deckers and von Storch (2010) have studied the energetics responses to CO_2 increases, by evaluating the changes in the Lorenz energy cycle using the output from the ECHAM5 climate model. Evidently, their study is related to the present study, which analyses the energetics responses to increases of greenhouse gas concentrations, that are inherent to the future climate scenario (A1B). They have been motivated by the fact that A depends both on the spatial variance of temperature over constant pressure levels and on the inverse mean static stability, γ, and therefore it would not be affected by a homogeneous temperature increase, but rather by changes in horizontal or vertical temperature gradients, that could trigger changes in the whole Lorenz energy cycle. Most of their principal results agree to the changes in the Lorenz energy cycle obtained in this study for the A1B climate relative to the present climate (20C), as will be discussed troughout this section.

A comparison between the global energy cycle of the five climate models for the present climate (20C) in both DJF and JJA, and that for the future climate scenario (A1B), is illustrated in Figure 5.1. It is apparent some global changes in the energetics for the A1B climate relative to the 20C climate. These include, a decrease in G_Z, which seems to imply a decrease in both the transfer rate from A_Z to A_E, and the conversion rate from A_E to K_E, and also a decrease in the dissipation of K_E. On the other hand, it is seen an increase in C_K, which seems to lead to a strong increase in K_Z. It is also seen global increases in G_E, A_Z and D_Z, whereas C_Z decreases slightly and K_E is virtually unchanged in DJF, but increases slightly in JJA. However, the global nature of the values in Figure 5.1 may have obscured opposite changes in the energetics responses to higher greenhouse gas concentrations of the A1B climate, that should be important for understanding the dynamical changes in the circulation of the atmosphere of a warmer planet. Therefore, the vertical cross-sections of the energetics terms are displayed in Figures 5.2 to 5.10, in order to assess the contributions for the energetics changes in the A1B climate as function of latitude and pressure. In these figures, the contours show the energetics quantities for the A1B climate, while the colour shadings indicates the 95% significant changes, obtained via the t-test, relative to the 20C climate.

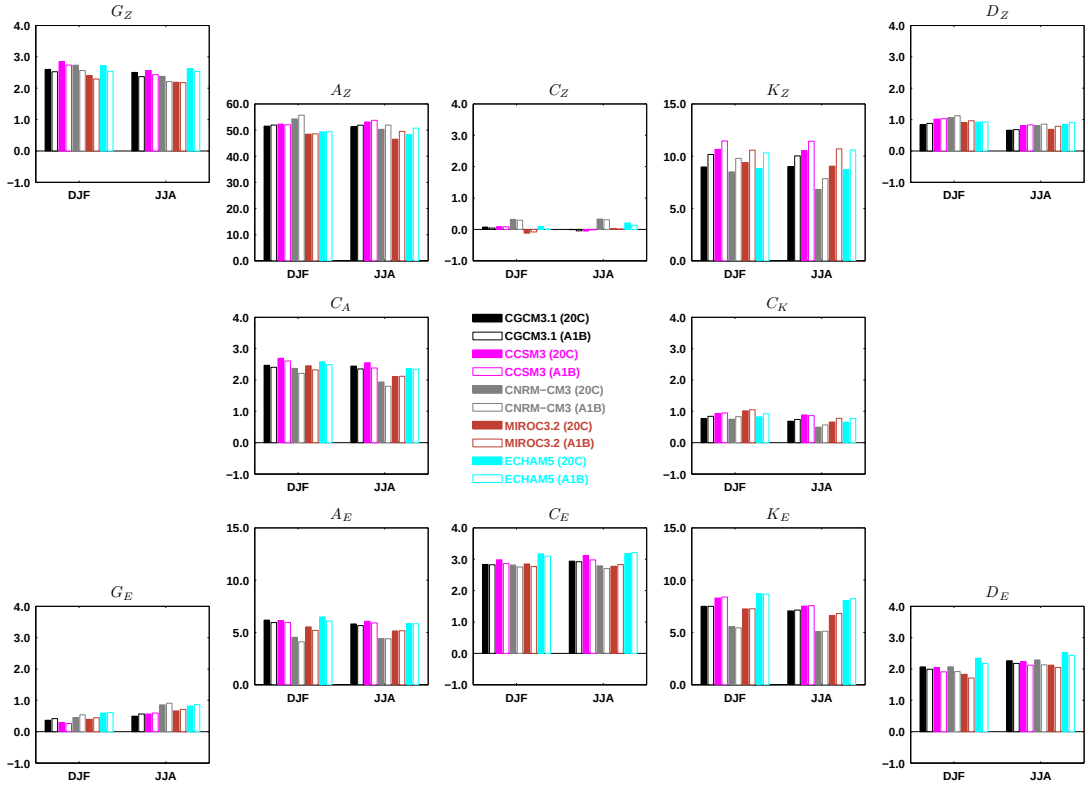

Figure 5.1: As in Figure 4.40, but for the climate models in the present climate (20C) versus the future climate scenario (A1B).

Figure 5.2 shows a strong increase of A_Z in the upper troposphere and lower stratosphere (UTLS), whereas throughout the middle and lower troposphere A_Z decreases. This pattern is specially evident in the winter hemisphere, and it is also seen in C_A, A_E, C_E, and K_E (Figures 5.3 to 5.6). On the other hand, an increase response dominates in C_K and K_Z (Figures 5.7 and 5.8). Following Hernández-Deckers and von Storch (2010), these different patterns in the changes of C_K and K_Z relative to the other terms, may be explained by the vertical distribution of these terms. Both C_K and K_Z are related to the jet streams, and thus are more concentrated in the upper levels of the troposphere, whereas the other terms are widely spread throughout the troposphere. Therefore, the global response of C_K and K_Z is dominated by the values in the upper troposphere, where the increase response is present, whereas the global response of the other terms is partially dominated by the values in the middle and lower troposphere, where the

decrease response is strong.

The positive and negative values of C_Z, depicted in Figure 5.9, are associated with the thermally direct Hadley cells, the indirect Ferrel cells and to some extent with the also direct Polar cells. It is generally seen an increase in the positive contributions to C_Z in the UTLS, whereas the same contributions show a decrease in the lower troposphere. On the other hand, the increase response dominates in the negative contributions to C_Z (it should be noted that, a strengthening in the negative contributions to C_Z, corresponds to a negative colour shading). The global decrease seen in C_Z seems therefore related to a higher conversion from K_Z to A_Z. This also implies that the increase in K_Z must be due by the increase in C_K, which agrees with Hernández-Deckers and von Storch (2010). They have concluded that the increase in K_Z must be mostly driven by the changes in the $A_Z \rightarrow A_E \rightarrow K_E \rightarrow K_Z$ side of the energy cycle, and not by changes in the direct conversion from A_Z to K_Z.

The analysis of the vertical cross sections suggests therefore a strengthening of the energy cycle in the upper levels and a weakening in the lower levels, which is seen in all the five climate models used in this study. Globally, the weakening of the Lorenz energy cycle in the lower levels dominates and leads to a decrease in the energy flow from A_Z to A_E to K_E. This weakening reflects a reduction in baroclinic activity and is consistent with earlier studies (Boer, 1995; Castanheira et al., 2009; Hernández-Deckers and von Storch, 2010). On the other hand, the strengthening of the Lorenz energy cycle in the upper levels leads to an increase in C_K together with a significant increase in K_Z. As shown by Hernández-Deckers and von Storch (2010), the two opposite responses result from the warming structure implied by higher greenhouse gas concentrations, with the strongest warming in the upper tropical troposphere and in the lower troposphere at high latitudes (e.g. Niehörster et al., 2008). This warming structure causes changes in the horizontal temperature variance and in the mean static stability, as seen in Figure 5.12, which increase zonal mean available potential energy A_Z in the upper troposphere and decrease it below, triggering the two opposite responses via changes in baroclinic activity.

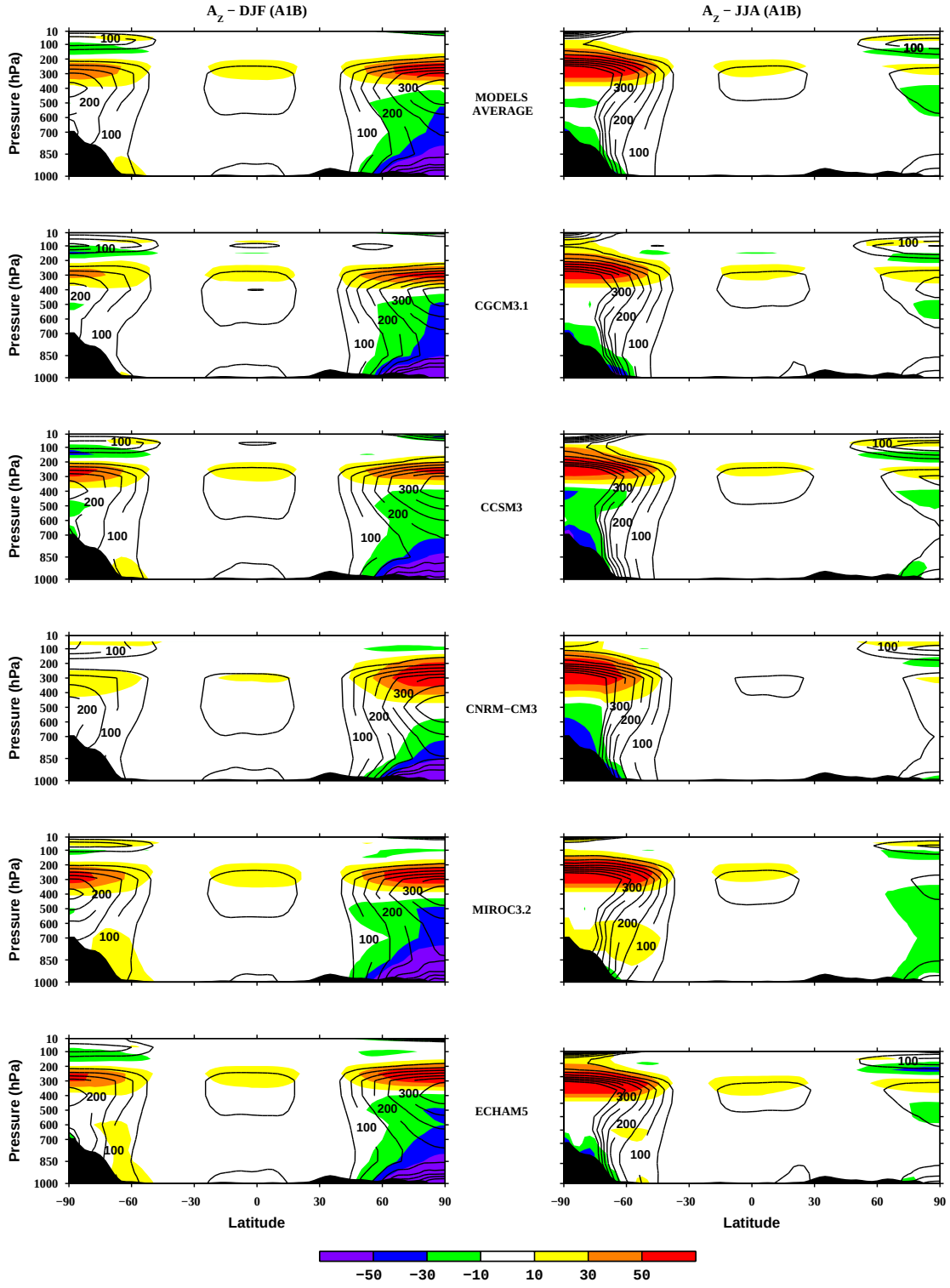

Figure 5.2: Cross-sections of zonal available potential energy, A_Z, averaged over 2070-2099 in DJF (left) and JJA (right). The A_Z quantities for the A1B climate are contoured (black) and the significant changes (95%) relative to the 20C climate are shaded (colour). Units are J m^{-2} Pa^{-1}.

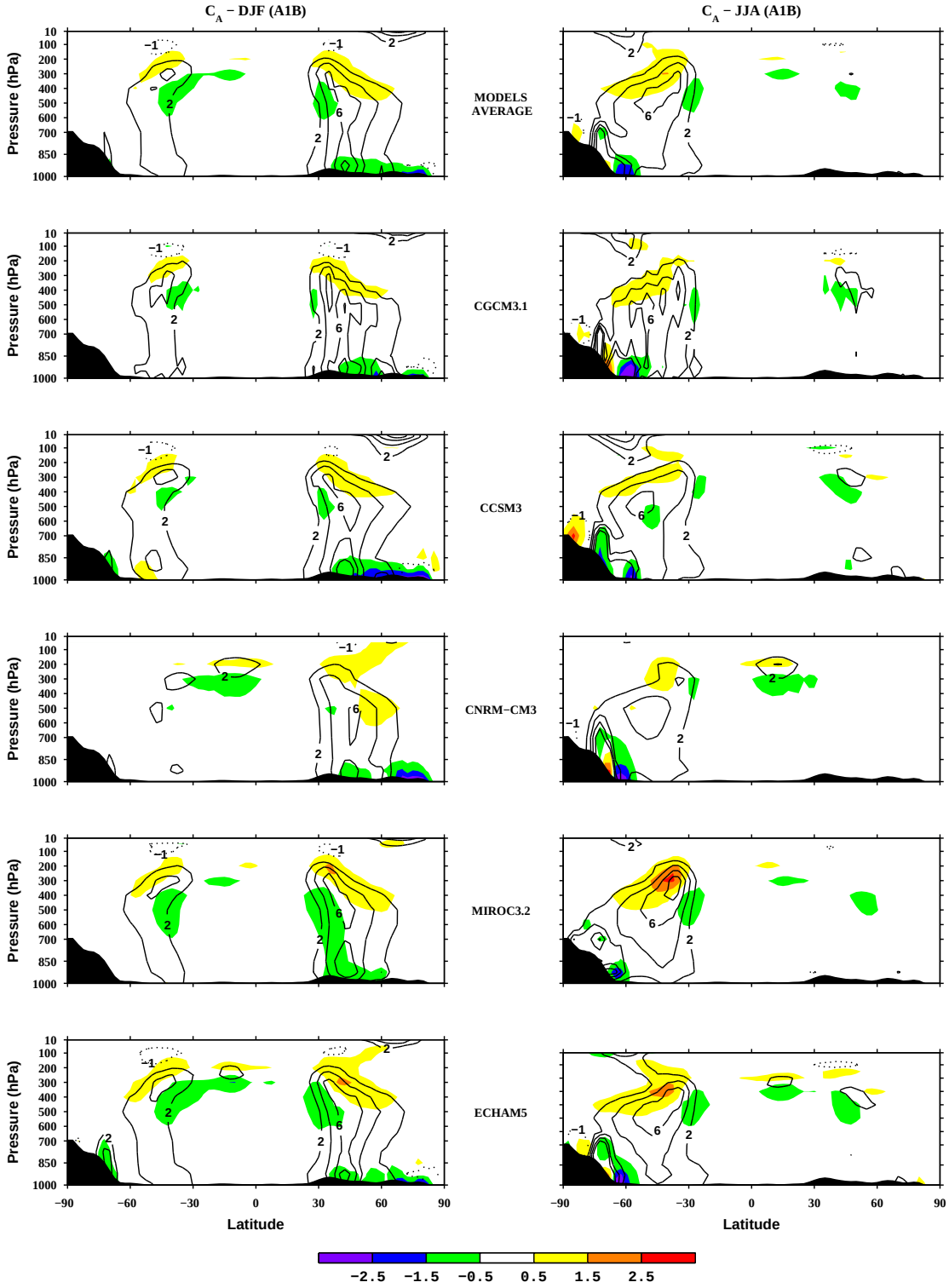

Figure 5.3: The same as in Figure 5.2, but for the rate of transfer from zonal to eddy available potential energy, C_A. Positive (Negative) values of C_A are represented by continuous (dotted) contours. Units are 10^5 W m^{-2} Pa^{-1}.

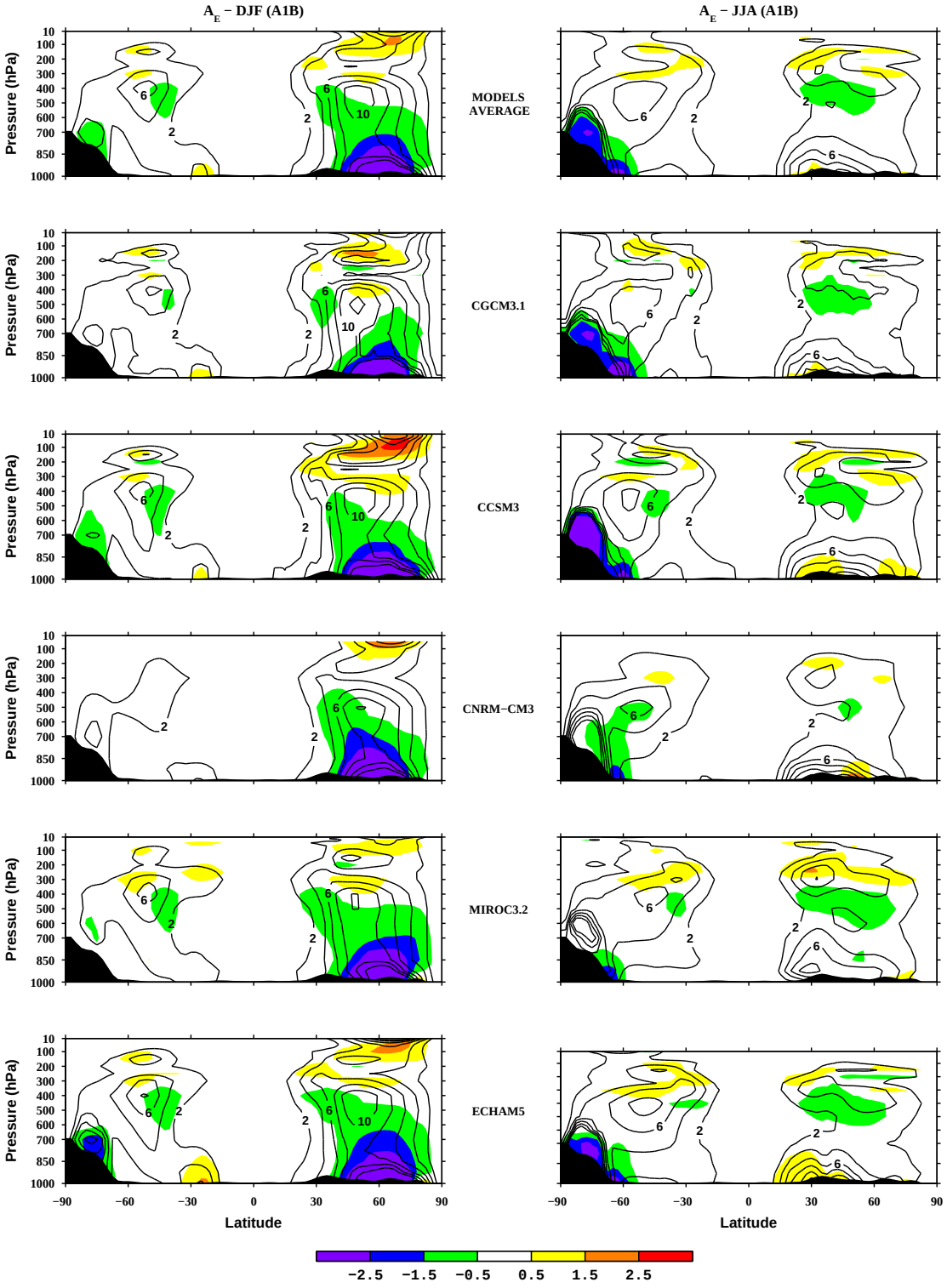

Figure 5.4: The same as in Figure 5.2, but for eddy available potential energy, A_E.

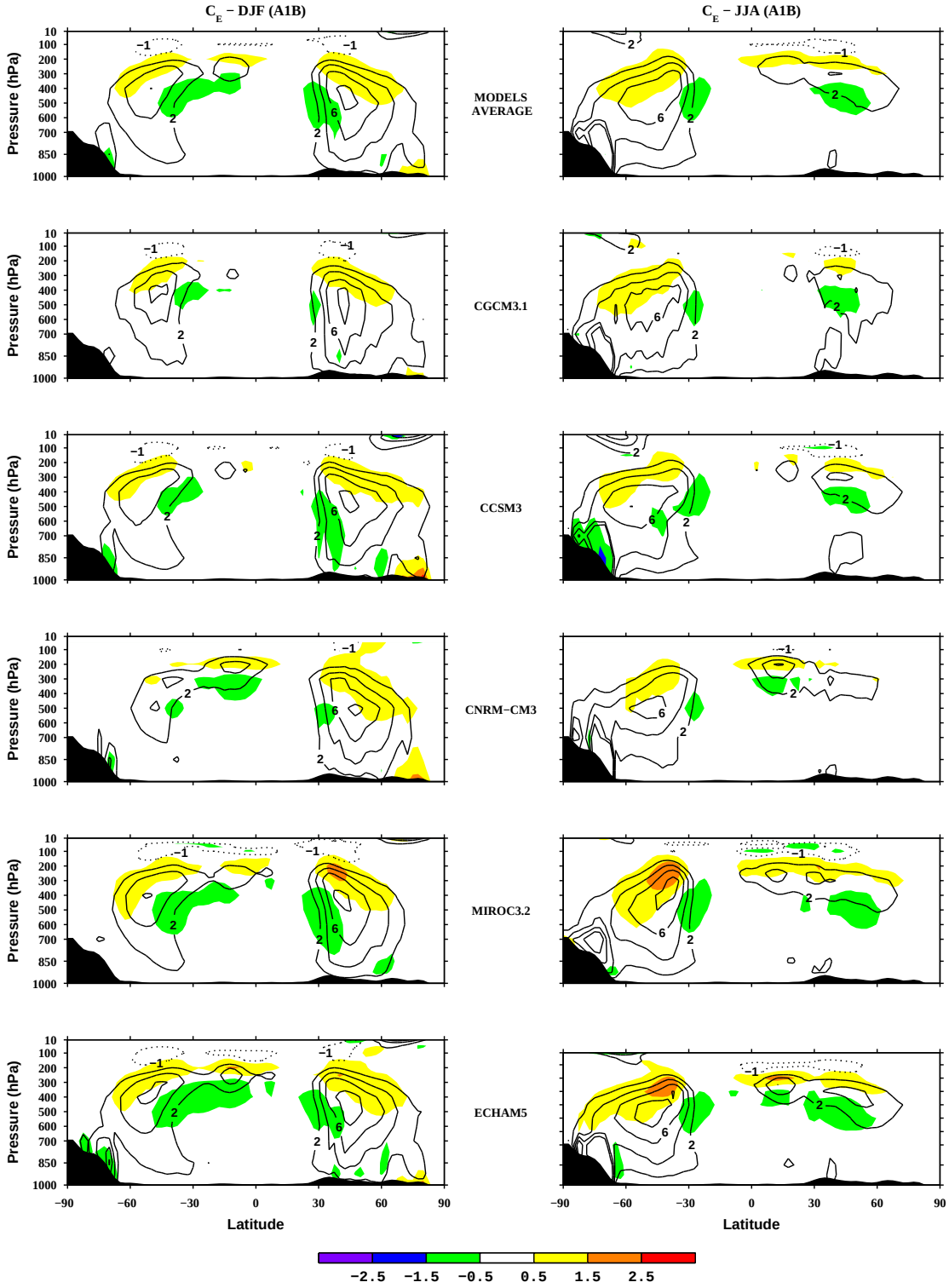

Figure 5.5: The same as in Figure 5.3, but for the conversion rate of eddy available potential energy to eddy kinetic energy, C_E, computed with the "$\omega\alpha$" formulation.

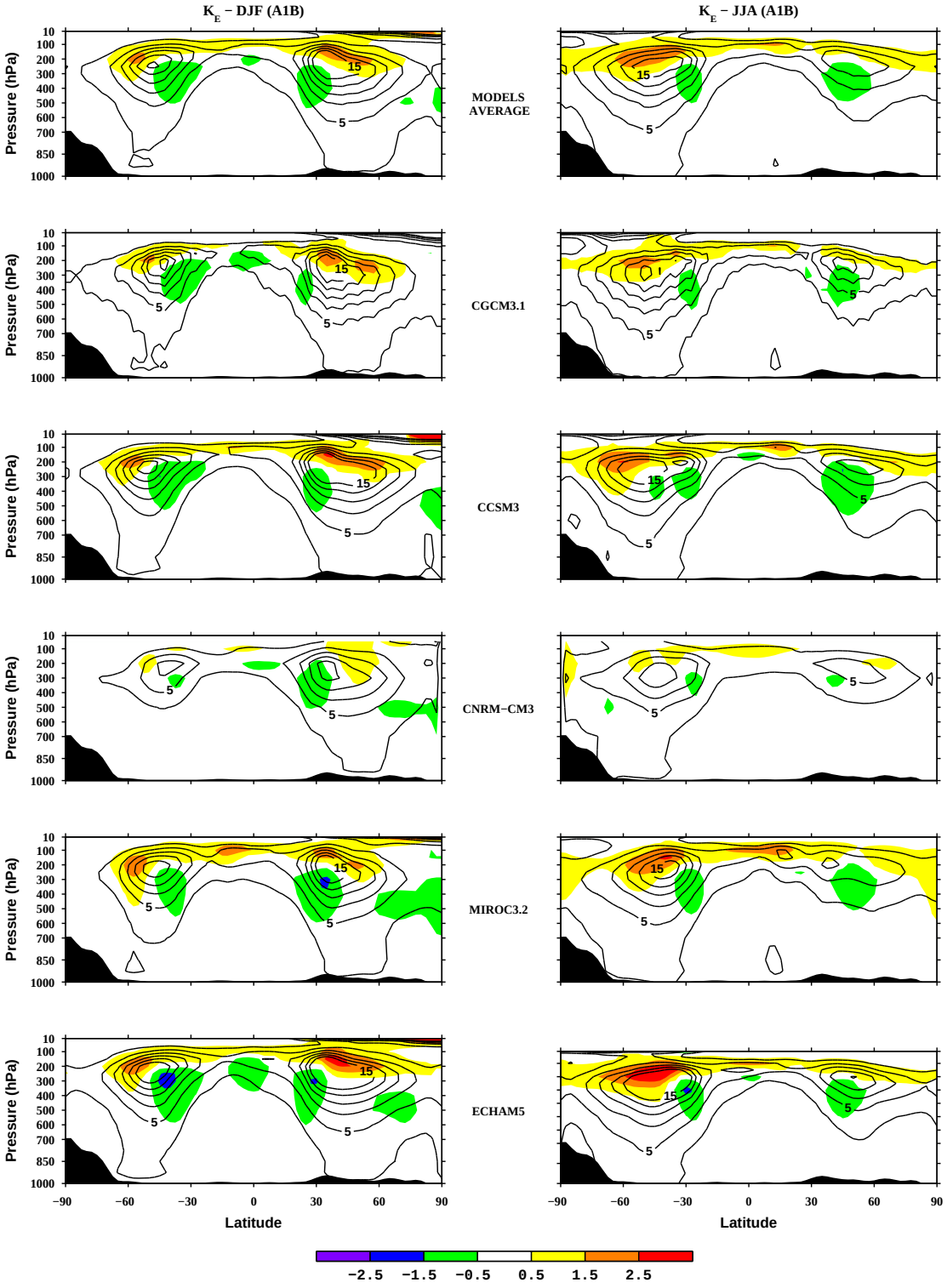

Figure 5.6: The same as in Figure 5.2, but for eddy kinetic energy, K_E.

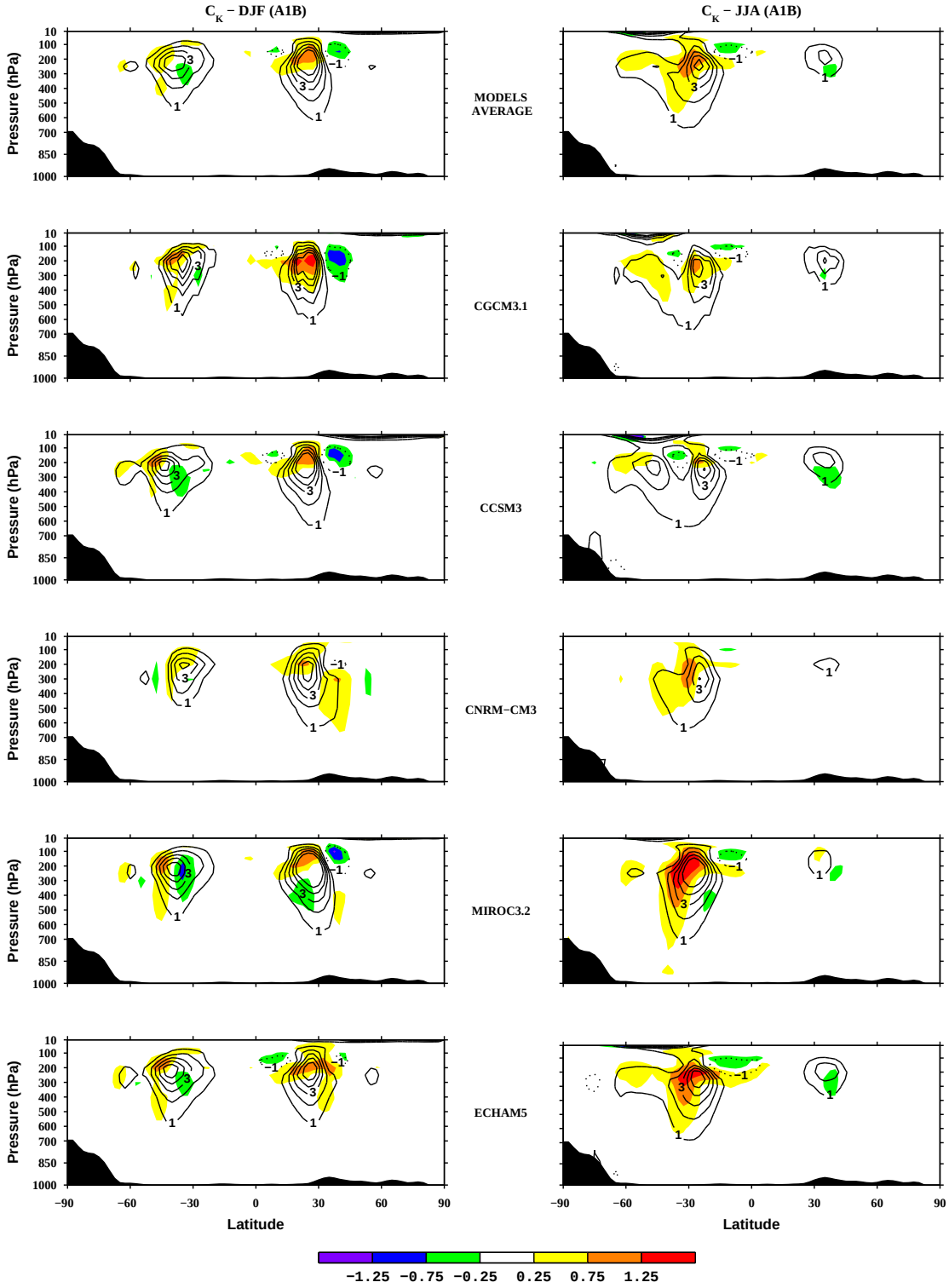

Figure 5.7: The same as in Figure 5.3, but for the rate of transfer from eddy to zonal kinetic energy, C_K.

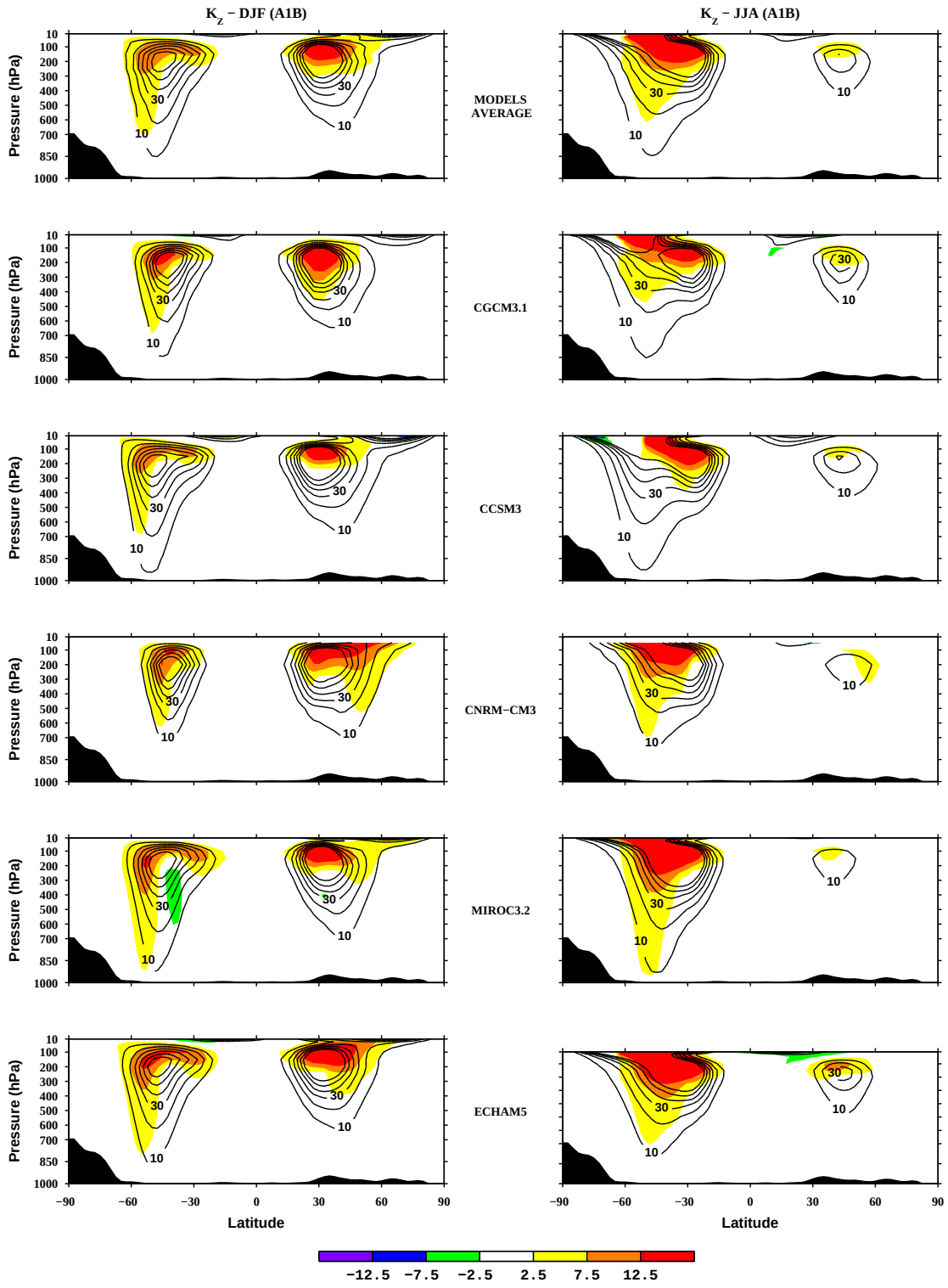

Figure 5.8: The same as in Figure 5.2, but for zonal kinetic energy, K_Z.

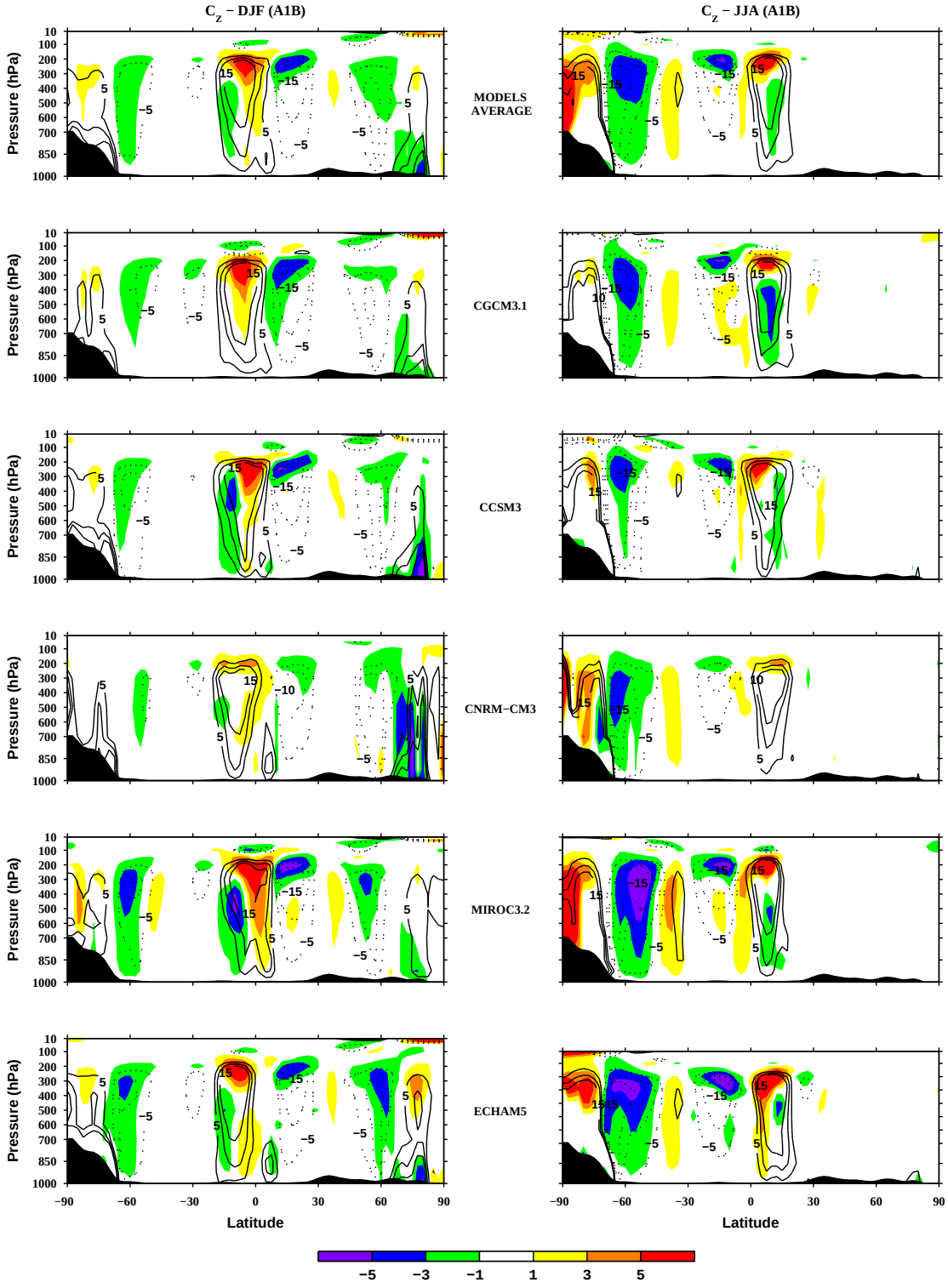

Figure 5.9: The same as in Figure 5.3, but for the conversion rate of eddy available potential energy to eddy kinetic energy, C_Z, computed with the "$\omega\alpha$" formulation.

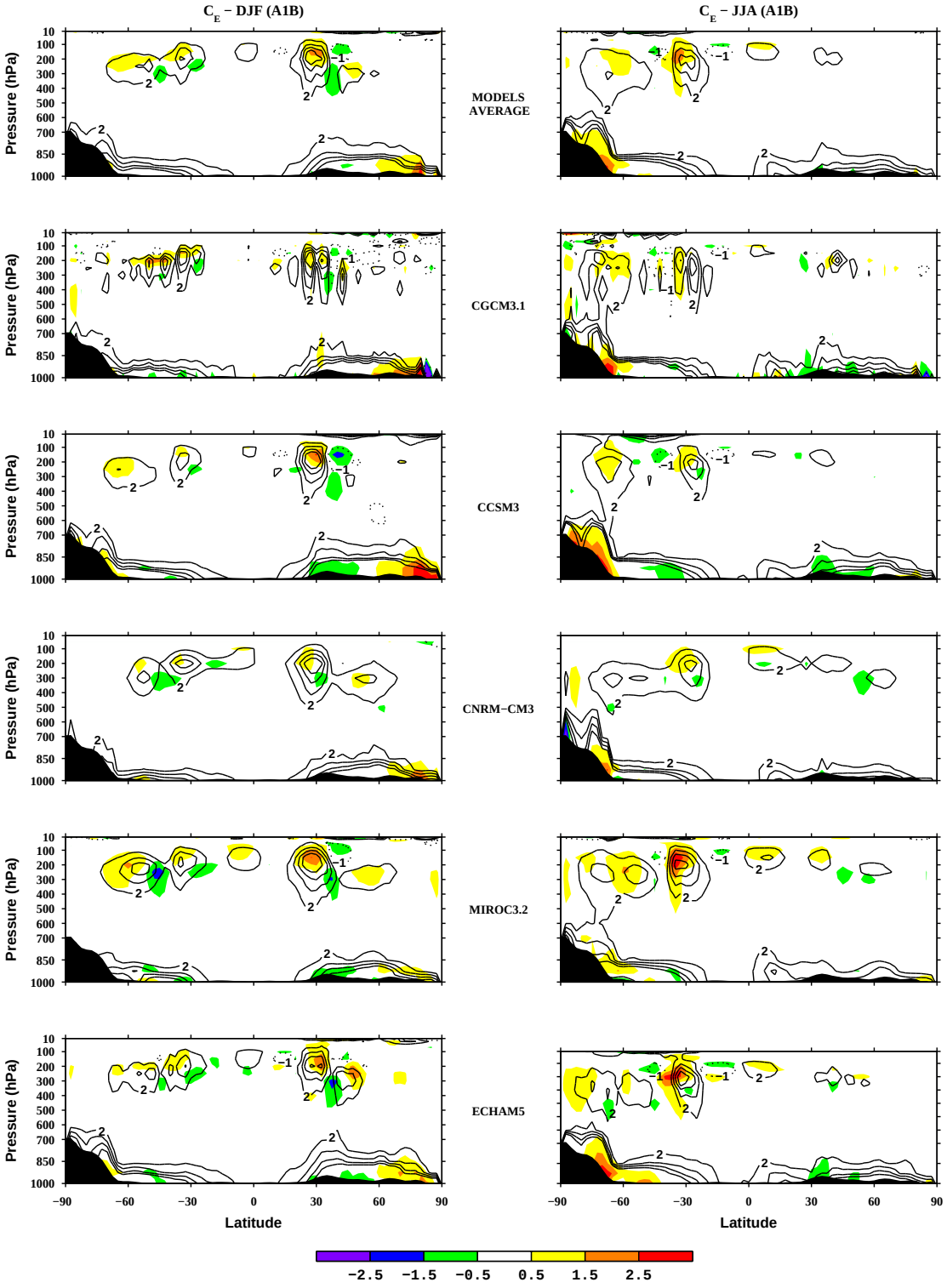

Figure 5.10: The same as in Figure 5.5, but computed with the "$\mathbf{v} \cdot \nabla z$" formulation.

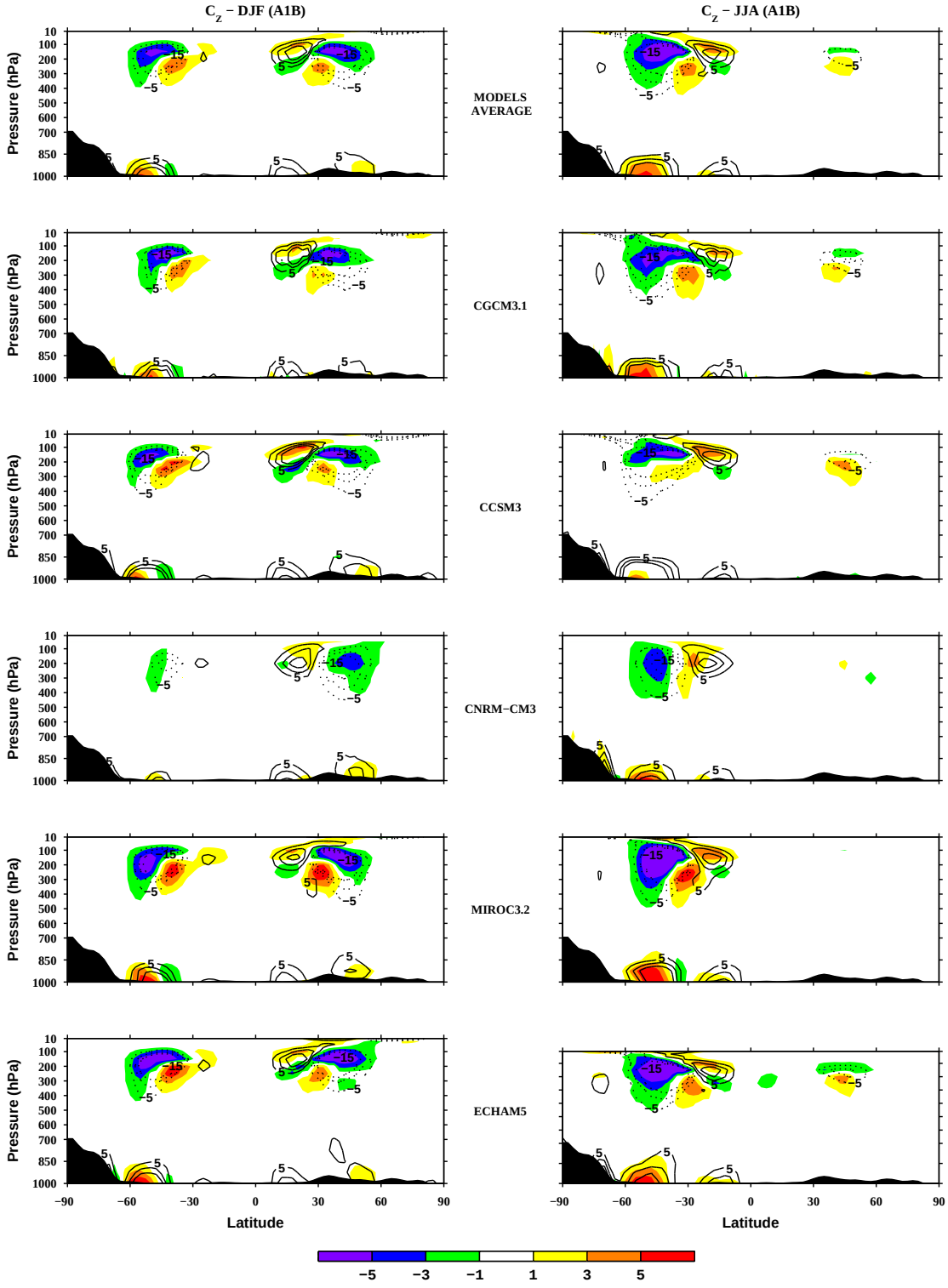

Figure 5.11: The same as in Figure 5.9, but computed with the "$\mathbf{v} \cdot \nabla z$" formulation.

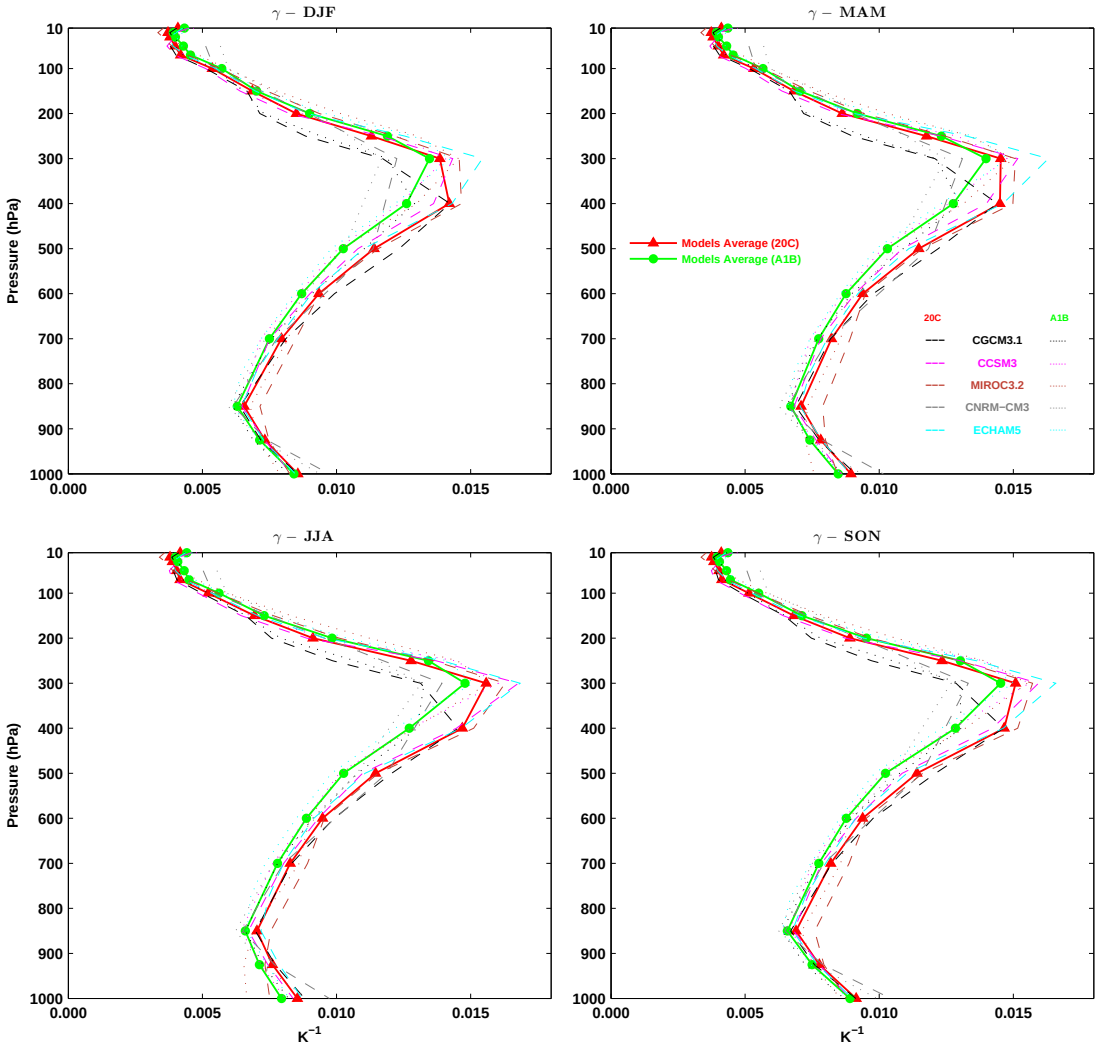

Figure 5.12: Mean vertical profile of the stability parameter, γ, for the climate models. Averages are over 1970-1999 for the 20C climate and over 2070-2099 for the A1B climate for all seasons: DJF (Top left), MAM (Top right), JJA (Bottom left) and SON (Bottom right). Units are K^{-1}.

For completeness, the cross-sections for the conversion rates C_E and C_Z computed with the $\mathbf{v}\cdot\nabla z$ formula are displayed in Figures 5.10 and 5.11, respectively. These terms are related to the horizontal cross isobaric flow down the pressure gradient in the eddies and the zonal mean, respectively, and therefore the structures in their cross-sections are locally different from that of same terms computed with the $\omega\alpha$ formula.

5.2 Saltzman energy cycle

In the previous section it has been shown a clear strengthening of the Lorenz energy cycle in the upper troposphere/lower stratosphere and the weakening of the cycle below, for the A1B climate relative to the 20C climate. These two opposite responses suggest an increase in baroclinic activity in the upper region and a reduction below, leading to a global decrease in the energy flow from A_Z to A_E to K_E, and to an increase in C_K together with a significant increase in K_Z.

In this section the zonal wavenumber spectra of the energy cycle terms are analysed to assess the changes in the A1B climate among the different scales of eddies. The spectra of the zonal-mean interactions of available potential and kinetic energies, $R(n)$ and $M(n)$, together with the conversion rate of available potential energy into kinetic energy in wavenumber n, $C(n)$, are shown in Figure 5.13, for DJF and JJA of both the 20C and A1B climates. The terms $R(n)$ and $C(n)$ are responsible for the energy flow from A_Z to A_E to K_E, whereas term $M(n)$ represents the energy transfer rate from K_E to K_Z (see section 2.2.3 for the correspondence between the energy cycle terms of Lorenz with that in the zonal wavenumber formulation of Saltzman). The spectra for the available potential and kinetic energies, $A(n)$ and $K(n)$, and for their wave-wave interactions, $S(n)$ and $L(n)$, are illustrated in Figure 5.14. The contributions from the longer waves $n = 1 - 6$ and from the intermediate to short waves $n = 7 - 72$ for the wavenumber energetics, are displayed in table 5.1, to help in the analysis of Figures 5.13 and 5.14.

For the A1B climate, it is generally seen an increase of $C(n)$ in the longer waves ($n = 1 - 6$), whereas in the intermediate to short waves ($n = 7 - 72$) it decreases (Figure 5.13 and Table 5.1). The same is also true for $R(n)$, although the increase in the longer waves is much smaller or even absent, as in the DJF season. On the other hand, the increase of $M(n)$ is clearly seen in the longer waves, but it remains virtually unchanged in the intermediate to short waves. This reflects that the increase of baroclinic activity at the upper region is due to the large-scale waves, whereas its

reduction at the lower region is due to the short-scale waves, which is in line with observations, the energy containing eddies in the wintertime stratosphere have larger horizontal wavelengths than the eddies in the troposphere (Held, 1993).

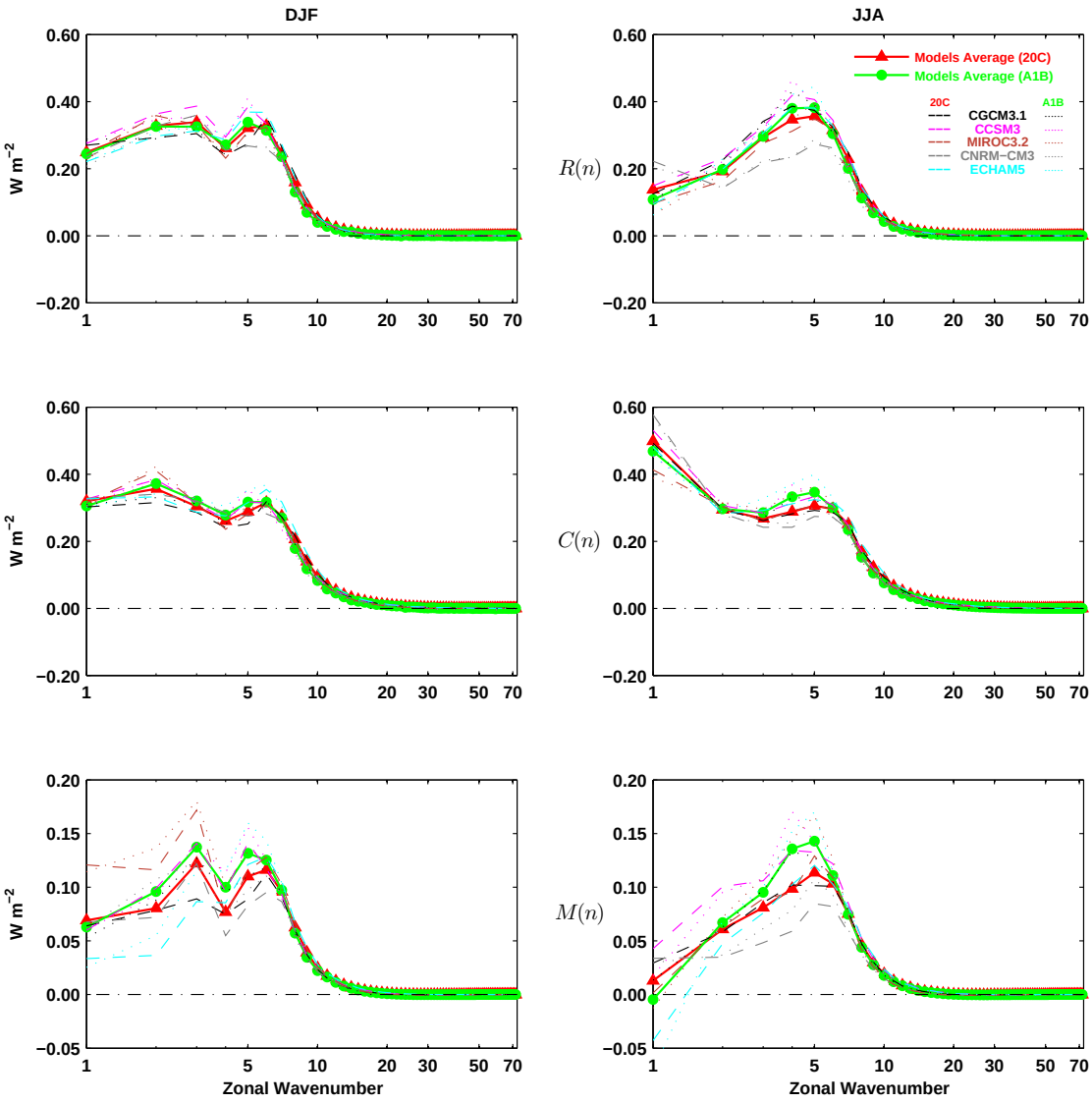

Figure 5.13: Zonal wavenumber spectra for zonal-wave interactions of available potential energy ($R(n)$, top row) and kinetic energy ($M(n)$, bottom row), and for the conversion of $A(n)$ to $K(n)$ ($C(n)$, middle row). The values for the individual models are represented for both the 20C (dashed lines) and the A1B (dotted lines) climates, along with the models' averages for both the 20C (red triangles) and A1B (green circles), for DJF (left) and JJA (right). Units are W m^{-2}.

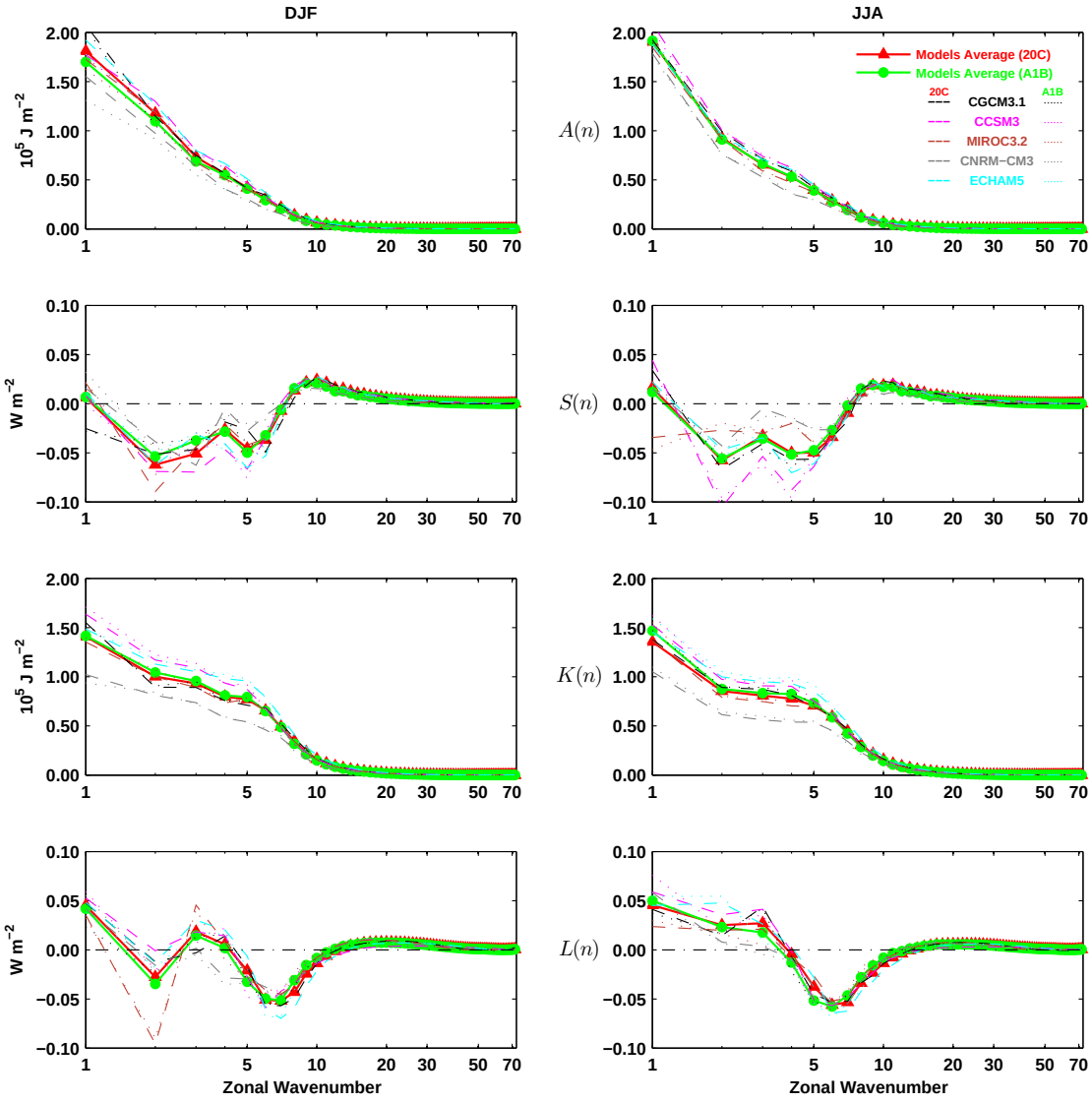

Figure 5.14: As in Figure 5.13 but for available potential and kinetic energies in wavenumber n, $A(n)$ and $K(n)$, and their wave-wave interactions, $S(n)$ and $L(n)$. Units are 10^5 J m^{-2} for energy levels and W m^{-2} for interactions.

The zonal wavenumber spectra of kinetic energy, $K(n)$, also shows an increase in the longer waves and a decrease in the intermediate to short waves for the A1B climate, which is consistent with the spectra of $C(n)$. On the other hand, the spectra of available potential energy, $A(n)$, shows a global decrease for all wavenumbers (Figure 5.14 and Table 5.1). It could have been expected an increase of $A(n)$ in the longer waves, reflecting the increase response in the stratosphere. However, analysing the cross-

sections for the largest scale planetary waves ($n = 1 - 3$), which contain most of $A(n)$, it is found that their distributions are spread over both the stratosphere and troposphere (not shown), and thus the increase stratospheric response is dominated by the decrease tropospheric response also in the longer waves. Globally, the wave-wave interactions of both the available potential and kinetic energies, $S(n)$ and $L(n)$, respectively, show less activity in the A1B climate. On the one hand, the long waves ($n \simeq 2 - 7$) transfer slightly less available potential energy to the shorter waves ($n \gtrsim 8$), and on the other hand, the synoptic waves ($n = 5 - 10$) also transfer slightly less kinetic energy to both the planetary and short waves.

Table 5.1: Energetics of the climate models average for the longer waves $n = 1 - 6$, and for the intermediate to short waves $n = 7 - 72$, in DJF and JJA of both the 20C and A1B climates. Units are 10^5 J m^{-2} for energy levels and W m^{-2} for conversion/transfer rates.

		DJF		JJA	
	n	20C	A1B	20C	A1B
$R(n)$	$1 - 6$	1.83	1.83	1.64	1.67
	$7 - 72$	0.69	0.59	0.64	0.53
$C(n)$	$1 - 6$	1.84	1.91	1.95	2.03
	$7 - 72$	1.08	0.95	1.01	0.90
$M(n)$	$1 - 6$	0.57	0.65	0.47	0.55
	$7 - 72$	0.28	0.27	0.21	0.20
$A(n)$	$1 - 6$	5.00	4.74	4.70	4.69
	$7 - 72$	0.77	0.72	0.75	0.70
$K(n)$	$1 - 6$	5.57	5.67	5.09	5.32
	$7 - 72$	1.89	1.78	1.77	1.65

5.3 Normal mode energetics

Energy levels

The strengthening of the atmospheric energy cycle in the upper troposphere/lower stratosphere and the weakening of the cycle below, suggesting an increase of baroclinic activity at the upper region mostly due to the large-scale waves, and a reduction at the lower region mainly due to the intermediate and short-scale waves, has been assessed in sections 5.1 and 5.2, for the A1B climate relative to the 20C climate. Furthermore, these changes were attributed to the warming pattern simulated for the A1B climate, with the strongest warming in the upper tropical troposphere and in the lower troposphere at high latitudes.

The 3-D normal mode energetics scheme may give further insight on the changes in the atmospheric energy cycle due to higher greenhouse gas concentrations. The results discussed in the previous sections may be complemented or additionally supported with the 3-D normal mode scheme, specially by using the separation of the energetics into the barotropic and baroclinic components. Thus, the results obtained with this scheme are presented and discussed troughout the remainder of this section.

Figure 5.15 shows the zonal wavenumber spectra of total energy, E_{nlk}, for each climate model and for the models' average in DJF, of both the 20C and A1B climates. The separations into barotropic-baroclinic and Rossby-gravity modes are presented as in Figure 4.26. It isn't detected relevant changes in the basic characteristics of total energy E_{nlk} spectra for the A1B climate relative to the 20C climate, appart from the expected changes in the magnitude of the spectra at each wavenumber, in line with the results of section 5.2. Globally, the total eddy energy in the A1B climate decreases at the higher wavenumbers for all components, both the barotropic and baroclinic, and Rossby and gravity, and increases (decreases) at the lower wavenumbers for the barotropic (baroclinic) component of both Rossby and gravity modes. On the other hand, the universal power law behaviour in the E_{nlk} spectra for the present climate (Figure 4.60), is also found in the future climate for both the barotropic and baroclinic

components, and within the Rossby and gravity modes.

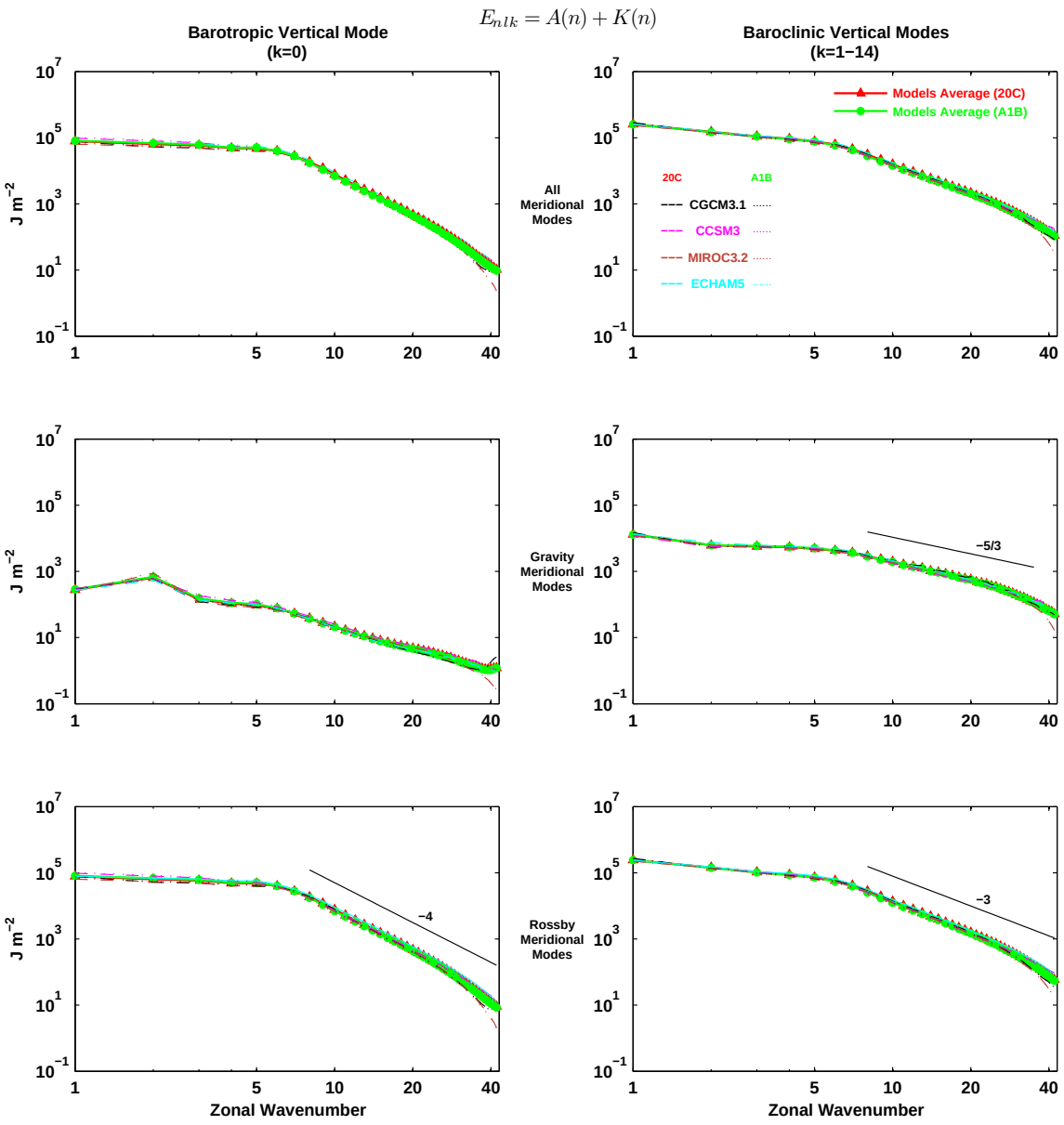

Figure 5.15: As in Figure 4.26, but for each climate model and the models' average in DJF of both 20C and A1B climates.

The wavenumber spectra of available potential energy, $A(n)$, and kinetic energy, $K(n)$, are depicted in the left and right panels of Figure 5.16, respectively. As for the spectra of E_{nlk}, the basic characteristics, related to the power law behaviour in the $A(n)$ and $K(n)$ spectra, are common to both climates. The global decrease of the total eddy

energy for the A1B climate, found above in the lower wavenumbers of the baroclinic component, is due to the decrease of $A(n)$ which dominates the increase of $K(n)$ in the same wavenumbers. For the barotropic component, $A(n)$ increases slightly in the lower wavenumbers, and thus E_{nlk} also increases in these wavenumbers.

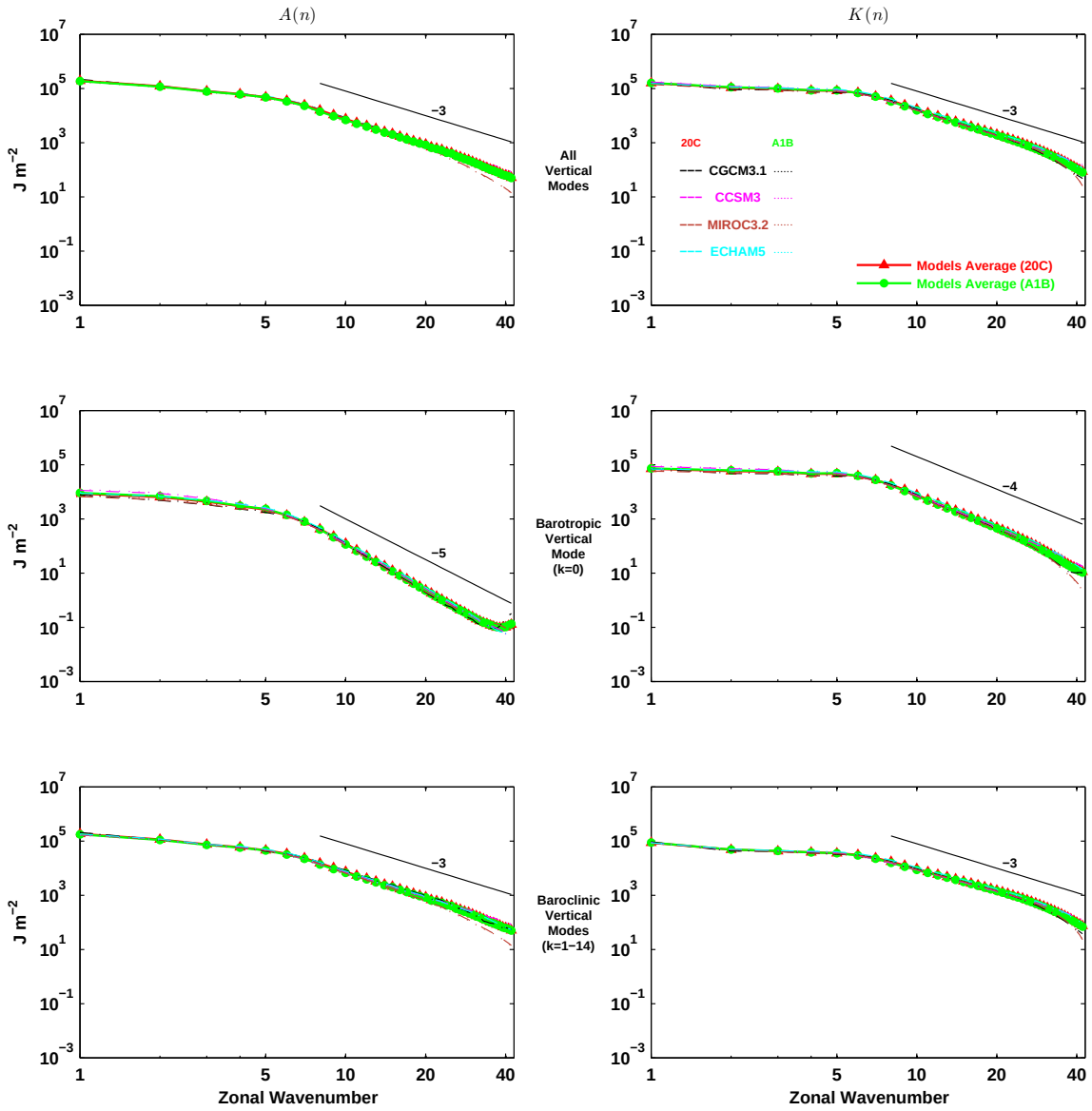

Figure 5.16: As in Figure 4.28, but for each climate model and the models' average in DJF of both 20C and A1B climates.

Figure 5.17 shows the total energy spectra in the vertical mode domain. For the A1B climate, it is seen typically an increase of total energy at the baroclinic modes $k = 3-4$, and also a slight increase at the barotropic mode $k = 0$, in both the zonal mean and eddy components, and in both the Rossby and gravity modes.

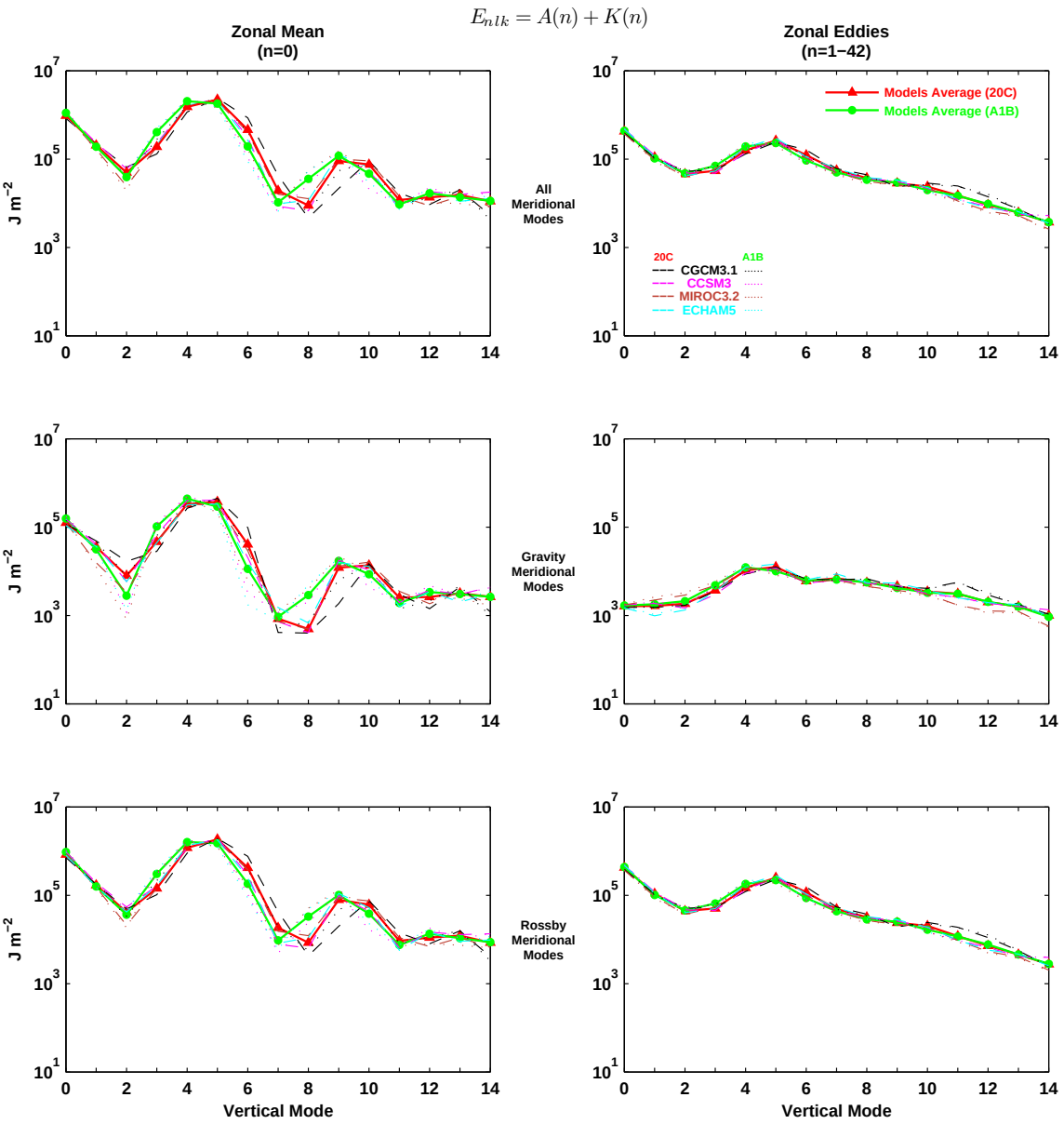

Figure 5.17: As in Figure 4.29, but for each climate model and the models' average in DJF of both 20C and A1B climates.

Most of the variations in vertical structures of the baroclinic modes $k = 3-4$ are found in the UTLS (see Figure 4.25), with their first node at about 300-400 hPa. Therefore, these modes should reflect essentially the energetics changes in the UTLS, as captured in their vertical structures. This is consistent with the increase of baroclinic energy in the upper region, leading to a strengthening of the energy cycle, due to the increase of baroclinic activity in response to the warming pattern in this region. This is also true for both the zonal mean and eddy components of available potential and kinetic energies, as seen in their vertical mode spectra illustrated in Figure 5.18.

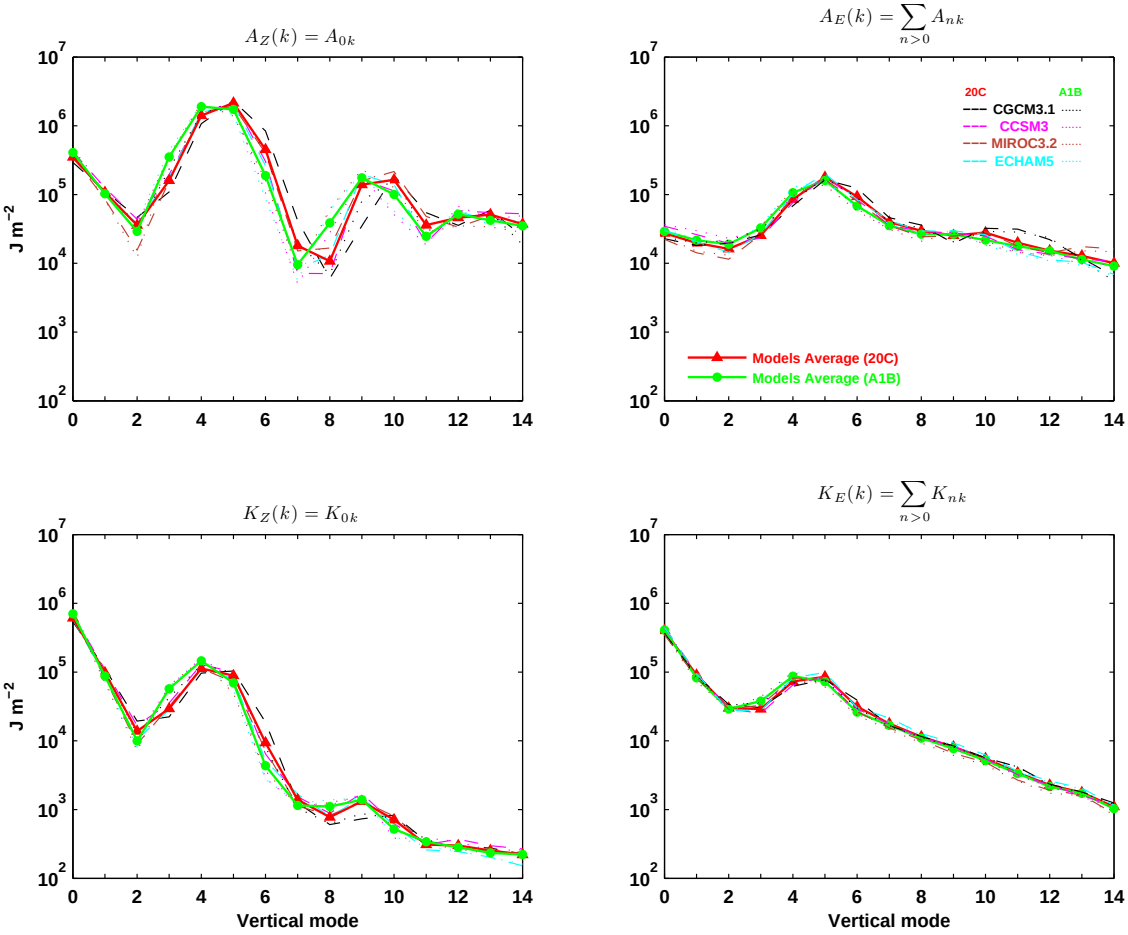

Figure 5.18: As in Figure 4.30, but for each climate model and the models' average in DJF of both 20C and A1B climates.

An energy decrease is seen in modes $k = 5 - 7$ (Figures 5.17 and 5.18), suggesting that the decrease response in the lower levels, is dominating via increased variations

in the vertical structures of these modes at lower levels, as compared to the low order modes $k \leq 4$. The maximum of $A_Z(k)$ and the secondary maximum of $K_E(k)$ are found at $k = 4$ for the A1B climate, whereas the same maxima where found at $k = 5$ for the 20C climate. The secondary maximum of $K_Z(k)$ is also more clearly defined at $k = 4$ for A1B, while for 20C the modes $k = 4$ and 5 have nearly the same amount of zonal kinetic energy. This also suggests a vertical structure change in the tropospheric jets.

Figure 5.19 shows the total eddy energy spectra in the meridional mode domain. For the A1B climate, it was found, in general, an increase of energy in the lowest meridional modes of both the barotropic and baroclinic components, and for both Rossby and gravity modes. On the other hand, an overall decrease of energy was found in the higher meridional modes of all components. Thus, these spectra also suggest a strengthening of the planetary and cyclone-scale waves, and, on the other hand, a weakening of the short-scale waves in the A1B climate.

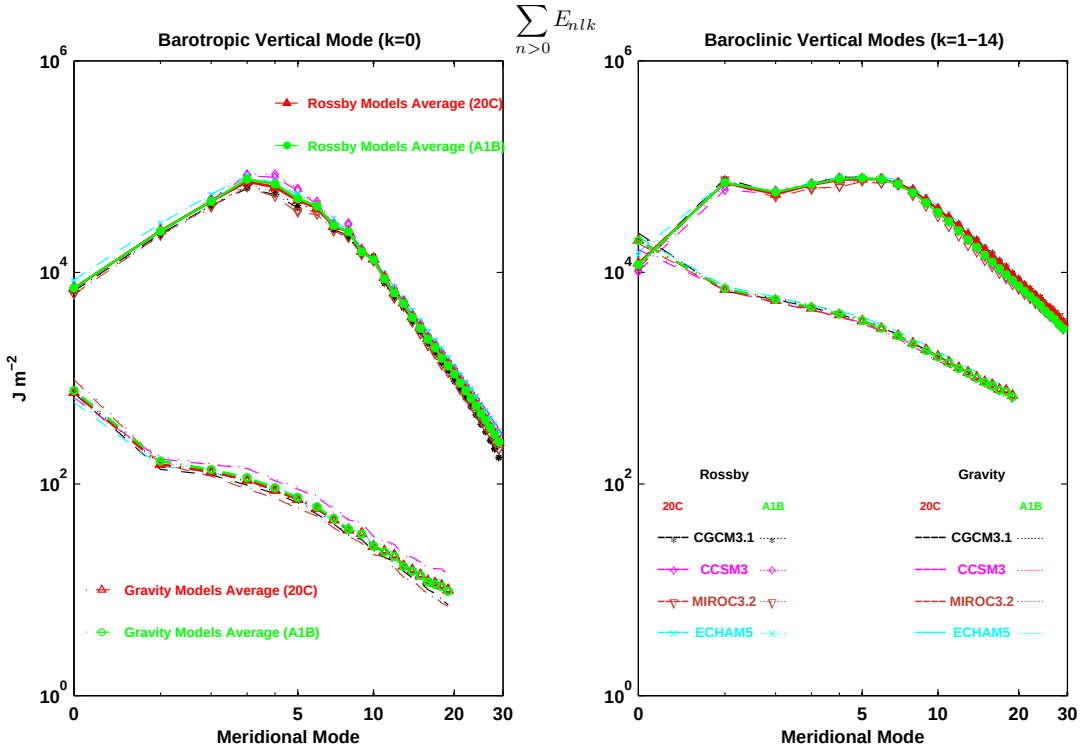

Figure 5.19: As in Figure 4.31, but for each climate model and the models' average in DJF of both 20C and A1B climates.

Energy interactions

The zonal wavenumber spectra for the interactions of available potential energy, C_{nlk}, are illustrated in Figure 5.20. For the A1B climate, it is seen a decrease in the baroclinic component of C_{nlk} for wavenumbers $n \geq 6$, which means a combined weakening of the wave-wave and wave-mean interactions of available potential energy, $S(n) + R(n)$. The net result for the lowest wavenumbers $n = 1 - 5$ of the baroclinic component, corresponding to the larger scales, yields virtually no change. In the barotropic component of C_{nlk} it is also undetected appreciable changes at all wavenumbers, suggesting therefore that most of the energetics responses to increases of greenhouse gas concentrations, are through changes in baroclinic activity.

Figure 5.21 shows the spectra for the interactions of kinetic energy, B_{nlk}, in the zonal wavenumber domain. The eddies in the baroclinic component of B_{nlk} show a strengthening in the larger scales, and a weakening in the smaller scales, for the A1B climate, which agrees with the increases and decreases of $M(n)$ in the same scales, as shown in Figure 5.13. The barotropic eddies in B_{nlk} don't show appreciable changes, which means that the amount of kinetic energy flowing from the baroclinic component into the barotropic component is virtually the same in both A1B and 20C climates. Therefore, the increase in the baroclinic component of B_{nlk}, must represent the increased transfer rate of kinetic energy from the eddy component to the zonal mean component, specially in the large-scale waves, which leads ultimately to the increase of the zonal mean kinetic energy in the A1B climate.

These results discussed above for the interactions of available potential and kinetic energies, C_{nlk} and B_{nlk}, support and complement the results of sections 5.1 and 5.2. The changes in the baroclinic component of C_{nlk}, correspond to the global decrease of C_A (Figure 5.3), and to the decrease of $R(n)$ in the higher wavenumbers, which is nearly unchanged in the lowest wavenumbers (Table 5.1). The increase in the large-scale waves of the baroclinic component of B_{nlk}, represents the global increase of C_K (Figure 5.7) and the increase of $M(n)$ in the lowest wavenumbers (Table 5.1). These

features abovementioned for interactions C_{nlk} and B_{nlk}, are mostly characteristic of the Rossby modes, since, on the one hand, the energetics of the gravity waves are usually small, and, on the other hand, the flow of energy within the gravity modes is sometimes in the opposite direction from that of the Rossby modes, as seen in Figure 5.21 for example.

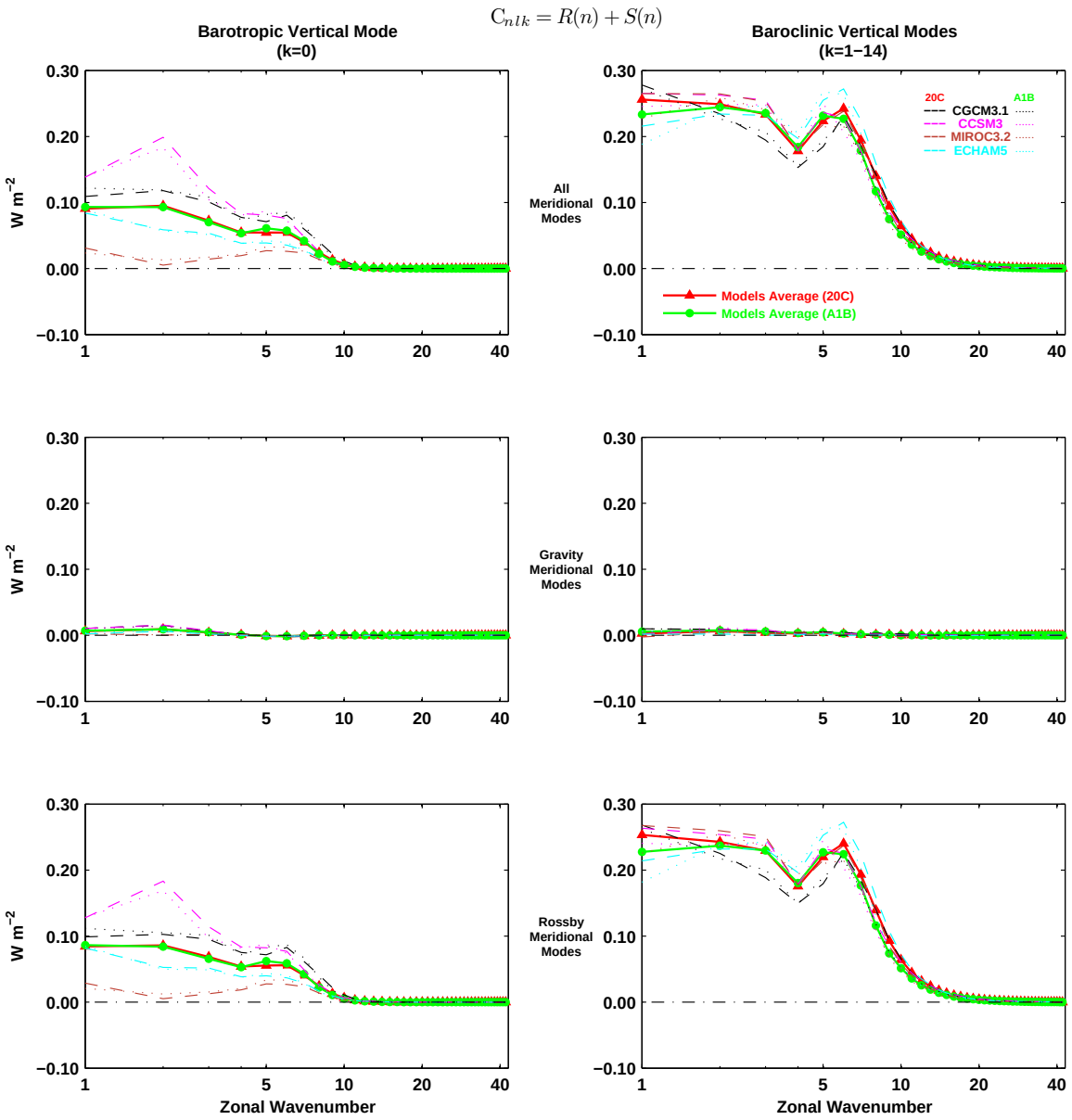

Figure 5.20: As in Figure 4.32, but for each climate model and the models' average in DJF of both 20C and A1B climates.

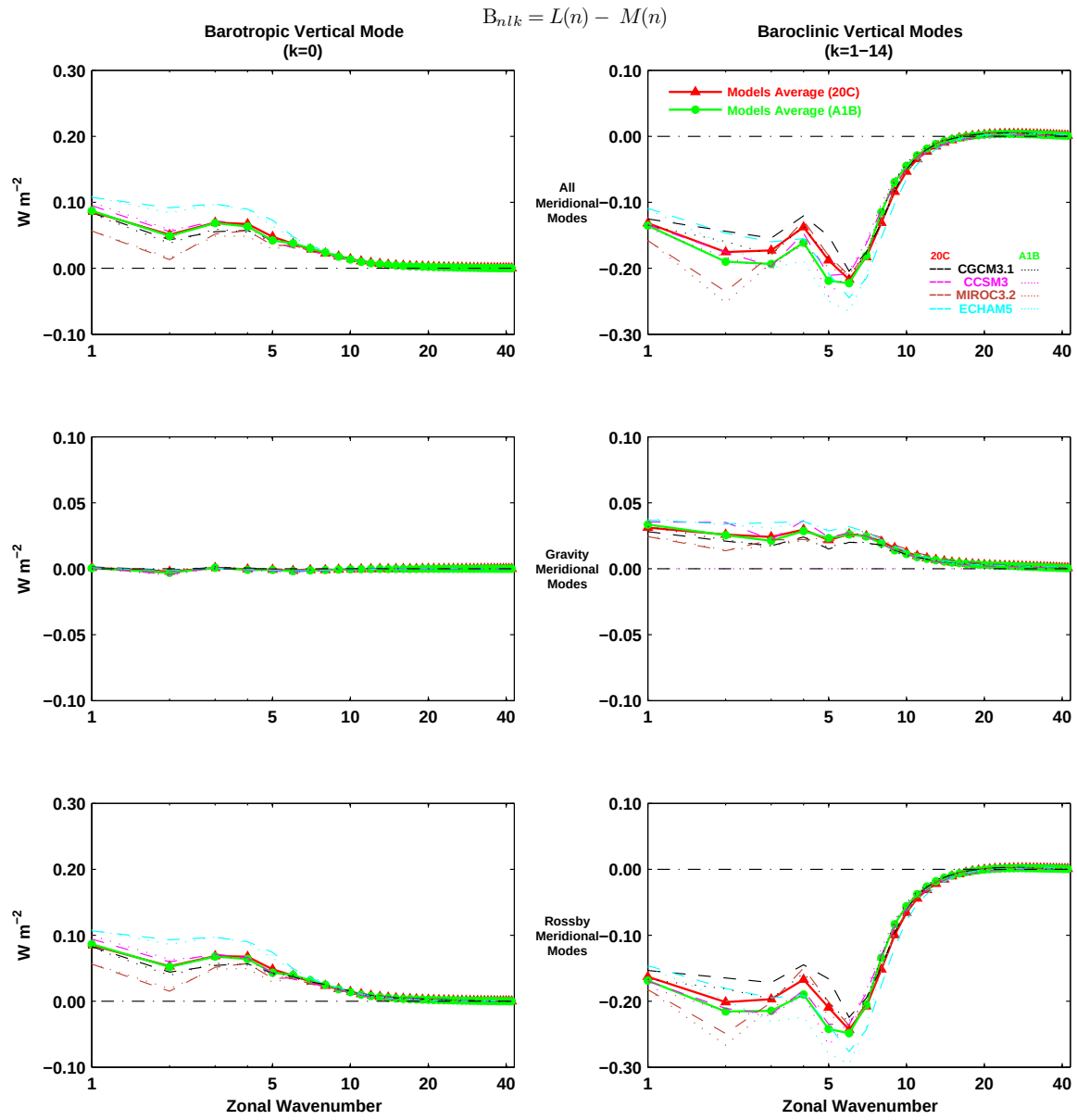

Figure 5.21: As in Figure 4.33, but for each climate model and the models' average in DJF of both 20C and A1B climates.

Figure 5.22 shows the interactions of available potential energy, C_{nlk}, in the vertical mode domain. For the Rossby modes of the future climate A1B, it is seen that the absolute value of the zonal mean component of C_{nlk} increases in the baroclinic modes $k = 3 - 4$, and secondly at the barotropic mode $k = 0$, whereas the absolute value of C_{nlk} decreases in the baroclinic modes $k = 5 - 6$ of the same component. These

changes in the zonal mean component of C_{nlk} are balanced by an increase of C_{nlk} in the baroclinic modes $k = 3 - 4$ of the eddy component, and by a decrease in the baroclinic modes $k = 5 - 7$ of the same component. When considering the contributions of all meridional modes, the absolute increase of C_{nlk} in the barotropic mode $k = 0$ of the zonal mean component, is reinforced due to the gravity mode, which has a comparable value in this vertical mode to that of the Rossby mode. The contribution from the gravity modes in the eddy component of C_{nlk} is neglegible for all vertical modes.

The spectra for the interactions of kinetic energy, B_{nlk}, are illustrated in Figure 5.23 as a function of the vertical mode. Within the Rossby modes of the future climate, it is seen that the baroclinic modes $k = 3 - 4$ ($k = 5 - 6$) of the eddy component supply higher (lower) amounts of kinetic energy, which must be transferred into both the barotropic mode of the same component, and the zonal mean flow. This is accompanied by an increase of B_{nlk} in the barotropic $k = 0$ and baroclinic modes $k = 3 - 4$ of the zonal mean component, and a decrease in the baroclinic mode $k = 5$ of the same component, whereas the barotropic mode of the eddy component is unchanged. Considering all meridional modes together, the increase in the zonal mean component of B_{nlk} is essentially seen in the barotropic mode and secondly in the baroclinic mode $k = 4$. For the gravity modes, the flow of kinetic energy is from the zonal mean to the eddy component, in the manner suggested by classical turbulence theory.

As for the energy spectra discussed previously, the overall increases seen in interactions C_{nlk} and B_{nlk} at the baroclinic modes of low order ($k = 3 - 4$), should reflect the changes in the UTLS of the future climate, whereas the decreases in the baroclinic modes of higher order ($k = 5 - 7$) must correspond to the changes in the lower and middle troposphere where the decrease response dominates. Therefore, the decrease in the lower region of the transfer rate of available potential energy from the zonal mean to the eddy component, C_A, as seen in Figure 5.3 for the A1B climate, is mostly due to a weakening in the baroclinic disturbances of intermediate to short scales, reflected in the internal (or baroclinic) modes $k = 5 - 7$, as seen in Figures 5.20 and 5.22. On the other hand, the increase in the upper region of the transfer rate from eddy to zonal

kinetic energy, C_K, as seen in Figure 5.7, is the consequence of a strengthening in the baroclinic disturbances of planetary to synoptic scales, reflected in the internal modes $k = 3 - 4$, as seen in Figures 5.21 and 5.23.

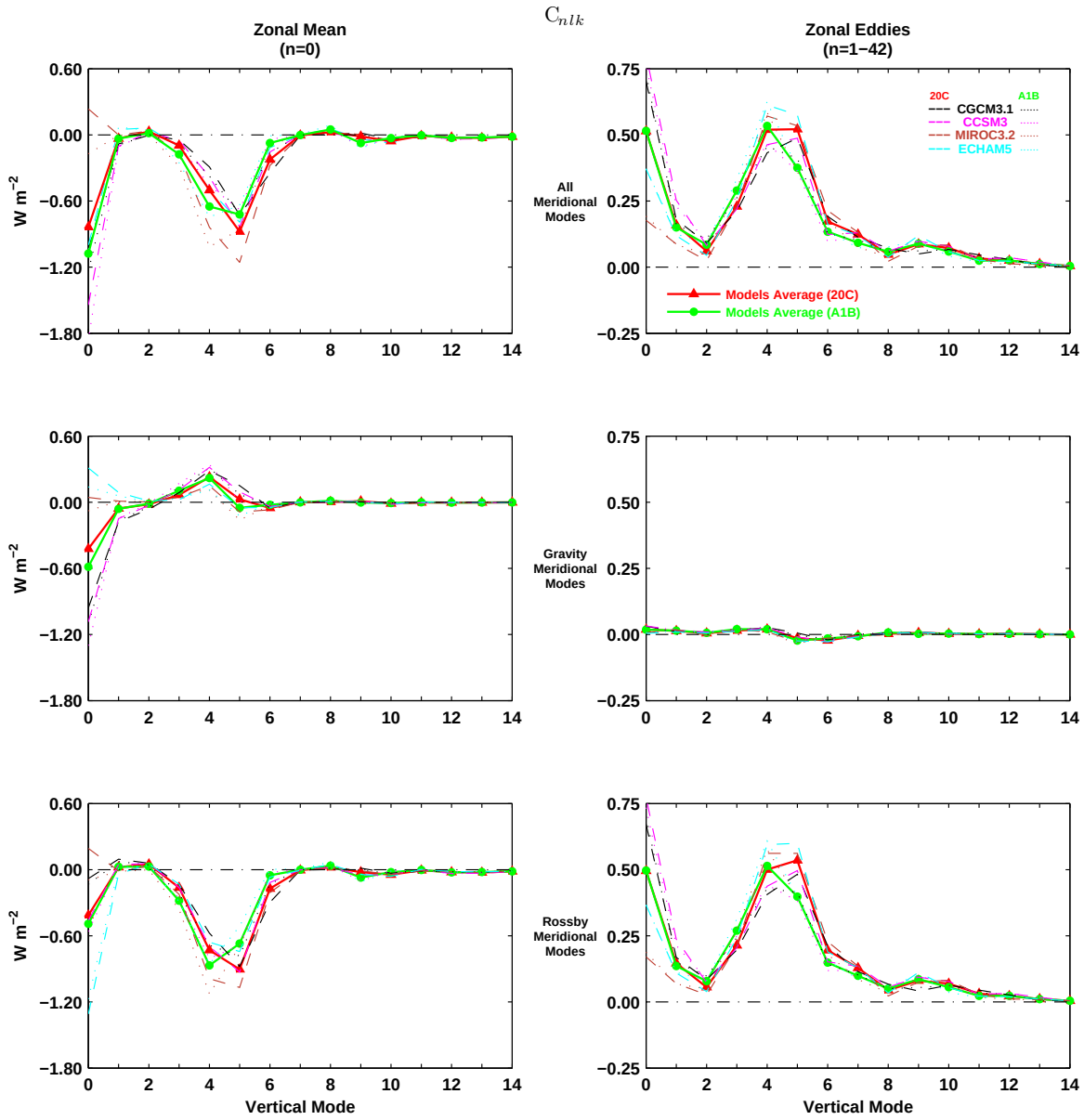

Figure 5.22: As in Figure 4.34, but for each climate model and the models' average in DJF of both 20C and A1B climates.

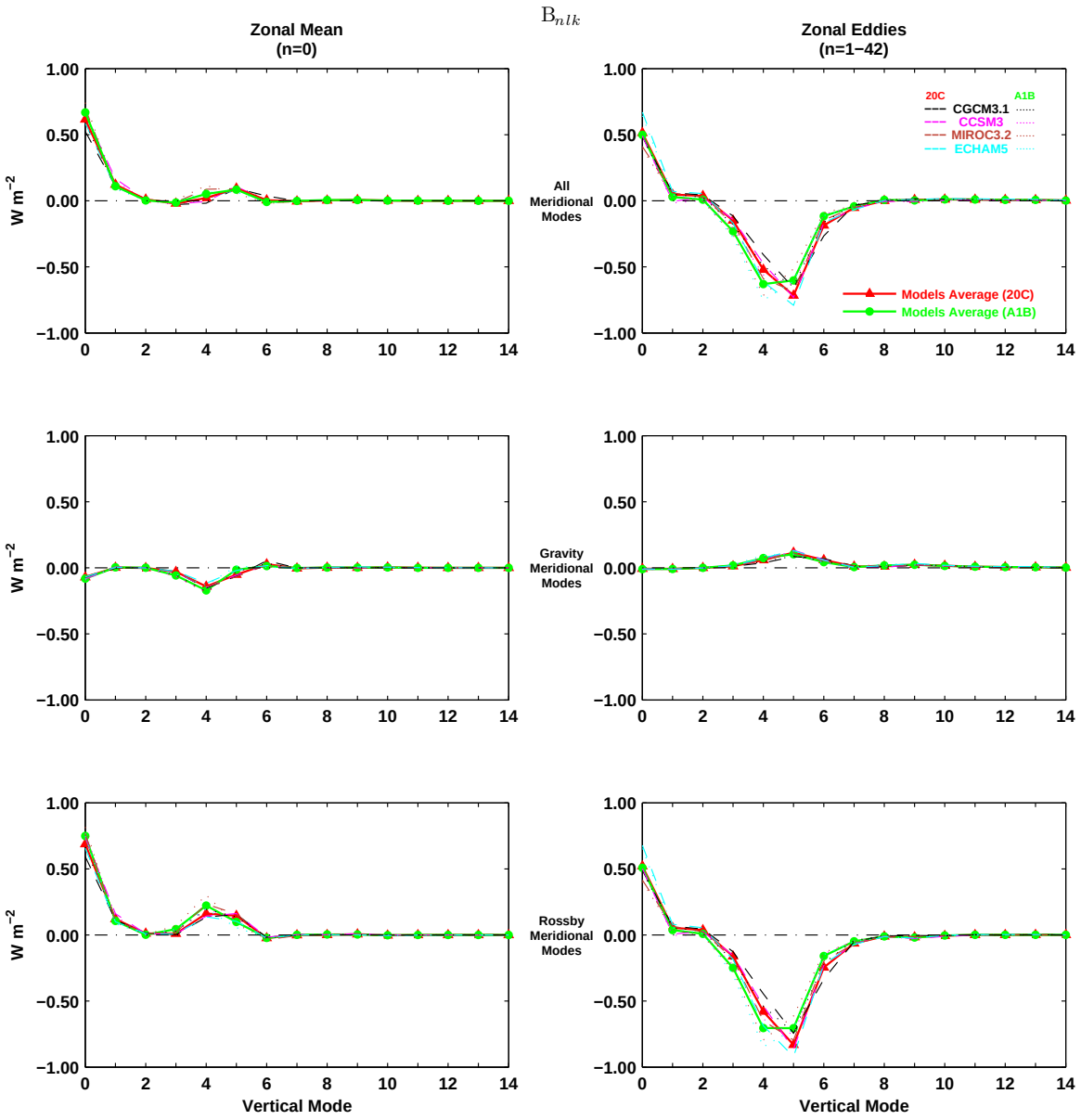

Figure 5.23: As in Figure 4.35, but for each climate model and the models' average in DJF of both 20C and A1B climates.

Figure 5.24 shows the interactions of eddy available potential, $\sum_{n>0} C_{nlk}$, and eddy kinetic energies, $\sum_{n>0} B_{nlk}$, in the meridional mode domain. Once again, it is seen that these interactions are essentially determined by the Rossby modes. The decrease response dominates in the baroclinic component of the interactions of eddy available potential energy, which means that less energy is globally supplied into the eddy com-

ponent in the future climate. On the other hand, the interactions of eddy kinetic energy are dominated by an increase of energy that is supplied from the eddy component in the modes $l_r = 3 - 6$. The net result for the barotropic component yelds virtually no change in both eddy interactions.

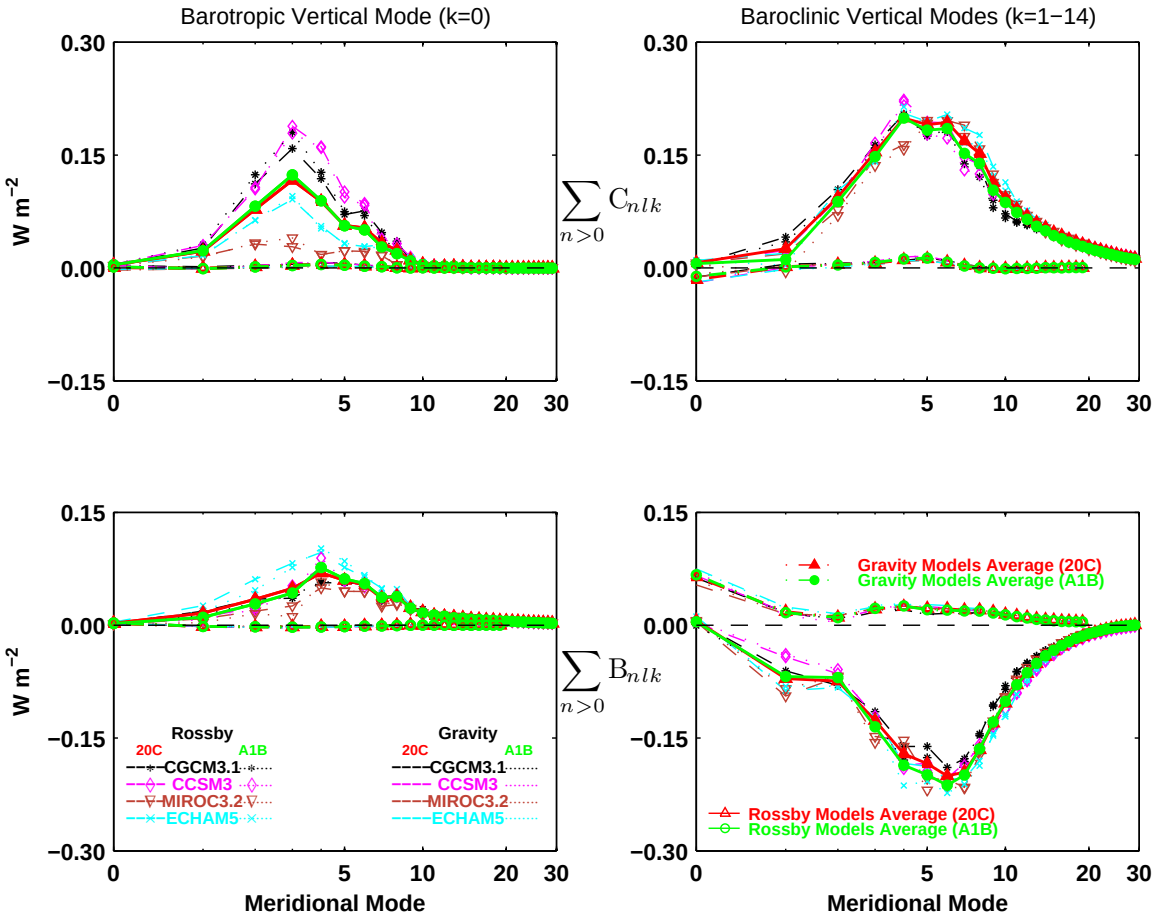

Figure 5.24: As in Figure 4.36, but for each climate model and the models' average in DJF of both 20C and A1B climates.

Energy conversion

The spectra for the conversion rate of eddy available potential energy into eddy kinetic energy, $C(n)$, are displayed in Figure 5.25, in the zonal wavenumber domain. The barotropic component is negligible, which confirms the baroclinic nature of conversion $C(n)$. It is seen increased baroclinic conversion rates for the A1B climate in the eddies of larger scales ($n \leq 6$), whereas the conversion rate is reduced in the eddies of smaller

scales ($n \geq 7$). This result is rather similar with that displayed in Figure 5.13, which was obtained using Saltzman's formulation.

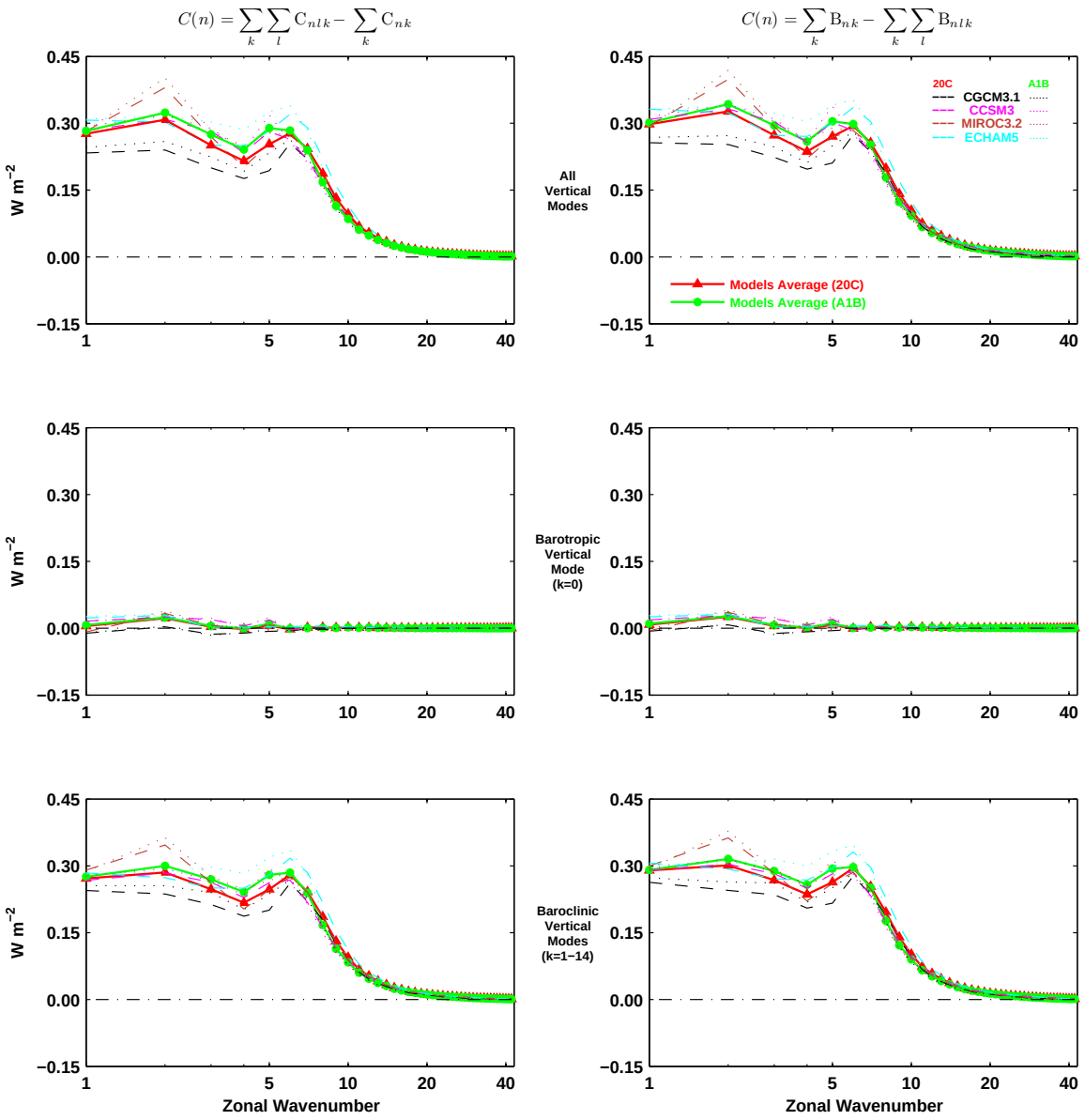

Figure 5.25: As in Figure 4.37, but for each climate model and the models' average in DJF of both 20C and A1B climates.

The vertical spectra for the conversion rate of available potential energy A into kinetic energy K, are illustrated in Figure 5.26. The conversion rate between the zonal mean components of A and K, i.e. $C_Z(k)$, is small in both climates, having therefore little

weight in the energetics. For the A1B climate, an increase of the conversion rate between the eddy components of available potential and kinetic energies, $C_E(k)$, is seen in the baroclinic modes $k = 3-4$, whereas a decrease of $C_E(k)$ is seen in the baroclinic modes $k = 5-6$. The maximum of $C_E(k)$ has changed from $k = 5$ to $k = 4$ in the A1B climate relative to the 20C climate.

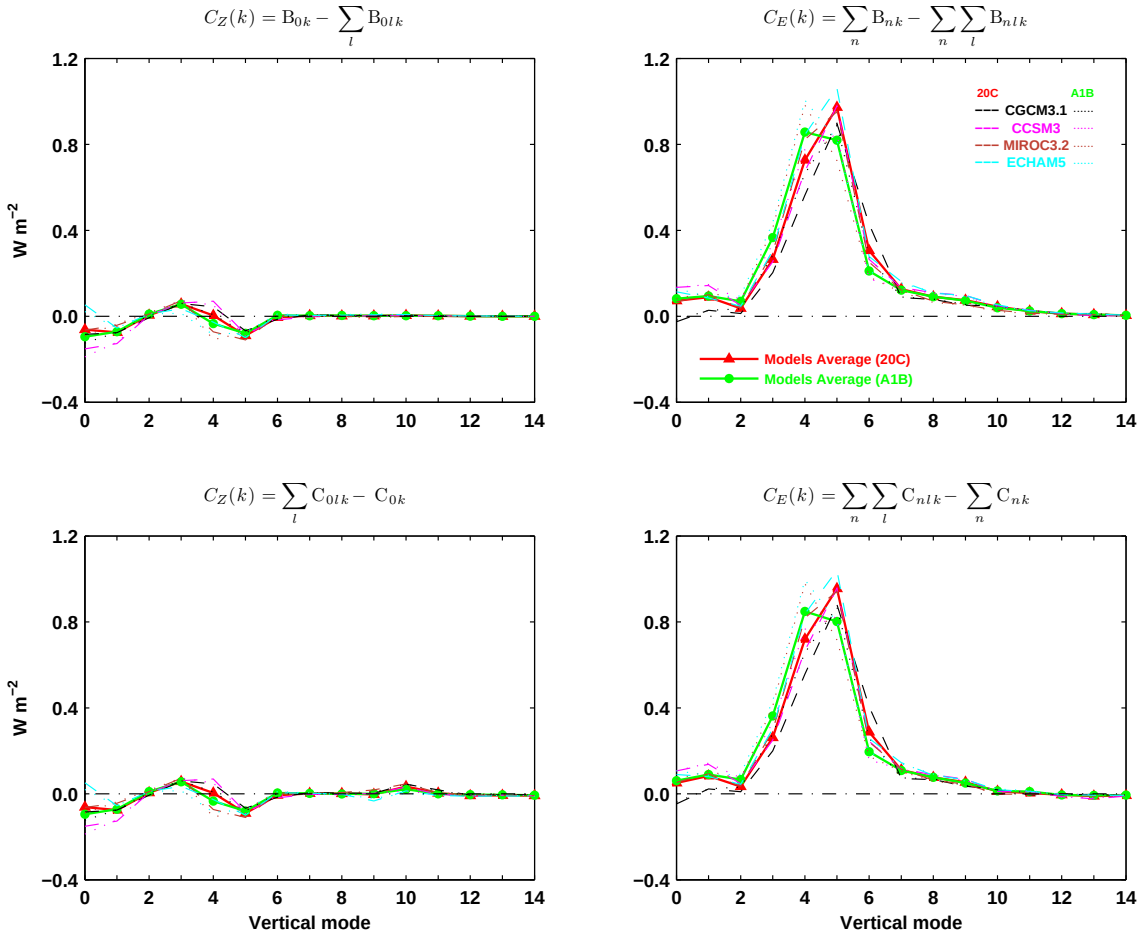

Figure 5.26: As in Figure 4.38, but for each climate model and the models' average in DJF of both 20C and A1B climates.

These results are in line with those for the interactions of available potential and kinetic energies, C_{nlk} and B_{nlk}, respectively. Therefore, the decrease in the A1B climate, of the conversion rate of eddy available potential energy into eddy kinetic energy, C_E, in the lower and middle troposphere, as seen in Figure 5.5, is also due to a weakening in the baroclinic disturbances of intermediate to short scales, which are projected in

the internal modes $k = 5 - 7$, as seen in Figures 5.25 and 5.26. On the other hand, the increase of C_E in the upper region, is driven by a strengthening in the baroclinic disturbances of planetary to synoptic scales, which are captured in the internal modes $k = 3 - 4$.

Energy generation and dissipation

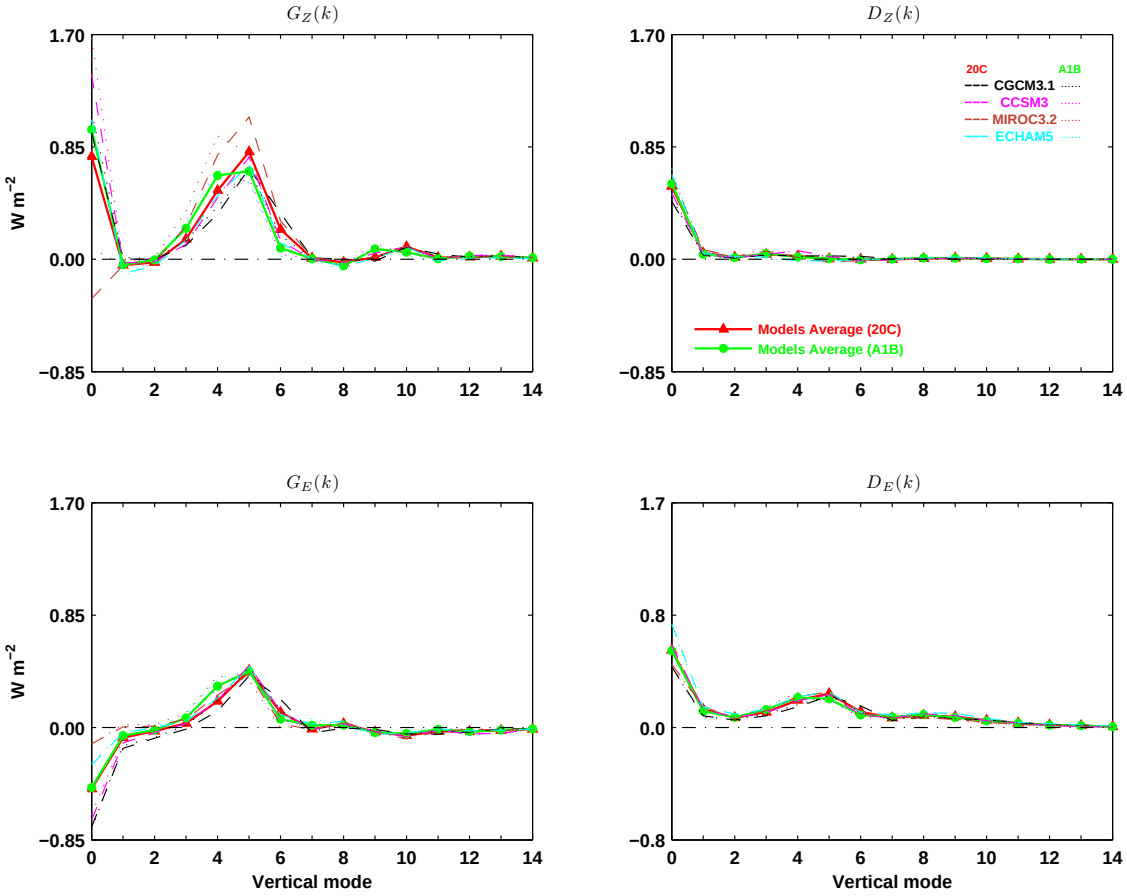

Figure 5.27: As in Figure 4.39, but for each climate model and the models' average in DJF of both 20C and A1B climates.

The vertical spectra of the generation and dissipation terms for the zonal mean and eddy components of available potential energy and kinetic energy, is finally illustrated in Figure 5.27. For the A1B climate, greater amounts of A_Z are generated in the barotropic $k = 0$ and baroclinic modes $k = 3 - 4$, whereas the generation of A_Z is

reduced in the baroclinic modes $k = 5 - 6$. An increase of G_E is seen in the baroclinic modes $k = 3 - 4$, while it is reduced in the baroclinic mode $k = 6$. The net result over all modes yields an increase of D_Z, which is rather small, since it is the result of a small increase in the barotropic mode, and a slight decrease over the baroclinic modes. A global decrease of D_E is obtained by summing the contributions over all vertical modes, with the decreases in the baroclinic modes $k = 5 - 6$ dominating over the increases in the baroclinic modes $k = 3 - 4$.

From the results presented troughout this section, it is concluded that, the energetics for the A1B climate show a global decrease in the Lorenz energy cycle strength, defined as the total conversion of available potential energy A into kinetic energy K, but also an increase in the zonal mean kinetic energy, K_Z, and in the wave-mean interactions of kinetic energy, C_K. These global changes agree rather well with the findings in the study of Hernández-Deckers and von Storch (2010) on the energetics responses to CO_2 increases. They are a consequence of the strengthening of the Lorenz energy cycle in the upper troposphere and lower stratosphere (UTLS), sustained by enhanced baroclinic eddies of large horizontal scales, and the weakening of the cycle below, mostly driven by weaker baroclinic eddies of intermediate to small scales. The results also show a greater generation of A in the upper troposphere, as a consequence of the increase in greenhouse gas concentrations, while it is reduced in the lower troposphere. This is seen in Hernández-Deckers and von Storch (2010), by the Lorenz energy cycle computed for the atmosphere splited at 350 hPa, whereas in this study it is seen by the increases of G_Z and G_E in the low-order baroclinic modes, $k = 3 - 4$, whose structure is concentrated essentially in the UTLS, and by their decreases in the baroclinic modes $k = 5 - 6$, which have increasing structure in the lower and middle troposphere where the decrease response dominates.

The two opposite responses result from the simulated warming pattern that shows the strongest warming in the upper tropical troposphere and in the lower troposphere at high latitudes (e.g. Niehörster et al., 2008). Held (1993) pointed out the dual role of this warming pattern for baroclinic eddies, which can be strengthened by an increase

in pole-to-equator temperature gradient in the upper troposphere but are weakened by the decrease in this gradient in the lower troposphere. An increase of UTLS wave baroclinicity and its decrease in the lower troposphere was reported by Castanheira et al. (2009), which is also consistent with this warming pattern.

In agreement with earlier studies (Boer, 1995; Hernández-Deckers and von Storch, 2010), the weakening of the energy cycle in the middle and lower troposphere is expected from the reduced equator-to-pole temperature gradients, because of high-latitude warming, and the reduced land-sea contrasts during the winter season, because of stronger warming over continents. It reflects a reduction in baroclinic activity, as one prominent change in the global energy cycle. The other prominent feature is the significant increase in K_Z, which is driven by an increase in C_K. The strong increase in K_Z is seen in all five climate models used in this study. Lorenz and DeWeaver (2007) found that the IPCC-AR4 climate models show a strengthening and poleward shifting of the tropospheric zonal jets and of momentum flux in response to global warming, that suggest an increase in both C_K and K_Z, which are dominated by the tropospheric jets. The poleward shifting of the tropospheric zonal jets is visible in both this study and that of Hernández-Deckers and von Storch (2010), as the increase of K_Z in the SH on the poleward side of the jet throughout the whole troposphere.

The tropical upper-troposphere warming is known to be related to moist convection within the tropics (Held, 1993). According to Hernández-Deckers and von Storch (2010), this would suggest that moisture is an important factor in the upper-level strengthening of the energy cycle, although Lorenz and DeWeaver (2007) have argued that the strengthening of the polar jets, which they find in all IPCC models, is mostly driven by the rising of the tropopause rather than by the increase in moisture content, the latter playing a secondary role. However, as pointed by Hernández-Deckers and von Storch (2010), it could be also argued that the tropopause rises mostly because of the strong tropical upper-troposphere warming, which is caused by moisture effects. On the other hand, Schneider et al. (2010) have shown that, because extratropical water vapour dynamics generally decreases meridional potential temperature gradients and

increases the (dry) static stability, it primarily damps eddies, rather than energising them. Therefore, it is also argued by Hernández-Deckers and von Storch (2010) that part of the weakening response of the energy cycle in the lower and middle troposphere is related to the increase in mean static stability (decrease of γ), which is also related to water vapour effects.

In addition, according to Held (1993), the dominant wintertime baroclinic eddies, cohering through the depth of the troposphere, transport energy poleward, and it is the balance between this transport and the pole-to-equator heating gradient that determines the statistically steady temperature gradient on the Earth, as well as the average strength of the eddies. Since the eddies carry moisture also, this transport contributes to the energy transferred poleward. If the water evaporated in the subtropics is transferred to higher latitudes before condensing and releasing its latent heat, the temperature gradient is reduced compared to that which would exist if the vapour condensed at the latitude of evaporation. As the atmosphere becomes moister, this latent heat transport increases, making the eddies more efficient at transporting energy polewards. Smaller eddies are then required to maintain the same temperature gradient, so that eddy amplitude will decrease as the moisture content increases. Pavan et al. (1999) have found that the presence of moisture can either increase or decrease the peak eddy kinetic energy of a developing wave, depending on the initial moisture distribution. A relative abundance of moisture at mid-latitudes tends to weaken the wave, while a relative abundance at low latitudes tends to strengthen it. This seems to be consistent with recent studies indicating a poleward shift of the storm tracks and the midlatitude precipitation zone in the warming world that will lead to subtropical drying and higher latitude moistening (e.g. Wu et al., 2010, and references therein).

Chapter 6

Summary and Conclusions

The global atmospheric energetics was evaluated in the frameworks of the basic decomposition of zonal mean and eddy components of Lorenz (1955), the zonal wavenumber decomposition of Saltzman (1957), and the 3-D normal mode energetics scheme of Tanaka (1985). An extension to the normal mode energetics formulation has been presented in the study, which enables an explicit evaluation of the conversion rate between available potential energy and kinetic energy along with their generation and dissipation rates, in both the zonal wavenumber and vertical mode domains. In addition, it has been proposed an extended energy cycle diagram describing the flow of energy among the zonal mean and eddy components, and also among the barotropic and baroclinic components. The energetics was first assessed for three reanalysis datasets and for the simulations of five state-of-the-art climate models representing the present climate conditions. The analysis was then extended using the datasets simulated by the same five climate models for a future climate scenario experiment, as defined in the SRES of the IPCC.

According to the results obtained from the datasets representing the present climate conditions, it was seen that the basic characteristics of the flow of energy in the atmosphere are determined by the Rossby modes, whereas the contributions from the gravity modes are relatively small. Most of the energy of the atmospheric general circulation is generated in both the barotropic and baroclinic components of zonal mean available po-

tential energy, A_Z, by the differential heating of solar radiation. Almost all the energy generated in A_Z is transformed into eddy available potential energy, A_E, mostly by the planetary and synoptic-scale eddies of both the barotropic and baroclinic components. Both A_Z and A_E are contained mainly in the baroclinic component of the atmosphere, because the energy generated at the barotropic component of A_Z is transformed into both the barotropic and baroclinic components of A_E, and the energy supplied into the barotropic component of A_E is dissipated radiatively, possible by the warming of cold air masses and the cooling of warm air masses in middle latitudes (Lorenz, 1955). Some energy is also generated at the baroclinic component of A_E, which together with the energy supplied from A_Z into the baroclinic component of A_E, is converted into the eddy kinetic energy, K_E, of the baroclinic component, mostly by the planetary and synoptic-scale eddies. Part of the energy supplied into the baroclinic K_E is dissipated by surface friction and viscosity, whereas the remainder part is transformed by the synoptic to planetary waves into barotropic kinetic energy of both the zonal mean and eddy components, K_Z and K_E, and also into zonal mean kinetic energy of the baroclinic component. The kinetic energy supplied to the barotropic component of both K_Z and K_E is also dissipated by surface friction and viscosity. Some energy dissipation also takes place in the baroclinic component of K_Z. The remainder small part of energy generated in the barotropic component of A_Z, seems to be converted into K_Z, whereas for the baroclinic component the conversion appears to be in the opposite direction.

The shape and location of the latitude-pressure distributions in the integrands of the various energetics terms, are rather similar among the three reanalysis. Differences are mainly related to the magnitude of some of those distributions, which are typically weaker in NCEP-R2 and almost exclusively located in the SH. In general, the differences are fairly unimpressive and are likely due to the different model biases and resolutions, and the different data assimilation methods used in the reanalysis systems.

In general, it was seen that the distributions in the integrands of the energetics terms are reasonably well simulated by the models in a qualitative sense, when compared to the reanalysis. However, the magnitude of the distributions in the integrands is gen-

erally greater in the models, resulting in larger quantities of energy and an overactive energy cycle. Accordingly, the magnitudes of the various energy and energy conversion/transfer spectra are generally excessive in the models, specially at the synoptic-scale wavenumbers from about $n = 4$ to 10, although the shape of most spectra agree reasonably well between models and reanalysis. The temperature cold bias and the too strong tropospheric jets, along with the jets' shifts in some cases, constitute some of the main deficiencies in the models simulations which are directly implicated in their excessive energy and too vigorous energy cycle. Improving these deficiencies should lead to significant benefits in the energy cycle of the models. Reducing the temperature cold bias should decrease A_Z and G_Z, leading also to a weaker meridional temperature gradient, that should reduce C_A. Weakening the jets and improving their position, should reduce both K_Z and C_K.

As have been suggested by Boer and Lambert (2008), the excessive generation of zonal mean available potential energy, G_Z, and excessive dissipation of eddy kinetic energy, D_E, in the models, seem to be implicated on the overactive energy cycle, and hence, efforts should be made to improve the physical processes controlling G_Z and D_E in the models. The processes controlling the generation, dissipation and the conversion/transfer rates terms should be closely related, since the models are devised to conserve energy. Therefore, the synoptic-scale processes should be of significant importance, since the models show excessive energy conversion/transfer rates typically at the synoptic-scale wavenumbers.

Overall, it is concluded that the inputs and outputs in the energy cycle of the models agree to those of the reanalysis. Differences between models and reanalysis are mainly related to the magnitudes of energy, energy conversion/transfer rates, and energy generation and dissipation rates. Too much A_Z is generated in the models at the baroclinic modes $k = 4-5$. The excessive transfer rates of zonal mean to eddy available potential energy and of eddy to zonal mean kinetic energy in the models, which are compactly expressed by terms C_A and C_K, are mostly due to the synoptic-scale Rossby waves of the baroclinic modes $k = 4$ and 5. This is seen by the too strong values in the $R(n)$ and

$M(n)$ spectra, typically at the synoptic scale wavenumbers $n \simeq 4-8$ for all models, being complemented further by the spectra of C_{nlk} and B_{nlk} in the zonal wavenumber domain, in which the excessive energy transfer rates in the models were typically found at the synoptic scale wavenumbers $n \simeq 4-8$ for the Rossby modes of the baroclinic component. In addition, the vertical spectra of both C_{nlk} and B_{nlk} has revealed the baroclinic modes $k = 4$ and 5, as those vertical modes in the models with the most excessive interactions of both available potential and kinetic energies. The same should be true for the conversion rate of eddy available potential energy to eddy kinetic energy, C_E. That is, the excessive values of C_E in the models were also typically found at the synoptic-scale waves of the baroclinic modes $k = 4$ and 5, yet the separation into Rossby and gravity modes is not possible for this term within the normal mode energetics scheme. Finally, the K_E is generally dissipated at a higher rate in the models at the baroclinic modes $k = 4-5$.

The energy cycle changes in the A1B climate, result from a dual role of the warming pattern, characterised by the strongest warming in the tropical upper troposphere and in lower level high latitudes. This pattern causes an increase of A_Z in the upper troposphere (upper region) and a decrease of A_Z in the lower troposphere, near the surface, which is in line with the results of Hernández-Deckers and von Storch (2010). They have also showed that in the free troposphere (roughly between 700 and 400 hPa) where the warming is approximately homogeneous, the increase in mean static stability is responsible for a decrease in A_Z, which was supported in this study by the decrease of γ (increase in mean static stability) found in the lower and middle troposphere (lower region). The result is a decrease in A_Z throughout the lower region and an increase in the upper region. The results also show that an increase in greenhouse gas concentrations leads to a greater generation of A in the upper troposphere and a reduced generation of A in the lower troposphere. This, together with the response of baroclinic activity due to the changes in temperature gradients and static stability, and therefore to the changes in A, explains the general strengthening of the energy cycle in the upper region and its weakening in the lower region for the future climate.

The changes in moisture content, implied by the warming pattern, should be also an important factor for the changes in the energy cycle, since the poleward moisture transport contributes to the poleward energy transport and, therefore, to the equator-to-pole temperature gradients.

Globally, the total dissipation decreases in A1B, although the zonal mean dissipation increases slightly. When integrated globally, the weakening of the energy cycle in the lower region dominates and leads to decreases in the part of the energy cycle that links A_Z to A_E to K_E. The strengthening of the energy cycle in the upper region, on the other hand, appears together with a significant increase in K_Z, due to an increase in the transfer rate of eddy to zonal kinetic energy, C_K. These global changes are a consequence of the strengthening of the Lorenz energy cycle in the upper troposphere and lower stratosphere, sustained by enhanced baroclinic eddies of large horizontal scales, and the weakening of the cycle below, mostly driven by weaker baroclinic eddies of intermediate to small scales.

Appendix A

Atmospheric Energetics

In the following sections, the equations describing the energy cycle of the global atmosphere are derived by using the fundamental equations presented in chapter 2 (section 2.2.1).

A.1 Lorenz energy cycle

A.1.1 Kinetic energy balance equations

The mechanical energy equations for the 'horizontal' wind components are obtained by multiplying equations (2.20) and (2.21) by u and v, respectively, and may be written as

$$\begin{aligned}\frac{\partial}{\partial t}\left(\frac{u^2}{2}\right) &= -\vec{V}\cdot\nabla\left(\frac{u^2}{2}\right) - \omega\frac{\partial}{\partial p}\left(\frac{u^2}{2}\right) + uv\left(f + u\frac{\tan\theta}{a}\right) \\ &\quad -\frac{gu}{a\cos\theta}\frac{\partial z}{\partial\lambda} - uF_u, \end{aligned} \tag{A.1}$$

$$\begin{aligned}\frac{\partial}{\partial t}\left(\frac{v^2}{2}\right) &= -\vec{V}\cdot\nabla\left(\frac{v^2}{2}\right) - \omega\frac{\partial}{\partial p}\left(\frac{v^2}{2}\right) - uv\left(f + u\frac{\tan\theta}{a}\right) \\ &\quad -\frac{gv}{a\cos\theta}\frac{\partial z}{\partial\theta} - vF_v. \end{aligned} \tag{A.2}$$

Averaging (A.1) and (A.2) with respect to longitude gives:

$$\begin{aligned}\frac{\partial}{\partial t}\left(\frac{[u^2]}{2}\right) &= -\left[\vec{V}\cdot\nabla\left(\frac{u^2}{2}\right)\right]-\left[\omega\frac{\partial}{\partial p}\left(\frac{u^2}{2}\right)\right]+\left[u^2v\right]\frac{\tan\theta}{a}\\ &\quad +f\left[uv\right]-\frac{g}{a\cos\theta}\left[u\frac{\partial z}{\partial\lambda}\right]-\left[uF_u\right],\end{aligned}\tag{A.3}$$

$$\begin{aligned}\frac{\partial}{\partial t}\left(\frac{[v^2]}{2}\right) &= -\left[\vec{V}\cdot\nabla\left(\frac{v^2}{2}\right)\right]-\left[\omega\frac{\partial}{\partial p}\left(\frac{v^2}{2}\right)\right]-\left[u^2v\right]\frac{\tan\theta}{a}\\ &\quad -f\left[uv\right]-\frac{g}{a}\left[v\frac{\partial z}{\partial\theta}\right]-\left[vF_v\right],\end{aligned}\tag{A.4}$$

where $[\mathcal{A}]$ denotes the zonal average of a quantity $\mathcal{A}$, and is defined by $[\mathcal{A}]=\frac{1}{2\pi}\int_0^{2\pi}\mathcal{A}\,\mathrm{d}\lambda$.

Multiplying (2.20) and (2.21) by $[u]$ and $[v]$, respectively, applying the continuity equation (2.23), and averaging the resulting equations along a latitude circle, yields the relations

$$\begin{aligned}\frac{\partial}{\partial t}\left(\frac{[u]^2}{2}\right) &= -\frac{[u]}{a\cos\theta}\frac{\partial}{\partial\theta}\left(\left[uv\right]\cos\theta\right)-\left[u\right]\frac{\partial}{\partial p}\left[u\omega\right]\\ &\quad +\left[u\right]\left(f\left[v\right]+\left[uv\right]\frac{\tan\theta}{a}\right)-\left[u\right]\left[F_u\right],\end{aligned}\tag{A.5}$$

$$\begin{aligned}\frac{\partial}{\partial t}\left(\frac{[v]^2}{2}\right) &= -\frac{[v]}{a\cos\theta}\frac{\partial}{\partial\theta}\left(\left[v^2\right]\cos\theta\right)-\left[v\right]\frac{\partial}{\partial p}\left[v\omega\right]\\ &\quad -\left[v\right]\left(f\left[u\right]+\left[u^2\right]\frac{\tan\theta}{a}\right)-\frac{g\left[v\right]}{a}\frac{\partial\left[z\right]}{\partial\theta}-\left[v\right]\left[F_v\right].\end{aligned}\tag{A.6}$$

These equations may be expanded further as

$$\begin{aligned}\frac{\partial}{\partial t}\left(\frac{[u]^2}{2}\right) &= \left\{\frac{1}{a\cos\theta}\frac{\partial}{\partial\theta}\left(\left([v]\,\frac{[u]^2}{2}-[u]\,[uv]\right)\cos\theta\right)\right\}\\ &+\left\{\frac{\partial}{\partial p}\left([\omega]\,\frac{[u]^2}{2}-[u]\,[u\omega]\right)\right\}+[u^*v^*]\,\frac{\cos\theta}{a}\frac{\partial}{\partial\theta}\left(\frac{[u]}{\cos\theta}\right)\\ &+[u^*\omega^*]\,\frac{\partial\,[u]}{\partial p}+[u]\,[v]\left(f+[u]\,\frac{\tan\theta}{a}\right)-[u]\,[F_u]\,, \end{aligned} \tag{A.7}$$

$$\begin{aligned}\frac{\partial}{\partial t}\left(\frac{[v]^2}{2}\right) &= \left\{\frac{1}{a\cos\theta}\frac{\partial}{\partial\theta}\left(\left([v]\,\frac{[v]^2}{2}-[v]\,[vv]\right)\cos\theta\right)\right\}\\ &+\left\{\frac{\partial}{\partial p}\left([\omega]\,\frac{[v]^2}{2}-[v]\,[v\omega]\right)\right\}+[v^*v^*]\,\frac{1}{a}\frac{\partial\,[v]}{\partial\theta}\\ &+[v^*\omega^*]\,\frac{\partial\,[v]}{\partial p}-[u^*u^*]\,[v]\,\frac{\tan\theta}{a}-[u]\,[v]\left(f+[u]\,\frac{\tan\theta}{a}\right)\\ &-g\frac{[v]}{a}\frac{\partial\,[z]}{\partial\theta}-[v]\,[F_v]\,. \end{aligned} \tag{A.8}$$

The rate of change of the kinetic energy of the zonally-averaged flow, is now obtained by adding (A.7) and (A.8), i.e.,

$$\begin{aligned}\frac{\partial}{\partial t}\frac{\left([u]^2+[v]^2\right)}{2} &= -[u^*u^*]\,[v]\,\frac{\tan\theta}{a}+[v^*v^*]\,\frac{1}{a}\frac{\partial\,[v]}{\partial\theta}+[u^*v^*]\,\frac{\cos\theta}{a}\frac{\partial}{\partial\theta}\left(\frac{[u]}{\cos\theta}\right)\\ &+[u^*\omega^*]\,\frac{\partial\,[u]}{\partial p}+[v^*\omega^*]\,\frac{\partial\,[v]}{\partial p}-g\frac{[v]}{a}\frac{\partial\,[z]}{\partial\theta}-[u]\,[F_u]+[v]\,[F_v]\\ &+\left\{\frac{1}{a\cos\theta}\frac{\partial}{\partial\theta}\left(\left([v]\,\frac{[u]^2+[v]^2}{2}-[u]\,[uv]-[v]\,[vv]\right)\cos\theta\right)\right\}\\ &+\left\{\frac{\partial}{\partial p}\left([\omega]\,\frac{[u]^2+[v]^2}{2}-[u]\,[u\omega]-[v]\,[v\omega]\right)\right\}. \end{aligned} \tag{A.9}$$

The equations for the rate of change of the mean eddy kinetic energy may be obtained by subtracting (A.7) and (A.8) from (A.3) and (A.4), respectively, in accordance with the relations

$$\left[u^2\right] = [u]^2+\left[(u^*)^2\right], \tag{A.10}$$

$$\left[v^2\right] = [v]^2+\left[(v^*)^2\right], \tag{A.11}$$

where the superscript asterisk represents deviations from the zonal mean, so that, e.g., $u = [u] + u^*$. The resulting equations may be expressed in the form

$$\begin{aligned}
\frac{\partial}{\partial t}\left(\frac{\left[(u^*)^2\right]}{2}\right) &= -\left\{\frac{1}{a\cos\theta}\frac{\partial}{\partial\theta}\left(\left[v\frac{(u^*)^2}{2}\right]\cos\theta\right)+\frac{\partial}{\partial p}\left(\left[\omega\frac{(u^*)^2}{2}\right]\right)\right\} \\
&\quad -[u^*v^*]\,\frac{\cos\theta}{a}\frac{\partial}{\partial\theta}\left(\frac{[u]}{\cos\theta}\right)-[u^*\omega^*]\,\frac{\partial\,[u]}{\partial p} \\
&\quad +[u^*v^*]\left(f+[u]\,\frac{\tan\theta}{a}\right)+\frac{\tan\theta}{a}\,[uu^*v^*] \\
&\quad +\frac{\tan\theta}{a}\,[v]\,[u^*u^*]-\frac{g}{a\cos\theta}\left[u^*\frac{\partial z^*}{\partial\lambda}\right]-[u^*F_u^*]\,, \qquad \text{(A.12)}
\end{aligned}$$

$$\begin{aligned}
\frac{\partial}{\partial t}\left(\frac{\left[(v^*)^2\right]}{2}\right) &= -\left\{\frac{1}{a\cos\theta}\frac{\partial}{\partial\theta}\left(\left[v\frac{(v^*)^2}{2}\right]\cos\theta\right)+\frac{\partial}{\partial p}\left(\left[\omega\frac{(v^*)^2}{2}\right]\right)\right\} \\
&\quad -[v^*v^*]\,\frac{1}{a}\frac{\partial\,[v]}{\partial\theta}-[v^*\omega^*]\,\frac{\partial\,[v]}{\partial p} \\
&\quad -[u^*v^*]\left(f+[u]\,\frac{\tan\theta}{a}\right)-\frac{\tan\theta}{a}\,[uu^*v^*] \\
&\quad -\frac{g}{a}\left[v^*\frac{\partial z^*}{\partial\theta}\right]-[v^*F_v^*]\,. \qquad \text{(A.13)}
\end{aligned}$$

Summing (A.12) and (A.13), yields

$$\begin{aligned}
\frac{\partial}{\partial t}\left(\frac{\left[(u^*)^2\right]+\left[(v^*)^2\right]}{2}\right) &= -\left\{\frac{1}{a\cos\theta}\frac{\partial}{\partial\theta}\left(\left[v\frac{(u^*)^2+(v^*)^2}{2}\right]\cos\theta\right)\right\} \\
&\quad -\left\{\frac{\partial}{\partial p}\left(\left[\omega\frac{(u^*)^2+(v^*)^2}{2}\right]\right)\right\} \\
&\quad -[u^*v^*]\,\frac{\cos\theta}{a}\frac{\partial}{\partial\theta}\left(\frac{[u]}{\cos\theta}\right)-[v^*v^*]\,\frac{1}{a}\frac{\partial\,[v]}{\partial\theta} \\
&\quad -[u^*\omega^*]\,\frac{\partial\,[u]}{\partial p}-[v^*\omega^*]\,\frac{\partial\,[v]}{\partial p}+\frac{\tan\theta}{a}\,[v]\,[u^*u^*] \\
&\quad -\frac{g}{a\cos\theta}\left[u^*\frac{\partial z^*}{\partial\lambda}\right]-\frac{g}{a}\left[v^*\frac{\partial z^*}{\partial\theta}\right] \\
&\quad -[u^*F_u^*]-[v^*F_v^*]\,. \qquad \text{(A.14)}
\end{aligned}$$

Finally, the balance equations for zonal mean and eddy kinetic energy, K_Z and K_E, are obtained by integrating equations (A.9) and (A.14) over a closed mass fluid (e.g.

the entire atmosphere), and may be written as

$$\frac{\partial}{\partial t}K_Z = C_K + C_Z - D_Z, \tag{A.15}$$

$$\frac{\partial}{\partial t}K_E = -C_K + C_E - D_E, \tag{A.16}$$

where,

$$K_Z = \int_{\mathcal{M}} \frac{[u]^2 + [v]^2}{2}\,\mathrm{d}m, \tag{A.17}$$

$$K_E = \int_{\mathcal{M}} \frac{\left[(u^*)^2\right] + \left[(v^*)^2\right]}{2}\,\mathrm{d}m, \tag{A.18}$$

$$\begin{aligned} C_K = \int_{\mathcal{M}} \Bigg(& [u^*v^*]\,\frac{\cos\theta}{a}\frac{\partial}{\partial\theta}\left(\frac{[u]}{\cos\theta}\right) + [u^*\omega^*]\,\frac{\partial\,[u]}{\partial p} + [v^*\omega^*]\,\frac{\partial\,[v]}{\partial p} \\ & + [v^*v^*]\,\frac{1}{a}\frac{\partial\,[v]}{\partial\theta} - [u^*u^*]\,[v]\,\frac{\tan\theta}{a}\Bigg)\,\mathrm{d}m, \end{aligned} \tag{A.19}$$

$$\begin{aligned} C_Z &= -\int_{\mathcal{M}} \frac{g}{a}\,[v]\,\frac{\partial\,[z]}{\partial\theta}\,\mathrm{d}m \\ &= -\int_{\mathcal{M}} \frac{R}{p}\,[\omega]''\,[\mathrm{T}]''\,\mathrm{d}m, \end{aligned} \tag{A.20}$$

$$D_Z = -\int_{\mathcal{M}} \left([u]\,[F_u] + [v]\,[F_v]\right)\,\mathrm{d}m. \tag{A.21}$$

$$\begin{aligned} C_E &= -\int_{\mathcal{M}} \left(\frac{g}{a\cos\theta}\left[u^*\frac{\partial z^*}{\partial\lambda}\right] + \frac{g}{a}\left[v^*\frac{\partial z^*}{\partial\theta}\right]\right)\mathrm{d}m \\ &= -\int_{\mathcal{M}} \frac{R}{p}\,[\omega^*\mathrm{T}^*]\,\mathrm{d}m, \end{aligned} \tag{A.22}$$

$$D_E = -\int_{\mathcal{M}} \left([u^*F_u^*] + [v^*F_v^*]\right)\,\mathrm{d}m. \tag{A.23}$$

In (A.17) to (A.23), $\mathrm{d}m = \frac{1}{g}\,a^2\cos\theta\,\mathrm{d}\lambda\,\mathrm{d}\theta\,\mathrm{d}p$ and $\mathcal{M}$ indicates that the integration is over the whole atmosphere. The terms between braces, $\{\,\}$, in equations (A.9) and (A.14) vanish in case of global integrals, and so they do not appear in equations (A.15) and (A.16). Using the hydrostatic equation (2.22) and the continuity equation (2.23), it

may be shown that the two alternative expressions for C_Z and C_E, in (A.20) and (A.22) respectively, are equivalent provided that global integrals are considered (Peixoto and Oort, 1992).

A.1.2 Available potential energy balance equations

Following Lorenz (1955), the balance equations for zonal and eddy available potential energy may be derived by applying similar averaging processes to the first law of thermodynamics (2.24) as those used in (2.20) and (2.21) to derive the zonal and eddy kinetic energy balance equations (A.15) and (A.16). These equations take the following form, respectively

$$\frac{\partial}{\partial t}A_Z = -C_Z - C_A + G_Z, \tag{A.24}$$

$$\frac{\partial}{\partial t}A_E = C_A - C_E + G_E, \tag{A.25}$$

where

$$A_Z = \int_{\mathcal{M}} \gamma \frac{c_p}{2} \left([\mathrm{T}]''\right)^2 \mathrm{d}m, \tag{A.26}$$

$$A_E = \int_{\mathcal{M}} \gamma \frac{c_p}{2} \left[(\mathrm{T}^*)^2\right] \mathrm{d}m, \tag{A.27}$$

$$C_A = -\int_{\mathcal{M}} \gamma\, c_p \left([v^*\mathrm{T}^*] \frac{1}{a}\frac{\partial [\mathrm{T}]}{\partial \theta} + [\omega^*\mathrm{T}^*] \frac{\mathrm{T}}{\Theta}\frac{\partial [\Theta]''}{\partial p} \right) \mathrm{d}m, \tag{A.28}$$

$$G_Z = \int_{\mathcal{M}} \gamma\, [\mathrm{T}]''\, [q]'' \, \mathrm{d}m, \tag{A.29}$$

$$G_E = \int_{\mathcal{M}} \gamma\, [\mathrm{T}^* q^*] \, \mathrm{d}m, \tag{A.30}$$

and the stability parameter, γ, is defined as

$$\gamma = -\frac{\Theta}{\mathrm{T}}\frac{R}{pc_p}\left(\frac{\partial \widetilde{\Theta}}{\partial p}\right)^{-1}. \tag{A.31}$$

A.2 Energetics in the zonal wavenumber domain

A.2.1 Basic concepts from the theory of Fourier analysis

Any real, single-valued function $f(\lambda)$, which is piecewise differentiable in the interval $(0, 2\pi)$, may be written in terms of a Fourier representation,

$$f(\lambda) = \sum_{n=-\infty}^{\infty} F(n) e^{in\lambda}, \tag{A.32}$$

where the complex coefficients, $F(n)$, are given by

$$F(n) = \frac{1}{2\pi} \int_0^{2\pi} f(\lambda) e^{-in\lambda} \, \mathrm{d}\lambda. \tag{A.33}$$

For the purposes of this discussion, it is considered the Fourier representation of meteorological quantities specified along a given latitude circle. Thus, in (A.32) and (A.33), λ is taken as longitude and n is the number of waves around the latitude circle. The functions $f(\lambda)$ and $F(n)$ to be considered are listed in Table A.1.

Table A.1: Fourier transform pairs.

$f(\lambda)$	-	u	v	ω	z	T	q	F_u	F_v
$F(n)$	-	U	V	Ω	Z	B	Q	F_U	F_V

The quantity $F(n)$ is the representation of $f(\lambda)$ in the domain of wavenumber and is called the *spectral function* of f. The set of equations, (A.32) and (A.33), is often referred to as a Fourier transform pair.

Using (A.32) and (A.33), the Fourier transform pairs for the derivatives of $f(\lambda, \theta, p, t)$ may be written as

$$\frac{\partial f}{\partial \lambda} = \sum_{n=-\infty}^{\infty} in\, F(n) e^{in\lambda}, \tag{A.34}$$

$$in\, F(n) = \frac{1}{2\pi} \int_0^{2\pi} \frac{\partial f}{\partial \lambda}\, e^{-in\lambda}\, \mathrm{d}\lambda, \tag{A.35}$$

$$\frac{\partial f}{\partial \xi} = \sum_{n=-\infty}^{\infty} F_\xi(n) e^{in\lambda}, \tag{A.36}$$

$$F_\xi(n) = \frac{1}{2\pi} \int_0^{2\pi} \frac{\partial f}{\partial \xi}\, e^{-in\lambda}\, \mathrm{d}\lambda. \tag{A.37}$$

where ξ may be θ, p, or t, and the use of subscript denotes a partial differentiation, i.e. $F_\xi(n) = \frac{\partial F(n)}{\partial \xi}$.

The product of two functions, $f(\lambda)$ and $g(\lambda)$, whose spectral functions defined by (A.33) are $F(n)$ and $G(n)$, respectively, may be written as

$$\frac{1}{2\pi} \int_0^{2\pi} f(\lambda)\, g(\lambda)\, e^{-in\lambda}\, \mathrm{d}\lambda = \frac{1}{2\pi} \int_0^{2\pi} f(\lambda) \left(\sum_{m=-\infty}^{\infty} G(m)\, e^{im\lambda} \right) e^{-in\lambda}\, \mathrm{d}\lambda. \tag{A.38}$$

The existence and uniqueness of the Fourier representation (A.32) is guaranteed since the atmospheric fields satisfy the Dirichlet conditions (MacRobert, 1967), which are a sufficient condition for the convergence of (A.32). Hence, $g(\lambda)$ may be assumed as uniformly convergent, and so the order of summation and integration in (A.38) may be interchanged, which yields

$$\begin{aligned} \frac{1}{2\pi} \int_0^{2\pi} f(\lambda)\, g(\lambda)\, e^{-in\lambda}\, \mathrm{d}\lambda &= \sum_{m=-\infty}^{\infty} G(m)\, \frac{1}{2\pi} \int_0^{2\pi} f(\lambda)\, e^{-i(n-m)\lambda}\, \mathrm{d}\lambda, \\ &= \sum_{m=-\infty}^{\infty} G(m)\, F(n-m). \end{aligned} \tag{A.39}$$

Expression (A.39) gives the spectral function for the product of two variables, and is often called the *multiplication theorem*. As a special case, the Parseval's theorem may

be obtained by setting $n = 0$ in (A.39):

$$\frac{1}{2\pi}\int_0^{2\pi} f(\lambda)\, g(\lambda)\, \mathrm{d}\lambda = \sum_{m=-\infty}^{\infty} G(m)\, F(-m). \tag{A.40}$$

If, further, $f = g$, yields

$$\frac{1}{2\pi}\int_0^{2\pi} f^2(\lambda)\, \mathrm{d}\lambda = \sum_{m=-\infty}^{\infty} |F(m)|^2. \tag{A.41}$$

It has been used in (A.41) the fact that $F(-m)$ is the complex conjugate of $F(m)$, which implies that $F(m)\, F(-m) = |F(m)|^2$. It may be noted, also, from (A.33) that $F(0) = [f]$.

A.2.2 Transformation of fundamental equations

Using of the relations presented above, the basic equations (2.20) to (2.24) may be transformed from the space domain to the domain of wavenumber. The transformation is effected by multiplying (2.20) to (2.24) by $\frac{1}{2\pi}e^{-in\lambda}$, integrating around a latitude circle, and applying (A.32) to (A.37) and (A.39). Therefore, the equations of motions for the horizontal components of the wind take the form (see Table A.1)

$$\begin{aligned}\frac{\partial}{\partial t}U(n) \;=\; & -\sum_{m=-\infty}^{\infty}\left(\frac{im}{a\cos\theta}U(m)\,U(n-m) + \frac{1}{a}\frac{\partial U(m)}{\partial\theta}\,V(n-m)\right.\\ & \left.+\frac{\partial U(m)}{\partial p}\,\Omega(n-m) - \frac{\tan\theta}{a}\,U(m)\,V(n-m)\right)\\ & -\frac{ing}{a\cos\theta}\,Z(n) + f\,V(n) - F_U(n),\end{aligned} \tag{A.42}$$

$$\begin{aligned}\frac{\partial}{\partial t}V(n) \;=\; & -\sum_{m=-\infty}^{\infty}\left(\frac{im}{a\cos\theta}\,V(m)\,U(n-m) + \frac{1}{a}\frac{\partial V(m)}{\partial\theta}\,V(n-m)\right.\\ & \left.+\frac{\partial V(m)}{\partial p}\,\Omega(n-m) + \frac{\tan\theta}{a}\,U(m)\,U(n-m)\right)\\ & -\frac{g}{a}\frac{\partial Z(n)}{\partial\theta} - f\,U(n) - F_V(n).\end{aligned} \tag{A.43}$$

The hydrostatic equation (2.22), the continuity equation (2.23) and the thermodynamical energy equation (2.24) take the form, respectively

$$\frac{\partial Z(n)}{\partial p} = -\frac{R}{gp}\,B(n). \tag{A.44}$$

$$\frac{\partial \Omega(n)}{\partial p} = -\frac{in}{a\cos\theta}\,U(n) - \frac{1}{a}\,\frac{\partial V(n)}{\partial \theta} + \frac{\tan\theta}{a}\,V(n). \tag{A.45}$$

$$\begin{aligned}\frac{\partial}{\partial t}B(n) = &-\sum_{m=-\infty}^{\infty}\left(\frac{im}{a\cos\theta}\,B(m)\,U(n-m) + \frac{1}{a}\,\frac{\partial B(m)}{\partial \theta}\,V(n-m)\right.\\ &\left.+\frac{\partial B(m)}{\partial p}\Omega(n-m) - \frac{1}{c_p}\,\frac{R}{p}\,B(m)\,\Omega(n-m)\right)\\ &+\frac{1}{c_p}\,Q(n).\end{aligned} \tag{A.46}$$

Equations (A.42) to (A.46) represent a closed system of equations governing the five dependent variables U, V, Ω, Z and B as functions of n, θ, p and t, provided that the heating distribution $Q(n)$ is specified.

A.2.3 Kinetic energy equations

The equations for the rate of change of kinetic energy of disturbances of given scale may now be derived using the transformed equations (A.42) to (A.46).

Multiplying (A.42) and (A.43) by $U(-n)$ and $V(-n)$, respectively, and applying (A.45), the expressions for the rate of change of the separate components of $K(n)$ may

be obtained as

$$
\begin{aligned}
\frac{\partial}{\partial t}|U(n)|^2 \;=\; & -\big(U(-n)\,V(n)+U(n)V(-n)\big)\frac{\cos\theta}{a}\,\frac{\partial}{\partial\theta}\left(\frac{[u]}{\cos\theta}\right)\\
& -\big(U(-n)\,\Omega(n)+U(n)\,\Omega(-n)\big)\frac{\partial\,[u]}{\partial p}+\,2\big(U(-n)\,U(n)\big)\;[v]\;\frac{\tan\theta}{a}\\
& -\sum_{\substack{m=-\infty\\ m\neq 0}}^{\infty}\left(\frac{in}{a\cos\theta}U(m)\,\big(U(-n)\,U(n-m)-U(n)\,U(-n-m)\big)\right.\\
& \qquad +\frac{1}{a\cos\theta}\,U(-n)\,\frac{\partial}{\partial\theta}\big(U(m)\,V(n-m)\;\cos\theta\big)\\
& \qquad +\frac{1}{a\cos\theta}\,U(n)\,\frac{\partial}{\partial\theta}\big(U(m)\,V(-n-m)\;\cos\theta\big)\\
& \qquad +U(-n)\frac{\partial}{\partial p}\big(U(m)\Omega(n-m)\big)+U(n)\,\frac{\partial}{\partial p}\big(U(m)\,\Omega(-n-m)\big)\\
& \qquad \left.-\frac{\tan\theta}{a}\,V(m)\,\big(U(-n)\,U(n-m)+U(n)\,U(-n-m)\big)\right)\\
& -\frac{ing}{a\cos\theta}\big(Z(n)U(-n)-Z(-n)U(n)\big)-\big(U(-n)F_U(n)+U(n)F_U(-n)\big)\\
& +\left(f+[u]\,\frac{\tan\theta}{a}\right)\,\big(U(-n)\,V(n)+U(n)\,V(-n)\big), \qquad \text{(A.47)}
\end{aligned}
$$

$$
\begin{aligned}
\frac{\partial}{\partial t}|V(n)|^2 \;=\; & -2\;V(-n)V(n)\frac{1}{a}\frac{\partial\,[v]}{\partial\theta}-\big(V(-n)\Omega(n)+V(n)\Omega(-n)\big)\frac{\partial\,[v]}{\partial p}\\
& -\sum_{\substack{m=-\infty\\ m\neq 0}}^{\infty}\left(\frac{in}{a\cos\theta}V(m)\,\big(V(-n)\,U(n-m)-V(n)\,U(-n-m)\big)\right.\\
& \qquad +\frac{1}{a\cos\theta}\,V(-n)\,\frac{\partial}{\partial\theta}\big(V(m)\,V(n-m)\;\cos\theta\big)\\
& \qquad +\frac{1}{a\cos\theta}\,V(n)\,\frac{\partial}{\partial\theta}\big(V(m)\,V(-n-m)\;\cos\theta\big)\\
& \qquad +V(-n)\,\frac{\partial}{\partial p}\big(V(m)\Omega(n-m)\big)+V(n)\,\frac{\partial}{\partial p}\big(V(m)\Omega(-n-m)\big)\\
& \qquad \left.+\frac{\tan\theta}{a}\,U(m)\,\big(V(-n)\,U(n-m)+V(n)\,U(-n-m)\big)\right)\\
& -\frac{g}{a}\left(\frac{\partial Z(n)}{\partial\theta}V(-n)+\frac{\partial Z(-n)}{\partial\theta}V(n)\right)-\big(V(-n)F_V(n)+V(n)F_V(-n)\big)\\
& -\left(f+[u]\,\frac{\tan\theta}{a}\right)\,\big(U(-n)\,V(n)+U(n)\,V(-n)\big). \qquad \text{(A.48)}
\end{aligned}
$$

The desired equation for the rate of change of the total kinetic energy of a given wavenumber may be finally obtained by summing (A.47) and (A.48), and integrating over the entire mass of the atmosphere. This equation may be written as

$$\frac{\partial}{\partial t}K(n) = -M(n) + L(n) + C(n) - D(n), \tag{A.49}$$

where

$$K(n) = \int_{\mathcal{M}} |U(n)|^2 + |V(n)|^2 \, \mathrm{d}m, \tag{A.50}$$

$$\begin{aligned} M\,(n) &= -\int_{\mathcal{M}} 2\,U(n)U(-n)\;[v]\;\frac{\tan\theta}{a}\,\mathrm{d}m \\ &\quad + \int_{\mathcal{M}} \left(2\,V(n)V(-n)\,\frac{1}{a}\,\frac{\partial\,[v]}{\partial\theta} + \big(V(n)\Omega(-n) + V(-n)\Omega(n)\big)\,\frac{\partial\,[v]}{\partial p}\right)\,\mathrm{d}m \\ &\quad + \int_{\mathcal{M}} \big(U(n)\Omega(-n) + U(-n)\Omega(n)\big)\,\frac{\partial\,[u]}{\partial p}\,\mathrm{d}m \\ &\quad + \int_{\mathcal{M}} \big(U(n)V(-n) + U(-n)V(n)\big)\,\frac{\cos\theta}{a}\,\frac{\partial}{\partial\theta}\left(\frac{[u]}{\cos\theta}\right)\,\mathrm{d}m, \end{aligned} \tag{A.51}$$

$$\begin{aligned} C\,(n) &= -\int_{\mathcal{M}} \frac{i\,n\,g}{a\,\cos\theta}\left(Z\,(n)\,U\,(-n) - Z\,(-n)\,U\,(n)\right)\,\mathrm{d}m \\ &\quad + \int_{\mathcal{M}} \frac{g}{a}\left(\frac{\partial Z(n)}{\partial\theta}V\,(-n) + \frac{\partial Z(-n)}{\partial\theta}V\,(n)\right)\,\mathrm{d}m \\ &= -\int_{\mathcal{M}} \frac{R}{p}\left(\Omega(n)B(-n) + \Omega(-n)B(n)\right)\,\mathrm{d}m, \end{aligned} \tag{A.52}$$

$$\begin{aligned} D\,(n) &= -\int_{\mathcal{M}} \big(U\,(n)\,F_U\,(-n) + U\,(-n)\,F_U\,(n)\big)\,\mathrm{d}m, \\ &\quad -\int_{\mathcal{M}} \big(\big(V\,(n)\,F_V\,(-n) + V\,(-n)\,F_V\,(n)\big)\,\mathrm{d}m, \end{aligned} \tag{A.53}$$

$$
\begin{aligned}
L(n) \;=\; & -\int_{\mathcal{M}} \sum_{\substack{m=-\infty \\ m\neq 0}}^{\infty} \frac{in}{a\cos\theta}\, U(m)\, \big(U(-n)\; U(n-m) - U(n)\; U(-n-m)\big)\; \mathrm{d}m \\
& + \int_{\mathcal{M}} \sum_{\substack{m=-\infty \\ m\neq 0}}^{\infty} \frac{in}{a\cos\theta}\, V(m)\, \big(V(-n)\; U(n-m) - V(n)\; U(-n-m)\big)\; \mathrm{d}m \\
& - \int_{\mathcal{M}} \sum_{\substack{m=-\infty \\ m\neq 0}}^{\infty} \frac{\tan\theta}{a}\, V(m)\; \big(U(n-m)\, U(-n) + U(-n-m)\; U(n)\big)\; \mathrm{d}m \\
& + \int_{\mathcal{M}} \sum_{\substack{m=-\infty \\ m\neq 0}}^{\infty} \frac{\tan\theta}{a}\, U(m)\; \big(U(n-m)\; V(-n) + U(-n-m)\; V(n)\big)\; \mathrm{d}m \\
& + \int_{\mathcal{M}} \sum_{\substack{m=-\infty \\ m\neq 0}}^{\infty} \big(U(-n)\, \frac{\partial}{\partial p}\big(U(m)\, \Omega(n-m)\big) + U(n)\, \frac{\partial}{\partial p}\big(U(m)\, \Omega(-n-m)\big)\; \mathrm{d}m \\
& + \int_{\mathcal{M}} \sum_{\substack{m=-\infty \\ m\neq 0}}^{\infty} \big(V(-n)\, \frac{\partial}{\partial p}\big(V(m)\, \Omega(n-m)\big) + V(n)\, \frac{\partial}{\partial p}\big(V(m)\, \Omega(-n-m)\big)\; \mathrm{d}m \\
& + \int_{\mathcal{M}} \sum_{\substack{m=-\infty \\ m\neq 0}}^{\infty} \frac{1}{a\cos\theta}\, U(-n)\; \frac{\partial}{\partial\theta}\big(U(m)\; V(n-m)\; \cos\theta\big)\; \mathrm{d}m \\
& + \int_{\mathcal{M}} \sum_{\substack{m=-\infty \\ m\neq 0}}^{\infty} \frac{1}{a\cos\theta}\, U(n)\; \frac{\partial}{\partial\theta}\big(U(m)\; V(-n-m)\; \cos\theta\big)\; \mathrm{d}m \\
& + \int_{\mathcal{M}} \sum_{\substack{m=-\infty \\ m\neq 0}}^{\infty} \frac{1}{a\cos\theta}\, V(-n)\; \frac{\partial}{\partial\theta}\big(V(m)\; V(n-m)\; \cos\theta\big)\; \mathrm{d}m \\
& + \int_{\mathcal{M}} \sum_{\substack{m=-\infty \\ m\neq 0}}^{\infty} \frac{1}{a\cos\theta}\, V(n)\; \frac{\partial}{\partial\theta}\big(V(m)\; V(-n-m)\; \cos\theta\big)\; \mathrm{d}m. \qquad \text{(A.54)}
\end{aligned}
$$

As a special case, the equation for the time rate of change of the kinetic energy of the mean flow may be obtained by setting $n = 0$ in (A.49) and using the continuity equation (A.45). This equation may be written as

$$
\frac{\partial}{\partial t} K(0) = \sum_{n=1}^{\infty} M(n) + C(0) - D(0), \qquad \text{(A.55)}
$$

where $K(0) = K_Z$, $C(0) = C_Z$ and $D(0) = D_Z$.

Equations (A.49) and (A.55) represent the transforms of (A.16) and (A.15) in the wave-number "space".

A.2.4 Available potential energy equations

The equation describing the variations of the separate scales of eddy available potential energy, may be obtained by applying the same procedure used to obtain (A.49) from the equations of motion to the thermodynamical energy equation (A.46). This equation, which is the Fourier transform of (A.25), may be written in the following form

$$\frac{\partial}{\partial t}A(n) = R(n) + S(n) - C(n) + G(n), \tag{A.56}$$

where

$$A(n) = \int_{\mathcal{M}} \gamma\, c_p\, |B(n)|^2 \,\mathrm{d}m, \tag{A.57}$$

$$\begin{aligned} R\,(n) \;=\; & -\int_{\mathcal{M}} \gamma\, c_p \big(V(n)B(-n) + V(-n)B(n)\big)\frac{1}{a}\,\frac{\partial\,[\mathrm{T}]}{\partial\theta}\;\mathrm{d}m \\ & -\int_{\mathcal{M}} \gamma\, c_p \big(\Omega(n)B(-n) + \Omega(-n)B(n)\big)\frac{\mathrm{T}}{\Theta}\,\frac{\partial\,[\Theta]''}{\partial p}\;\mathrm{d}m, \end{aligned} \tag{A.58}$$

$$\begin{aligned} S\,(n) \;=\; & -\int_{\mathcal{M}} \gamma\, c_p \sum_{\substack{m=-\infty \\ m\neq 0}}^{\infty} \frac{in}{a\cos\theta}\, B(m)\big(B(-n)\,U(n-m) + B(n)\,U(-n-m)\big)\;\mathrm{d}m \\ & +\int_{\mathcal{M}} \gamma\, c_p \sum_{\substack{m=-\infty \\ m\neq 0}}^{\infty} \frac{1}{a}\, B(m)\left(V(n-m)\frac{\partial B(-n)}{\partial\theta} + V(-n-m)\frac{\partial B(n)}{\partial\theta}\right)\;\mathrm{d}m \\ & +\int_{\mathcal{M}} \gamma\, c_p \sum_{\substack{m=-\infty \\ m\neq 0}}^{\infty} B(m)\left(\Omega(n-m)\,\frac{\partial B(-n)}{\partial p} + \Omega(-n-m)\,\frac{\partial B(n)}{\partial p}\right)\;\mathrm{d}m \\ & +\int_{\mathcal{M}} \gamma\, c_p \sum_{\substack{m=-\infty \\ m\neq 0}}^{\infty} \frac{R}{pc_p}\, B(m)\big(\Omega(n-m)\,B(-n) + \Omega(-n-m)\,B(n)\big)\;\mathrm{d}m, \end{aligned} \tag{A.59}$$

$$G\,(n) = \int_{\mathcal{M}} \gamma\,\big(B(n)Q(-n) + B(-n)Q(n)\big)\;\mathrm{d}m. \tag{A.60}$$

For completeness, the Fourier transform of the balance equation for the zonal mean available potential energy, (A.24), is written in the form

$$\frac{\partial}{\partial t}A(0) = -\sum_{n=1}^{\infty} R(n) - C(0) + G(0), \tag{A.61}$$

where $A(0) = A_Z$ and $G(0) = G_Z$.

A.3 Atmospheric normal modes

A.3.1 Linearised primitive equations

Under the usual approximation of a shallow-atmosphere, i.e. an atmosphere with a vertical dimension much smaller than the horizontal dimension, and using coordinates (λ, θ, p, t), a system of primitive equations may be written as

$$\frac{\partial u}{\partial t} - fv + \frac{1}{a\cos\theta}\frac{\partial \phi}{\partial \lambda} = -\vec{V}\cdot\nabla u - \omega\frac{\partial u}{\partial p} + \frac{\tan\theta}{a}uv + F_u, \tag{A.62}$$

$$\frac{\partial v}{\partial t} + fu + \frac{1}{a}\frac{\partial \phi}{\partial \theta} = -\vec{V}\cdot\nabla v - \omega\frac{\partial v}{\partial p} - \frac{\tan\theta}{a}u^2 + F_v, \tag{A.63}$$

$$\nabla\cdot\vec{V} + \frac{\partial \omega}{\partial p} = 0, \tag{A.64}$$

$$\frac{\partial \phi}{\partial p} = -\frac{RT}{p}, \tag{A.65}$$

$$\frac{\mathrm{dT}}{\mathrm{d}t} - \frac{R}{p\,c_p}\,\omega\,\mathrm{T} = \frac{q}{c_p}, \tag{A.66}$$

In (A.62)-(A.66) the approximations of constant gravity acceleration, g, and earth radius, a, are also considered.

By considering the reference state temperature, T_0, which is a function of pressure only, and the deviation from T_0, denoted by T for simplicity, then temperature T in (A.66) may be partitioned as $\mathrm{T} = T + T_0$. Therefore, the thermodynamic equation

(A.66) may be written as

$$\frac{\mathrm{d}T}{\mathrm{d}t} + \frac{\mathrm{d}T_0}{\mathrm{d}t} - \frac{R}{p\,c_p}\,\omega\,(T + T_0) \;=\; \frac{q}{c_p}. \tag{A.67}$$

Assuming that the perturbation temperature, T, is neglegible compared to the reference state temperature, T_0, i.e. $T \ll T_0$, expanding the total time derivatives, and recalling that T_0 is a function of pressure only, equation (A.67) is now written as

$$\frac{\partial T}{\partial t} + \vec{V}\cdot\nabla T + \omega\frac{\partial T}{\partial p} + \omega\frac{\mathrm{d}T_0}{\mathrm{d}p} - \frac{R}{p\,c_p}\,\omega\,T_0 = \frac{q}{c_p}, \tag{A.68}$$

or

$$\frac{\partial T}{\partial t} - \frac{p}{R}\,S_0\,\omega = -\vec{V}\cdot\nabla T - \omega\frac{\partial T}{\partial p} + \frac{q}{c_p}, \tag{A.69}$$

where

$$S_0 = \frac{R}{p}\left(\frac{R}{p\,c_p}\,T_0 - \frac{\mathrm{d}T_0}{\mathrm{d}p}\right). \tag{A.70}$$

Multiplying (A.69) by $-\frac{R}{p\,S_0}$ and using (A.65), results in

$$\frac{1}{S_0}\,\frac{\partial}{\partial t}\left(\frac{\partial\phi}{\partial p}\right) + \omega = \frac{R}{p\,S_0}\left(\vec{V}\cdot\nabla T + \omega\,\frac{\partial T}{\partial p}\right) - \frac{R\,q}{p\,c_p\,S_0}. \tag{A.71}$$

Taking the derivative of (A.71) relative to pressure and using (A.64), yields

$$\frac{\partial}{\partial t}\frac{\partial}{\partial p}\left(\frac{1}{S_0}\,\frac{\partial\phi}{\partial p}\right) - \nabla\cdot\vec{V} = \frac{\partial}{\partial p}\left[\frac{R}{p\,S_0}\left(\vec{V}\cdot\nabla T + \omega\,\frac{\partial T}{\partial p}\right)\right] - \frac{\partial}{\partial p}\left(\frac{R\,q}{p\,c_p\,S_0}\right). \tag{A.72}$$

The right-hand of equations (A.62), (A.63) and (A.72) contain the nonlinear terms, frictional forces and the diabatic heat sources. By setting the right-hand sides of those equations to zero, the linearised system of equations for the three dependent variables u, v and ϕ is written as

$$\frac{\partial u}{\partial t} - fv + \frac{1}{a\cos\theta}\frac{\partial\phi}{\partial\lambda} \;=\; 0, \tag{A.73}$$

$$\frac{\partial v}{\partial t} + fu + \frac{1}{a}\frac{\partial\phi}{\partial\theta} \;=\; 0, \tag{A.74}$$

$$\frac{\partial}{\partial p}\left[\frac{1}{S_0}\,\frac{\partial}{\partial p}\left(\frac{\partial\phi}{\partial t}\right)\right] - \nabla\cdot\vec{V} \;=\; 0. \tag{A.75}$$

Multiplying (A.73), (A.74) and (A.75) by u, v and $-\phi$, respectively, and summing the resulting equations, yields

$$\frac{\partial}{\partial t}\left(\frac{u^2+v^2}{2}\right) - \phi\,\frac{\partial}{\partial p}\left[\frac{1}{S_0}\,\frac{\partial}{\partial p}\left(\frac{\partial \phi}{\partial t}\right)\right] = -\nabla\cdot\phi\vec{V}. \tag{A.76}$$

Integrating (A.76) over the whole atmospheric mass, gives

$$\int_S\int_0^{p_s}\frac{\partial K}{\partial t}\,\mathrm{d}p\,\mathrm{d}s - \int_S\int_0^{p_s}\phi\,\frac{\partial}{\partial p}\left[\frac{1}{S_0}\,\frac{\partial}{\partial p}\left(\frac{\partial \phi}{\partial t}\right)\right]\,\mathrm{d}p\,\mathrm{d}s = -\int_S\int_0^{p_s}\nabla\cdot\phi\vec{V}\,\mathrm{d}p\,\mathrm{d}s$$
$$= 0. \tag{A.77}$$

Integrating by parts the second integral in (A.77), results in

$$\int_S\int_0^{p_s}\frac{\partial K}{\partial t}\,\mathrm{d}p\,\mathrm{d}s - \int_S\left[\frac{\phi}{S_0}\,\frac{\partial}{\partial p}\left(\frac{\partial \phi}{\partial t}\right)\right]_0^{p_s}\mathrm{d}s + \int_S\int_0^{p_s}\frac{\partial \phi}{\partial p}\,\frac{1}{S_0}\,\frac{\partial}{\partial p}\left(\frac{\partial \phi}{\partial t}\right)\,\mathrm{d}p\,\mathrm{d}s = 0, \tag{A.78}$$

or, by interchanging the time and pressure derivatives of ϕ in the third integral,

$$\int_S\int_0^{p_s}\frac{\partial K}{\partial t}\,\mathrm{d}p\,\mathrm{d}s - \int_S\left[\frac{\phi}{S_0}\,\frac{\partial}{\partial p}\left(\frac{\partial \phi}{\partial t}\right)\right]_0^{p_s}\mathrm{d}s + \int_S\int_0^{p_s}\frac{1}{2\,S_0}\,\frac{\partial}{\partial t}\left(\frac{\partial \phi}{\partial p}\right)^2\,\mathrm{d}p\,\mathrm{d}s = 0. \tag{A.79}$$

Using (A.64) into the linearised thermodynamical equation (A.75), yields

$$\omega \;=\; -\frac{1}{S_0}\,\frac{\partial}{\partial p}\left(\frac{\partial \phi}{\partial t}\right), \tag{A.80}$$

and substituting (A.80) into (A.79), gives

$$\int_S\int_0^{p_s}\frac{\partial K}{\partial t} + \frac{1}{2\,S_0}\,\frac{\partial}{\partial t}\left(\frac{\partial \phi}{\partial p}\right)^2\,\mathrm{d}p\,\mathrm{d}s = -\int_S\left[\phi\,\omega\right]_0^{p_s}\mathrm{d}s$$
$$= -\int_S\phi_s\,\omega_s\mathrm{d}s + \int_S\lim_{p\to 0}(\phi\,\omega)\,\mathrm{d}s. \tag{A.81}$$

or,

$$\int_S\int_0^{p_s}\frac{\partial K}{\partial t} + \frac{1}{2\,S_0}\,\frac{\partial}{\partial t}\left(\frac{\partial \phi}{\partial p}\right)^2 + \frac{\phi_s\,\omega_s}{p_s}\,\mathrm{d}p\,\mathrm{d}s = \int_S\lim_{p\to 0}(\phi\,\omega)\,\mathrm{d}s, \tag{A.82}$$

where the subscript s denote the variables at $p = p_s$.

Specifying the lower boundary condition to be the actual vertical velocity, w, equal to zero at the surface, which corresponds to no mass flux through the earth's surface (Cohn and Dee, 1989), gives

$$w = 0 \quad \Rightarrow \quad \frac{\mathrm{d}z}{\mathrm{d}t} = 0 \quad \Rightarrow \quad \frac{\mathrm{d}}{\mathrm{d}t}\left(\phi + \phi_0\right) = 0, \quad \text{at} \quad p = p_s. \tag{A.83}$$

Expanding the total derivative in (A.83), yields

$$\frac{\partial \phi}{\partial t} + \vec{V} \cdot \nabla \phi + \omega \frac{\partial \phi}{\partial p} + \frac{\partial \phi_0}{\partial t} + \vec{V} \cdot \nabla \phi_0 + \omega \frac{\partial \phi_0}{\partial p} \;\; = \;\; 0, \tag{A.84}$$

or, by recalling that ϕ_0 is a function of pressure only,

$$\frac{\partial \phi}{\partial t} + \vec{V} \cdot \nabla \phi + \omega \frac{\partial \phi}{\partial p} + \omega \frac{\partial \phi_0}{\partial p} \;\; = \;\; 0. \tag{A.85}$$

Linearizing equation (A.85), results in

$$\left(\frac{\partial \phi}{\partial t}\right)_{p=p_s} + \left(\omega \frac{\partial \phi_0}{\partial p}\right)_{p=p_s} \;\; = \;\; 0. \tag{A.86}$$

Using (A.80) into (A.86), gives

$$\left(\frac{\partial \phi}{\partial t}\right)_{p=p_s} - \left[\frac{1}{S_0}\frac{\partial}{\partial p}\left(\frac{\partial \phi}{\partial t}\right)\left(\frac{\partial \phi_0}{\partial p}\right)\right]_{p=p_s} \;\; = \;\; 0, \tag{A.87}$$

Using the hydrostatic equation (A.65) for the reference state into (A.87), the lower boundary condition for the linearised system (A.73)-(A.75) may be finally written as

$$\frac{\partial}{\partial p}\left(\frac{\partial \phi}{\partial t}\right) + \frac{S_0\, p}{R\, T_0}\left(\frac{\partial \phi}{\partial t}\right) \;\; = \;\; 0, \quad \text{at} \quad p = p_s. \tag{A.88}$$

Specifying the upper boundary condition by

$$\lim_{p \to 0}\left(\phi\, \omega\right) = 0, \tag{A.89}$$

would guarantee energy conservation in (A.82). Substituting (A.80) into (A.89), and since the atmosphere must be considered bounded, i.e. $\lim_{p\to 0} |\phi\,(p)\,| < \infty$, for consistency with the shallowness approximations in the nonlinear primitive equations (Cohn and Dee, 1989), the upper boundary condition takes the form:

$$\lim_{p \to 0} \frac{1}{S_0}\frac{\partial}{\partial p}\left(\frac{\partial \phi}{\partial t}\right) = 0. \tag{A.90}$$

The system of linearised primitive equations (A.73)-(A.75) with the boundary conditions (A.88) and (A.90) constitutes a linearised model of the atmosphere, whose solutions should be square-integrable functions over $[0, p_s]$.

A.3.2 Vertical structure functions

In the linearised system (A.73)-(A.75) the vertical coordinate only appears troughout the vertical differential operator

$$\mathcal{D} = \frac{\partial}{\partial p}\left[\frac{1}{S_0}\frac{\partial}{\partial p}(\cdot)\right]. \tag{A.91}$$

The properties of $\mathcal{D}$ may be used to design a vertical transform in such a way that it eliminates the vertical structure in (A.73)-(A.75), represented by the vertical derivatives, in order to obtain separable solutions for this system (Sneddon, 1972; Fulton and Schubert, 1985). Such a vertical transform, $\mathcal{T}$, may be defined for a generic function of pressure, $f(p)$, as

$$f_k = \mathcal{T}\left[f\left(p\right)\right] = \frac{1}{p_s}\int_0^{p_s} f(p) G_k(p) \mathrm{d}p, \tag{A.92}$$

where $G_k(p)$ is the kernel of the vertical transform, which is to be chosen so that

$$\mathcal{T}\left[\mathcal{D}\frac{\partial f\left(p\right)}{\partial t}\right] \;=\; -\,\xi_k \frac{\partial}{\partial t}\mathcal{T}\left[f\left(p\right)\right], \tag{A.93}$$

with ξ_k a constant (Fulton and Schubert, 1985).

Applying the vertical differential operator $\mathcal{D}$ to $f(p)$ in (A.92) and integrating by parts twice, yields

$$\begin{aligned}\mathcal{T}\left[\mathcal{D}f\left(p\right)\right] \;=\; & \frac{1}{p_s}\left(G_k(p_s)\left(\frac{1}{S_0}\frac{\mathrm{d}f(p)}{\mathrm{d}p}\right)_{p=p_s} - f\left(p_s\right)\left(\frac{1}{S_0}\frac{\mathrm{d}G_k(p)}{\mathrm{d}p}\right)_{p=p_s}\right) \\ & + \frac{1}{p_s}\lim_{p\to 0}\frac{1}{S_0}\left(f\left(p\right)\frac{\mathrm{d}G_k(p)}{\mathrm{d}p} - G_k(p)\frac{\mathrm{d}f(p)}{\mathrm{d}p}\right) \\ & + \frac{1}{p_s}\int_0^{p_s} f(p)\,\mathcal{D}G_k(p)\mathrm{d}p.\end{aligned} \tag{A.94}$$

For consistency with the shallowness approximations, the functions $G_k(p)$ must be bounded, i.e. $\lim_{p\to 0}\left|G_k\left(p\right)\right| < \infty$, and if they satisfy analogous boundary conditions

as (A.88) and (A.90), i.e.

$$\frac{\partial G}{\partial p} + \frac{p\, S_0}{R\, T_0}\, G \;=\; 0 \quad \text{at} \quad p = p_s, \tag{A.95}$$

$$\lim_{p\to 0} \frac{1}{S_0}\frac{\partial G}{\partial p} \;=\; 0. \tag{A.96}$$

then, by setting $f(p) = \frac{\partial \phi}{\partial t}$ equation (A.94) is reduced to

$$\begin{aligned} \mathcal{T}\left[\mathcal{D}\frac{\partial \phi}{\partial t}\right] &= \frac{1}{p_s}\int_0^{p_s} \frac{\partial \phi}{\partial t}\, \mathcal{D}G_k(p)\mathrm{d}p \\ &= \frac{\partial}{\partial t}\left\{\frac{1}{p_s}\int_0^{p_s} \phi\, \mathcal{D}G_k(p)\mathrm{d}p\right\}. \end{aligned} \tag{A.97}$$

Equation (A.97) shows that the desired property (A.93) will hold provided that $G_k(p)$ and ξ_k are chosen as eigensolutions of the *vertical structure equation*

$$\mathcal{D}G_k(p) + \xi_k G_k(p) \;=\; 0. \tag{A.98}$$

In fact, using (A.92) and (A.98) it may be shown that

$$\mathcal{T}\left[\mathcal{D}\frac{\partial \phi}{\partial t}\right] \;=\; -\,\xi_k\, \frac{\partial}{\partial t}\,\mathcal{T}\left[\phi\right]. \tag{A.99}$$

Assuming a bounded atmosphere Cohn and Dee (1989) have obtained the following results:

(i) The solutions of (A.98) that satisfy boundary conditions (A.95) and (A.96) are bounded functions.

(ii) The eigenvalues ξ_k are all positive and their spectrum is totally discrete.

(iii) The eigenfunctions $G_k(p)$ form a complete orthogonal basis for the space of functions which are square-integrable over $0 < p < p_s$, with the inner product defined by

$$\langle f, g\rangle = \frac{1}{p_s}\int_0^{p_s} f(p)\, g(p)\, \mathrm{d}p. \tag{A.100}$$

Moreover, G_k has precisely k zeros on $0 \le p \le p_s$.

Statement (iii) justifies the use of the *vertical structure functions* G_k as a basis for spectral expansions. That is, any function of pressure, $f(p)$, may be expanded as

$$f\,(p) = \sum_{k=0}^{\infty} f_k\, G_k\,(p)\,, \tag{A.101}$$

with f_k given by (A.92). Using the vertical transform pair (A.92) and (A.101), the column vector $(u, v, \phi)^{\mathrm{T}}$, whose components are the dependent variables of the linearised system (A.73)-(A.75), may be expanded as

$$(u, v, \phi)^{\mathrm{T}} = \sum_{k=0}^{\infty} (u_k, v_k, \phi_k)^{\mathrm{T}}\; G_k\,(p)\,, \tag{A.102}$$

where

$$(u_k, v_k, \phi_k)^{\mathrm{T}} = \frac{1}{p_s} \int_0^{p_s} (u, v, \phi)^{\mathrm{T}}\; G_k\,(p)\,\mathrm{d}p, \tag{A.103}$$

with the superscript $^{\mathrm{T}}$ denoting transpose.

A.3.3 Horizontal structure functions

Applying the vertical transform (A.92) to the system of equation (A.73)-(A.75) results in

$$\frac{\partial u_k}{\partial t} - f v_k + \frac{1}{a\cos\theta}\frac{\partial \phi_k}{\partial \lambda} = 0, \tag{A.104}$$

$$\frac{\partial v_k}{\partial t} + f u_k + \frac{1}{a}\frac{\partial \phi_k}{\partial \theta} = 0, \tag{A.105}$$

$$\frac{\partial \phi_k}{\partial t} + \frac{g\,h_k}{a\,\cos\theta}\left[\frac{\partial u_k}{\partial \lambda} + \frac{\partial}{\partial \theta}\,(v_k\,\cos\theta)\right] = 0, \tag{A.106}$$

where $g\,h_k = \xi_k^{-1}$.

The system of equations (A.104)-(A.106) is often referred to as Laplace's tidal equations without the tide-generating terms. This system appears as that of the *horizontal structure equations* when the linearised model of an atmosphere at rest is resolved into its vertical and horizontal parts using the method of separation of variables. In

this case, the mean free surface height h_k is interpreted as the constant of separation which links the vertical and horizontal operators and is known as the equivalent height (Swarztrauber and Kasahara, 1985).

In the case of free oscillations (normal modes) the solutions of interest for (A.104)-(A.106), are those for positive values of h_k, although a negative value of h_k may be admitted for cases of forced oscillations.

Introducing the dimensionless variables

$$\hat{u}_k = \frac{u_k}{\sqrt{g\,h_k}}, \quad \hat{v}_k = \frac{v_k}{\sqrt{g\,h_k}}, \quad \hat{\phi}_k = \frac{\phi_k}{g\,h_k}, \quad \text{and} \quad \hat{t} = 2\,\Omega\,t, \tag{A.107}$$

then (A.104)-(A.106) can be written in the form

$$\frac{\partial}{\partial \hat{t}}\mathbf{W}_k + \mathbf{L}\,\mathbf{W}_k = 0, \tag{A.108}$$

where $\mathbf{W}_k$ denotes the vector dependent variable

$$\mathbf{W}_k = \left(\hat{u}_k, \hat{v}_k, \hat{\phi}_k\right)^{\mathrm{T}}. \tag{A.109}$$

The linear differential matrix operator $\mathbf{L}$ is given by

$$\mathbf{L} = \begin{bmatrix} 0 & -\sin\theta & \frac{\alpha_k}{\cos\theta}\frac{\partial}{\partial\lambda} \\ \sin\theta & 0 & \alpha_k\frac{\partial}{\partial\theta} \\ \frac{\alpha_k}{\cos\theta}\frac{\partial}{\partial\lambda} & \frac{\alpha_k}{\cos\theta}\frac{\partial}{\partial\theta}\left(\cos\theta\,(\cdot)\right) & 0 \end{bmatrix}, \tag{A.110}$$

in which

$$\alpha_k = \frac{\sqrt{g\,h_k}}{2\,\Omega\,a}, \tag{A.111}$$

is a dimensionless constant that characterises the nature of shallow-water flows. The related quantity, $\varepsilon_k = \alpha_k^{-2}$ is called Lamb's parameter.

Since (A.108) is a linear system with respect to $\hat{t}$, the solution $\mathbf{W}_k$ can be expressed as a linear combination of functions that have the form

$$\mathbf{W}_k\left(\lambda, \theta, \hat{t}\right) = \mathbf{H}_{nlk}\left(\lambda, \theta\right)\, e^{-i\,\sigma_{nlk}\,\hat{t}}, \tag{A.112}$$

where $\mathbf{H}_{nlk}(\lambda,\theta)$ is the horizontal structure of the normal mode and σ_{nlk} is the corresponding frequency scaled by 2Ω. Substituting (A.112) into (A.108) gives

$$-i\,\sigma_{nlk}\mathbf{H}_{nlk}(\lambda,\theta)+\mathbf{L}\,\mathbf{H}_{nlk}(\lambda,\theta)=0, \tag{A.113}$$

and thus the problem reduces to finding $\mathbf{H}_{nlk}(\lambda,\theta)$ and σ_{nlk} that satisfy the eigenvalue equation (A.113).

Because (A.108) is also linear with respect to longitude λ, the *horizontal structure functions* $\mathbf{H}_{nlk}(\lambda,\theta)$, which are referred to as Hough harmonics (after Hough, 1898), can be expressed in the form

$$\mathbf{H}_{nlk}(\lambda,\theta)=\mathbf{\Theta}_{nlk}(\theta)\,e^{i\,n\,\lambda}, \tag{A.114}$$

where n denotes the zonal wavenumber and $\mathbf{\Theta}_{nlk}(\theta)$ the meridional modal functions, which are referred to as Hough vector functions and depend only on latitude θ.

It can be shown by direct substitution followed by integration by parts with respect to λ and θ that

$$\langle u,\mathbf{L}v\rangle=-\langle\mathbf{L}u,v\rangle\,, \tag{A.115}$$

where u and v are arbitrary functions defined on the sphere and the inner product is defined by

$$\langle u,v\rangle=\int_0^{2\pi}\int_{-\frac{\pi}{2}}^{\frac{\pi}{2}}u^{\star}v\cos\theta\mathrm{d}\theta\mathrm{d}\lambda, \tag{A.116}$$

in which $u^{\star}$ is the conjugate transpose of u. Thus, for real α or positive ε, $\mathbf{L}$ is skew-Hermitian, and (A.115) can be used to determine that all the frequencies σ_{nlk} in (A.113) are real and that any modes corresponding to distinct frequencies are orthogonal. Let $\mathbf{H_1}$ and $\mathbf{H_2}$ be modes that correspond to frequencies σ_1 and σ_2, respectively. Then, setting $u=\mathbf{H_1}$ and $v=\mathbf{H_2}$ in (A.115), gives

$$\langle\mathbf{H_1},i\sigma_2\mathbf{H_2}\rangle=-\langle i\sigma_1\mathbf{H_1},\mathbf{H_2}\rangle\,, \tag{A.117}$$

or,

$$(\sigma_2-\overline{\sigma}_1)\,\langle\mathbf{H_1},\mathbf{H_2}\rangle=0, \tag{A.118}$$

where the overbar denotes a complex conjugate.

If $\mathbf{H_1} = \mathbf{H_2}$, then $\sigma_1 = \sigma_2$ and (A.118) only holds if $\sigma_1 = \overline{\sigma}_1$. Thus, all the frequencies σ are real. On the other hand, if the frequencies are real and distinct, then $(\sigma_2 - \overline{\sigma}_1)$ is nonzero and (A.118) only holds if $\langle \mathbf{H_1}, \mathbf{H_2} \rangle = 0$, meaning that the modes are orthogonal.

There are a number of Hough vector functions corresponding to each wavenumber. Hence, the Hough harmonics $\mathbf{H}_{nlk}(\lambda, \theta)$ and the associated frequencies σ_{nlk} depend on the zonal wavenumber n, the meridional mode denoted by index l and the vertical mode denoted by index k.

In the case $n \geq 1$, there are two different kinds of motion with distinct frequencies. The first kind corresponds to eastward and westward propagating *gravity-inertia* waves, and the second kind to westward propagating *rotational* waves of the Rossby-Haurwitz type. The meridional mode number is therefore defined as a sequence of three distinct modes. One is a westward propagating Rossby mode specified by l_r, and the other two are westward and eastward propagating gravity modes, l_w and l_e, respectively. In the case of $n = 0$, the frequencies of gravity-inertia motion appear as pairs of positive and negative values with equal magnitudes. The meaning of eastward and westward propagations is lost in this case, but the term eastward (westward) is nevertheless used to indicate positive (negative) frequency. On the other hand, the frequencies of the rotational motion, as well as the gravity frequencies corresponding to the lowest meridional index $l = 0$, are zero (Longuet-Higgins, 1968; Swarztrauber and Kasahara, 1985).

For $n > 0$, all the frequencies are distinct and thus the modes are orthogonal. However, for $n = 0$, the frequencies of the rotational modes are all zero and hence the modes are not necessarily orthogonal. Nevertheless, it is possible to derive an orthogonal set of rotational modes for $n = 0$ (Shigehisa, 1983), which are also orthogonal to the modes for $n > 0$. Hence, all the modes are orthogonal for $n \geq 0$, that is the Hough harmonics $\mathbf{H}(\lambda, \theta)$ satisfy the orthonormal condition given by

$$\frac{1}{2\,\pi} \int_{-\frac{\pi}{2}}^{\frac{\pi}{2}} \int_{0}^{2\,\pi} \mathbf{H}^{\star}_{nlk} \cdot \mathbf{H}_{n'l'k} \cos\theta \mathrm{d}\lambda \mathrm{d}\theta = \delta_{nn'}\, \delta_{ll'}, \tag{A.119}$$

where the right-hand side is unity if $n = n^{'}$ and $l = l^{'}$, and zero otherwise.

Using orthonormal condition (A.119) a set of Fourier-Hough transforms may be constructed as

$$\mathbf{W}_k\left(\lambda,\theta,t\right) = \sum_{l=0}^{\infty}\sum_{n=-\infty}^{\infty} w_{nlk}(t)\,\mathbf{H}_{nlk}\left(\lambda,\theta\right), \tag{A.120}$$

$$w_{nlk}(t) = \int_{-\frac{\pi}{2}}^{\frac{\pi}{2}}\int_{0}^{2\,\pi} \mathbf{H}^{\star}_{nlk}\left(\lambda,\theta\right)\cdot\mathbf{W}_k\left(\lambda,\theta,t\right)\cos\theta \mathrm{d}\lambda\mathrm{d}\theta, \tag{A.121}$$

or,

$$\left(u_k,v_k,\phi_k\right)^{\mathrm{T}} = \sum_{l=0}^{\infty}\sum_{n=-\infty}^{\infty} w_{nlk}(t)\,\mathbf{X}_k\,\mathbf{H}_{nlk}\left(\lambda,\theta\right), \tag{A.122}$$

$$w_{nlk}(t) = \int_{-\frac{\pi}{2}}^{\frac{\pi}{2}}\int_{0}^{2\,\pi} \mathbf{H}^{\star}_{nlk}\left(\lambda,\theta\right)\cdot\left(\mathbf{X}_k^{-1}\left(u_k,v_k,\phi_k\right)^{\mathrm{T}}\right)\cos\theta \mathrm{d}\lambda\mathrm{d}\theta, \tag{A.123}$$

with $\mathbf{X}_k$ given by (2.60).

A.3.4 3-D Normal mode functions

The eigensolutions of the linearised primitive equations (A.73)-(A.75), are referred to as normal mode functions. The normal mode functions, $\Pi_{nlk}\left(\lambda,\theta,p\right)$, are defined by the product of the vertical normal modes and the horizontal normal modes (Kasahara, 1976). The vertical normal modes $G_k(p)$ are solutions of the vertical structure equation and the horizontal normal modes $\mathbf{H}_{nlk}\left(\lambda,\theta\right)$ the solutions of the horizontal structure equation.

Replacing $\left(u_k,v_k,\phi_k\right)^{\mathrm{T}}$ in (A.102) by expansion (A.122) results in

$$\left(u,v,\phi\right)^{\mathrm{T}} = \sum_{k=0}^{\infty}\sum_{l=0}^{\infty}\sum_{n=-\infty}^{\infty} w_{nlk}(t)\,\Pi_{nlk}\left(\lambda,\theta,p\right), \tag{A.124}$$

where

$$w_{nlk}(t) = \int_{-\frac{\pi}{2}}^{\frac{\pi}{2}}\int_{0}^{2\,\pi}\int_{0}^{p_s} \Pi^{\star}_{nlk}\left(\lambda,\theta,p\right)\cdot\left(\mathbf{X}_k^{-1}\,\left(u,v,\phi\right)^{\mathrm{T}}\right)\,\cos\theta\,\mathrm{d}p\,\mathrm{d}\lambda\,\mathrm{d}\theta, \tag{A.125}$$

and

$$\Pi_{nlk}\left(\lambda,\theta,p\right)=\mathbf{X}_k\,G_k\left(p\right)\,\mathbf{H}_{nlk}\left(\lambda,\theta\right)=\mathbf{X}_k\,G_k\left(p\right)\,\mathbf{\Theta}_{nlk}\left(\theta\right)e^{i\,n\,\lambda}. \tag{A.126}$$

The three-dimensional (3-D) normal mode functions, $\Pi_{nlk}\left(\lambda,\theta,p\right)$, define the 3-D structures of the normal modes of an adiabatic atmosphere linearised about a state at rest. They form a complete set of expansion basis and satisfy the following orthonormal condition under an inner product $\langle\,,\,\rangle$

$$\langle\Pi_{nlk},\Pi_{n'l'k'}\rangle \;=\; \frac{1}{2\,\pi\,p_s}\int_{-\frac{\pi}{2}}^{\frac{\pi}{2}}\int_0^{2\,\pi}\int_0^{p_s}\Pi^{\star}_{nlk}\cdot\Pi_{n'l'k'}\,\cos\theta\,\mathrm{d}p\,\mathrm{d}\lambda\,\mathrm{d}\theta. \tag{A.127}$$

The vertical index, k, represents the number of nodes of the vertical structure functions $G_k(p)$ over the interval $0\leq p\leq ps$ (Cohn and Dee, 1989). Therefore, since $G_0(p)$ has no node and is approximately constant in the vertical, the modes Π_{nl0} are called external or barotropic modes. The modes Π_{nlk} for $k\geq 1$ are called internal or baroclinic modes, and have k nodes in the vertical.

The expansion of the horizontal wind and mass fields simultaneously in terms of 3-D normal mode functions, that permits the partion of energy into two distinct kinds of motions, the gravity-inertia modes and the rotational modes of the Rossby-Haurwitz type, was introduced by Kasahara and Puri (1981). By applying the three-dimensional expansion into normal mode functions, Tanaka (1985) has developed a 3-D normal mode energetics scheme, which describes the energy flow among the different normal modes in the atmosphere.

Bibliography

Boer, G. J., 1995. Some Dynamical Consequences of Greenhouse Gas Warming. Atmos.Ocean 33, 731–751.

Boer, G. J., Denis, B., 1997. Numerical convergence of the dynamics of a GCM. Clim. Dyn. 13, 359–374.

Boer, G. J., Lambert, S., 2008. The energy cycle in atmospheric models. Clim. Dyn. 30, 371–390.

Castanheira, J. M., 2000. Climatic variability of the atmospheric circulation at the global scale. Ph.D. Thesis, University of Aveiro, Portugal, 186 pp.

Castanheira, J. M., Añel, J. A., Marques, C. A. F., Antuña, J. C., Liberato, M. L. R., de la Torre, L., Gimeno, L., 2009. Increase of upper troposphere/lower stratosphere wave baroclinicity during the second half of the 20th century. Atmos. Chem. Phys. 9, 18597–18619.

Castanheira, J. M., DaCamara, C. C., Rocha, A., 1999. Numerical solutions of the vertical structure equation and associated energetics. Tellus 51A, 337–348.

Charney, J. G., 1971. Geostrophic turbulence. J. Atmos. Sci. 28, 1087–1095.

Chen, J., Bosilovich, M. G., 2007. Hydrological Variability and Trends in Global Reanalyses. In: 19^{th} Conference on Climate Variability and Change. The 87^{th} AMS Annual Meeting, San Antonio, TX, p. 5, JP4.4.

Cohn, S. E., Dee, D. P., 1989. An analysis of the vertical structure equation for arbitrary thermal profiles. Q. J. R. Meteorol. Soc. 115, 143–171.

Collins, W. D., Bitz, C. M., Blackmon, M. L., Bonan, G. B., Bretherton, C. S., Carton, J. A., Chang, P., Doney, S. C., Hack, J. J., Henderson, T. B., Kiehl, J. T., Large, W. G., McKenna, D. S., Santer, B. D., Smith, R. D., 2006. The Community Climate System Model Version 3 (CCSM3). J. Climate 19, 2122–2143.

DaCamara, C. C., 1991. Planetary wave activities and energetics in the northern hemisphere winter circulation. Ph.D. Thesis, University of Missouri-Columbia, 105 pp.

Dell'Aquilla, A., Lucarini, V., Ruti, P. M., Calmanti, S., 2005. Hayashi spectra of the northern hemisphere mid-latitude atmospheric variability in the NCEP-NCAR and ECMWF reanalyses. Clim. Dyn. 25, 639–652.

Déqué, M., Dreveton, C., Braun, A., Cariolle, D., 1994. The ARPEGE/IFS atmosphere model: a contribution to the french community climate modelling. Clim. Dyn. 10, 249–266.

Dutton, J. A., 1995. Dynamics of Atmospheric Motion (Formerly The Ceaseless Wind). Dover Publications, New York.

Eliasen, E., Machenhauer, B., 1965. A study of the fluctuations of the atmospheric planetary flow patterns represented by spherical harmonics. Tellus 17, 220–238.

Fulton, S. R., Schubert, W. H., 1985. Vertical Normal Modes Transforms: Theory and Application. Mon. Wea. Rev. 113, 647–657.

Gibson, J. K., Kållberg, P., Uppala, S., Hernandez, A., Nomura, A., Serrano, E., 1997. ERA-15 Description. ECMWF Re-Analysis Project Report Series 1.

Grotjahn, R., 1993. Global Atmospheric Circulations: Observations and Theories. Oxford University Press, Printed in the USA.

Hamilton, K., Wilson, R. J., Hemler, R. S., 1999. Middle Atmosphere Simulated with High Vertical and Horizontal Resolution Versions of a GCM: Improvements in the Cold Pole Bias and Generation of a QBO-like Oscillation in the Tropics. J. Atmos. Sci. 56, 3829–3846.

Hasegawa, A., Tanaka, H. L., Hirakuchi, H., Taguchi, S., 1997. Comparative energetics analysis of CCM2 with different horizontal resolutions. Clim. Dyn. 13, 521–532.

Hayashi, Y., 1980. Estimation of nonlinear energy transfer spectra by the cross-spectral method. J. Atmos. Sci. 37, 299–307.

Hayashi, Y., Golder, D. G., 1987. Effects of Wave-Wave and Wave-Mean Flow Interactions on the Growth and Maintenance of Transient Planetary Waves in the Presence of a Mean Thermal Restoring Force. J. Atmos. Sci. 44, 3392–3401.

Held, I. M., 1993. Large-scale dynamics and global warming. Bull. Amer. Meteor. Soc. 74, 228–240.

Held, I. M., Suarez, M. J., 1994. A proposal for the intercomparison of the dynamical cores of atmospheric general circulation models. Bull. Am. Meteorol. Soc. 75, 1825–1830.

Hernández-Deckers, D., von Storch, J.-S., 2010. Energetics Responses to Increases in Greenhouse Gas Concentration. J. Climate 23, 3874–3887.

Holmström, I., 1963. On a method for parametric representation of the state of the atmosphere. Tellus 15, 127–149.

Holton, J. R., 2004. An introduction to Dynamic Meteorology, Fourth Edition. International Geophysics Series, Vol. 88. Elsevier Academic Press.

Hough, S. S., 1898. On the application of harmonic analysis to the dynamical theory of the tides Part II. On the general integration of Laplaces tidal equations. Phil. Trans. Roy. Soc. London A191, 139–185.

Jones, P. W., 1999. First- and Second-Order Conservative Remapping Schemes for Grids in Spherical Coordinates. Mon. Wea. Rev. 127, 2204–2210.

Kalnay, E., Kanamitsu, M., Kistler, R., Collins, W., Deaven, D., Gandin, L., Iredell, M., Saha, S., White, G., Woollen, J., Zhu, Y., Chelliah, M., Ebisuzaki, W., Higgins, W., Janowiak, J., Mo, K. C., Ropelewski, C., Wang, J., Leetmaa, A., Reynolds,

R., Jenne, R., Joseph, D., 1996. The NMC/NCAR 40-Year Reanalysis Project. Bull. Amer. Meteor. Soc. 77, 437–471.

Kanamitsu, M., Ebisuzaki, W., Woollen, J., Yang, S.-K., Hnilo, J. J., Fiorino, M., Potter, G. L., 2002. NCEP-DOE AMIP-II Reanalysis (R-2). Bull. Amer. Meteor. Soc. 83, 1631–1643.

Kao, S. K., 1968. Governing equations and spectra for atmospheric motion and transports in frequency-wavenumber space. J. Atmos. Sci. 25, 32–38.

Kasahara, A., 1976. Normal modes of ultralong waves in the atmosphere. Mon. Wea. Rev. 104, 669–690.

Kasahara, A., 1977. Numerical Integration of the Global Barotropic Primitive Equations with Hough Harmonic Expansions. J. Atmos. Sci. 34, 687–701.

Kasahara, A., 1984. The Linear Response of a Stratified Global Atmosphere to Tropical Thermal Forcing. J. Atmos. Sci. 41, 2217–2237.

Kasahara, A., Puri, K., 1981. Spectral representation of three-dimensional global data by expansion in normal mode functions. Mon. Wea. Rev. 109, 37–51.

Kistler, R., Kalnay, E., Collins, W., Saha, S., White, G., Woollen, J., Chelliah, M., Ebisuzaki, W., Kanamitsu, M., Kousky, V., van den Dool, H., Jenne, R., Fiorino, M., 2001. The NCEP/NCAR 50-Year Reanalysis: Documentation and monthly-means CD-ROM. Bull. Amer. Meteor. Soc. 82, 247–267.

Krueger, A. F., Winston, J. S., Haines, D. A., 1965. Computations of the atmospheric energy and its transformation for the northern hemisphere for a recent five-year period. Mon. Wea. Rev. 93, 227–238.

Kung, E. C., Tanaka, H., 1983. Energetics Analysis of the Global Circulation during the Special Observation Periods of FGGE. J. Atmos. Sci. 41, 2575–2592.

Kung, E. C., Tanaka, H. L., Baker, W. E., 1989. Energetics Examination of Winter Blocking Simulations in the Northern Hemisphere. Mon. Wea. Rev. 117, 2019–2040.

Kunz, T., Fraedrich, K., Kirk, E., 2008. Optimisation of simplified GCMs using circulation indices and maximum entropy production. Clim. Dyn. 30, 803–813.

Lambert, S. J., 1984. A Global Available Potential Energy-Kinetic Energy Budget in Terms of the Two-Dimensional Wavenumber for the FGGE Year. Atmosphere-Ocean 22, 265–282.

Li, L., Ingersoll, A. P., Jiang, X., Feldman, D., Yung, Y. L., 2007. Lorenz energy cycle of the global atmosphere based on reanalysis datasets. Geophys. Res. Lett. 34, L16813.

Lindzen, R. L., Fox-Rabinovitz, M., 1989. Consistent Vertical and Horizontal Resolution. Mon. Wea. Rev. 11, 2575–2583.

Longuet-Higgins, M. S., 1968. The eigenfunctions of Laplaces tidal equations over a sphere. Phil. Trans. Roy. Soc. London A262, 511–607.

Lorenc, A. C., Swinbank, R., 1984. On the accuracy of general circulation statistics calculated from FGGE data - a comparison of results from two sets of analyses. Quart. J. R. Met. Soc. 110, 915–942.

Lorenz, D. J., DeWeaver, E. T., 2007. Tropopause height and zonal wind response to global warming in the IPCC scenario integrations. J. Geophys. Res. 112, D10119.

Lorenz, E. N., 1955. Available potential energy and the maintenance of the general circulation. Tellus 7, 157–167.

Lorenz, E. N., 1967. The nature and theory of the general circulation of the atmosphere. In: WMO Publication. No. 218. Geneva, 161 pp.

MacRobert, T. M., 1967. Spherical Harmonics. An Elementary Treatise on Harmonic Functions with Applications. Pergamon Press, Oxford/London, 349 pp.

Margules, M., 1903. Über die Energie der Stürme. Jahrb. kais-kön Zent. für Met. 40, 1–26, Translation by C. Abbe in Smithson. Misc. Coll., 51. 553-595, 1910.

Marques, C. A. F., Rocha, A., Corte-Real, J., 2010a. Comparative energetics of ERA-40, JRA-25 and NCEP-R2 reanalysis, in the wave number domain. Dynamics of Atmospheres and Oceans 50 (3), 375–399.

Marques, C. A. F., Rocha, A., Corte-Real, J., 2010b. Global diagnostic energetics of five state-of-the-art climate models. Clim. Dyn., 1–28.
URL http://dx.doi.org/10.1007/s00382-010-0828-9

Marques, C. A. F., Rocha, A., Corte-Real, J., Castanheira, J. M., Ferreira, J., Melo-Gonçalves, P., 2009. Global atmospheric energetics from NCEP-Reanalysis 2 and ECMWF-ERA40 Reanalysis. Int. J. Climatol. 29, 159–174.

McFarlane, N. A., Scinocca, J., Lazare, M., Harvey, R., Verseghy, D., Li, J., 2005. The CCCma third generation atmospheric general circulation model. CCCma internal rep., 25 pp.

Merilees, P. E., Warn, T., 1972. The resolution implications of geostrophic turbulence. J. Atmos. Sci. 29, 990–991.

Mo, K.-C., Higgins, R. W., 1996. Large-scale atmospheric moisture transport as evaluated in the NCEP/NCAR and the NASA/DAO reanalyses. J. Climate 9, 1531–1545.

Nastrom, G. D., Gage, K. S., 1985. A climatology of atmospheric wavenumber spectra of wind and temperature observed by commercial aircraft. J. Atmos. Sci. 42, 950–960.

Niehörster, F., Fast, I., Huebener, H., Cubasch, U., 2008. The stream one ENSEMBLES projections of future climate change. Ensembles technical report no. 3, Met Office Hadley Centre, UK, 30 pp.

Nozawa, T., Nagashima, T., Ogura, T., Yokohata, T., Okada, N., Shiogama, H., 2007. Climate change simulations with a coupled ocean-atmosphere GCM called the model for interdisciplinary research on climate: MIROC. CGER's Supercomputer Monograph Report 12, Center for Global Environmental Research, National Institute for Environmental Studies, Tsukuba, Japan, 79 pp.

Nozawa, T., Nagashima, T., Shiogama, H., Crooks, S. A., 2005. Detecting natural influences on surface air temperature change in the early twentieth century. Geophys. Res. Lett. 32 (L20719).

Onogi, K., Tsutsui, J., Koide, H., Sakamoto, M., Kobayashi, S., Hatsushika, H., Matsumoto, T., Yamazaki, N., Kamahori, H., Takahashi, K., Kadokura, S., Wada, K., Kato, K., Oyama, R., Ose, T., Mannoji, N., Taira, R., 2007. The JRA-25 Reanalysis. J. Meteor. Soc. Japan 85, 369–432.

Oort, A. H., 1964. On estimates of the atmospheric energy cycle. Mon. Wea. Rev. 92, 483–493.

Oort, A. H., Peixoto, J. P., 1974. The Annual Cycle of the Energetics of the Atmosphere on a Planetary Scale. J. Geophys. Res. 79, 2705–2719.

Oriol, E., 1982. Energy budget calculations at ECMWF. Part 1 - Analysis 1980-81. ECMWF Technical Report 35.

Pavan, V., Hall, N., Valdes, P., Blackburn, M., 1999. The importance of moisture distribution for the growth and energetics of mid-latitude systems. Ann. Geophysicae 17, 242–256.

Peixoto, J. P., Corte-Real, J. A. M., 1982. The Energetics of the General Circulation of the Atmosphere in Southern Hemisphere During the IGY. Part I: The Distribution of Atmospheric Energy. Arch. Met. Geoph. Biokl. 31, 277–301.

Peixoto, J. P., Corte-Real, J. A. M., 1983. The Energetics of the General Circulation of the Atmosphere in Southern Hemisphere During the IGY. Part II: The Cycle of the Energetics of the Atmosphere in Southern Hemisphere. Arch. Met. Geoph. Biokl. 32, 1–21.

Peixoto, J. P., Oort, A. H., 1974. The Annual Distribution of Atmospheric Energy on a Planetary Scale. J. Geophys. Res. 79, 2149–2159.

Peixoto, J. P., Oort, A. H., 1992. Physics of Climate. American Institute of Physics, New York, 520 pp.

Pope, V. D., Pamment, J. A., Jackson, D. R., Slingo, A., 2001. The Representation of Water Vapor and Its Dependence on Vertical Resolution in the Hadley Centre Climate Model. J. Climate 14, 3065–3085.

Pope, V. D., Stratton, R., 2002. The processes governing horizontal resolution sensitivity in a climate model. Clim. Dyn. 19, 211–236.

Roeckner, E., Bäuml, G., Bonaventura, L., Brokopf, R., Esch, M., Giorgetta, M., Hagemann, S., Kirchner, I., Kornblueh, L., Manzini, E., Rhodin, A., Schlese, U., Schulzweida, U., Tompkins, A., 2003. The atmospheric general circulation model ECHAM5. Part I: Model description. Max Planck Institute for Meteorology Rep. 349, 127 pp.

Roeckner, E., Brokopf, R., Esch, M., Giorgetta, M., Hagemann, S., Kornblueh, L., Manzini, L., Schlese, U., Schulzweida, U., 2006. Sensitivity of Simulated Climate to Horizontal and Vertical Resolution in the ECHAM5 Atmosphere Model. J. Climate 19, 3771–3791.

Roman, J. C., Miguez-Macho, G., Byerle, L. A., Paegle, J., 2004. Intercomparison of Global Research and Operational Forecasts. Wea. Forecasting 19, 534–551.

Ruti, P. M., Rocco, D. D., Gualdi, S., 2006. Impact of increased vertical resolution on simulation of tropical climate. Theor. Appl. Climatol. 85, 61–80.

Salas-Mélia, D., Chauvin, F., Déqué, M., Douville, H., Gueremy, J. F., Marquet, P., Planton, S., Royer, J. F., Tyteca, S., 2003. Description and validation of the CNRM-CM3 global coupled model. CNRM working note 103.

Saltzman, B., 1957. Equations governing the energetics of the larger scales of atmospheric turbulence in the domain of wave number. J. Meteor. 14, 513–523.

Saltzman, B., 1970. Large-Scale Atmospheric Energetics in the Wave-Number Domain. Rev. Geophys. Space Phys. 8, 289–302.

Schneider, T., O'Gorman, P. A., Levine, X., 2010. Water vapor and the dynamics of climate changes. Rev. Geophys. 48, RG3001.

Shigehisa, Y., 1983. Normal modes of the shallow water equations for zonal wavenumber zero. J. Meteor. Soc. Japan 61, 479–494.

Sneddon, I. N., 1972. The use of integral transforms. McGraw-Hill, New York, 539 pp.

Steinberg, H. L., 1971. On power laws and nonlinear cascades in large scale atmospheric flow. Tech. rept. 002630-4-t, Dept. of Meteorology and Oceanography, University of Michigan, 162 pp.

Stendel, M., Arpe, K., 1997. Evaluation of the hydrological cycle in reanalyses and observations. Max-Planck-Institut für Meteorologie Report 228.

Stratton, R., 1999. A high resolution AMIP integration using the Hadley Centre model HadAM2b. Clim. Dyn. 15, 9–28.

Stratton, R. A., 2004. Report on aspects of variability in high-resolution versions of HadAM3. Hadley Centre technical note 53, 31 pp.

Swarztrauber, P. N., Kasahara, A., 1985. The vector harmonic analysis of Laplaces tidal equations. SIAM J. Sci. Stat. Comput. 6, 464–491.

Tanaka, H. L., 1985. Global energetics analysis by expansion into three-dimensional normal-mode functions during the FGGE winter. J. Meteor. Soc. Japan 63, 180–200.

Tanaka, H. L., 1994. Normal Mode Energetics of the General Circulation during the FGGE Winter. Sci. Rept. Sect. A., Vol.15, Inst. Geosci., Univ. Tsukuba, 19 pp.

Tanaka, H. L., Ji, Q., 1995. Comparative Energetics of FGGE Re-analyses Using the Normal Mode Expansion. J. Meteor. Soc. Japan 73, 1–12.

Tanaka, H. L., Kimura, K., 1996. Normal Mode Energetics Analyses and Intercomparison for the Recent ECMWF, NMC, and JMA Global Analyses. J. Meteor. Soc. Japan 74, 525–538.

Tanaka, H. L., Kung, E. C., 1988. Normal-mode energetics of the general circulation during the FGGE year. J. Atmos. Sci. 45, 3723–3736.

Tanaka, H. L., Kung, E. C., Baker, W. E., 1986. Energetics analysis of the observed and simulated general circulation using three-dimensional normal mode expansions. Tellus 38A, 412–428.

Tanaka, H. L., Kung, E. C., Baker, W. E., 1989. Normal Mode Energetics and Error Analysis of GLA GCM Simulations with Different Horizontal Resolutions during a Winter Month. Beitr. Phys. Atmosph. 62, 99–111.

Tanaka, H. L., Watarai, Y., Kanda, T., 2004. Energy spectrum proportional to the squared phase speed of Rossby modes in the general circulation of the atmosphere. Geophys. Res. Lett. 31, 13109.

Tenenbaum, J., 1975. Spectral and Spatial Energetics of the GISS Model Atmosphere. Mon. Wea. Rev. 104, 15–29.

Terasaki, K., Tanaka, H. L., 2007a. An Analysis of the 3-D Atmospheric Energy Spectra and Interactions Using Analytical Vertical Structure Functions and Two Reanalyses. J. Meteor. Soc. Japan 85, 785–796.

Terasaki, K., Tanaka, H. L., 2007b. Barotropic Energy Spectrum by the Rossby Wave Saturation in the Zonal Wavenumber Domain. SOLA 3, 25–28.

Terasaki, K., Tanaka, H. L., 2008. Spectral energetics analysis of the general circulation of the atmosphere in the vertical wavenumber domain. In: Proc. First International Symposium on the Arctic Research. Nov. 4-6, Miraikan, Tokyo, Japan., pp. 230–233.

Trenberth, K. E., Berry, J. C., Buja, L. E., 1993. Vertical Interpolation and Truncation of Model-Coordinate Data. NCAR Technical Note. NCAR/TN-396+STR, 54 pp.

Trenberth, K. E., Dole, R., Xue, Y., Onogi, K., Dee, D., Balmaseda, M., Bosilovich, M., Schubert, S., Large, W., 2010. Atmospheric reanalyses: A major resource for ocean product development and modeling. In: Proc. "OceanObs09: Sustained Ocean Observations and Information for Society" Conference (Vol. 2). J. Hall, D. E. Harrison and D. Stammer, Eds., Venice, Italy, 21-25 September 2009, p. 8, ESA Publication WPP-306.

Trenberth, K. E., Stepaniak, D. P., 2002. A pathological problem with NCEP reanalyses in the stratosphere. J. Climate 15, 690–695.

Trenberth, K. E., Stepaniak, D. P., Caron, J. M., 2002. Accuracy of Atmospheric Energy Budgets from Analyses. J. Climate 15, 3343–3360.

Tung, K. K., Orlando, W. W., 2003. On the differences between 2D and QG turbulence. Discrete and Continuous Dynamical Systems–Series B 3, 145–162.

Ulbrich, U., Ponater, M., 1992. Energy Cycle Diagnosis of Two Versions of a Low Resolution GCM. Meteorol. Atmos. Phys. 50, 197–210.

Uppala, S. M., Kållberg, P. W., Simmons, A. J., Andrae, U., da Costa Bechtold, V., Fiorino, M., Gibson, J., Haseler, J., Hernandez, A., Kelly, G. A., Li, X., Onogi, K., Saarinen, S., Sokka, N., Allan, R. P., Andersson, E., Arpe, K., Balmaseda, M. A., Beljaars, A. C. M., van de Berg, L., Bidlot, J., Bormann, N., Caires, S., Chevallier, F., Dethof, A., Dragosavac, M., Fisher, M., Fuentes, M., Hagemann, S., Hlm, E., Hoskins, B. J., Isaksen, L., Janssen, P. A. E. M., Jenne, R., McNally, A. P., Mahfouf, J.-F., Morcrette, J.-J., Rayner, N. A., Saunders, R. W., Simon, P., Sterl, A., Trenberth, K. E., Untch, A., Vasiljevic, D., Viterbo, P., Woollen, J., 2005. The ERA-40 re-analysis. Q. J. R. Meteorol. Soc. 131, 2961–3012.

Vallis, G. K., 2006. Atmospheric and Oceanic Fluid Dynamics. Cambridge University Press, Cambridge, U.K.

Watarai, Y., Tanaka, H. L., 2007. Characteristics of the JRA-25 Dataset from the Viewpoint of Global Energetics. SOLA 3, 009–012.

Wiin-Nielsen, A., 1967. On the annual variation and spectral distribution of atmospheric energy. Tellus 19, 540–559.

Williamson, D. L., Kiehl, J. T., Hack, J. J., 1995. Climate sensitivity of the NCAR Community Climate Model (CCM2) to horizontal resolution. Clim. Dyn. 11, 377–397.

Wu, Y., Ting, M., Seager, R., Huang, H.-P., Cane, M. A., 2010. Changes in storm tracks and energy transports in a warmer climate simulated by the GFDL CM2.1 model. Clim. Dyn.